

ADDING A DIMENSION

Engineering a 3D heart valve disease model and timed release of RNA therapeutics

Casper van der Ven

ADDING A DIMENSION

Engineering a 3D heart valve disease model and timed release of RNA therapeutics

PhD thesis, Utrecht University, The Netherlands

Author: Casper van der Ven
ISBN: 978-94-93184-72-5
Cover Art: Laura Schäffer
Layout: Guus Gijben, Proefschrift All-In-One | Proefschrift-aio.nl
Printing: Proefschrift-aio.nl

The research in this thesis was conducted at the University Medical Center Utrecht, Utrecht University and the Regenerative Medicine Center in Utrecht, The Netherlands; Harvard Medical School and Brigham and Women's Hospital in Boston MA, United States of America; and the Koch Institute for Integrative Cancer Research, Massachusetts Institute of Technology in Cambridge MA, United States of America . The research was supported by a fellowship grant from Cardiovascular Research The Netherlands (CVON), the Harvard Catalyst Reactor Program of the Harvard Clinical and Translational Science Center, an unrestricted grant from CELLINK AB, and a grant from Stichting Zabawas.

Financial support by the Dutch Heart Foundation for the publication of this thesis is gratefully acknowledged.

Copyright © Casper van der Ven 2020. All rights reserved. No parts of this thesis may be reproduced, stored in a retrieval system of any nature, or transmitted in any form or by any means, without prior written consent of the author. The copyright of the articles that have been published has been transferred to the respective journals.

ADDING A DIMENSION

Engineering a 3D heart valve disease model and timed release of RNA therapeutics

EEN DIMENSIE TOEVOEGEN

Ontwikkeling van een 3D hartklepziektemodel en
gecontroleerde afgifte van RNA-therapeutica

(met een samenvatting in het Nederlands)

Proefschrift

ter verkrijging van de graad van doctor aan de Universiteit Utrecht
op gezag van rector magnificus prof. dr. H.R.B.M. Kummeling,
ingevolge het besluit van het college voor promoties
in het openbaar te verdedigen op
dinsdag 10 november 2020 des ochtends 9.15 uur

door

Casper Frederick Theodoor van der Ven
geboren op 2 februari 1989 te Zutphen

PROMOTOREN:

Prof. dr. J.P.G. Sluijter

Prof. dr. P.A.F.M. Doevendans

COPROMOTOREN:

Dr. A. van Mil

Dr. J. Hjortnaes

Table of content

Preface		7
Chapter 1	<i>In vitro</i> 3D model and miRNA drug delivery to target calcific aortic valve disease	11
Chapter 2	Engineering a 3D-bioprinted model of human heart valve disease using nano-indentation based biomechanics	43
Chapter 3	MicroRNA-214 attenuates formation of microcalcifications in a three-dimensional model of human calcific aortic valve disease	77
Chapter 4	Controlled delivery of gold nanoparticle-coupled miRNA therapeutics via an injectable self-healing hydrogel	99
Chapter 5	Non-coding RNAs in cardiac regeneration	125
Chapter 6	Summarizing discussion and future perspectives	153
	Nederlandse Samenvatting	173
	Curriculum Vitae	179
	Acknowledgements	183

Preface

To this date, the sole treatment option for people with calcific aortic valve disease is surgical valve replacement. This procedure is both invasive and costly, and the number of people requiring this procedure is expected to triple by 2050 to roughly 750,000 worldwide, annually. Surgical valve replacement, the gold standard therapy for aortic stenosis, replaces the diseased valve with a prosthetic valve. Aortic valve calcification was perceived a passive disease until aortic valve cells were identified as active players in disease progression. However, there are currently no therapeutic treatment options that can halt or prevent disease progression. Advancements in laboratory research techniques allow for mapping of major pathways in disease progression and identification of potential therapeutic targets. Advances in biofabrication, bioengineering, and biomaterials yield more clinically relevant models, as well as novel drug delivery approaches. Yet, a representative human model of aortic valve calcification is lacking.

Aortic valve interstitial cells inhabit the flexible, dynamic, 3D environment of the aortic valve. They are mechanosensitive cells that maintain and remodel the fibrous extracellular matrix, which makes up the three distinct aortic valve leaflet layers that constantly stretch and relax as the valve opens and closes. However, in a laboratory setting, cells are mostly cultured in stiff, 2D polystyrene flasks, and these culture systems do not accurately represent the native environment of these cells. As a result, the aortic valve interstitial cells behave differently *in vitro* than they would in the heart valve. A model that would mimic the flexible, 3D extracellular matrix, would be a better representation of the native aortic valve to study aortic valve disease.

Newly identified RNAs play a role in the biopathology of aortic valve disease. Non-coding RNAs are strands of nucleic acid that do not code for protein transcription directly, but rather regulate protein expression in cells on a post-transcriptional level. They can stimulate or inhibit protein production and thereby maintain healthy protein levels in the cell. Differential expression of these non-coding RNAs has been found to play a role in disease development, and non-coding RNA can thus be targeted or used for therapeutic purposes. One of the main challenges for these RNA therapeutics is controlled delivery and stability. Serum nucleases break down naked RNA molecules, and entering cells is difficult due to their charge. Chemical modifications and carriers are commonly researched to improve stability and delivery, and there is a great potential for delivery strategies based on RNA therapeutics.

The **main objectives** of the research presented in this thesis are to develop a representative *in vitro* model of human aortic valve disease, and to engineer a drug delivery platform to deliver non-coding RNA over an extended period of time. These are important next steps towards a better understanding of aortic valve disease, towards identification of therapeutic targets, and towards a therapeutic treatment that can slow or halt disease progression.

Chapter 1 introduces the anatomy of the aortic valve and pathobiology of calcific aortic valve disease. Known microRNAs involved in aortic valve disease are discussed, and the opportunities for microRNAs as therapeutic agents are identified. Additionally, requirements for better and more accurate *in vitro* models of aortic valve disease are proposed. The identified challenges and opportunities form the basis for the research presented in this thesis. Applying the previously outlined recommendations, **Chapter 2**, describes how the first human 3D bioprinted heart valve disease model is engineered. Nano-indentation is used to measure the biomechanical properties of the individual layers of the native aortic valve, which are in turn replicated in the model by fine-tuning the concentration and ratio of biopolymers used to mimic the aortic valve extracellular matrix. Non-diseased aortic valve interstitial cells are mixed with these gelatin- and hyaluronic acid-based biopolymers and bioprinted into 3D constructs with the same mechanical properties as the native valve. The cells inside the constructs are exposed to osteogenic factors to mimic disease progression. **Chapter 3** is taking a first important step towards using the 3D aortic valve disease *in vitro* model in search of novel therapeutics by testing the effect of manipulating microRNA expression on the formation of microcalcifications in calcific aortic valve disease. Specifically, aortic valve interstitial cells are producing microcalcifications in the 3D constructs as a result of osteogenic stimulation and microRNA-214 expression is either increased or repressed via mimics or anti-miRs, respectively. Overexpressing miR-214 results in the formation of fewer microcalcifications compared to non-transfected controls.

In a broader perspective, **Chapter 4** describes the role of non-coding RNAs in cardiac regeneration, the repair of cardiac tissue, which in turn enhances or restores the functional capabilities of the heart. Specifically, it studies the role of non-coding RNAs in species with inherent cardiac regenerative capacity to uncover and understand the mechanisms that drive cardiac regeneration, such as cardiomyocyte proliferation and neovascularization. Elaborating on the regenerative capacity in lower vertebrates and rodents and their role as scientific models aids in comprehending the role of non-coding RNAs in cardiomyocyte proliferation and neovascularization. In order to use these non-coding RNAs for therapeutic purposes, reliable delivery strategies need to be developed. **Chapter 5** describes how a drug delivery system is engineered to deliver microRNA therapeutics locally that are released over an extended period of time. An injectable, self-healing hydrogel is designed to release microRNA therapeutics coupled to gold nanoparticles. The interaction of a polymer chain with a nanoparticle gives this

gel shear-thinning and self-assembling properties, making it suitable for injection. The gold nanoparticles are functionalized with a polymer for stability, a peptide to facilitate cellular uptake, and microRNA therapeutics. The gold nanoparticle-coupled miRNAs were released from the hydrogel over the course of several days, proven functional in an *in vitro* assay, and shown to infiltrate the cells in the 3D valve disease model. Furthermore, biodistribution of the gold nanoparticle-coupled miRNA after subcutaneous injection of the loaded hydrogel in mice showed hepatic and renal clearance.

The studies presented in this thesis are summarized in **Chapter 6**, discussing the major findings and future directions.

Chapter 1

***In vitro* 3D model and miRNA drug delivery to target calcific aortic valve disease**

Casper F.T. van der Ven
Pin-Jou Wu
Mark W. Tibbitt
Alain van Mil
Joost P.G. Sluijter
Robert Langer
Elena Aikawa

ABSTRACT

Calcific aortic valve disease (CAVD) is the most prevalent valvular heart disease in the Western population, claiming 17000 deaths per year in the United States and affecting 25% of people older than 65 years of age. Contrary to traditional belief, CAVD is not a passive, degenerative disease but rather a dynamic disease, where initial cellular changes in the valve leaflets progress into fibrotic lesions that induce valve thickening and calcification. Advanced thickening and calcification impair valve function and lead to aortic stenosis (AS). Without intervention, progressive ventricular hypertrophy ensues, which ultimately results in heart failure and death. Currently, aortic valve replacement (AVR), surgical or transcatheter, is the only effective therapy to treat CAVD. However, these costly interventions are often delayed until the late stages of the disease. Nonetheless, 275000 are performed per year worldwide, and this is expected to triple by 2050. Given the current landscape, next-generation therapies for CAVD are needed to improve patient outcome and quality of life. Here, we first provide a background on the aortic valve (AV) and the pathobiology of CAVD as well as highlight current directions and future outlook on the development of functional 3D models of CAVD *in vitro*. We then consider an often-overlooked aspect contributing to CAVD: miRNA (mis) regulation. Therapeutics could potentially normalize miRNA levels in the early stages of the disease and may slow its progression or even reverse calcification. We close with a discussion of strategies that would enable the use of miRNA as a therapeutic for CAVD. This focuses on an overview of controlled delivery technologies for nucleic acid therapeutics to the valve or other target tissues.

Keywords: aortic valve, calcification, 3D model, drug delivery, microRNA (miRNA)

INTRODUCTION

The most prevalent heart valve disease in Western societies is calcific aortic valve disease (CAVD), claiming 17000 lives per year in the United States alone [1] and affecting 25% of people older than 65 years of age [2]. CAVD is a dynamic disease; initial cellular changes that begin at the base of valve leaflets manifest into fibrotic lesions that induce valve thickening, termed aortic sclerosis [3]. The disease later progresses to calcification of the valve, where large calcific masses gradually impair leaflet motion and valve function, eventually causing aortic stenosis (AS) [4]. Without intervention, progressive ventricular hypertrophy ensues, which ultimately results in heart failure and death. CAVD treatment remains challenging as it is difficult to visualize or detect calcification in the early, asymptomatic stage (Figure 1) and no pharmacological therapies have been developed to slow or halt the progression of CAVD [5]. Although lipid-lowering therapy was proposed as a potential therapy for CAVD based on identified lesions similar to those in atherosclerotic plaques, it was shown to be ineffective in a meta-analysis of randomized placebo-controlled clinical trials on 2344 patients [6]. Currently, aortic valve replacement (AVR) remains the only available clinical treatment option for AS [7]. These costly and invasive procedures are often delayed until a patient's functional leaflet movement is severely impaired by gross calcium deposition [8]. Each year, over 275000 patients undergo surgical AVR worldwide [9] and this number is projected to triple by 2050 [9]. The emergence of transcatheter AVR technologies in 2002 created a less-invasive alternative; however, due to an increased risk for complications, this option is currently reserved for patients with severe comorbidities who are unsuitable for conventional open-heart surgery [10]. To date, there have been more than 80000 transcatheter AVRs performed worldwide [11]. As the prevalence of CAVD is expected to increase with the rising global life expectancy, CAVD becomes a growing burden that demands further understanding of the disease process and exploration of potential non-invasive (drug-based) therapies.

In this review, we provide a background on the aortic valve (AV) and the pathobiology of CAVD. We then highlight current directions in the community to develop functional 3D models of the AV as tools to dissect pathological processes in a controlled manner as well as forecast future directions in the development of *in vitro* valve models. Additionally, we consider an often-overlooked aspect of valve biology and pathology: miRNA regulation and misregulation. miRNAs present an attractive therapeutic alternative to intervene early during the disease process and potentially delay or even reverse disease processes after initiation. For miRNAs and other potential (bio)therapeutics, the controlled delivery of the molecules to the target tissues and cells of the valve is an additional challenge. In the present study, we review current directions within the drug-delivery community and suggest how they may affect the treatment of CAVD.

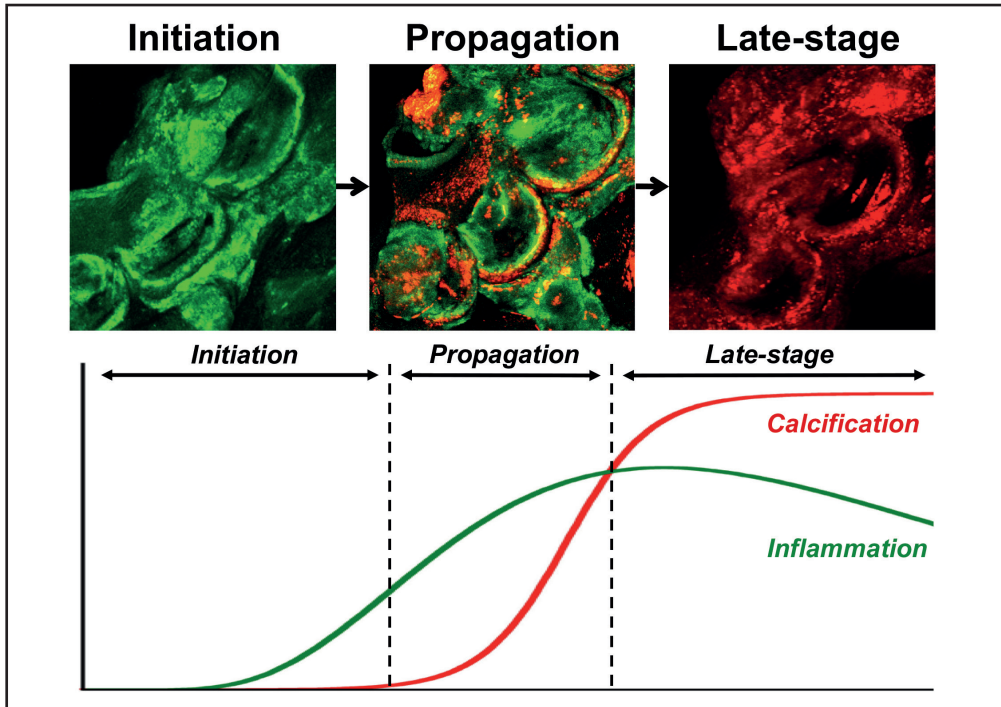


Figure 1 - CAVD progression

Initiation, propagation and late-stage calcification are three distinct stages of calcification in CAVD that can be identified by molecular imaging. Macrophages are labelled green and calcification is labelled red in a molecular imaging strategy to highlight the inflammation-dependent mechanism of calcification [128].

THE AORTIC HEART VALVE

The AV is located at the junction between the left ventricle and the aorta and ensures unidirectional blood flow into the systemic circulation from the heart. In a healthy AV, the three thin, semilunar leaflets recoil and open the pathway for blood flow during systole. When the heart relaxes during diastole, under the backpressure from the aorta, the leaflets stretch and seal the orifice, preventing regurgitation of blood into the left ventricle. Hence, an efficient opening and closing of the AV is imperative to the proper functioning of the heart. The valvular tissue microstructure, particularly the composition and orientation of the extracellular matrix (ECM), plays an important role in maintaining the mechanical and biochemical behavior of the valve. Each leaflet has a complex architecture and comprises three distinct layers: the ventricularis, the spongiosa and the fibrosa. The zona fibrosa, closest to the outflow surface, is a layer densely packed with collagen fibers that provide the tensile strength needed to bear diastolic stress and prevent leaflet prolapse. The zona spongiosa predominantly consists of glycosaminoglycans and proteoglycans and acts as a bearing surface, reducing friction

between the zona fibrosa and the zona ventricularis. The zona ventricularis is an elastic layer rich in elastin fibers that allow the leaflet to extend and recoil [12]. There are two major types of valve cells that populate the AV and maintain its health: the valve endothelial cells (VECs) that coat the blood-contacting surfaces and the more abundant valve interstitial cells (VICs) that populate the three distinct layers of the leaflets. VICs are a heterogeneous and dynamic cell mixture; multiple VIC phenotypes have been identified in AV leaflets [13]. The role of VICs includes synthesizing, degrading, and repairing the ECM, which are all crucial in maintaining the tissue homeostasis of the valve and its function.

PATHOBIOLOGY OF CAVD

Cell phenotypes contributing to the disease progression

Based on its association with aging, CAVD was traditionally assumed to be a passive, degenerative disease resulting from years of wear and tear due to mechanical stress. However, CAVD is now viewed as an active, cellular-driven disease [14]. In native healthy AVs, VICs reside primarily as quiescent fibroblast-like cells but can undergo phenotypic activation in response to injury or pathology (Figure 2). Upon exogenous pathological stimulation, VICs can differentiate into activated myofibroblast-like cells (aVICs), which undergo tissue repair and remodeling [15]. Persistent activation of VICs leads to pathological ECM remodeling and valve fibrosis [15]. These pro-fibrotic cells are characterized by increased expression of markers such as α -smooth muscle actin (α -SMA) [16]. Further, myofibroblast-like cells can differentiate into osteoblast-like cells (oVICs), which are ultimately responsible for the deposition of calcium and formation of osteogenic nodules. These pro-calcific cells are characterized by the presence of osteoblast-related proteins such as osteocalcin, osteonectin, and osteogenic transcription factors such as runt-related transcription factor 2 (Runx2) [17,18]. In addition, expression of progenitor cell markers has been identified in distinct subpopulations of VICs. Particularly, VICs positive for the progenitor cell marker ATP-binding cassette, sub-family G, member 2 (ABCG2) were found to deposit a more calcified matrix upon osteogenic induction, suggesting a possible role in the development of osteogenic VICs during valve pathology [19]. Furthermore, the level of circulating osteogenic progenitor cells in CAVD patients was significantly higher than in control patients in a study of 46 patients and 46 control subjects [20].

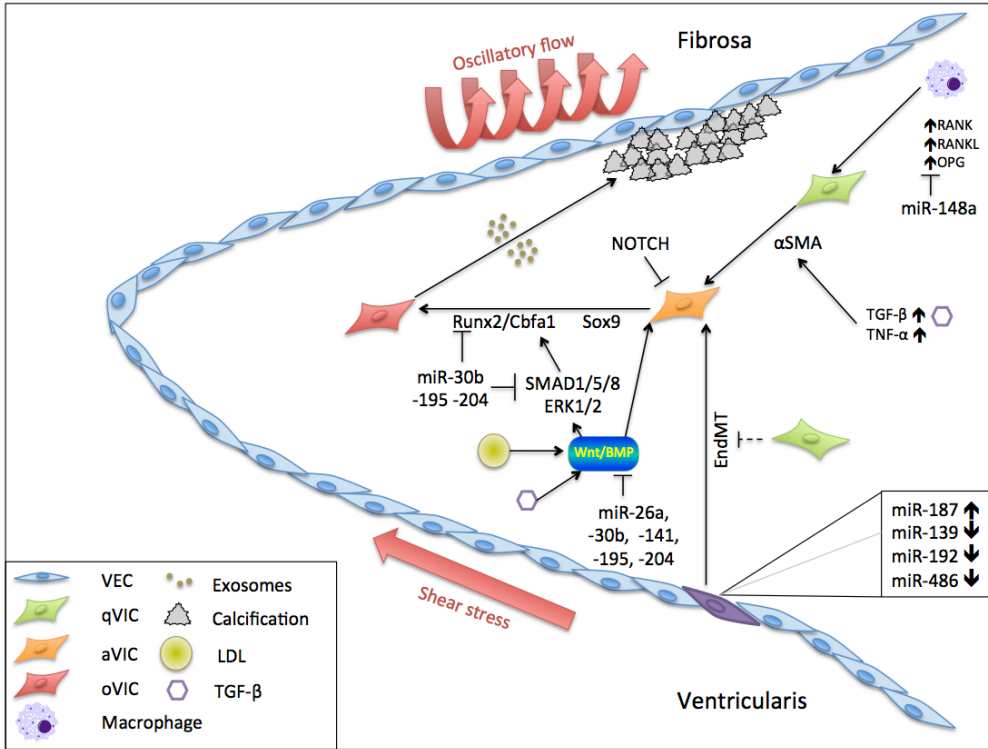


Figure 2 - Molecular and cellular mechanisms in CAVD

VICs differentiate from a quiescent state (qVIC) through an activated state (aVIC) into osteogenic cells (oVIC) that contribute to calcification of the fibrosa side of the AV. Mechanical stresses, EndMT, LDL, TGF-β and TNF-α affect the mechanism of disease via multiple pathways, including RANK, RANKL, OPG, α-SMA, Runx2 and BMP.

Mechanisms and signaling pathways

CAVD is multifactorial disease; many mechanisms and events contribute to the development of CAVD. *In vivo* studies have shown that early CAVD lesions initiate on the fibrosa side of the valve [21]. Pathological triggers such as growth factors, inflammatory cytokines, subendothelial deposits of oxidized low-density lipoproteins (LDLs), mechanical stress, and oxidative stress have been described to cause endothelial dysfunction, which in turn may initiate the activation of VICs [22–26]. In addition to VIC activation, VECs are known to have the capacity to differentiate into endothelial-derived VICs (eVICs) through endothelial-to-mesenchymal transition (EndMT) and can further differentiate into osteoblastic cells, promoting pathological remodeling in CAVD. It has been demonstrated that VIC–VEC communication is critical to maintain valve homeostasis [27], and that disruption of VIC–VEC communication accelerates the EndMT process, advancing valvular osteogenesis [28].

At the molecular level, a number of studies have shown increased expression of various osteogenic factors and signaling pathways that may be involved in CAVD. For example, pathological ECM remodeling contributes to the release of cytokines, such as transforming growth factor β 1 (TGF- β 1) and tumor necrosis factor α (TNF- α), which are potent inducers of VIC myofibroblast activation [29,30]. Notably, TGF- β 1 works in synergy with its downstream effector osteoblast-cadherin through a number of downstream signaling pathways, such as extracellular signal-regulated protein kinases 1 and 2 (ERK1/2) and the similar to mothers against decapentaplegic 2 and 3 (SMAD2/3) pathways, in the regulation of myofibroblast activation of VICs [31]. Moreover, bone morphogenetic protein 2 (BMP-2), a key inducer of VIC calcification, is thought to act through p-SMAD1/5/8 and p-ERK1/2 signaling to increase Runx2 expression [32]. On the other hand, Notch signaling has been demonstrated, through *in vivo* studies, as a negative regulator that represses osteoblast-like calcification pathways mediated by BMP-2 [33]. In addition, inflammation stimulates osteoblast differentiation; cytokines produced by inflammatory cells affect the expression of receptor activator of nuclear factor κ -B ligand (RANKL) and osteoprotegerin (OPG) in the RANKL/receptor activator of nuclear factor κ -B (RANK)/OPG pathway and consequently stimulate the Runx2 pathway [30]. Studies also found that excess of circulatory LDL acts through the low-density lipoprotein receptor-related protein 5 (LRP5)/Wnt signaling pathway, which stimulates the Runx2-mediated pathway and thereby induces mineralization [34]. Interestingly, studies have also suggested that mechanical stiffness promotes VIC activation through an up-regulation of phosphoinositide 3-kinase (PI3K)/Akt signaling pathway [35,36]. Although a number of pathophysiological cues have been associated with the activation of VICs leading to CAVD, knowledge on the regulation of pathologic changes in VIC phenotype is still limited due to the unavailability of adequate disease models. Understanding the mechanism involved in VIC regulation of tissue homeostasis requires a suitable *in vitro* system that closely resembles the *in vivo* microenvironment native to the AV.

TOWARDS 3D CAVD MODELS

Understanding the cellular contribution to the progression of CAVD has proven to be challenging both *in vivo* and *in vitro*. Although *in vivo* animal models, such as porcine and murine models, offer complexity comparable with that in humans, these models are often based on high cholesterol diets to induce hypercholesterolaemia and subsequent atherosclerosis, which is not currently considered as a main etiology of CAVD [5]. In addition, most common 2D *in vitro* approaches have been shown to spontaneously activate pathological differentiation of VICs into myofibroblast-like cells. Furthermore, the contributions that knowledge of valvulogenesis could make to improve *in vitro* models are often overlooked [37]. Soft hydrogels have maintained VIC phenotype *ex vivo* [35]; however, they lack the complexity of VIC-VEC interactions and

multilaminar structure in the native valve. Emerging evidence suggests that hydrogel-based 3D culture systems may provide a more tissue-like environment given their similarity to the natural ECM [38]. Recent studies have used various materials, such as hyaluronan hydrogels [39] and synthetic PEG-based hydrogels [38,40], to engineer heart valve tissue scaffolds for the study of VIC behavior. VICs cultured in materials derived from natural ECM polymers, such as collagen and fibrin, showed high viability; however, these hydrogel materials are not ideal due to their susceptibility to degradation and compaction [41]. On the other hand, methacrylated gelatin (GelMA) and methacrylated hyaluronic acid (HAMA) have successfully been used as a photocrosslinkable VIC-laden hydrogel scaffold. However, GelMA alone posed challenges to quick degradation whereas HAMA alone demonstrated limited cell adhesiveness. Recently, we utilized a hybrid GelMA–HAMA hydrogel platform to encapsulate VICs, which maintained VICs in a quiescent phenotype. These quiescent VICs further differentiated into myofibroblast-like cells upon TGF- β 1 stimulation [28] and osteoblast-like cells when treated with osteogenic medium [42]. In addition, our recent study demonstrated the formation and growth of microcalcification recapitulating early disease states of native cardiovascular tissue [43]. Although these 3D hydrogel platforms provided controllable models that more closely recapitulate the *in vivo* environment to study the transition of VICs from a quiescent to an activated phenotype and formation of microcalcifications, they were not complete as they did not include the three distinct layers present within the native valve that contribute independently to the calcification process or the layer of endothelial cells that covers the leaflets. For future improvement, 3D-bioprinting technologies present promising approaches for engineering better representations of the native valve by incorporating all three distinct layers of the valve (Figure 3). A layer of endothelial cells can be co-cultured on top of the three layers to mimic cell–cell communication and paracrine signaling in the native valve. Moreover, the benefit of an automated system may alleviate some construct-to-construct variability and increase reproducibility as opposed to manual pipetting. This new approach could further be used to study cellular and molecular mechanisms of CAVD and serve as a drug-screening tool to aid in the development of a therapeutic treatment for CAVD. Furthermore, 3D printing opens doors to other disciplines as well, such as tissue engineering and biofabrication. Expanding the tri-layered 3D model to a geometrically accurate AV is the first step towards understanding how hemodynamic flow patterns affect the disease development when studied in a bioreactor. These efforts could lead to personalized tissue-engineered biofabricated heart valves that can be seeded with a patient’s autologous living valve cells, replacing the current prosthetic valves in AVR, bringing personalized therapy one step closer to reality. AV replacement is the current gold standard of therapy, but with the current advances of *in vitro* disease modeling and drug screening, an improvement through drug-based therapy is within reach and could potentially treat or even prevent CAVD.

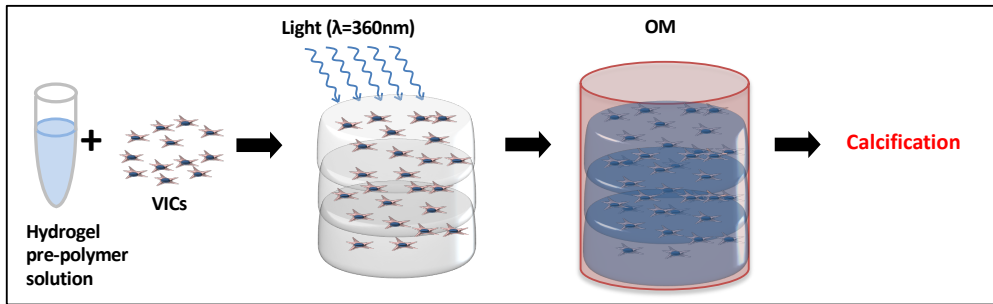


Figure 3 - 3D-bioprinted CAVD model

Isolated human aortic VICs are suspended in a hydrogel pre-polymer solution with photo-initiator cross-linking agent. Three distinct layers are bioprinted and cross-linked using UV light. Exposure to osteogenic medium (OM) activates the quiescent VICs to differentiate into activated VICs and osteogenic VICs, leading to the formation of microcalcifications, thereby mimicking CAVD progression.

Unfortunately, common valve specific drug targets required for pharmacologic approaches to treat vascular disease are not transferable to CAVD [5]. These targets could include G-protein coupled receptors, cadherin-11, or lipids, and can be targeted with small molecules, antibodies or nucleic acid therapeutics. Identifying if other pathways could be potential drug targets in CAVD and validating these approaches may be studied in appropriate 3D disease models of CAVD. In the next section, we will focus on potential drug targets and provide an overview of the candidates for therapeutic targeting, highlight modifications to improve their function and discuss potential delivery strategies.

miRNA IN AORTIC VALVE DISEASE

Biogenesis and activity of miRNA

miRNAs and miRNA regulation are often overlooked as therapeutic targets, especially in cardiac valve disease. miRNAs were first discovered by Victor Ambros and his team in 1993 [44]. They found that the *lin14* gene codes not for a protein but for a pair of small RNAs, later named ‘microRNA’ (miRNA or miR). Functional mature miRNAs are single stranded, approximately 22 nucleotides long, RNAs that regulate protein expression by partial complementary binding to their target mRNA, thus inhibiting its translation. RNA polymerase II transcribes primary miRNA transcripts (pri-miRNAs) that contain one or multiple hairpin loops [45]. Drosha, a dsRNA-specific type III endoribonuclease, and DiGeorge syndrome critical region gene 8 (DGCR8) process pri-miRNAs into precursor miRNAs (pre-miRNAs) of approximately 70 nucleotides [46,47]. If correctly processed, nuclear export factor exportin 5 transports pre-miRNAs from the nucleus to the cytoplasm where Dicer, endoribonuclease III, removes the hairpin loop yielding a miRNA duplex of 18–22 bp [48,49]. When the duplex

unwinds, the argonaute protein loads one strand, the guide strand or mature strand, into the RNA-induced silencing complex (RISC) [50]. This can lead to mRNA degradation or to obstruction of translation, depending on the level of complementarity between the mRNA target and the miRNA [51–53]. The other strand, the passenger strand, is often degraded although in selected cases it also serves as a functional miRNA. The complete process of strand selection is not yet fully understood. Argonaute and Dicer are two of the multiple proteins that play a role in this process [54]. Since the discovery by Ambros and his team, upwards of 1800 miRNAs have been identified in humans regulating a broad range of biological processes [55]. On account of the imperfect base pairing of miRNAs and their target mRNAs, one miRNA can affect multiple processes. Assigning the mRNA targets and biological roles to a miRNA has identified expression patterns specific to tissues, developmental processes, and disease development [56]. From these findings, miRNAs are now thought to be key regulators of pathological processes in cardiovascular diseases, including cardiovascular calcification [57]. Furthermore, circulating miRNAs can potentially function as biomarkers for early detection of heart disease [58,59] for modification of disease mechanisms, and for determining the ideal timing of surgical intervention [60]. Here, we provide an overview of studies that have identified miRNAs in CAVD and AS.

Known miRNAs in aortic valve disease

miRNAs that have been identified in cardiovascular diseases serve as regulators of multiple processes (Figure 2) [61]. Using the broad parameters “aortic | valve”, Abcam Firefly Discovery Engine identified 30 publications on 41 miRNAs related to various biological processes, including fibrosis (miR-21 [62]), inflammation (miR-125b [63]; miR-148a [64]), differentiation (miR-204 [65]), and calcification (miR-141 [66]; miR-204 [65]; miR-30b [67]; miR-214 [68]). Tables 1 and 22 provide an overview of the profiling and functional studies that have been conducted to highlight the roles of these miRNAs in their respective target pathways.

As shown in Table 1, five of these studies used a miRNA candidate approach or microarray to identify the expression of miRNAs in AV leaflets from patients with AS undergoing AVR surgery. Real-time quantitative PCR (RT-qPCR) validated microarray data. First, AS patients were compared with aortic insufficiency patients, which demonstrated that in bicuspid valve samples miR-26a, -30b and -195 were down-regulated in patients with AS [69]. Second, microarray profiling identified 35 differentially expressed miRNAs between bicuspid and tricuspid AVs in patients with AS [66]. RT-qPCR validated down-regulation of miR-141. Third, a comparison of calcified and non-calcified AV tissues confirmed lower expression levels of miR-30b in the calcified valves using RT-qPCR [67]. Fourth, down-regulation of miR-148-3p was shown in bicuspid compared with tricuspid valves [64]. Fifth, microarray analysis of calcified valve tissue compared with control tissue yielded the identification of up-regulated miR-125b, and down-regulated miR-374b, -602 and -939 [63].

Table 1 - Overview of miRNA profiling studies in CAVD

This table provides an overview of the differentially expressed miRNAs in diseased AV tissues. AI, aortic insufficiency; TAV, tricuspid aortic valve.

miRNA	Tissue	Finding	Method	Patients	Reference
26a, 30b, 195	Whole bicuspid AVs	Down-regulated	Microarray + RT-qPCR	9 BAV patients with AS/AI	[69]
30e, 32, 145, 151-3p, 152, 190, 373, 768-5p 22, 27a, 124-3-pre, 125b-1-pre, 141, 185-pre, 187, 194, 330-5p, 377, 449b, 486-3p, 551a-pre, 564, 566-pre, 575, 622, 637, 648-pre, 1202, 1282, 1469, 1908, 1972	Bicuspid and tricuspid AVs	Up-regulated Down-regulated	Microarray + RT-qPCR	19 BAVs 17 TAVs patients with AS	[66]
30b	Calcific AV and adjacent tissue	Down-regulated	RT-qPCR	10 patients with AS	[67]
148-3p	Excised AV tissue	Down-regulated	RT-qPCR	4 BAVs compared with healthy AV	[64]
125b 374b, 602, 939	Calcific AV and healthy AV	Up-regulated Down-regulated	Microarray + RT-qPCR	20 patients with AS	[63]
214	Porcine AV	Up-regulated	Microarray + RT-qPCR	Ex vivo shear stress calcification model	[20]

Table 2 - Overview of functional studies of miRNAs and their roles in CAVD

This table provides an overview of the differentially expressed miRNAs in diseased AV tissues that have been validated in functional studies. haVIC, human aortic valve interstitial cell; paVIC, porcine aortic valve interstitial cell.

miRNA	Target (genes)	Cell	Results
30b	RUNX2, SMAD1, CASP3, SMAD3, BMP2, NOTCH1	haVICs	Vitiates BMP2-induced osteoblast differentiation and apoptosis through direct targeting of Runx2, Smad1 and caspase-3 [67]. Down-regulates calcification-related gene pathways [69]
26a	ALPL, BMP2, SMAD1	haVICs	Repressed several of the calcification-related genes and increased the mRNA levels of genes that may have roles inhibiting calcification (JAG2, SMAD7) [69]
195	BMP2, RUNX2, SMAD1,-3,-5 JAG2, SMAD7	haVICs	Activates pro-calcification gene expression [69] Increases calcification repressing genes JAG2 and SMAD7 [69]
148a-3p	IKBKB	haVICs	Cyclic stretch represses miR-148a-3p and activates NF-κB-dependent inflammatory signaling pathway [64]
141	BMP2	paVICs	Blocks TGF-β-triggered BMP2 signaling [66]
204	RUNX2, BMP2	haVICs	Negatively regulates osteogenic differentiation by repressing RUNX2 [65]
214	TGF-β1	paVICs	Regulates TGF-β1 regulator of calcification in early stages of CAVD [68]

To understand the role these miRNAs play in AV pathophysiology, functional studies have been conducted in 2D *in vitro* models. Table 2 provides an overview of current knowledge of miRNAs and their target genes in fibrocalcific valve remodeling. Multiple studies demonstrated that miR-30b is functionally involved in the prevention of osteogenesis and apoptosis by direct targeting of Runx2, Smad1, and caspase-3 [67,69]. Similarly, miR-26a down-regulates multiple genes related to calcification [69], miR-141 blocks TGF- β -triggered BMP-2 signaling, and miR-204 represses Runx2 [66], consequently inhibiting osteogenic differentiation [65]. Thus, valve calcification could be caused by negative regulation of these miRs, which would abrogate various protective mechanisms. Furthermore, abnormal hemodynamics around the AV, as observed in patients with AS, aid disease progression by activating an inflammatory response through the NF- κ B-dependent signaling pathway, which may be a result of miR-148a-3p repression [64]. This pathway is also activated in the aortic VECs on the fibrosa layer of the valve by shear-sensitive miR-139-3p, -187, -192, and -486-5p [70]. This inflammatory response recruits immune cells to the valve, increasing the levels of CCL4 chemokine and, as a consequence, down-regulating miR-125b in infiltrating macrophages [63], leading to calcification. Conclusively, AV disease progression is stimulated by inhibition of miRs that regulate protective mechanisms and by disturbed hemodynamics that activate an inflammatory response. Lastly, it is hypothesized that osteoblast differentiation, by repressing the activity of TGF- β type I receptor as part of the osteoblast lineage commitment program [71] and by inhibiting osteonectin expression through canonical Wnt pathway, applies to valve calcification in a similar fashion.

In addition to the classic approach of miRNA array analysis and RT-qPCR validation, a recent study identified miR-214 as a regulator of AV calcification via the TGF- β 1 pathway using an *ex vivo* shear and calcification model with porcine aortic VECs. The porcine miRs identified in the present study are homologous with human miRs, as confirmed by miRBase. In the shear and calcification model, the cells were subjected to oscillatory shear stress for 2 days. When the fibrosa side was exposed to the oscillatory shear, calcification was triggered, whereas no calcification was observed when the ventricularis side of the valve was subjected to the same condition. In these experiments, miR-214 was significantly up-regulated by oscillatory shear in the fibrosa side compared with the ventricularis side and compared with fresh AV tissue. These results support the conclusion that in fibrosa miR-214 is regulated in a shear- and location-dependent fashion. Immunofluorescent staining of TGF- β 1 revealed increased expression in the fibrosa layer in the endothelium, sub-endothelium, and in the interstitial cells upon miR-214 silencing. This strongly suggests that miR-214 serves as a key regulator of AV calcification through modulation of TGF- β 1 signaling. Inhibiting miR-214, however, did not attenuate calcification initiated by exposure to oscillatory shear, which suggests that miR-214 modulates gene expression in AV disease in the early stages of AV pathogenesis rather than the late stages [68].

Moreover, the aforementioned circulating osteogenic progenitor cells are thought to play a significant role in CAVD pathogenesis. A recent study that compared AS patients with control subjects showed that these circulating osteogenic progenitor cells may be regulated by miRNAs. Specifically, miR-30c levels were higher in the AS groups compared with the control group, whereas miR-31, -106a, -148a, -204, -211, and -424 levels were lower. The study also highlighted a correlation between miR-30c expression levels and calcification in AS patients, and that the level of miR-30c and the number of circulating osteogenic progenitor cells decreased after AVR. The study concluded that differential expression of ossification-related miRNAs could be related to the differentiation into circulating osteogenic progenitor cells [20].

Recently, we have shown that extracellular vesicles play a role in cardiovascular calcification [72–74,43,75]. In addition, it was shown that these calcifying vesicles are exosomes [76] and that they may contain miRNA [77–80]. It is yet to be determined how these extracellular vesicles release their content and by which mechanisms they interact with cells and the ECM to induce formation of microcalcifications. Evidence of the presence of miRNA in calcifying extracellular vesicles gives weight to the hypothesis that these miRNAs can be potential therapeutic targets for CAVD.

miRNAs AS THERAPEUTIC TARGETS

The discovery that miRs play essential roles in a plethora of biological processes and that differential expression of miRNAs is a common contributor to cardiovascular disease, specifically to inflammatory responses and calcification, has sparked interest in targeting miRNAs with therapeutics. Expression vectors, small-molecule inhibitors, antisense oligonucleotides (ASOs) (or antagomirs or antimirs), and miR-mimics are the four avenues that are currently explored for therapeutic intervention.

Expression vectors, or miRNA sponges, are artificial miRNA-binding sites that isolate endogenous miRNAs when overexpressed for a specific mRNA, consequently eliminating the effect the miRNAs have on their target mRNA [81]. Small molecule-based approaches function as translational regulators of the target miRNAs, rather than targeting the miRNAs themselves. Due to the high effector concentration for half-maximum response (EC50) and the unknown direct targets, the therapeutic potential of small-molecule inhibitors is constrained. Antimirs are fully complementary to their specific target miR and, by binding to them, relieve mRNA targets from degradation or translational blockage by the specific miR. Oligonucleotides without any modification or encapsulation are prone to serum nucleases, have a low binding affinity for their target miRs, demonstrate poor pharmacodynamics/pharmacokinetics (PD/

PK), and are incapable of crossing negatively charged cell membranes on account of their positive charge. The next section therefore highlights several modifications and multiple delivery strategies used to improve the therapeutic use of miR and antimiR oligonucleotides.

Chemical modifications of miRs and antimiRs

It is imperative to improve stability and efficacy of miR and antimiRs, and to reduce their degradation by serum nucleases, prior to applying these oligonucleotides as therapeutic agents. Stability can be increased by 2'-O-methyl (2'-OMe) modification, though this does not increase the resistance to serum nucleases [82]. 2'-OMe oligonucleotides can be further stabilized by replacing non-bridging oxygen atoms in the phosphate backbone with sulfur atoms, creating phosphorothioate bonds, making them less susceptible to serum nucleases that cleave phosphate bonds. Replacing all non-bridging oxygen atoms, however, often removes all binding affinity for the target miRNA [83]. Replacing a limited number of phosphodiester bonds with phosphorothioate bonds allows for more nuclease resistance without reducing the binding affinity. Injecting these phosphorothioate-modified (anti)miRs directly into the bloodstream prolonged their time in the circulation due to their higher plasma protein binding, which improved their PD/PK. This does not inhibit uptake by tissues, as the plasma protein binding affinity is still lower than the binding affinity of tissues [84].

Further chemical modification of (anti)miRNA strands leads to improved efficacy and tissue distribution *in vivo*. Specifically, a combination of 2'-OMe modifications, asymmetric phosphorothioate modification on the 3' and 5' ends, plus a 3' cholesterol tail is now a commonly used strategy for stable miRNA modification [85,86]. At the same time, additional modifications at the 2' sugar position were shown to improve nuclease resistance and binding affinity. These modifications are 2'-O-methoxyethyl (2'-MOE), 2'-fluoro (2'-F), and locked nucleic acid (LNA) modifications. Superior efficacy was achieved by 2'-MOE-modifications over 2'-OMe-modification [87,88]. 2'-F-modifications alone do not yield nuclease-resistant oligonucleotides, though in combination with phosphorothioate backbone modification, these oligonucleotides achieved better miRNA inhibition than any of the aforementioned modified oligonucleotides [89]. LNA modifications achieve a higher binding by tethering the 2' oxygen via a methylene bridge to the 4' carbon [90]. The best miRNA inhibition at a low dose with increased efficacy was achieved by combining LNA modifications in a recurring pattern of two DNA bases and one LNA base with 2'-F modifications [82]. This higher binding affinity creates room for miRNA inhibition with shorter sequences, and for oligonucleotides that only bind the seed region of their target miRNAs [91]. This evidence supports the hypothesis that one individual oligonucleotide with LNA modification can silence an entire miRNA family without inducing any off-target effects (OTEs). More recent modifications focus on changing the oligonucleotide conformation at non-nucleotide locations. N,N-diethyl-4-(4-nitronaphthalen-1-ylazo)-phenylamine (ZEN) modification at both ends of the sequence

increases binding affinity and efficiency of a 2'-OMe-modified oligonucleotide, while simultaneously reducing toxicity [92]. All of these discoveries demonstrate the tremendous achievements in improving binding affinity, nuclease resistance, and efficacy of (anti)miRs. However, for *in vivo* applications of (anti)miRs as nucleic acid therapeutics, a delivery vehicle is often required to achieve optimal efficacy at a reasonable dose.

Delivery vehicles for miR and antimiR oligonucleotides

Despite the improvements with direct chemical modification of miRNA molecules, delivery efficiency is largely dependent on the design of delivery vehicles for *in vivo* applications. Limited tissue distribution and excretion occur shortly after administration when chemically modified (anti)miR oligonucleotides are introduced without a carrier, requiring a higher dosage to achieve *in vivo* effect, thereby increasing the chances of undesirable OTEs and increasing overall cost. Thus, the engineering of an appropriate delivery system is critical to efficient *in vivo* application of miR and antimiRs. The main functions of these delivery systems are protecting against nucleases to prevent premature degradation [93], avoiding recognition by the immune system, preventing non-specific interactions with other proteins and cells, preventing excretion via the liver and kidneys, exiting the circulation into the target tissue, facilitating uptake by the target cells, and releasing their content intracellularly for incorporation into the RNA processing machinery [94–100]. There are many approaches to aid in the delivery of (anti)miRs, including polymer-, lipid-, conjugation-, antibody-, microbubble-, and inorganic nanoparticle-based approaches. We elaborate on some of the most promising strategies here.

Nanoparticle/polymer-based approaches focus on the interaction between the (anti)miRs and the functional block of the polymer, allowing more flexibility while controlling nanoparticle size, yielding a nearly homogeneous solution of nanoparticles with minimal size distribution. Effective drug delivery *in vivo* is highly dependent on the size of the nanoparticles. Nanoparticles with a diameter between 10 and 100 nm have been shown to functionally deliver (anti)miRs, siRNA, and small molecules [101]. Common polymers used for the synthesis of this kind of nanoparticles include polyethyleneimine (PEI), poly(lactic acid) (PLA), and poly-L-lysine (PLL).

Lipid-based approaches are based on the interactions between the hydrophobic group of lipids and water molecules that lead to the formation of micelles or liposomes [102] and release their content by destroying the stability of the endosomal membrane via fusogenic lipids or pH-sensitive peptides. This creates liposomes that can be categorized as neutral liposomes, ionizable lipids, fusogenic lipids, and PEG liposomes. Neutral liposomes interact little with serum proteins, because of their lack of charge, leading to improved stability [103,104]. Depending on both internal factors (lipid composition) and external factors (e.g. type of solution, temperature), liposomes of different sizes can be created. Typically, small

liposomes are 20–200 nm, large liposomes 200 nm–1 μm , and giant liposomes $>1 \mu\text{m}$ [105]. Their relatively large size slows cellular uptake and can be counteracted by incorporating 1,2-dioleoyl-sn-glycero-3-phosphoethanolamine [106]. Cationic liposomes consist of a cationic head, a connecting bond, and a hydrophobic tail, and form complexes with the (anti)miR based on their electrostatic interaction with the negatively charged (anti)miR [107]. Fusogenic lipids have the capability to fuse with the target membrane without external stimulation to release their therapeutic content into the cell, facilitating delivery of therapeutics that would otherwise not be permeable to the cell membrane [108,109]. PEG liposomes have an increased PD/PK compared with non-PEGylated liposomes due to increased water solubility, reduced enzymatic degradation, limited immunogenic responses, and lower renal clearance [110].

Conjugation-based approaches rely on direct conjugation of the cargo to the delivery material. Conjugation of siRNA to cholesterol [111] and other lipophilic molecules [112] showed the first efficacy *in vivo*. Other delivery materials that have been tested are antibodies, aptamers, peptides, polymers, and small molecules [113]. One example is Dynamic PolyConjugates, which are injected intravenously and target hepatocytes in the liver using N-acetylgalactosamine (GalNAc) ligands. After endocytosis, the PEG decomplexes from the membrane-disrupting polymer poly(butyl amino vinyl ether) (PBAVE) due to the increasingly acidic environment inside the endosome, exposing this polymer and allowing for endosomal escape. The bond linking the siRNA to this polymer is reduced in the cytoplasm, releasing the functional siRNA, causing RNA interference [114]. Another example of a conjugate system uses the same hepatocyte targeting ligand GalNAc conjugated with siRNA. A triantennary spacer links the 3' end of the sense strand of the siRNA to three GalNAc molecules [115,116]. Alnylam Pharmaceuticals produced a GalNAc conjugate that was administered both intravenously and subcutaneously. The latter showed greater uptake of siRNA in the liver and increased knockdown [117].

Microbubbles have been used in combination with ultrasound to deliver anti-miRs to the myocardium in an ischemia reperfusion mouse model [118]. The microbubbles are formed by vigorously mixing 1,2-distearoyl-sn-glycero-3-phosphocholine, 1,2-stearoyl-3-trimethylammonium-propane and polyoxyethylene-40-stearate in H₂O, glycerol and propylene glycol, in the presence of perfluorobutane gas. The anti-miRs are bound to the microbubbles via electrostatic interaction between the cationic microbubble and the anionic anti-miRs, and injected intravenously. Local ultrasound waves ensured destruction of the microbubbles releasing the anti-miRs at the target location, a process named ultrasound triggered microbubble destruction (UTMD). This resulted in sustained intracellular delivery of the anti-miRs in cardiomyocytes without causing apoptosis and with a mild immune response.

A combinatorial approach of the aforementioned lipids results in the most effective transfection agents. Lipid nanoparticles (LNPs) (Figure 4) consist of an ionizable lipid that complexes with the siRNA, increases cellular uptake, and aids endosomal escape; a phospholipid that provides structure to the lipid bilayer; a cholesterol that provides stability to the lipid bilayer; and a lipid-anchored PEG that limits aggregations and non-specific uptake, and that lowers the degradation rate [119,120]. PEGylation of delivery vehicles reduces the non-specific interactions with serum proteins, immune cells, and non-target tissues, thereby prolonging the time until they are filtered by the liver and renal system. Most LNPs, and other delivery systems, rely on endocytosis for entering their target cells. Ionizable lipids and ligands specific for receptors on the target cells in the outer shell delivery systems aim to trigger receptors to expedite endocytosis [121]. After endocytosis, the LNPs must release their content into the cytoplasm before the endosome is degraded by lysosomes. During maturation of an endosome, its pH is lowered to 5. The pKa of common ionizable lipids is often approximately 6.5. At this pH, the nitrogen atoms on the ionizable lipid deprotonate and decomplex from the miRs and anti-miRs. It is hypothesized that the ionizable lipid induces a lipid phase transition and thereby disrupts the endosomal membrane, releasing the ASOs into the intracellular environment [122]. There, the guide strand of the ASOs is loaded into the RISC machinery. Therefore, conjugation of the 5'-end of this strand must be avoided [123]. Thus, conjugation of the sequences and modifications of the backbone have to be carefully considered to establish proper strand selection by the RNA processing machinery RISC and to avoid incomplete hybridization to other, non-target mRNAs leading to OTEs [97].

Recently, effective delivery has been achieved with the use of gold nanoparticles as a delivery vehicle for both siRNA and miRNA. Gold nanoparticles were functionalized with siRNA, made possible by modification with thiol groups on the 5'-end of the antisense strand, and with a fusogenic peptide linked to a thiol-modified PEG for targeting. The thiol groups allow covalent bonding of the nucleic acid and the PEG-peptide complex to the gold nanoparticle. These functionalized gold nanoparticles were doped in a hydrogel and implanted in a colorectal cancer mouse model adjacent to the tumor, leading to functional *in vivo* silencing of Kras, an important gene in cancer progression, leading to complete remission. In further experiments, the doped hydrogels were implanted after tumor resection, preventing recurrence [124]. In a second study, miRNA was linked to gold nanoparticles and loaded in a hydrogel using the aforementioned strategy, and implanted in a breast cancer mouse model. This resulted in local, selective, and sustained delivery of the miRNA, attenuating the metastatic tendencies of the tumour [125].

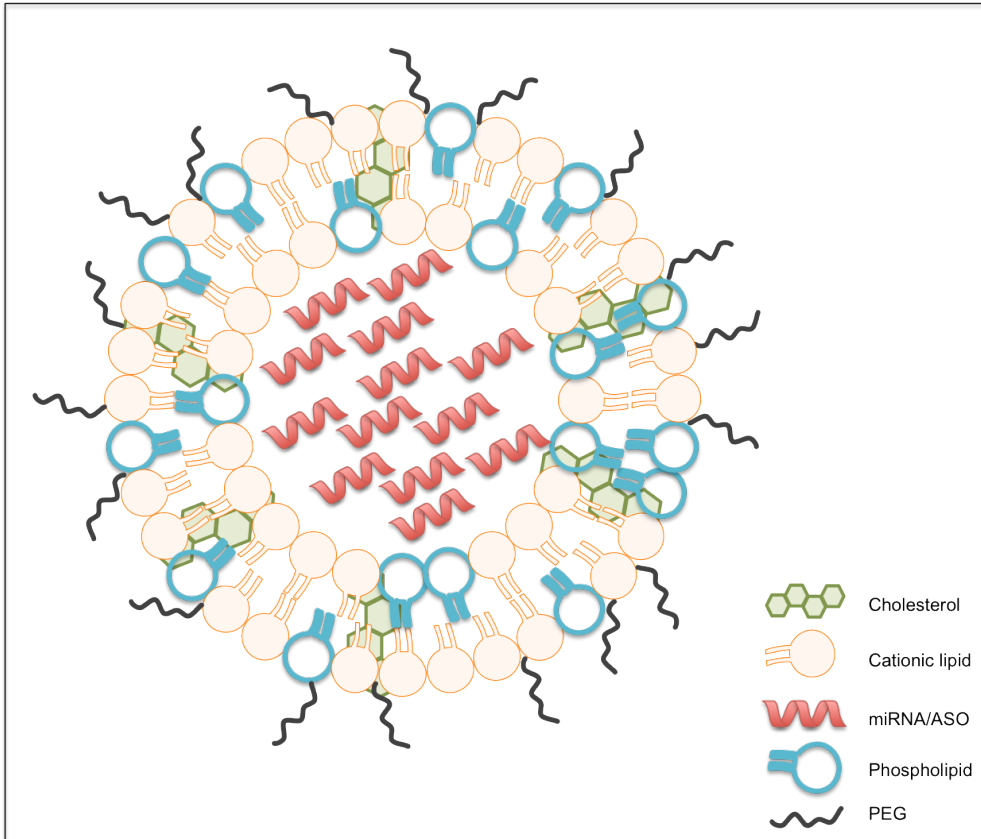


Figure 4 – LNP Schematic representation of a LNP made up of cationic lipids that covalently bind with the nucleic acid content, e.g. miRNA or ASO, phospholipids that provide structure to the lipid bilayer, cholesterol that provides stability of the lipid bilayer, and lipid-anchored PEG that limits aggregation and non-specific uptake.

FUTURE PERSPECTIVES

As illustrated, large variation between the aforementioned delivery systems exists. Many allow for efficacious drug delivery and for fine tailoring to specific needs. On the other hand, scale-up and broad application of a single nanoparticle-based delivery system remains challenging [126]. The process of mixing the individual components of these delivery systems is critical to guarantee the uniform quality of the particles. A microfluidic approach may be the answer to the scale-up of these delicate manufacturing processes [127].

Currently, nanoparticle-based drug-delivery systems mainly target tumor and the liver as these tissues are highly perfused and the endothelium is often fenestrated (not continuous), allowing

for easy passage of the particles. It remains a challenge to target less accessible tissues, like the AV. This challenge can be addressed by tailor-made delivery systems, such as the injection of a reservoir of particles directly into the target tissue using injectable carriers, such as hydrogels or degradable biopolymers, or by employing strategies like UTMD.

Moreover, there is room for improving the delivery process of nucleic acid therapeutics, as the exact mechanisms remain poorly understood. Recent evidence has provided certain principles and guidelines for particle-based delivery. Currently, particles are designed to avoid renal filtration and clearance by the immune system. This limits their size to approximately 20–200 nm. Shielding particles by PEGylation has increased the circulation time and reduced serum protein binding, preventing undesirable interactions. The (anti)miRs are chemically modified to improve stability and reduce degradation by nucleases, as well as immunostimulation. Receptor-specific ligands can be included in the formulation of particles to stimulate endocytosis and improve uptake by the target cells. Acidity-dependent membrane-disrupting materials can be shielded until needed and activated after endosomal uptake to facilitate release of the content. Therefore, research efforts should focus on creative and innovative delivery platforms that can deliver particles and drugs to specific target tissues, and on elucidating the mechanisms of particle circulation, homing, uptake, and release.

Prior to making the translational step to the clinic, drug-delivery devices are validated on *in vitro* and *in vivo* disease models. Employing 3D disease models with human cells has the potential to reduce the burden on animal models. The use of human cells is beneficial, as discoveries and results based on animal studies do not always translate directly to humans. Additionally, eliminating the need for animal models greatly reduces the time between bench and bedside. Specifically, for CAVD, where *in vivo* models are costly and time consuming to create, a 3D *in vitro* disease model with human cells that mimics the native valve tri-layered structure would be a valuable tool that can aid in the design of drug-delivery devices and allow for rapid testing of the functionality of novel nucleic acid therapeutics.

An innovative and reproducible 3D-bioprinted model of human CAVD can be employed (i) to study cellular and molecular mechanisms of CAVD, and (ii) as a drug screening tool. Furthermore, it can be used to identify potential therapeutic targets for CAVD, a disease without a drug-based therapy, and it can be used as a proof of concept for drug-delivery platforms that can then be expanded to target other tissues and diseases. Specifically, the multiple approaches that aid the delivery of (anti)miRs can be tested on this 3D model, simultaneously testing the efficacy of (anti)miRs in treating CAVD by reducing calcification and testing the efficiency of the drug-delivery approach. The aforementioned approaches can be tested as is, or in combination with a delivery device, such as an implantable or an injectable hydrogel. In the clinical setting, these hydrogels would function as a local depository, allowing for a single

intervention to store multiple doses of therapeutics, which are released gradually over an extended period of time.

CLINICAL PERSPECTIVES

Employing human 3D *in vitro* models of CAVD for identifying the underlying mechanisms and potential targets, and for drug screening, may accelerate the discovery and validation of a drug-based therapy for CAVD. With this, patients would be able to receive treatment in an earlier stage of the disease, slowing disease progression or even reversing and curing it.

Furthermore, validation of drug delivery platforms on a human *in vitro* model could expedite the translation from bench to bedside of local delivery systems.

In addition, the facile production process of the proposed delivery system allows for a broad range of applications and as miRNA therapeutics are identified for different diseases, for different target cells, tissues, or organs, similar drug delivery platforms may be applied in multiple clinical settings to treat a range of diseases.

ACKNOWLEDGEMENTS

Funding

This work was supported by the Netherlands CardioVascular Research Initiative (CVON: The Dutch Heart Foundation, Dutch Federation of University Medical Centers, the Netherlands Organization for Health Research and Development, and the Royal Netherlands Academy of Science) (to C.V., A.M. and J.P.G.S.); the Harvard Catalyst Advanced Microscopy Pilot (to C.V. and E.A.); the NIH through a Ruth L. Kirschstein National Research Service Award [grant number F32HL122009 (to M.W.T)]; the National Institutes of Health (to R.L.); and the National Institutes of Health [grant numbers R01HL114805, R01HL109506 and R01HL109889 (to E.A.)]. Harvard Catalyst support is provided by The Harvard Clinical and Translational Science Center (National Center for Research Resources and the National Center for Advancing Translational Sciences, National Institutes of Health Award [grant number UL1 TR001102] and financial contributions from Harvard University and its affiliated academic healthcare centers. The content is solely the responsibility of the authors and does not necessarily represent the official views of Harvard Catalyst, Harvard University and its affiliated academic healthcare centers, or the National Institutes of Health.

ABBREVIATIONS

ABCG2	ATP-binding cassette, sub-family G, member 2
AS	aortic stenosis
ASO	antisense oligonucleotide
AV	aortic valve
AVR	aortic valve replacement
BAV	bicuspid aortic valve
BMP-2	bone morphogenetic protein 2
CAVD	calcific aortic valve disease
ECM	extracellular matrix
EndMT	endothelial-to-mesenchymal transition
ERK1/2	extracellular signal-regulated protein kinases 1 and 2
DGCR8	DiGeorge syndrome critical region gene 8
2'-F	2'-fluoro
GelMA	methacrylated gelatin
HAMA	methacrylated hyaluronic acid
LDL	low-density lipoprotein
LNA	locked nucleic acid
LNP	lipid nanoparticle
LRP5	low-density lipoprotein receptor-related protein 5
2'-MOE	2'-O-methoxyethyl
2'-OMe	2'-O-methyl
NF- κ B	nuclear factor kappa-B
OPG	osteoprotegerin
OTE	off-target effects
PD/PK	pharmacodynamics/pharmacokinetics
PEI	polyetheleneimine
PI3K	phosphoinositide 3-kinase
PLA	poly(lactic acid)
PLL	poly-L-lysine
pre-miRNA	precursor miRNA
pri-miRNA	primary miRNA transcript
RANK	receptor activator of nuclear factor κ -B
RANKL	receptor activator of nuclear factor κ -B ligand
RISC	RNA-induced silencing complex
RT-qPCR	real-time quantitative PCR
Runx2	runt-related transcription factor 2
α -SMA	α -smooth muscle actin

SMAD	similar to mothers against decapentaplegic
TGF- β 1	transforming growth factor- β 1
TNF- α	tumour necrosis factor- α
UTMD	ultrasound triggered microbubble destruction
VEC	valvular endothelial cell
VIC	valve interstitial cell
ZEN	N,N-diethyl-4-(4-nitronaphthalen-1-ylazo)-phenylamine

REFERENCES

1. Mozaffarian D, Benjamin EJ, Go AS, Arnett DK, Blaha MJ, Cushman M, Das SR, de Ferranti S, Després JP, Fullerton HJ, et al. Executive summary: heart disease and stroke statistics—update A report from the American Heart Association. *Circulation*. 2016;133:447–454. [PubMed] [Google Scholar]
2. Iung B, Vahanian A. Epidemiology of valvular heart disease in the adult. *Nat Rev Cardiol*. 2011;8:162–172. [PubMed] [Google Scholar]
3. Rajamannan NM, Bonow RO, Rahimtoola SH. Calcific aortic stenosis: an update. *Nat Rev Cardiol*. 2007;4:254–262. [PubMed] [Google Scholar]
4. Otto CM. Calcific aortic stenosis — time to look more closely at the valve. *N Engl J Med*. 2008;359:1395–1398. [PubMed] [Google Scholar]
5. Hutcheson JD, Aikawa E, Merryman WD. Potential drug targets for calcific aortic valve disease. *Nat Rev Cardiol*. 2014;11:218–231. [PMC free article] [PubMed] [Google Scholar]
6. Teo KK, Corsi DJ, Tam JW, Dumesnil JG, Chan KL. Lipid lowering on progression of mild to moderate aortic stenosis: meta-analysis of the randomized placebo-controlled clinical trials on 2344 patients. *Can J Cardiol*. 2011;27:800–808. [PubMed] [Google Scholar]
7. Iung B, Baron G, Butchart EG, Delahaye F, Gohlke-Bärwolf C, Levang OW, Tornos P, Vanoverschelde JL, Vermeer F, Boersma E, et al. A prospective survey of patients with valvular heart disease in Europe: the Euro Heart Survey on valvular heart disease. *Eur Heart J*. 2003;24:1231–1243. [PubMed] [Google Scholar]
8. Bach DS. Prevalence and characteristics of unoperated patients with severe aortic stenosis. *J Heart Valve Dis*. 2011;20:284–291. [PubMed] [Google Scholar]
9. Takkenberg JJ, Rajamannan NM, Rosenhek R, Kumar AS, Carapetis JR, Yacoub MH, Society for Heart Valve Disease The need for a global perspective on heart valve disease epidemiology. The SHVD working group on epidemiology of heart valve disease founding statement. *J Heart Valve Dis*. 2008;17:135–139. [PubMed] [Google Scholar]
10. Lindman BR, Bonow RO, Otto CM. Current management of calcific aortic stenosis. *Circ Res*. 2013;113:223–237. [PMC free article] [PubMed] [Google Scholar]
11. Berlin DB, Davidson MJ, Schoen FJ. The power of disruptive technological innovation: transcatheter aortic valve implantation. *J Biomed Mater Res B: Appl Biomater*. 2015;103:1709–1715. [PubMed] [Google Scholar]
12. Sacks MS, Yoganathan AP. Heart valve function: a biomechanical perspective. *Philos Trans R Soc B Biol Sci*. 2007;362:1369–1391. [PMC free article] [PubMed] [Google Scholar]
13. Rabkin E, Aikawa M, Stone JR, Fukumoto Y, Libby P, Schoen FJ. Activated interstitial myofibroblasts express catabolic enzymes and mediate matrix remodeling in myxomatous heart valves. *Circulation*. 2001;104:2525–2532. [PubMed] [Google Scholar]
14. Rajamannan NM, Evans FJ, Aikawa E, Grande-Allen KJ, Demer LL, Heistad DD, Simmons CA, Masters KS, Mathieu P, O'Brien KD, et al. Calcific aortic valve disease: not simply a degenerative process: a review and agenda for research from the National Heart and Lung and Blood Institute Aortic Stenosis Working Group Executive summary: calcific aortic valve disease—update. *Circulation*. 2011;124:1783–1791. [PMC free article] [PubMed] [Google Scholar]
15. Rabkin-Aikawa E, Farber M, Aikawa M, Schoen FJ. Dynamic and reversible changes of interstitial cell phenotype during remodeling of cardiac valves. *J Heart Valve Dis*. 2004;13:841–847. [PubMed] [Google Scholar]
16. Taylor PM, Batten P, Brand NJ, Thomas PS, Yacoub MH. The cardiac valve interstitial cell. *Int J Biochem Cell Biol*. 2003;35:113–118. [PubMed] [Google Scholar]
17. Rajamannan NM, Subramaniam M, Rickard D, Stock SR, Donovan J, Springett M, Orszulak T, Fullerton DA, Tajik AJ, Bonow RO, et al. Human aortic valve calcification is associated with an osteoblast phenotype. *Circulation*. 2003;107:2181–2184. [PMC free article] [PubMed] [Google Scholar]

18. Mohler ER, Gannon F, Reynolds C, Zimmerman R, Keane MG, Kaplan FS. Bone formation and inflammation in cardiac valves. *Circulation*. 2001;103:1522–1528. [PubMed] [Google Scholar]
19. Wang H, Sridhar B, Leinwand LA, Anseth KS. Characterization of cell subpopulations expressing progenitor cell markers in porcine cardiac valves. *PLoS ONE*. 2013;8:e69667. [PMC free article] [PubMed] [Google Scholar]
20. Takahashi K, Satoh M, Takahashi Y, Osaki T, Nasu T, Tamada M, Okabayashi H, Nakamura M, Morino Y. Dysregulation of ossification-related miRNAs in circulating osteogenic progenitor cells obtained from patients with aortic stenosis. *Clin Sci (Lond Engl 1979)* 2016;130:1115–1124. [PMC free article] [PubMed] [Google Scholar]
21. Sucusky P, Balachandran K, Elhammali A, Jo H, Yoganathan AP. Altered shear stress stimulates upregulation of endothelial VCAM-1 and ICAM-1 in a BMP-4- and TGF-beta1-dependent pathway. *Arterioscler Thromb Vasc Biol*. 2009;29:254–260. [PMC free article] [PubMed] [Google Scholar]
22. Arjunon S, Rathan S, Jo H, Yoganathan AP. Aortic valve: mechanical environment and mechanobiology. *Ann Biomed Eng*. 2013;41:1331–1346. [PMC free article] [PubMed] [Google Scholar]
23. Ferdous Z, Jo H, Nerem RM. Strain magnitude-dependent calcific marker expression in valvular and vascular cells. *Cells Tissues Organs*. 2013;197:372–383. [PubMed] [Google Scholar]
24. Schoen FJ. Evolving concepts of cardiac valve dynamics. *Circulation*. 2008;118:1864–1880. [PubMed] [Google Scholar]
25. Miller JD, Weiss RM, Serrano KM, Castaneda LE, Brooks RM, Zimmerman K, Heistad DD. Evidence for active regulation of pro-osteogenic signaling in advanced aortic valve disease. *Arterioscler Thromb Vasc Biol*. 2010;30:2482–2486. [PMC free article] [PubMed] [Google Scholar]
26. New SE, Aikawa E. Molecular imaging insights into early inflammatory stages of arterial and aortic valve calcification. *Circ Res*. 2011;108:1381–1391. [PMC free article] [PubMed] [Google Scholar]
27. Gould ST, Matherly EE, Smith JN, Heistad DD, Anseth KS. The role of valvular endothelial cell paracrine signaling and matrix elasticity on valvular interstitial cell activation. *Biomaterials*. 2014;35:3596–3606. [PMC free article] [PubMed] [Google Scholar]
28. Hjortnaes J, Shapero K, Goettsch C, Hutcheson JD, Keegan J, Kluin J, Mayer JE, Bischoff J, Aikawa E. Valvular interstitial cells suppress calcification of valvular endothelial cells. *Atherosclerosis*. 2015;242:251–260. [PMC free article] [PubMed] [Google Scholar]
29. Jian B, Narula N, Li Q, Mohler ER, Levy RJ. Progression of aortic valve stenosis: TGF-beta1 is present in calcified aortic valve cusps and promotes aortic valve interstitial cell calcification via apoptosis. *Ann Thorac Surg*. 2003;75:457–465. [PubMed] [Google Scholar]
30. Kaden JJ, Dempfle CE, Grobholz R, Fischer CS, Vocke DC, Kiliç R, Sarıkoç A, Piñol R, Hagl S, Lang S, et al. Inflammatory regulation of extracellular matrix remodeling in calcific aortic valve stenosis. *Cardiovasc Pathol*. 2005;14:80–87. [PubMed] [Google Scholar]
31. Wang H, Leinwand LA, Anseth KS. Roles of transforming growth factor-β1 and OB-cadherin in porcine cardiac valve myofibroblast differentiation. *FASEB J*. 2014;28:4551–4562. [PMC free article] [PubMed] [Google Scholar]
32. Yang X, Meng X, Su X, Mauchley DC, Ao L, Cleveland JC, Jr, Fullerton DA. Bone morphogenic protein 2 induces Runx2 and osteopontin expression in human aortic valve interstitial cells: role of Smad1 and extracellular signal-regulated kinase 1/2. *J Thorac Cardiovasc Surg*. 2009;138:1008–1015. [PubMed] [Google Scholar]
33. Nigam V, Srivastava D. Notch1 represses osteogenic pathways in aortic valve cells. *J Mol Cell Cardiol*. 2009;47:828–834. [PMC free article] [PubMed] [Google Scholar]
34. Rajamannan NM, Subramaniam M, Caira F, Stock SR, Spelsberg TC. Atorvastatin inhibits hypercholesterolemia-induced calcification in the aortic valves via the Lrp5 receptor pathway. *Circulation*. 2005;112(Suppl 9):I-229–I-234. [PMC free article] [PubMed] [Google Scholar]

35. Wang H, Tibbitt MW, Langer SJ, Leinwand LA, Anseth KS. Hydrogels preserve native phenotypes of valvular fibroblasts through an elasticity-regulated PI3K/AKT pathway. *Proc Natl Acad Sci USA*. 2013;110:19336–19341. [PMC free article] [PubMed] [Google Scholar]
36. Kloxin AM, Benton JA, Anseth KS. In situ elasticity modulation with dynamic substrates to direct cell phenotype. *Biomaterials*. 2010;31:1–8. [PMC free article] [PubMed] [Google Scholar]
37. Riem Vis PW, Kluin J, Sluijter JP, van Herwerden LA, Bouten CV. Environmental regulation of valvulogenesis: implications for tissue engineering. *Eur J Cardiothorac Surg*. 2011;39:8–17. [PubMed] [Google Scholar]
38. Mabry KM, Lawrence RL, Anseth KS. Dynamic stiffening of poly(ethylene glycol)-based hydrogels to direct valvular interstitial cell phenotype in a three-dimensional environment. *Biomaterials*. 2015;49:47–56. [PMC free article] [PubMed] [Google Scholar]
39. Puperi DS, O’Connell RW, Punske ZE, Wu Y, West JL, Grande-Allen KJ. Hyaluronan hydrogels for a biomimetic spongiosa layer of tissue engineered heart valve scaffolds. *Biomacromolecules*. 2016;17:1766–1775. [PMC free article] [PubMed] [Google Scholar]
40. Puperi DS, Balaing LR, O’Connell RW, West JL, Grande-Allen KJ. 3-Dimensional spatially organized PEG-based hydrogels for an aortic valve co-culture model. *Biomaterials*. 2015;67:354–364. [PMC free article] [PubMed] [Google Scholar]
41. Walker GA, Masters KS, Shah DN, Anseth KS, Leinwand LA. Valvular myofibroblast activation by transforming growth factor- β implications for pathological extracellular matrix remodeling in heart valve disease. *Circ Res*. 2004;95:253–260. [PubMed] [Google Scholar]
42. Hjortnaes J, Goettsch C, Hutcheson JD, Camci-Unal G, Lax L, Scherer K, Body S, Schoen FJ, Kluin J, Khademhosseini A, et al. Simulation of early calcific aortic valve disease in a 3D platform: a role for myofibroblast differentiation. *J Mol Cell Cardiol*. 2016;94:13–20. [PMC free article] [PubMed] [Google Scholar]
43. Hutcheson JD, Goettsch C, Bertazzo S, Maldonado N, Ruiz JL, Goh W, Yabusaki K, Faits T, Bouten C, Franck G, et al. Genesis and growth of extracellular-vesicle-derived microcalcification in atherosclerotic plaques. *Nat Mater*. 2016;15:335–343. [PMC free article] [PubMed] [Google Scholar]
44. Lee RC, Feinbaum RL, Ambros V. The *C. elegans* heterochronic gene *lin-4* encodes small RNAs with antisense complementarity to *lin-14*. *Cell*. 1993;75:843–854. [PubMed] [Google Scholar]
45. Bartel DP. MicroRNAs: genomics, biogenesis, mechanism, and function. *Cell*. 2004;116:281–297. [PubMed] [Google Scholar]
46. Lee Y, Ahn C, Han J, Choi H, Kim J, Yim J, Lee J, Provost P, Rådmark O, Kim S, et al. The nuclear RNase III Drosha initiates microRNA processing. *Nature*. 2003;425:415–419. [PubMed] [Google Scholar]
47. Gregory RI, Yan K, Amuthan G, Chendrimada T, Doratotaj B, Cooch N, Shiekhattar R. The microprocessor complex mediates the genesis of microRNAs. *Nature*. 2004;432:235–240. [PubMed] [Google Scholar]
48. Lund E, Güttinger S, Calado A, Dahlberg JE, Kutay U. Nuclear export of microRNA precursors. *Science*. 2004;303:95–98. [PubMed] [Google Scholar]
49. Hutvagner G, McLachlan J, Pasquinelli AE, Bálint É, Tuschl T, Zamore PD. A cellular function for the RNA-interference enzyme dicer in the maturation of the *let-7* small temporal RNA. *Science*. 2001;293:834–838. [PubMed] [Google Scholar]
50. Gregory RI, Chendrimada TP, Cooch N, Shiekhattar R. Human RISC couples microRNA biogenesis and posttranscriptional gene silencing. *Cell*. 2005;123:631–640. [PubMed] [Google Scholar]
51. Huntzinger E, Izaurralde E. Gene silencing by microRNAs: contributions of translational repression and mRNA decay. *Nat Rev Genet*. 2011;12:99–110. [PubMed] [Google Scholar]
52. Guo H, Ingolia NT, Weissman JS, Bartel DP. Mammalian microRNAs predominantly act to decrease target mRNA levels. *Nature*. 2010;466:835–840. [PMC free article] [PubMed] [Google Scholar]
53. Bartel DP. MicroRNAs: target recognition and regulatory functions. *Cell*. 2009;136:215–233. [PMC free article] [PubMed] [Google Scholar]
54. Meijer HA, Smith EM, Bushell M. Regulation of miRNA strand selection: follow the leader? *Biochem Soc Trans*. 2014;42:1135–1140. [PubMed] [Google Scholar]

55. Griffiths-Jones S, Grocock RJ, van Dongen S, Bateman A, Enright AJ. miRBase: microRNA sequences, targets and gene nomenclature. *Nucleic Acids Res.* 2006;34(Suppl 1):D140–D144. [PMC free article] [PubMed] [Google Scholar]
56. Carthew RW, Sontheimer EJ. Origins and mechanisms of miRNAs and siRNAs. *Cell.* 2009;136:642–655. [PMC free article] [PubMed] [Google Scholar]
57. Goettsch C, Hutcheson JD, Aikawa E. MicroRNA in cardiovascular calcification: focus on targets and extracellular vesicle delivery mechanisms. *Circ Res.* 2013;112:1073–1084. [PMC free article] [PubMed] [Google Scholar]
58. Oerlemans MI, Mosterd A, Dekker MS, de Vrey EA, van Mil A, Pasterkamp G, Doevendans PA, Hoes AW, Sluijter JPG. Early assessment of acute coronary syndromes in the emergency department: the potential diagnostic value of circulating microRNAs. *EMBO Mol Med.* 2012;4:1176–1185. [PMC free article] [PubMed] [Google Scholar]
59. Deddens JC, Colijn JM, Oerlemans MI, Pasterkamp G, Chamuleau SA, Doevendans PA, Sluijter JPG. Circulating microRNAs as novel biomarkers for the early diagnosis of acute coronary syndrome. *J Cardiovasc Transl Res.* 2013;6:884–898. [PubMed] [Google Scholar]
60. Romaine SP, Tomaszewski M, Condorelli G, Samani NJ. MicroRNAs in cardiovascular disease: an introduction for clinicians. *Heart.* 2015;101:921–928. [PMC free article] [PubMed] [Google Scholar]
61. Sluijter JPG. MicroRNAs in cardiovascular regenerative medicine: directing tissue repair and cellular differentiation. *Int Sch Res Not.* 2013;2013:e593517. [Google Scholar]
62. Villar AV, García R, Merino D, Llano M, Cobo M, Montalvo C, Martín-Durán R, Hurlé MA, Nistal JF. Myocardial and circulating levels of microRNA-21 reflect left ventricular fibrosis in aortic stenosis patients. *Int J Cardiol.* 2013;167:2875–2881. [PubMed] [Google Scholar]
63. Ohukainen P, Syvänta S, Näpänkangas J, Rajamäki K, Taskinen P, Peltonen T, Helske-Suihko S, Kovanen PT, Ruskoaho H, Rysä J. MicroRNA-125b and chemokine CCL4 expression are associated with calcific aortic valve disease. *Ann Med.* 2015;47:423–429. [PubMed] [Google Scholar]
64. Patel V, Carrion K, Hollands A, Hinton A, Gallegos T, Dyo J, Sasik R, Leire E, Hardiman G, Mohamed SA, et al. The stretch responsive microRNA miR-148a-3p is a novel repressor of IKBKB, NF- κ B signaling, and inflammatory gene expression in human aortic valve cells. *FASEB J.* 2015;29:1859–1868. [PMC free article] [PubMed] [Google Scholar]
65. Wang Y, Chen S, Deng C, Li F, Wang Y, Hu X, Shi F, Dong N. MicroRNA-204 targets Runx2 to attenuate BMP-2-induced osteoblast differentiation of human aortic valve interstitial cells. *J Cardiovasc Pharmacol.* 2015;66:63–71. [PubMed] [Google Scholar]
66. Yanagawa B, Lovren F, Pan Y, Garg V, Quan A, Tang G, Singh KK, Shukla PC, Kalra NP, Peterson MD, et al. miRNA-141 is a novel regulator of BMP-2-mediated calcification in aortic stenosis. *J Thorac Cardiovasc Surg.* 2012;144:256–262. [PubMed] [Google Scholar]
67. Zhang M, Liu X, Zhang X, Song Z, Han L, He Y, Xu Z. MicroRNA-30b is a multifunctional regulator of aortic valve interstitial cells. *J Thorac Cardiovasc Surg.* 2014;147:1073–1080. [PubMed] [Google Scholar]
68. Rathan S, Ankeny CJ, Arjunon S, Ferdous Z, Kumar S, Esmerats JF, Heath JM, Nerem RM, Yoganathan AP, Jo H. Identification of side- and shear-dependent microRNAs regulating porcine aortic valve pathogenesis. *Sci Rep.* 2016;6 [PMC free article] [PubMed] [Google Scholar]
69. Nigam V, Sievers HH, Jensen BC, Sier HA, Simpson PC, Srivastava D, Mohamed SA. Altered micrnas in bicuspid aortic valve: a comparison between stenotic and insufficient valves. *J Heart Valve Dis.* 2010;19:459–465. [PMC free article] [PubMed] [Google Scholar]
70. Holliday CJ, Ankeny RF, Jo H, Nerem RM. Discovery of shear- and side-specific mRNAs and miRNAs in human aortic valvular endothelial cells. *Am J Physiol Heart Circ Physiol.* 2011;301:H856–H867. [PMC free article] [PubMed] [Google Scholar]
71. Li Z, Hassan MQ, Volinia S, van Wijnen AJ, Stein JL, Croce CM, Lian JB, Stein GS. A microRNA signature for a BMP2-induced osteoblast lineage commitment program. *Proc Natl Acad Sci USA.* 2008;105:13906–13911. [PMC free article] [PubMed] [Google Scholar]

72. New SE, Goetsch C, Aikawa M, Marchini JF, Shibasaki M, Yabusaki K, Libby P, Shanahan CM, Croce K, Aikawa E. Macrophage-Derived Matrix Vesicles: An Alternative Novel Mechanism for Microcalcification in Atherosclerotic Plaques. *Circ Res*. 2013;113:72–77. [PMC free article] [PubMed] [Google Scholar]
73. New SE, Aikawa E. Role of extracellular vesicles in de novo mineralization: an additional novel mechanism of cardiovascular calcification. *Arterioscler Thromb Vasc Biol*. 2013;33:1753–1758. [PMC free article] [PubMed] [Google Scholar]
74. Krohn JB, Hutcheson JD, Martínez-Martínez E, Aikawa E. Extracellular vesicles in cardiovascular calcification: expanding current paradigms. *J Physiol*. 2016;594:2895–2903. [PMC free article] [PubMed] [Google Scholar]
75. Goetsch C, Hutcheson JD, Aikawa M, Iwata H, Pham T, Nykjaer A, Kjolby M, Rogers M, Michel T, Shibasaki M, et al. Sortilin mediates vascular calcification via its recruitment into extracellular vesicles. *J Clin Invest*. 2016;126:1323–1336. [PMC free article] [PubMed] [Google Scholar]
76. Kapustin AN, Chatrou ML, Drozdov I, Zheng Y, Davidson SM, Soong D, Furmanik M, Sanchis P, De Rosales RTM, Alvarez-Hernandez D, et al. Vascular smooth muscle cell calcification is mediated by regulated exosome secretion. *Circ Res*. 2015;116:1312–1323. [PubMed] [Google Scholar]
77. Raposo G, Stoorvogel W. Extracellular vesicles: exosomes, microvesicles, and friends. *J Cell Biol*. 2013;200:373–383. [PMC free article] [PubMed] [Google Scholar]
78. Mittelbrunn M, Gutiérrez-Vázquez C, Villarroya-Beltri C, González S, Sánchez-Cabo F, González MÁ, Bernad A, Sanchez-Madrid F. Unidirectional transfer of microRNA-loaded exosomes from T cells to antigen-presenting cells. *Nat Commun*. 2011;2:282. [PMC free article] [PubMed] [Google Scholar]
79. Montecalvo A, Larregina AT, Shufesky WJ, Stolz DB, Sullivan ML, Karlsson JM, et al. Mechanism of transfer of functional microRNAs between mouse dendritic cells via exosomes. *Blood*. 2012;119:756–766. [PMC free article] [PubMed] [Google Scholar]
80. Li J, Zhang Y, Liu Y, Dai X, Li W, Cai X, Baty CJ, Gibson GA, Erdos G, Wang Z, et al. Microvesicle-mediated transfer of microRNA-150 from monocytes to endothelial cells promotes angiogenesis. *J Biol Chem*. 2013;288:23586–23596. [PMC free article] [PubMed] [Google Scholar]
81. Ebert MS, Neilson JR, Sharp PA. MicroRNA sponges: competitive inhibitors of small RNAs in mammalian cells. *Nat Methods*. 2007;4:721–726. [PMC free article] [PubMed] [Google Scholar]
82. Lennox KA, Behlke MA. A direct comparison of anti-microRNA oligonucleotide potency. *Pharm Res*. 2010;27:1788–1799. [PubMed] [Google Scholar]
83. Krützfeldt J, Rajewsky N, Braich R, Rajeev KG, Tuschl T, Manoharan M, Stoffel M. Silencing of microRNAs *in vivo* with “antagomirs. *Nature*. 2005;438:685–689. [PubMed] [Google Scholar]
84. Geary RS. Antisense oligonucleotide pharmacokinetics and metabolism. *Expert Opin Drug Metab Toxicol*. 2009;5:381–391. [PubMed] [Google Scholar]
85. Thum T, Gross C, Fiedler J, Fischer T, Kissler S, Bussen M, Galuppo P, Just S, Rottbauer W, Frantz S, et al. MicroRNA-21 contributes to myocardial disease by stimulating MAP kinase signalling in fibroblasts. *Nature*. 2008;456:980–984. [PubMed] [Google Scholar]
86. Ma L, Reinhardt F, Pan E, Soutschek J, Bhat B, Marcussen EG, Teruya-Feldstein J, Bell GW, Weinberg RA. Therapeutic silencing of miR-10b inhibits metastasis in a mouse mammary tumor model. *Nat Biotechnol*. 2010;28:341–347. [PMC free article] [PubMed] [Google Scholar]
87. Manoharan M. 2'-carbohydrate modifications in antisense oligonucleotide therapy: importance of conformation, configuration and conjugation. *Biochim Biophys Acta BBA - Gene Struct Expr*. 1999;1489:117–130. [PubMed] [Google Scholar]
88. Esau C, Davis S, Murray SF, Yu XX, Pandey SK, Pear M, Watts L, Booten SL, Graham M, McKay R, et al. miR-122 regulation of lipid metabolism revealed by *in vivo* antisense targeting. *Cell Metab*. 2006;3:87–98. [PubMed] [Google Scholar]
89. Davis S, Lollo B, Freier S, Esau C. Improved targeting of miRNA with antisense oligonucleotides. *Nucleic Acids Res*. 2006;34:2294–2304. [PMC free article] [PubMed] [Google Scholar]
90. Singh SK, Koshkin AA, Wengel J, Nielsen P. LNA (locked nucleic acids): synthesis and high-affinity nucleic acid recognition. *Chem Commun*. 1998;4:455–456. [Google Scholar]

91. Obad S, dos Santos CO, Petri A, Heidenblad M, Broom O, Ruse C, Fu C, Lindow M, Stenvang J, Straarup EM, et al. Silencing of microRNA families by seed-targeting tiny LNAs. *Nat Genet.* 2011;43:371–378. [PMC free article] [PubMed] [Google Scholar]
92. Lennox KA, Owczarzy R, Thomas DM, Walder JA, Behlke MA. Improved performance of anti-miRNA oligonucleotides using a novel non-nucleotide modifier. *Mol Ther Nucleic Acids.* 2013;2:e117. [PMC free article] [PubMed] [Google Scholar]
93. Larson SD, Jackson LN, Chen LA, Rychahou PG, Evers BM. Effectiveness of siRNA uptake in target tissues by various delivery methods. *Surgery.* 2007;142:262–269. [PMC free article] [PubMed] [Google Scholar]
94. Whitehead KA, Langer R, Anderson DG. Knocking down barriers: advances in siRNA delivery. *Nat Rev Drug Discov.* 2009;8:129–138. [PMC free article] [PubMed] [Google Scholar]
95. Alexis F, Pridgen E, Molnar LK, Farokhzad OC. Factors affecting the clearance and biodistribution of polymeric nanoparticles. *Mol Pharm.* 2008;5:505–515. [PMC free article] [PubMed] [Google Scholar]
96. Petros RA, DeSimone JM. Strategies in the design of nanoparticles for therapeutic applications. *Nat Rev Drug Discov.* 2010;9:615–627. [PubMed] [Google Scholar]
97. Kanasty RL, Whitehead KA, Vegas AJ, Anderson DG. Action and reaction: the biological response to siRNA and its delivery vehicles. *Mol Ther.* 2012;20:513–524. [PMC free article] [PubMed] [Google Scholar]
98. Schroeder A, Levins CG, Cortez C, Langer R, Anderson DG. Lipid-based nanotherapeutics for siRNA delivery. *J Intern Med.* 2010;267:9–21. [PMC free article] [PubMed] [Google Scholar]
99. Jackson AL, Linsley PS. Recognizing and avoiding siRNA off-target effects for target identification and therapeutic application. *Nat Rev Drug Discov.* 2010;9:57–67. [PubMed] [Google Scholar]
100. van Mil A, Doevendans PA, Sluijter JP. The potential of modulating small RNA activity *in vivo*. *Mini Rev Med Chem.* 2009;9:235–248. [PubMed] [Google Scholar]
101. Davis ME, Chen ZG, Shin DM. Nanoparticle therapeutics: an emerging treatment modality for cancer. *Nat Rev Drug Discov.* 2008;7:771–782. [PubMed] [Google Scholar]
102. Malam Y, Loizidou M, Seifalian AM. Liposomes and nanoparticles: nanosized vehicles for drug delivery in cancer. *Trends Pharmacol Sci.* 2009;30:592–599. [PubMed] [Google Scholar]
103. Zhao Z, Zhuang S, Qi XR. Comparative study of the *in vitro* and *in vivo* characteristics of cationic and neutral liposomes. *Int J Nanomedicine.* 2011;6:3087–3098. [PMC free article] [PubMed] [Google Scholar]
104. Castaing M, Loiseau A, Mulliert G. Multidrug resistance modulator interactions with neutral and anionic liposomes: membrane binding affinity and membrane perturbing activity. *J Pharm Pharmacol.* 2005;57:547–554. [PubMed] [Google Scholar]
105. Jesorka A, Orwar O. Liposomes: technologies and analytical applications. *Annu Rev Anal Chem (Palo Alto Calif)* 2008;1:801–832. [PubMed] [Google Scholar]
106. Jubeli E, Raju L, Khaliq NA, Bilchuk N, Zegel C, Chen A, Lou HH, Øpstad CL, Zeeshan M, Sliwka HR, et al. Polyene-based cationic lipids as visually traceable siRNA transfer reagents. *Eur J Pharm Biopharm.* 2015;89:280–289. [PubMed] [Google Scholar]
107. Dar GH, Gopal V, Rao NM. Systemic delivery of stable siRNA-encapsulating lipid vesicles: optimization, biodistribution, and tumor suppression. *Mol Pharm.* 2015;12:610–620. [PubMed] [Google Scholar]
108. Bailey AL, Cullis PR. Liposome fusion. In: Epan R, editor. *Current topics in Membranes.* Academic Press; San Diego: 1997. pp. 359–373. [Google Scholar]
109. Bailey AL, Cullis PR. Modulation of membrane fusion by asymmetric transbilayer distributions of amino lipids. *Biochemistry (Mosc)* 1994;33:12573–12580. [PubMed] [Google Scholar]
110. Milla P, Dosio F, Cattel L. PEGylation of proteins and liposomes: a powerful and flexible strategy to improve the drug delivery. *Curr Drug Metab.* 2012;13:105–119. [PubMed] [Google Scholar]
111. Soutschek J, Akinc A, Bramlage B, Charisse K, Constien R, Donoghue M, Elbashir S, Geick A, Hadwiger P, Harborth J, et al. Therapeutic silencing of an endogenous gene by systemic administration of modified siRNAs. *Nature.* 2004;432:173–178. [PubMed] [Google Scholar]

112. Wolfrum C, Shi S, Jayaprakash KN, Jayaraman M, Wang G, Pandey RK, Rajeev KG, Nakayama T, Charrise K, Ndungo EM, et al. Mechanisms and optimization of *in vivo* delivery of lipophilic siRNAs. *Nat Biotechnol*. 2007;25:1149–1157. [PubMed] [Google Scholar]
113. Jeong JH, Mok H, Oh YK, Park TG. siRNA conjugate delivery systems. *Bioconjugate Chem*. 2009;20:5–14. [PubMed] [Google Scholar]
114. Rozema DB, Ekena K, Lewis DL, Loomis AG, Wolff JA. Endosomolysis by masking of a membrane-active agent (EMMA) for cytoplasmic release of macromolecules. *Bioconjugate Chem*. 2003;14:51–57. [PubMed] [Google Scholar]
115. Biessen EA, Beuting DM, Roelen HC, van de Marel GA, van Boom JH, van Berkel TJ. Synthesis of cluster galactosides with high affinity for the hepatic asialoglycoprotein receptor. *J Med Chem*. 1995;38:1538–1546. [PubMed] [Google Scholar]
116. Rensen PC, van Leeuwen SH, Sliedregt LA, van Berkel TJ, Biessen EA. Design and synthesis of novel N-acetylgalactosamine-terminated glycolipids for targeting of lipoproteins to the hepatic asialoglycoprotein receptor. *J Med Chem*. 2004;47:5798–5808. [PubMed] [Google Scholar]
117. Kallanthottathil R. Conjugation strategies for *in vivo* siRNA delivery. 2012 <http://www.alnylam.com/web/wp-content/uploads/2012/11/ALNY-OTS-Conjugate-Oct2012.pdf>.
118. Kwekkeboom RF, Sluijter JP, van Middelaar BJ, Metz CH, Brans MA, Kamp O, Paulus WJ, Musters RJP. Increased local delivery of antagomir therapeutics to the rodent myocardium using ultrasound and microbubbles. *J Control Release*. 2016;222:18–31. [PubMed] [Google Scholar]
119. Dong Y, Love KT, Dorkin JR, Sirirungruang S, Zhang Y, Chen D, Bogorad RL, Yin H, Chen Y, Vegas AJ, et al. Lipopeptide nanoparticles for potent and selective siRNA delivery in rodents and nonhuman primates. *Proc Natl Acad Sci USA*. 2014;111:3955–3960. [PMC free article] [PubMed] [Google Scholar]
120. Love KT, Mahon KP, Levins CG, Whitehead KA, Querbes W, Dorkin JR, Qin J, Cantley W, Qin LL, Racie T, et al. Lipid-like materials for low-dose, *in vivo* gene silencing. *Proc Natl Acad Sci USA*. 2010;107:1864–1869. [PMC free article] [PubMed] [Google Scholar]
121. Yu B, Zhao X, Lee LJ, Lee RJ. Targeted delivery systems for oligonucleotide therapeutics. *AAPS J*. 2009;11:195–203. [PMC free article] [PubMed] [Google Scholar]
122. Kanasty R, Dorkin JR, Vegas A, Anderson D. Delivery materials for siRNA therapeutics. *Nat Mater*. 2013;12:967–977. [PubMed] [Google Scholar]
123. Schwarz DS, Hutvagner G, Du T, Xu Z, Aronin N, Zamore PD. Asymmetry in the assembly of the RNAi enzyme complex. *Cell*. 2003;115:199–208. [PubMed] [Google Scholar]
124. Conde J, Oliva N, Zhang Y, Artzi N. Local triple-combination therapy results in tumour regression and prevents recurrence in a colon cancer model. *Nat Mater*. 2016;15:1128–1138. [PMC free article] [PubMed] [Google Scholar]
125. Gilam A, Conde J, Weissglas-Volkov D, Oliva N, Friedman E, Artzi N, Shomron N. Local microRNA delivery targets palladin and prevents metastatic breast cancer. *Nat Commun*. 2016;7 [PMC free article] [PubMed] [Google Scholar]
126. Ragelle H, Danhier F, Préat V, Langer R, Anderson DG. Nanoparticle-based drug delivery systems: a commercial and regulatory outlook as the field matures. *Expert Opin Drug Deliv*. 2016 in the press. [PubMed] [Google Scholar]
127. Gindy ME, Leone AM, Cunningham JJ. Challenges in the pharmaceutical development of lipid-based short interfering ribonucleic acid therapeutics. *Expert Opin Drug Deliv*. 2012;9:171–182. [PubMed] [Google Scholar]
128. Aikawa E, Otto CM. Look more closely at the valve imaging calcific aortic valve disease. *Circulation*. 2012;125:9–11. [PubMed] [Google Scholar]

Chapter 2

Engineering a 3D-bioprinted model of human heart valve disease using nano-indentation based biomechanics

Casper F.T. van der Ven
Dewy C. van der Valk
Mark C. Blaser
Joshua M. Grolman
Pin-Jou Wu
Owen S. Fenton
Lang H. Lee
Mark W. Tibbitt
Jason L. Andresen
Jennifer R. Wen
Anna H. Ha

Fabrizio Buffolo
Alain van Mil
Carlijn V.C. Bouten
Simon C. Body
David J. Mooney
Joost P.G. Sluijter
Masanori Aikawa
Jesper Hjortnaes
Robert Langer
Elena Aikawa

ABSTRACT

In calcific aortic valve disease (CAVD), microcalcifications originating from nanoscale calcifying vesicles disrupt the aortic valve (AV) leaflets, which consist of three (biomechanically) distinct layers: the fibrosa, spongiosa, and ventricularis. CAVD has no pharmacotherapy and lacks *in vitro* models as a result of complex valvular biomechanical features surrounding resident mechanosensitive valvular interstitial cells (VICs). We measured layer-specific mechanical properties of the human AV and engineered a three-dimensional (3D)-bioprinted CAVD model that recapitulates leaflet layer biomechanics for the first time. Human AV leaflet layers were separated by microdissection, and nanoindentation determined layer-specific Young's moduli. Methacrylated gelatin (GelMA)/methacrylated hyaluronic acid (HAMA) hydrogels were tuned to duplicate layer-specific mechanical characteristics, followed by 3D-printing with encapsulated human VICs. Hydrogels were exposed to osteogenic media (OM) to induce microcalcification, and VIC pathogenesis was assessed by near infrared or immunofluorescence microscopy. Median Young's moduli of the AV layers were 37.1, 15.4, and 26.9 kPa (fibrosa/spongiosa/ventricularis, respectively). The fibrosa and spongiosa Young's moduli matched the 3D 5% GelMa/1% HAMA UV-crosslinked hydrogels. OM stimulation of VIC-laden bioprinted hydrogels induced microcalcification without apoptosis. We report the first layer-specific measurements of human AV moduli and a novel 3D-bioprinted CAVD model that potentiates microcalcification by mimicking the native AV mechanical environment. This work sheds light on valvular mechanobiology and could facilitate high-throughput drug-screening in CAVD.

Keywords: aortic valve, calcific aortic valve disease, calcification, mechanobiology, bioprinting, 3D printing, microdissection, nanoindentation

INTRODUCTION

Calcific aortic valve disease (CAVD) is the most prevalent heart disease, affecting more than $\frac{1}{4}$ of individuals over age 65 in the Western world [1]. Despite this high prevalence and many risk factors shared with atherosclerosis, there are no pharmacological therapies for CAVD— aortic valve (AV) replacement currently is the sole treatment option. The healthy AV is composed of three semilunar leaflets. The leaflets are comprised of three stacked layers, each with its own unique extracellular matrix (ECM) composition: the collagen-rich fibrosa layer, the proteoglycan-rich spongiosa, and the elastin-rich ventricularis [2]. As CAVD progresses, the leaflets of the AV become fibrotic and calcify as their constituent cell population of valve interstitial cells (VICs) undergo myofibrogenic and osteogenic differentiation [2]. Calcification is likely to initiate via aggregation of nanoscale calcifying vesicles into larger microcalcifications [3,4], which eventually form extensive regions of ectopic calcific nodules that impair AV opening/closure, leading to heart failure and death [5]. Importantly, the onset and progression of CAVD is layer-specific: it preferentially initiates within the fibrosa and progresses to the spongiosa, while the ventricularis is largely unaffected until the final stages of disease [6,7].

Preferential disease development in the fibrosa may be a result of VICs sensing and responding to the biomechanics of their microenvironment. Similar to mesenchymal stem cells [8], pathological differentiation of normally quiescent VICs to myofibroblasts and osteoblasts is regulated *in vitro* by the local mechanics (e.g., compressive stiffness) of the ECM [9,10,11]. Tensile mechanical properties of whole human AV leaflets have been studied [12] as well as those of microdissected human fibrosa and ventricularis [13,14]. Micropipette aspiration has been used to measure the Young's modulus of normal porcine fibrosa and ventricularis [10]; however, the only measurements of spongiosa biomechanics originate from atomic force microscopy of layers on thin porcine leaflet cryosections [15]. Importantly, all three layers of the human AV have not been separated and subjected to measurements of local compressive stiffness. VIC mechanosensitivity is likely a key limiting factor in current *in vitro* platforms for high-throughput drug discovery, which are based on tissue culture polystyrene (TCPS) with high, non-physiological stiffness. Existing *in vitro* models of CAVD cannot account for mechanosensitive cellular responses that may modulate otherwise-drugable signaling axes *in vivo*.

Although many putative therapeutic targets have been identified in recent years [16,17], the mechanosensitive nature of VICs and layer-specific biomechanics of the native AV necessitate a suitably scalable *in vitro* system that recapitulates key aspects of the valvular architecture and microenvironment (e.g., layer-specific mechanical properties) to reliably screen and test novel targets. To this end, a variety of soft gel substrates have been utilized to examine VIC

phenotype and function, including those based on poly(ethylene-glycol) (PEG) [18], PEG-dimethacrylate-poly(l-lactide) (PEGdma-PLA) [15], polyacrylamide [10], and collagen [9]. We and others have shown previously that hybrid GelMA/HAMA hydrogels are able to maintain VICs in a quiescent fibroblastic state [19], while also supporting differentiation of VICs towards diseased phenotypes after exogenous delivery of pathological cytokines or other calcifying stimuli [11,20]. 3D-bioprinting has been shown to provide superior cell seeding and cell attachment compared with traditional scaffold biofabrication techniques, along with lower gel-to-gel variability and hands-off (high-throughput) fabrication [reviewed in S.V. Murphy et al. and C.F. van der Ven et al. [21,22]]. 3D-bioprinting has been utilized to fabricate complex tissues *in vitro* (e.g., co-culture tumor models, branched vascular trees, and cartilaginous structures such as ears and trachea [23,24,25,26]), and is compatible with GelMA-based hydrogels [27]. This technique has been utilized to manufacture large-format valvular conduits [28] and flow phantoms [29] but has not been applied to model the complexities of the valvular microenvironment.

In the present study, we first performed systematic microdissection and mechanical testing of human AV tissue, then coupled this data with 3D-bioprinting and mechanical characterization of a tunable hydrogel system to mimic the native valve. Here, we demonstrate (1) the first approach to separate all three layers of the human AV; (2) nanoindentation measurements of layer-specific biomechanical properties of the native human AV; (3) direct recapitulation of layer-specific Young's moduli using a 3D GelMA/HAMA hydrogel system; (4) bioprinting of 3D hydrogels with encapsulated primary human VICs; (5) controllable formation of layer-specific microcalcification and ECM degradation by VICs; and (6) bioprinting of multi-layered 3D hydrogel AV constructs. Together, these data establish a novel 3D model for studying the mechanisms of valvular diseases and a platform suitable for high-throughput screening in CAVD.

MATERIAL & METHODS

Layer Separation of CAVD Leaflets is Confirmed by Histological Evaluation

AV leaflets were obtained from patients undergoing surgical valve replacement at Brigham and Women's Hospital (Boston, MA, USA) as a result of AV calcification and/or stenosis. Leaflets were obtained and utilized in accordance with protocols approved by the Institutional Review Board (IRB protocol #2011P001703/PHS). After removal, leaflets were kept on ice in Dulbecco's Modified Eagle's Medium (DMEM, Lonza, Walkersville, MD, USA) for a maximum of 1 h, then stored for a maximum of 10 h in DMEM at 37 °C/5% CO₂. Leaflet layers were microdissected as described previously [13,14] with modifications to additionally

obtain spongiosa samples. Non-calcified regions of the CAVD leaflets were selected by gross morphology and absence of any palpable regions of stiff/brittle calcific deposits, and cut using #10 scalpels (Fine Science Tools, North Vancouver, BC, Canada). In a recent paper from our laboratory [17], we demonstrate the high specificity of this stage-separation approach in human AVs by proteomics (LC-MS/MS) and transcriptomics. Regions that were to undergo testing on whole (intact) leaflets were marked with tissue-marking dye (TMD, General Data Company Inc., Cincinnati, OH, USA) on the fibrosa side to ensure orientation. Regions selected for layer separation were pinned through the ventricularis layer to a cork dissecting board using 30 g needles, with the fibrosa surface facing upward. Samples were submerged in DMEM during the procedure. Fibrous interconnections within the spongiosa that ran between the ventricularis and fibrosa were exposed by gently lifting the fibrosa with forceps. Under a dissecting microscope, these fibrous interconnections were cut by microscissors at the bottom of the fibrosa, and fibrosa segments were marked by TMD on the aortic-facing surface to ensure testing of only the collagenous fibrosa layer. Segments were gently transferred to a separate container with DMEM and kept on ice. The exposed spongiosa layer was gently grasped, cut away from the ventricularis layer, and transferred to DMEM on ice. The remaining ventricularis layer was marked on the ventricle-facing side with TMD and placed in DMEM on ice. Samples underwent mechanical testing within <10 h of layer separation. Following mechanical testing, samples were embedded in Optimal Cutting Temperature compound (OCT, Tissue-Tek Sakura, Torrance, CA, USA), cryopreserved on a dry ice and isopentane bath, then sectioned and stained with Movat's pentachrome (MP, American MasterTech—KTRMP) to confirm sample layer specificity and tissue viability.

Cryoslides were dried and sections were fixed in formalin and rinsed with water. Using the MP kit, the sections were immersed in Verhoeff's elastic stain for 15 min and differentiated with 2% ferric chloride. The slides were then placed in Alician blue solution for 10 min, Crocein scarlet-acid fuchsin for 2 min, and alcoholic saffron solution for 15 min, clearing and rinsing the slides between stains. The slides were finally cleared in xylene and coverslipped using a xylene-based mounting media. Three non-serial 10 μm -thick sections per sample were stained, and imaged with an Eclipse 50i microscope (Nikon Instruments Inc., Melville, NY, USA). Spongiosa samples that contained collagen-rich areas or elastin-rich areas larger than 5% of the total sample area or fibrosa samples with >5% proteoglycan content were excluded from final analyses as contaminants from the adjacent layers.

Methacrylated Gelatin (GelMA) and Methacrylated Hyaluronic Acid (HAMA) Synthesis and Characterization

GelMA and HAMA were prepared as described previously [30,31]. In brief, gelatin (20.0 g) from porcine skin (Sigma-Aldrich, St. Louis, MO, USA, G2500) was suspended in deionized water (200 mL) in a 500-mL round bottom flask with moderate stirring for 1 h. The mixture

was heated to 50 °C and was stirred until the gelatin was completely dissolved. Methacrylic anhydride (12.0 g) (Sigma-Aldrich, 276685) was then added to the flask, and the mixture was stirred at 50 °C for 1.5 h. The product was transferred to 50 mL conical tubes and centrifuged at 3500× g for 5 min. The supernatant was decanted into a beaker, leaving behind an opaque solid at the bottom of the conical tubes. The supernatant was then diluted with two volumes of 40 °C deionized water and was transferred to dialysis tubing (10 kDa MWCO, SpectraPor 7, Spectrum Laboratories, Rancho Dominguez, CA, USA, 123120). This tubing (containing the GelMA supernatant) was dialyzed against 3500 mL of deionized water at 40 °C for seven days, with the water changed twice per day. The contents of the dialysis tubing were then transferred to a beaker and pH adjusted to 7.4 using a 1 M solution of NaHCO₃. The solution was sterile filtered with a 0.2 µm vacuum filtration unit and a polyethersulfone (PES) membrane, transferred to 50 mL conical tubes, snap frozen on liquid nitrogen, and lyophilized until complete dryness (approximately 10–14 days) to produce GelMA as a white solid powder.

For HAMA synthesis, sodium hyaluronate (1.0 g) (Lifecore Biomedical, Chaska, MN, USA, HA40K) was dissolved in 1X phosphate-buffered saline (PBS) (100 mL) in a 250 mL round bottom flask and cooled to 4 °C. Methacrylic anhydride (1.0 mL) was added and stirred at 4 °C for 24 h; pH was maintained between 8.0 and 10.0 at the beginning, middle, and end of the reaction period using aliquots of 5 M NaOH. After 24 h the reaction was transferred to 50 mL conical tubes, centrifuged at 3500× g for 5 min, and the supernatant was decanted into dialysis tubing (10 kDa MWCO, SpectraPor 7). The tubing containing the HAMA solution was dialyzed against 3500 mL of deionized water at 4 °C for seven days, with the water changed twice per day. Tubing contents were transferred to a beaker and the pH adjusted to 7.4 using a 1 M solution of NaHCO₃. The solution was sterile filtered with a 0.2 µm vacuum filtration unit with a PES membrane, transferred to 50 mL conical tubes, snap frozen on liquid nitrogen, and lyophilized until complete dryness (approximately 10–14 days) to produce HAMA as a white solid powder.

Pre-polymer solutions were mixed prior to printing. Measured weights of lyophilized GelMA, lyophilized HAMA, and lithium phenyl-2,4,6-trimethylbenzoylphosphinate (LAP, Tokyo Chemical Industry Co., Portland, OR, USA) were dissolved in PBS at 80 °C to form 20 wt %, 3 wt %, and 5 wt % solutions, respectively. GelMA solution sonicated at 37 °C, and the pH of HAMA was adjusted to 7.5 using 1 M HCl. Solutions were reheated to 80 °C for 20 min and sterile-filtered using a 0.2 µm syringe filter. Final solutions were stored at 4 °C and warmed to 37 °C prior to each experiment. For the fabrication of hybrid hydrogels, the 20 wt % GelMA, 3 wt % HAMA, and 5 wt % LAP solutions were mixed in PBS at 37 °C. This yielded hybrid hydrogel pre-polymer solutions with concentrations of 0.3% (v/v) LAP, 1% (v/v) HAMA, and 5% (v/v), 6.67% (v/v), 8.33% (v/v), or 10% (v/v) GelMA.

3D-Bioprinting of Hybrid Hydrogels

Single-Layer Hydrogel Constructs

Constructs were designed in Tinkercad (AutoDesk, Inc., San Rafael, CA, USA), and encoded using Repetier-Host (version 2.0.0; Hot-World GmbH & Co. KG, Willich, Germany), and Sublime Text 3 (Sublime HQ, Pty Ltd., Darlinghurst, NSW, Australia). 3D-bioprinting was performed using the Inkredible+ (Cellink, Cambridge, MA, USA). Pluronic gel (Pluronic F-127; Allevi, Philadelphia, PA, USA) was printed as a cylindrical mold (outer diameter = 9.0 mm, inner diameter = 8.6 mm, height = 1.5 mm) using a stainless steel needle nozzle (JG27-0.25HPX; Jensen Global Inc., Santa Barbara, CA, USA) at a fill density of 95%, layer height of 0.1 mm, printing speed of 4mm/s, and printing pressure of 320 kPa.

The second extruder was filled with the required hydrogel pre-polymer compositions and heated to 37 °C. A hydrogel disc was then printed inside the mold from the second extruder using a 23 g stainless steel nozzle (Fisnar 5901005, Ellsworth Adhesives, Germantown, WI, USA) by opening the valve of the second extruder for 40 ms at 15-20 kPa. Crosslinking the pre-polymers for 30 or 90 s with 365 nm UV light produced 8.6 mm × 1.0 mm hydrogel discs. The UV light was calibrated to an intensity of 2.5 mW/cm² using a radiometer (85009, Sper Scientific Direct, Scottsdale, AZ, USA). After printing, the Pluronic gel was dissolved by washing in 37 °C PBS. Hydrogel porosity was evaluated by embedding and cryosectioning as described above. Pore structure was assessed by staining with Natural Blue food dye (Whole Foods Market, Austin, TX, USA). Bright field microscopy images were then taken using an Eclipse 50i microscope (Nikon Instruments, Melville, NY, USA). Average pore size was then measured with ImageJ (National Institutes of Health, Bethesda, MD, USA, version 1.51s). To perform swelling ratio testing, acellular hydrogels were printed and crosslinked. The Pluronic mold was then cut away, and gels were weighed immediately then immersed in PBS for 24 h at room temperature, at which point they were quickly blotted dry of surface liquid and weighed again.

Dual-Layer Hydrogel Constructs

The Pluronic mold was printed as described above. A hydrogel pre-polymer solution of 0.3% LAP, 5% GelMA, and 1% HAMA at 37 °C was loaded into the second extruder. The first layer was printed by opening the valve of the second extruder for 30 ms at 15-20 kPa. After crosslinking the first layer for 60 s at 2.5 mW/cm², the extruder was raised 1 mm and a second layer was printed on top by opening the valve of the second extruder for 30 ms. After 5 min incubation at 37 °C, the combined layers were crosslinked together for an additional 30 s. To visualize the layer interface, 70.000 MW lysine-fixable Dextran labeled with Texas Red or Fluorescein (Thermo Fischer Scientific, Waltham, MA, USA) were mixed into each hydrogel layer, and the constructs were imaged by confocal (Nikon) in cross-sectional z-stacks to assess layer-layer integration.

Mechanical Testing of CAVD Leaflets and Hydrogels

Mechanical testing was performed using an Agilent G200 nanoindenter (Agilent, Santa Clara, CA, USA) with a 90° diamond conical probe tip with a 50 μm radius (DCMII, Micro Star Technologies, Huntsville, TX, USA) to enable measurement of bulk properties [32]. The tip area function was calibrated using fused quartz, and a punch diameter of 45.153 μm was calculated at a 5 μm pre-compression depth. A 3 × 3 array of indents with 200 μm spacing was generated. Tests were run as dynamic indentations to afford the complex shear modulus under the shear mode [33] at room temperature at a constant frequency of 110 Hz. Storage modulus G' was measured as the energy stored during one oscillation cycle, and loss modulus G'' was measured as the energy dissipated during an oscillation cycle [34]. The loss tangent ($\tan \delta$) was measured as the ratio between G'' and G' . The complex modulus G^* was calculated using:

$$|G^*| = \sqrt{G'^2 + G''^2}$$

Poisson's ratio (ν) was estimated for both the leaflet layers and the hydrogels using two different-sized conical probes and were found to be approximately 0.5, corresponding to values confirmed in the literature for bulk measurements of hydrogel polymers [35] and AV leaflet tissue [36]. Using the rubber elasticity theory, Young's modulus (E) was calculated as:

$$E = 2G^*(1 + \nu)$$

The median of nine indents was taken for every sample. For the mechanical measurement of dual-layer hydrogels, two tests were performed. First, hydrogels were tested from both sides to evaluate layer-to-layer differences. Second, the cross-section of the hydrogels was tested along the z-axis using 10 nanoindentation measurements equally spaced from the top of the fibrosa-like side to the bottom of the spongiosa-like side.

Unconfined compression testing was also performed on selected hydrogels using an Instron 5566 (Instron, Norwood, MA, USA). Compression occurred at a rate of 1 mm/minute between two parallel steel plates, and the Young's modulus was calculated from the slope of the linear region of the loading curve.

Human Aortic Valvular Interstitial Cell (VIC) Isolation, Culture, and Encapsulation in Hydrogels

CAVD AV leaflets were obtained as described above, and non-diseased AV leaflets were obtained from patients undergoing heart transplantation surgery due to cardiomyopathy at UMC Utrecht (the Netherlands). Leaflets were obtained there in accordance with protocols approved by the Medical Ethical Assessment Committee of UMC Utrecht.

VICs from CAVD AV leaflets and non-diseased AV leaflets were isolated as previously described [9,37]. In brief, CAVD leaflets were incubated for 3 h in a 10 mL collagenase solution at 37 °C, 5% CO₂, homogenized with a serological pipette and passed through a cell strainer (40 μm). The digested tissue was centrifuged, the supernatant was aspirated, and the pellet was resuspended in 5 mL of VIC cell culture media. The cells were centrifuged a second time, resuspended in 10 mL media, and plated in a T75 culture flask. Non-CAVD leaflets were incubated for 45–50 min at 37 °C in 8% collagenase solution in PBS supplemented with 1% FBS and 2% gentamycin. The digested tissue was passed through a cell strainer (100 μm), rinsed 3 × 5 mL in DMEM, and centrifuged. The supernatant was aspirated, and the pellet was resuspended in 5 mL VIC cell culture media and plated in 6-well plates. VIC culture media (DMEM, ThermoFisher, Grand Island, NY, USA) was supplemented with 10% (CAVD VICs) or 15% (non-diseased VICs) fetal bovine serum (Gibco), 5% human serum (first three passages of non-diseased VICs only), and 1% Penicillin/Streptomycin (P/S, Gibco). Media was refreshed every 48 h, DMEM was supplemented with 10% FBS and 1% P/S after passage three regardless of VIC type, and VICs between passage five and six were used for further experiments. VICs were incorporated in the hydrogel pre-polymers by mixing VICs and media (to a final in-gel concentration of 10×10^6 cells/mL) with a 10 wt % GelMA, 3 wt % HAMA, and 5 wt % LAP solution at 37 °C to form a 5% GelMA, 1% HAMA, and 0.3% LAP hydrogel. As a 2D control, VICs were also cultured on tissue culture polystyrene (TCPS) in a 24-well plate. One day after printing, hydrogels were switched to normal media (5% FBS, 1% P/S) or osteogenic media (NM supplemented with 10 nM dexamethasone, 10 ng/mL ascorbic acid, and 10 mM β-glycerolphosphate) as previously described [4] for up to 14 days. Media was changed every 48 h for all 3D hydrogels and 2D controls.

Calcification and Apoptosis Assays

A near infrared fluorescence (NIRF) imaging agent (OsteoSense 680EX; PerkinElmer, Waltham, MA, USA) was used to visualize nano- and microcalcification. OsteoSense 680EX was added to the cell culture media at a 1:100 dilution and cells were incubated overnight at 37 °C, 5% CO₂ for 12 h prior to imaging. Apoptosis was assessed by Click-iT TUNEL (Thermo Fisher Scientific, Waltham, MA, USA) assays according to the manufacturer's instructions. Confocal imaging (Nikon A1) was performed as follows: three hydrogels per condition were imaged with three z-stacks (10 μm/slice) per hydrogel. Z-stacks were compressed into maximum intensity projections in ImageJ and positive stain area was quantified.

Analysis of VIC Remodeling Capability

Hydrogels were snap frozen in OCT as described above and 10 μm cryosections were made. Ability of VICs to remodel ECM was gauged by collagen production and its degradation by matrix metalloproteinase 9 (MMP-9). Sections were stained for collagen using the CNA35 probe by incubating sections (1:50 in PBS) for 1 h at 37 °C [38]. MMP-9 immunofluorescence

was performed as follows: sections were permeabilized with 0.1% Triton-X, then dried and fixed in 4% paraformaldehyde for 5 min. Slides were rinsed in water and PBS, and endogenous peroxidase activity was blocked with 0.3% hydrogen peroxide. After rinsing, sections were blocked in 4% donkey and goat serum (D9663, Sigma, St. Louis, MO, USA, S-1000, Vector, Burlingame, CA, USA) and then incubated with an anti-MMP-9 mouse (NBP2-13173g, 1:100, Novus, Littleton, CO, USA) primary antibody for 90 min at room temperature, followed by an Alexa Fluor 488-conjugated (A11017, Invitrogen, Carlsbad, CA, USA) secondary antibody. Sections were washed in PBS and mounted in mounting media with DAPI (H-1500, Vector Laboratories, Burlingame, CA, USA) to stain nuclei. Confocal imaging was performed as above, and positively stained cells were quantified by manual counting.

Electron Microscopy

Hydrogels were fixed and stored in a buffer of 2% gluteraldehyde, 0.115 M sucrose, in 0.1 M sodium cacodylate (Electron Microscopy Science, Hatfield, PA, USA, 11653) until use. Constructs were dehydrated in a series of 30%, 50%, 70%, 90%, 100%, 100%, and 100% ethanol on ice for 15 min each, prior to critical point drying (Critical Point Dryer Tousimis 931 GL; Tousimis, Rockville, MD, USA). Constructs were then coated with platinum/palladium in a sputtering system (EMS 300 T D Dual Target Sequential Sputtering System; Electron Microscopy Systems, Hatfield, PA, USA). Scanning electron microscopy (SEM) images were taken on a field emission scanning electron microscope (Supra55VP; Zeiss, Thornwood, NY, USA).

Statistical Methods

Nanoindentation data are presented as the median value per tissue sample, with each data point representing nine nanoindentation measurements per sample. Other quantitative data are presented as mean \pm standard error. Two-tailed, one-sample t-tests were used to compare G''/G' values vs. the theoretical value of 1, Student's t-tests were performed for two-group comparisons, and one-way or two-way ANOVA with Tukey's post-hoc HSD test were used as appropriate to evaluate statistically significant differences in multiple group comparisons (R or GraphPad Prism 7, GraphPad Software, La Jolla, CA, USA).

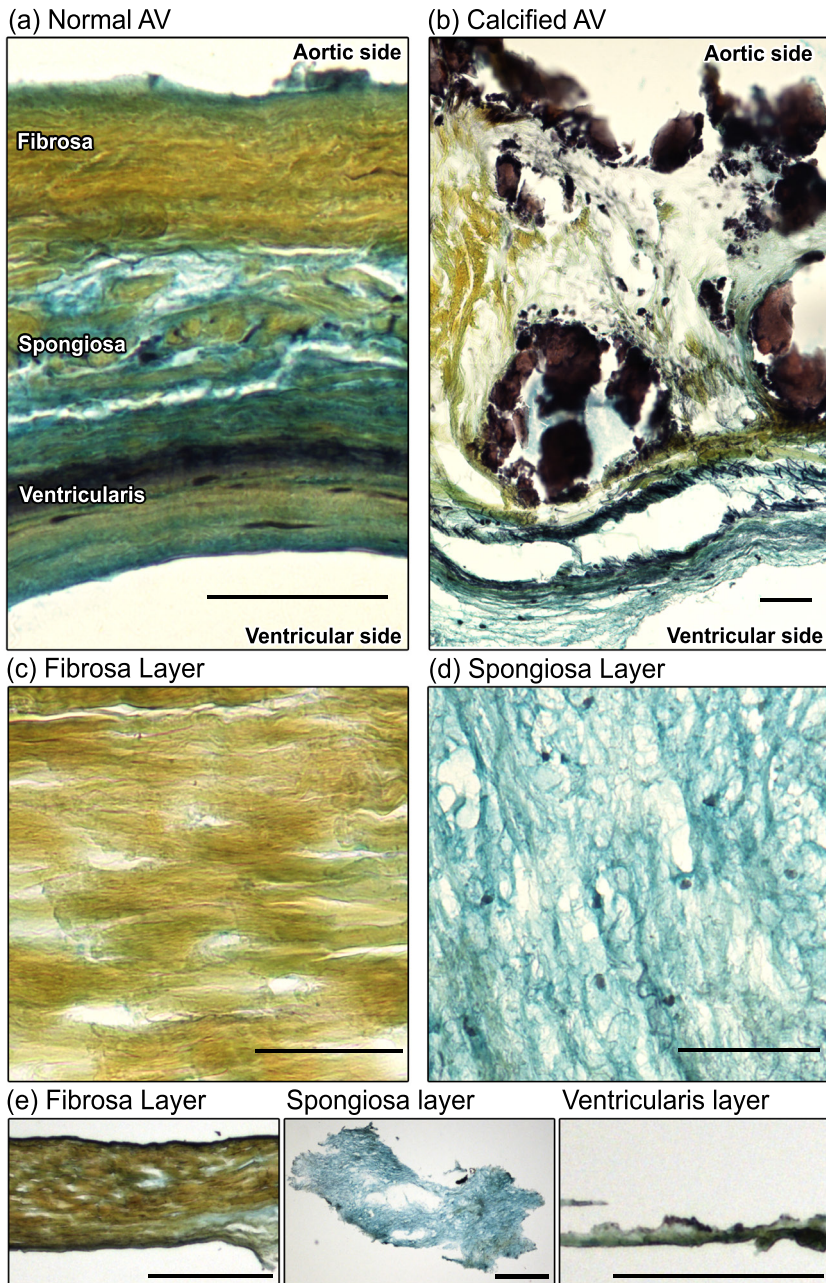


Figure 1. Movat's pentachrome staining of structural organization in a circumferential cross-section of a human AV leaflet. Yellow = collagen, blue = glycosaminoglycans (GAGs), black = elastin, dark brown/black = calcification: (a) Tri-layered arrangement of the fibrosa (collagen-rich), spongiosa (GAG-rich), and ventricularis (elastin-rich) layers in a healthy leaflet; (b) Disruption of the leaflet layers by calcifications (black) and fibrosis (yellow regions) in CAVD; (c,d) Staining of collagen in the dissected fibrosa layer and GAGs in the dissected spongiosa layer confirmed distinct layer separation; scale bar = 50 μm ; (e) Low-magnification images of microdissected fibrosa, spongiosa, and ventricularis layers; scale bar = 500 μm .

RESULTS

Leaflet Layer Separation of Human Aortic Valves by Microdissection

The human AV is composed of three distinct layers with unique ECM composition and VIC phenotypes [17]. The fibrosa layer is composed primarily of circumferentially oriented collagen fibers (yellow by Movat's); the spongiosa layer sits in the middle of the leaflet and is rich in hydrated proteoglycans (blue-green); the ventricularis is rich in radially oriented elastin fibers [39] (black; Figure 1a). As CAVD progresses, calcification and fibrosis develop preferentially in the fibrosa layer [6,7] and the layers themselves are thickened and disrupted (Figure 1b). We separated non-calcified leaflet layers by microdissection and confirmed that dissected layers were successfully divided by Movat's pentachrome staining, which identified collagen-rich samples from the fibrosa layer and glycosaminoglycan-rich samples dissected from the spongiosa layer (Figure 1c–e).

3D-Bioprinting of Hybrid Hydrogel Constructs

To produce an *in vitro* model of human CAVD that was capable of recapitulating AV leaflet layer-specific mechanical properties, we employed a tunable hydrogel system that we had previously shown to be capable of maintaining porcine VIC quiescence under basal conditions in 3D [19]. Our platform utilized methacrylated gelatin (GelMA), methacrylated hyaluronic acid (HAMA), and the UV photoinitiator lithium phenyl-2,4,6-trimethylbenzoylphosphinate (LAP) (schematic of hydrogel synthesis shown in Figure 2a). Upon exposure to ultraviolet light, the polymers formed crosslinks between the methacrylate groups, producing a synthetic ECM. These hydrogels (encapsulated VICs, culture media, hydrogel pre-polymers, and LAP) were 3D-bioprinted into sacrificial Pluronic molds using a heated-extruder to produce disc-shaped hydrogels (8.6 mm in diameter \times 1.0 mm in height) suitably sized for culture in 12-well plates (Figure 2b,d). Two distinct bioprinting regimes were performed: single-layer hydrogels were printed as above (Figure 2b), while novel dual-layer constructs were produced by serial printing and UV crosslinking of layers (Figure 2c).

Leaflet Layer Mechanical Properties Were Recapitulated in Hydrogels

Nanoindentation revealed significant differences in mechanical properties between human AV leaflet layers. The fibrosa layer had a significantly higher median Young's modulus (37.1 kPa) than the spongiosa layer (15.4 kPa) (Figure 3a), while that of the ventricularis was 26.9 kPa (Table S1). The storage modulus G' had a similar distribution across leaflet layers as that of the Young's modulus (Figure 3b), and nanoindentation measurements exhibited low measurement-to-measurement variability per tissue sample (Supplemental Figure S1a). Although compressive Young's moduli were heterogeneous (the fibrosa layer ranged from 20.3–56.7 kPa, spongiosa = 12.8–26.8 kPa, ventricularis = 16.6–33.5 kPa [Table S1]), there were distinct ranges of stiff fibrosa (above \sim 30 kPa) and soft spongiosa (below \sim 20 kPa)

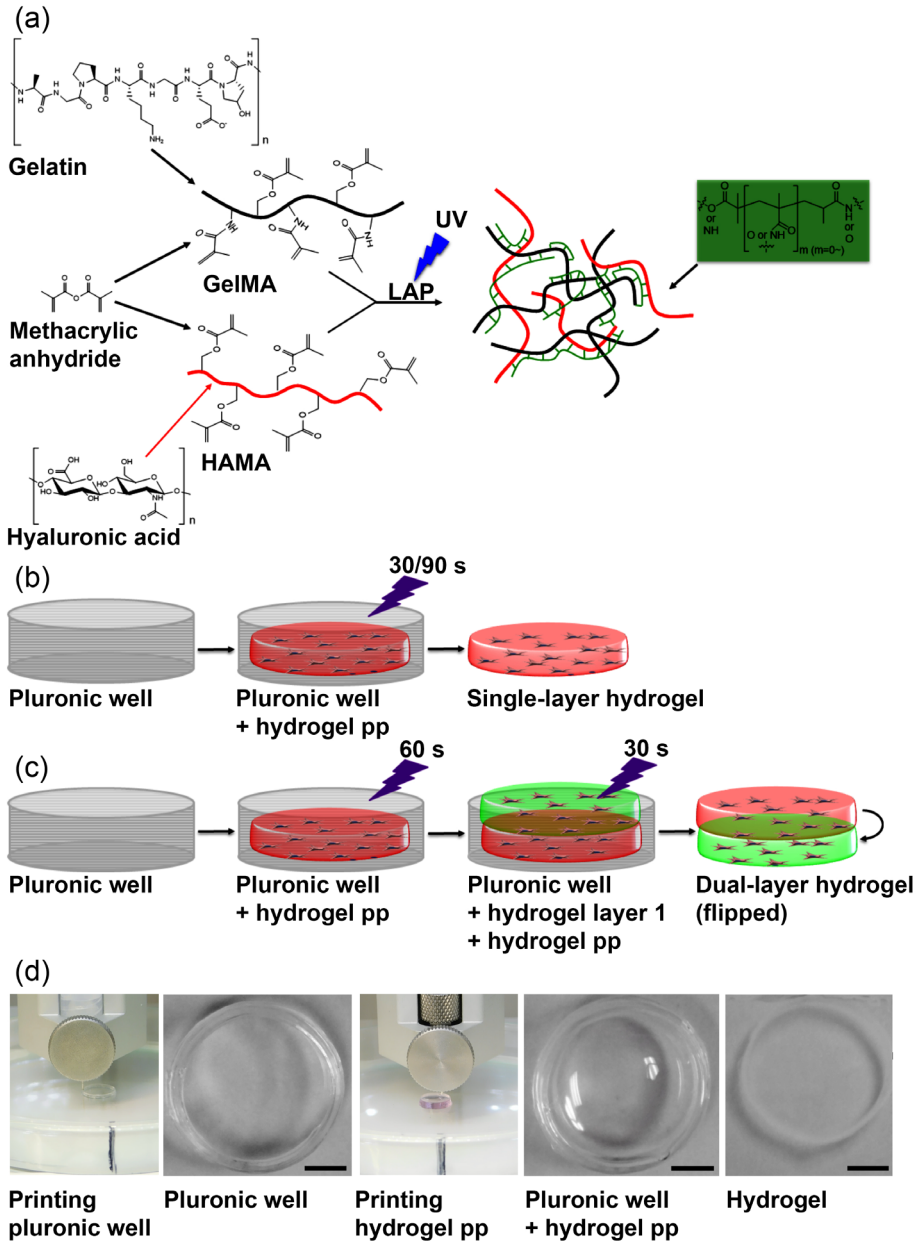


Figure 2. Bioprinting of hybrid hydrogel constructs using methacrylated gelatin (GelMA) and methacrylated hyaluronic acid (HAMA): (a) Schematic of hybrid GelMA/HAMA hydrogel synthesis and gelation. Black = gelatin, Red = hyaluronic acid, green = crosslinks, UV = photocrosslinking with 365 nm UV light at 2.5 mW/cm²; (b,c) 3D printing of single- and dual-layer hydrogel constructs by printing a Pluronic ring, followed by hydrogel pre-polymer (pp) inside, and photocrosslinking for a total of 30 and/or 90 s per layer; (d) Representative images of (left to right): 3D bioprinting the Pluronic ring, the completed Pluronic ring, 3D bioprinting the hydrogel pre-polymer into the Pluronic ring, the completed Pluronic ring + printed hydrogel pre-polymer, and hydrogel after crosslinking and washing away the Pluronic (right). Scale bar = 2 mm.

that were unique to their respective layer. The median Young's modulus of the intact leaflet (26.7 kPa) lay between the upper and lower bounds of stiff fibrosa and soft spongiosa and highlighted the importance of assessing layer-specific biomechanics when studying layer-specific VIC phenotypes. To assess the relative contributions of viscous and elastic responses in CAVD tissue, quantification of the loss tangent $\tan \delta$ (loss modulus G'' over storage modulus G' ; Figure 3e) found that $\tan \delta$ was significantly less than 1 in all layer samples, indicating that elastic deformation was the primary contributor to the complex modulus G^* and thus to the Young's modulus of valvular tissue.

Once compressive moduli of the AV leaflet layers had been determined, we then 3D-bioprinted a series of acellular hybrid hydrogels composed of 5–10% GelMA and 1% HAMA and crosslinked for 30–90 s. Nanoindentation was performed on all hydrogels (Table S2). We found that the 5% GelMA/1% HAMA hydrogel exposed for 30 s had the lowest median modulus (21.7 kPa) and was the best match to the Young's modulus of the spongiosa layer (Figure 3c). Two hydrogel formulations had Young's moduli comparable to that of the fibrosa layer: 5% GelMA/1% HAMA/90 s cross-linking (38.5 kPa; Figure 3c), and 6.67% GelMA/1% HAMA/30 s cross-linking (38.6 kPa; Table S2). The former had lower gel-to-gel variability, less overlap in stiffness with the softer 5% GelMA/1% HAMA/30 s hydrogel, and an identical hydrogel composition to that of the 5% GelMA/1% HAMA/30 s hydrogel. As was the case with the AV tissue, hydrogel storage moduli (G') significantly differed between the 30 s and 90 s 5% GelMA/1% HAMA hydrogels and closely matched those values of their tissue counterparts (Figure 3d). In contrast, $\tan \delta$ values remained significantly less than one in the hydrogel system (Figure 3e). Unconfined compression testing of 30 s and 90 s 5% GelMA/1% HAMA hydrogels (Supplemental Figure S1b–d) demonstrated that the modulus of 90 s gels was twice that of 30 s gels (as was the case for testing by nanoindentation, Figure 3c). Together, these findings indicated that the specific hydrogel biomechanics closely mimicked those of the individual layers of native AV tissue. On the basis of these data, the 5% GelMA/1% HAMA/30 s hydrogel was utilized as a spongiosa-like (S-like) model and the 5% GelMA/1% HAMA/90 s hydrogel became the fibrosa-like (F-like) model for the remainder of this work.

VIC Encapsulation Affects Hydrogel Mechanics

After characterizing acellular hydrogel mechanics, we bioprinted VIC-free and VIC-laden F-like and S-like hydrogels, then cultured them in normal media (NM) or osteogenic media (OM) to assess the long-term impact of VIC encapsulation on hydrogel mechanics. After 14 days in NM (Figure 4a), the median Young's modulus of VIC-free F-like and S-like hydrogels was unchanged and that of the F-like gel remained significantly higher than that of the S-like gel. At day 1 there was no significant difference between VIC-free and VIC-laden moduli (ANOVA, data not shown). In S-like gels, encapsulation of VICs and culture in NM or OM for 14 days did not affect hydrogel mechanical properties. In contrast to the acellular condition and

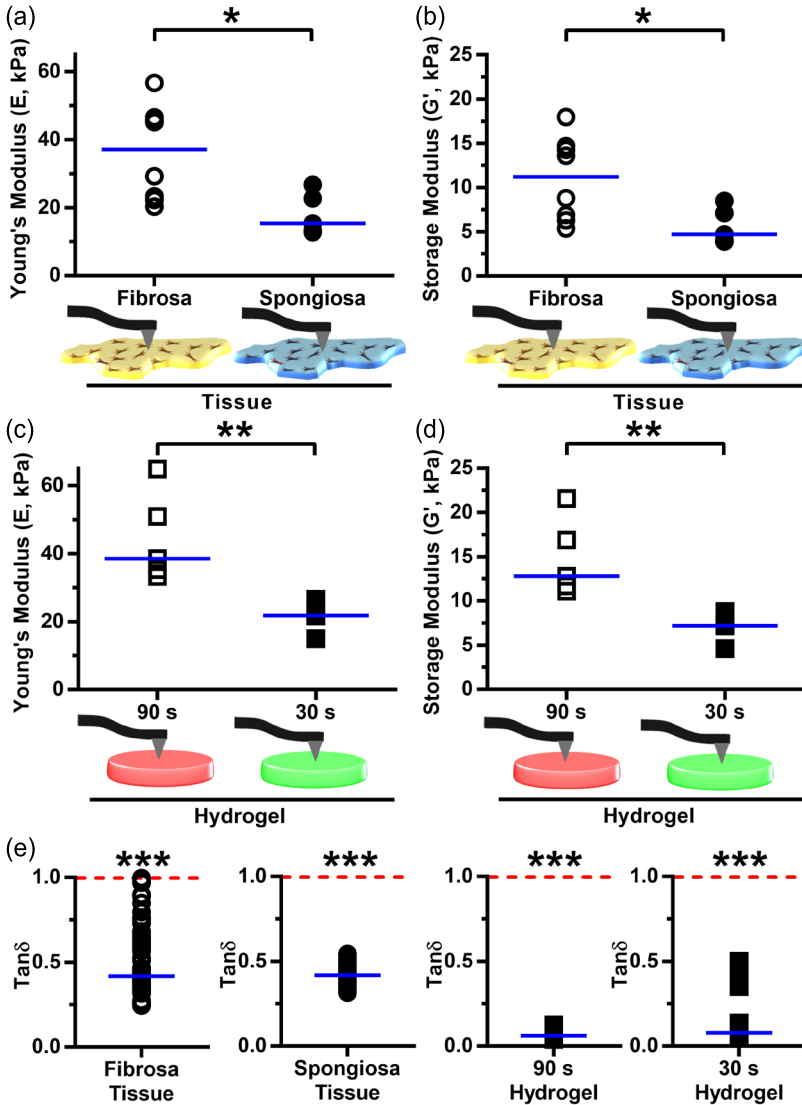


Figure 3. Measurement of layer-specific leaflet mechanical properties and matching of biomechanics with GelMA/HAMA hydrogels: (a,b) Nanoindentation of the CAVD leaflet layers determined that the median Young's modulus of the fibrosa layer (37.1 kPa) was significantly higher than that of the spongiosa layer (15.4 kPa), and that the median storage modulus (G') of the fibrosa layer (11.2 kPa) was significantly higher than that of the spongiosa layer (4.7 kPa); (c,d) Nanoindentation of hybrid hydrogels found that the median Young's modulus of the 5% GelMA/1% HAMA hydrogel after UV crosslinking for 90 s (38.5 kPa) was significantly higher than that of the 5% GelMA/1% HAMA/30 s crosslinked hydrogel (21.7 kPa). GelMA/HAMA gels crosslinked for 90 s and 30 s recapitulated Young's moduli of the fibrosa and spongiosa layers, respectively. G' of the 90 s crosslinked hydrogel (12.8 kPa) was significantly higher than that of the 30 s crosslinked hydrogel (7.2 kPa). Hydrogel storage moduli again mimicked those properties of the native tissue; (e) The $\tan \delta$ (G''/G' , loss tangent: viscous vs. elastic deformation) of individual samples within the fibrosa layer, spongiosa layer, 90 s hydrogel, and 30 s hydrogel were all significantly smaller than 1. In comparison to the leaflet layers, $\tan \delta$ remained lower for both hydrogels. Median shown; * $p < 0.05$, ** $p < 0.01$, *** $p < 0.001$; $n = 5-9$ samples per condition (nine measurements per sample).

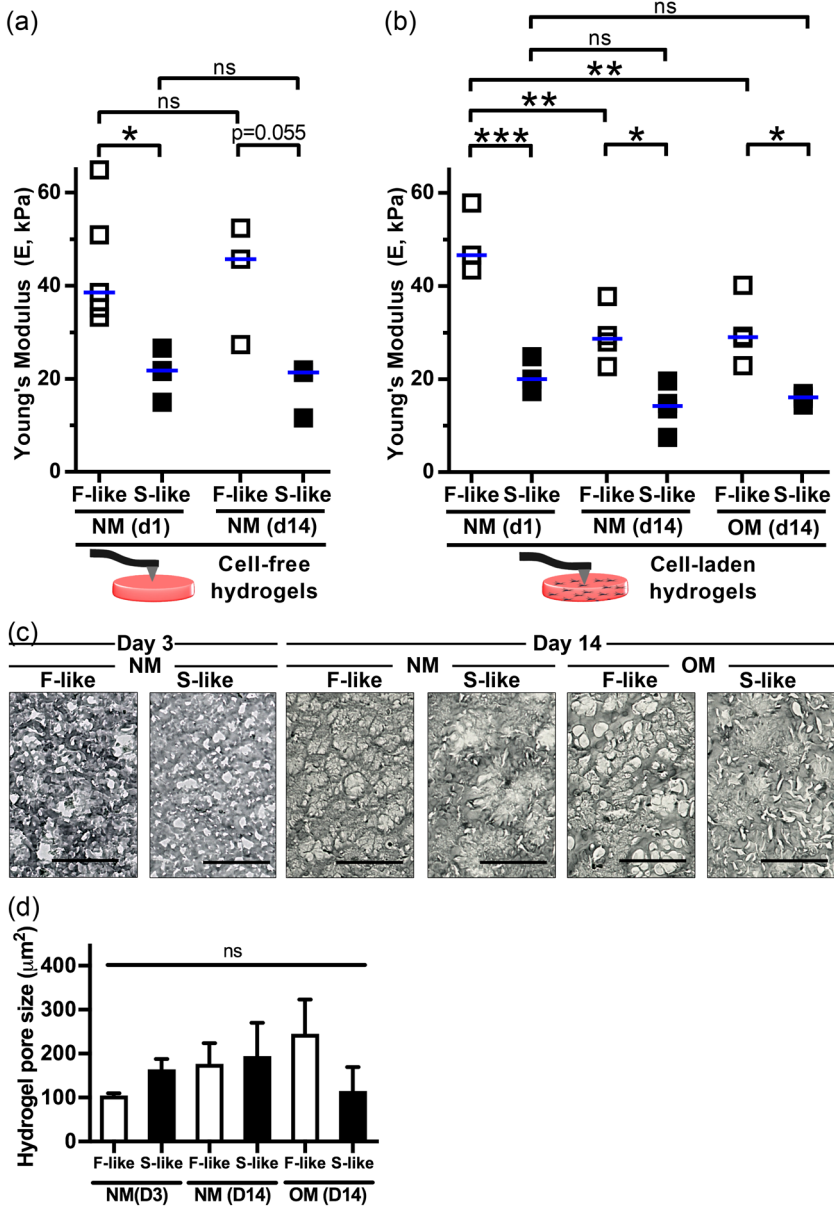


Figure 4. Encapsulation and culture of VICs within fibrosa-like (F-like) but not spongiosa-like (S-like) hydrogels affected hydrogel mechanics: (a) The median Young's modulus of cell-free 3D-bioprinted F-like (5% GelMA/1% HAMA/90 s crosslinking) and S-like (5% GelMA/1% HAMA/30 s crosslinking) hydrogels did not change over 14 days of culture in NM; (b) The median Young's modulus of VIC-laden F-like hydrogels (and not S-like hydrogels) decreased significantly over time in culture (14 days), regardless of NM or OM treatment conditions. Median shown; n = 3–5 samples per condition (9 measurements per sample); (c,d) Representative images and quantification of bright-field microscopy demonstrated that after 3 and 14 days in culture (NM and/or OM), pore sizes of F-like and S-like hydrogels were not significantly different. Mean + SEM; * p < 0.05, ** p < 0.01; *** p < 0.001; n = 3 samples per condition; scale bar = 100 μm.

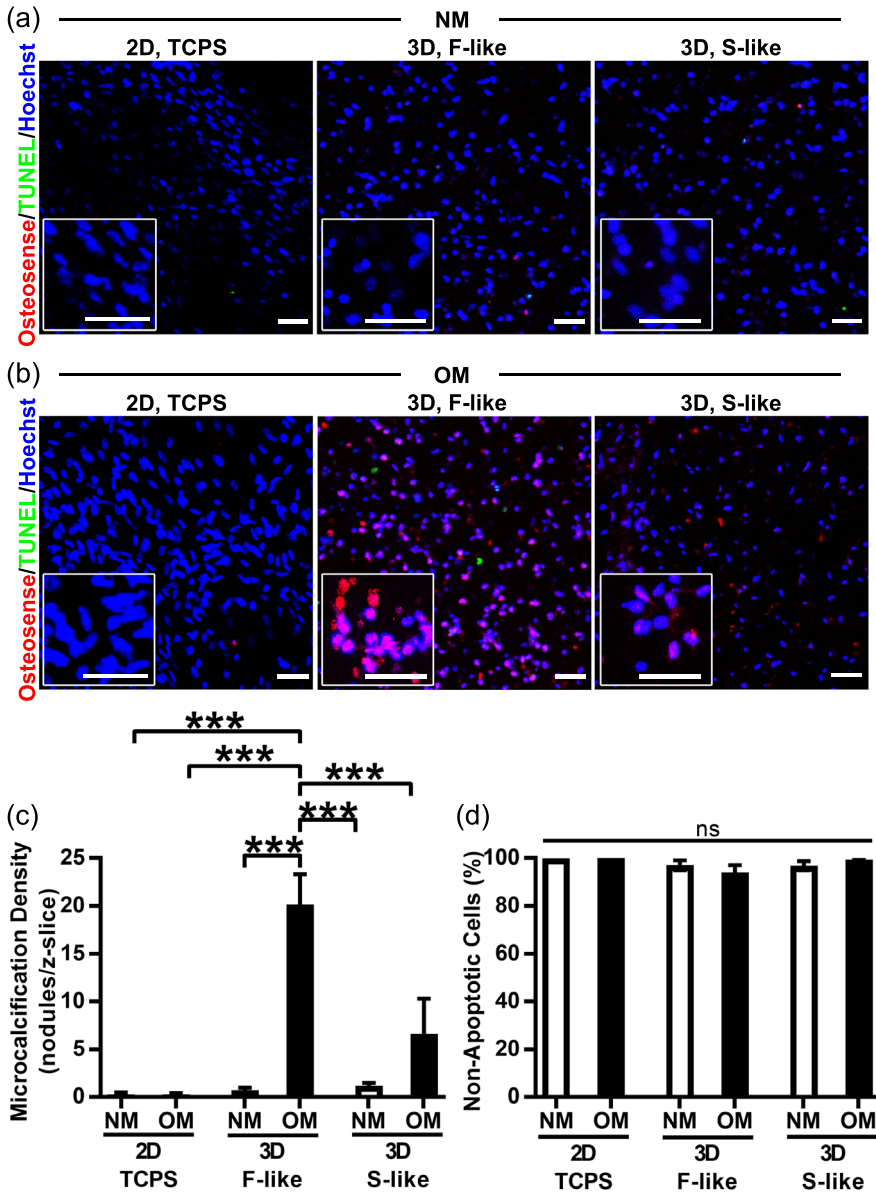


Figure 5. Fibrosa-like hydrogels preferentially induced production of osteogenic microcalcification by VICs. Red = NIRF Osteosense 680 imaging agent (nano- and microcalcifications), green = TUNEL apoptosis assay, blue = Hoechst nuclear stain: (a) VICs isolated from non-diseased human AV did not undergo calcification when cultured in NM on/in either 2D tissue culture polystyrene (TCPS), 3D fibrosa-like (F-like) hydrogels, or 3D spongiosa-like (S-like) hydrogels (representative images); (b,c) Importantly, under OM treatment this naïve VIC population developed significant production of microcalcification only in 3D F-like hydrogels that mimic the biomechanics of the disease-prone layer of the native tissue. OM treatment did not induce significant microcalcification on 2D TCPS or in 3D S-like hydrogels. (d) Apoptosis was negligible and unchanged across all conditions, confirming that apoptotic cell death was not the source of preferential calcification in OM-treated F-like hydrogels. Mean + SEM; *** $p < 0.001$; $n = 3$ samples per condition (3 images per sample); scale bar = 50 μm .

to VIC-laden S-like hydrogels, VIC-laden F-like gels underwent cell-dependent remodeling and significant reductions in stiffness by the 14-day time point (Figure 4b). Notably however, these cultured VIC-laden F-like hydrogels remained significantly stiffer than their S-like counterparts. By bright-field microscopy (Figure 4c,d), we confirmed that there were no significant changes in VIC-laden hydrogel pore sizes between NM/OM and F-like/S-like conditions after 3 or 14 days of culture, and pore size was consistent with those of 5% GelMA/1% HAMA/30 s crosslinked gels described previously by SEM [19]. Swelling ratio testing of acellular F-like and S-like hydrogels (Supplemental Figure S2) found a significantly increased swelling of S-like hydrogels, likely a result of reduced free volume with greater crosslinking [40].

Preferential Formation of Microcalcification in Fibrosa-Like Hydrogels

After we confirmed our ability to print hydrogels that mimicked the mechanical properties of individual native leaflet layers with encapsulated VICs that maintained an ability to remodel hydrogels, we proceeded to assess the calcifying potential of our 3D-bioprinted model. Naïve VICs derived from non-diseased AV were seeded in 2D well plates or encapsulated in F-like or S-like hydrogels. Under NM treatment (Figure 5a,c), there was no formation of nano- or microcalcification in any culture condition, as assessed by confocal imaging of the calcium binding NIRF imaging agent [41,42]. In contrast, although there was no microcalcification in OM-treated 2D culture and limited amounts in 3D S-like hydrogels, VICs in 3D F-like hydrogels (that recapitulated the biomechanics of the disease-prone fibrosa layer) responded to osteogenic stimuli by significantly increasing microcalcification nodule density vs. all other culture conditions after 14 days (Figure 5b,c). Importantly, apoptotic cell death was (i) almost completely absent and (ii) unchanged across all conditions, thus confirming that apoptotic processes were not driving (or caused by) preferential calcification of OM-treated F-like gels (Figure 5d). We also found minimal apoptosis by day three in culture, shortly after bioprinting/crosslinking (Supplemental Figure S3). Apoptosis levels were again unchanged across all conditions, consistent with an absence of short-term LAP/UV-induced cytotoxicity.

VIC Remodeling of Fibrosa-Like Hydrogels

To further study pathological differentiation and remodeling in our hydrogel model, we treated VIC-laden F-like and S-like hydrogels with NM and OM, then assessed collagen production using the collagen-binding CNA probe [38]. Diseased CAVD fibrosa tissue samples were demonstrably rich in collagen, and OM treatment induced significant increases in collagen production by VICs in both F-like and S-like hydrogels (OM F-like collagen levels were significantly elevated beyond those of OM S-like constructs; Figure 6a,c), with a further substantial increase in collagen production after 28 days in culture (Supplemental Figure S5). As a result of the reduction in F-like stiffness over culture time identified in Figure 4b, we also examined expression of MMP-9, a collagenase/gelatinase previously shown to be upregulated in CAVD [43]. MMP-9 levels trended towards elevation in F-like OM-treated

hydrogels (Figure 6b,d). In addition, scanning-electron microscopy (SEM) of VIC-laden hydrogels confirmed that OM treatment drove elevated formation of *in vivo*-like microcalcific nodules (Figure 6e–g) after 21 days in culture, consistent with the calcium binding NIRF imaging agent staining presented in Figure 5. At day 3, encapsulated VICs were seeded consistently across the height of hydrogels, and this uniform distribution was maintained by day 14 (Supplemental Figure S4).

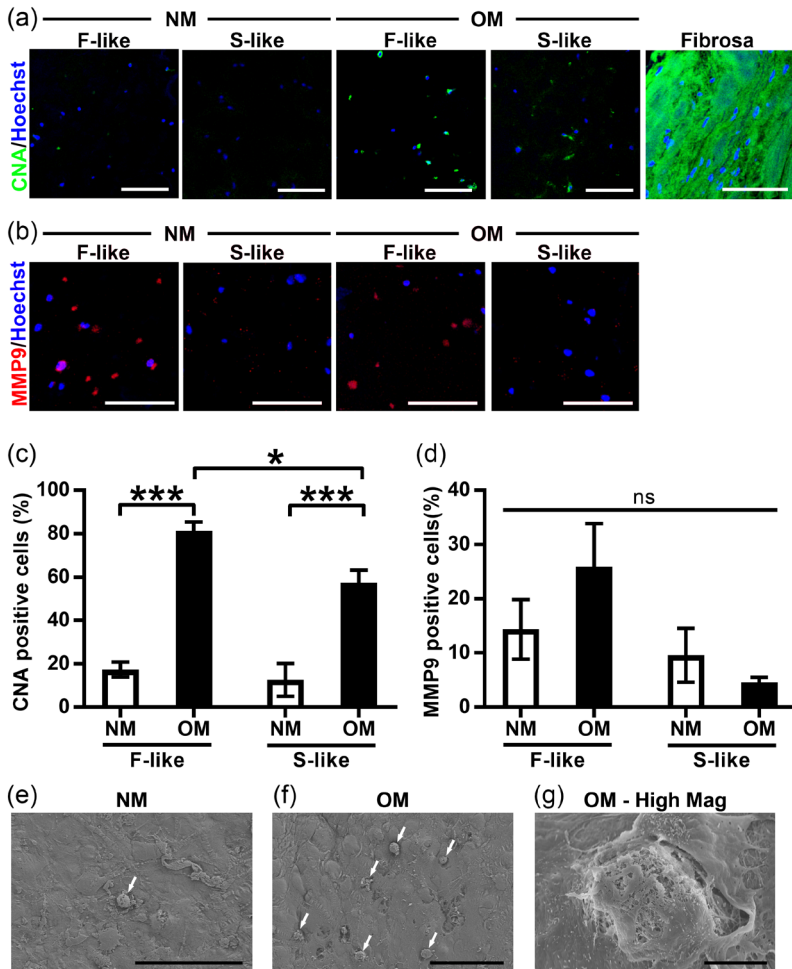


Figure 6. OM stimulation induced VIC pathogenesis in 3D-bioprinted hydrogels: (a,c) VICs isolated from non-diseased human AV and exposed to OM (and not NM) for 14 days stimulated production of collagen, as shown by representative images of collagen-binding probe (CNA35) fluorescence; (b,d) OM-treated F-like VICs trended towards increased expression of the ECM-degrading collagenase enzyme MMP-9 (representative immunofluorescence images). Mean \pm SEM; * $p < 0.05$, *** $p < 0.001$; $n =$ three samples per condition (three images per sample); scale bar = 200 μm ; (e–g) SEM of hydrogels showed that OM treatment drove formation of *in vivo*-like microcalcific nodules (white arrows), scale bar = 100 μm (e,f) or 10 μm (g).

Integration of Single-Layer Fibrosa-Like and Spongiosa-Like Hydrogels into a 3D-Bioprinted Dual-Layer Construct

Having established 3D-bioprinting of single-layer hydrogels that, individually, modeled the behavior of the fibrosa and spongiosa *in vitro*, we focused on combining these gels into an integrated model of valvular tissue. Using a strategy of serial bioprinting and partial UV crosslinking, dual-layer constructs that mimicked both the fibrosa and spongiosa were printed as per Figure 2c. When red and green fluorescent Dextran beads were incorporated into individual layers, confocal imaging found evidence of layer fusion with a yellow gradient at the interface (Figure 7a), suggestive of layer intercalation that was also present in the native tissue (see transitions between layers in native AV by Movat's pentachrome in Figure 1a). The layer interface appeared strong and withstood all processing, handling, and culture without evidence of delamination or degradation. By nanoindentation, we found that F-like or S-like layer Young's moduli did not differ significantly between their respective single- and dual-layer conformations. Importantly, significant differences between the F-like and S-like layers were maintained when these hydrogel formulations were printed and crosslinked together in dual-layer constructs (Figure 7b). Finally, we used nanoindentation to examine how Young's modulus varied along the cross-section (z-axis) of dual-layer hydrogels (Figure 7c). Three distinct stiffness regimes were identified: a layer with F-like stiffness, followed by a region of intermediate stiffness in the center of the construct, and lastly, an S-like layer. VICs were successfully encapsulated, bioprinted, and cultured for 14 days in these dual-layered hydrogels (Figure 7d). Together, these findings indicated that our 3D-bioprinted multi-layered AV models were potentially suitable for evaluating layer-specific differences in VIC function.

DISCUSSION

The AV is a complex and dynamic microenvironment (reviewed in C. Y. Yip et al. [44]) with a mechanosensitive resident cell population that actively contributes to disease progression under conditions of altered biomechanics (e.g., hypertension [45] or bicuspid aortic valve [46]). This inherent complexity has retarded efforts to appropriately model CAVD *in vitro* and negatively impacted drug development for this deadly disease. Here, we successfully paired layer-specific measurements of human AV mechanical properties with 3D-bioprinted hydrogel model systems for the first time.

The tensile properties of the human AV (relevant to cyclic stretch) have been the focus of many studies and have even been performed in a layer-specific manner [12,13,14]. However, tensile factors may be less relevant than valvular substrate stiffness/compressive Young's moduli, particularly as they relate to static culture models of disease. In non-diseased porcine AVs, a prior study found the fibrosa and ventricularis stiffnesses by micropipette aspiration to

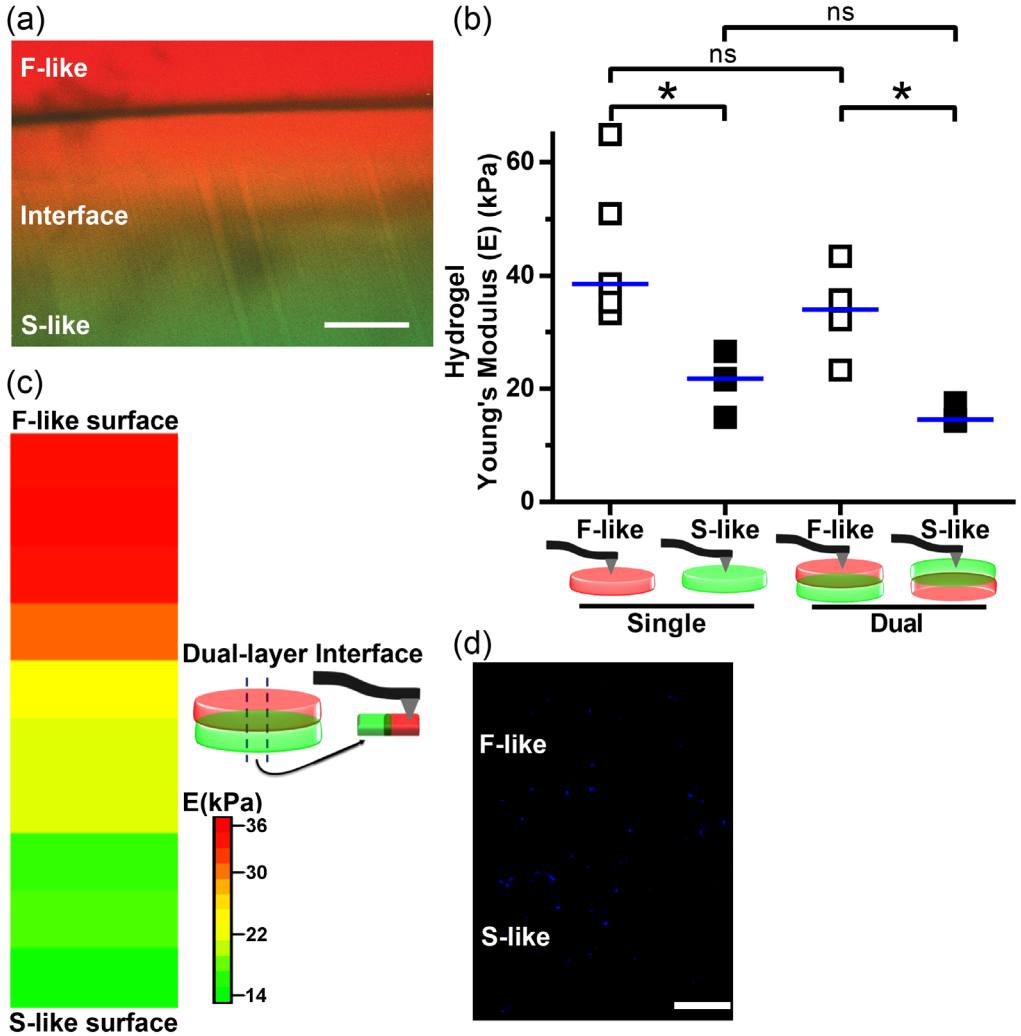


Figure 7. Integration of fibrosa-like (F-like) and spongiosa-like (S-like) single-layer hydrogels into a 3D-bioprinted dual-layer construct maintains leaflet layer-specific mechanical properties: (a) Cross-section of a dual-layered 5% GelMA/1% HAMA hydrogel stained with fluorescein-labeled Dextran (shown in red) for the 90 s crosslinked F-like layer, and Texas Red-labeled Dextran (shown in green) for the 30 s crosslinked S-like layer demonstrated layer fusion with a gradient (yellow) at the interface. Scale bar = 200 μm ; (b) Nanoindentation found no significant differences in the Young's moduli of the F-like nor S-like layers between single-layer and dual-layer hydrogels; however, significant differences in stiffness between F-like and S-like layers were maintained within dual-layer hydrogel constructs. Median shown; * $p < 0.05$; $n = 3\text{--}4$ samples per condition (nine measurements per sample); (c) Heatmap of Young's moduli measured by nanoindentation along the z-axis cross section of dual-layer hydrogels demonstrated a stiffness gradient across hydrogel layers; (d) Representative cross-sectional image of a Hoescht-stained multi-layered hydrogel with encapsulated VICs at day 14, demonstrating uniform cell encapsulation after long-term culture of dual-layered constructs, scale bar = 200 μm . Median shown; $n = 3$ samples (10 z-axis measurements per sample).

be ~22 and 10 kPa, respectively [10], while atomic force microscopy on thin cryosections [47] of porcine valves found the fibrosa, spongiosa, and ventricularis to be ~12, ~4, and ~8 kPa, respectively [15]. Apart from the current study, to our knowledge, the latter is the only other report of spongiosa stiffness in any species. The layer-specific stiffnesses we report here are the first such assessments for the human AV. Notably, we measured stiffnesses of 37.1, 15.4, and 26.9 kPa for the fibrosa, spongiosa, and ventricularis of human AV, respectively, that are higher than those previously reported in animal studies. Two limitations may apply: first, we used surgically excised human AV tissue, whereas prior studies were limited to non-diseased valves from other species. We were careful to (i) omit any regions of macrocalcification and (ii) measured macrocalcifications separately to ensure we could identify and neglect any nanoindentation measurements that inadvertently encompassed calcified areas (Table S1). Along with calcification, CAVD is accompanied by fibrotic changes to all leaflet layers [6], with excess production of disorganized and fragmented collagens that are likely responsible for stiffness increases in diseased vs. non-diseased human AVs. Alteration of valvular stiffness in these diseased yet non-calcified regions of the AV is believed to strongly contribute to biomechanically mediated pathogenesis (reviewed in J.H. Chen et al. [48]). We omitted any spongiosa samples with notable collagen accumulation but cannot discount that our nanoscale measurements included regions with low-level collagenous changes. Second, although the porcine AV has many similarities to that of the human (including a tri-layered structure) and is often used as a model of AV disease [49], there are substantial differences in ECM composition and disease progression between these two species, as the porcine AV does not calcify readily [50,51]. Together, this indicates that species-specific differences in non-diseased AV layer stiffnesses are likely to exist. Non-diseased human AV tissue is exceedingly difficult to obtain because early/non-diseased human tissue is rarely targeted for surgical replacement; further studies will be needed to delineate the biomechanical properties of non-diseased human valve layers. A prior study found whole-leaflet Young's moduli of cryopreserved, non-diseased human AVs from older donors to be ~15–20 kPa [52], which is reasonably consistent with the median Young's modulus of 26.7 kPa we measured in intact CAVD leaflets. We also determined that the loss tangent ($\tan \delta$) was significantly skewed towards elastic, and not viscous, deformation in all layers of the human AV.

Gel systems have been used to examine the impact of substrate stiffness modulation on VIC phenotypes. Substrate stiffnesses between 3–144 kPa on 2D polyacrylamide gels modulate responses in Wnt and β -catenin signaling pathways and myofibrogenesis in VICs [10]; however, VICs preferentially undergo calcification and osteogenic differentiation on thick 27 kPa in comparison with thin 113 kPa 2D collagen gels [9]. Others have shown that PEGdma-PLA gels with stiffness of ~120 kPa potentiate myofibrogenic responses in VICs [15]. As with many other cell types [53], VIC mechanobiological responses appear to be regulated by the dimensionality of their surroundings. Microarray studies have identified distinct differences in

VIC transcriptional profiles between 2D vs. 3D cultures, particularly in genes associated with cellular structure, polarity, and motility [54]. In 3D, VICs subjected to a transient gradient of photoinitiated thiol-ene polymerization within PEG hydrogels that increased gel moduli transitioned from an initial myofibroblastic nature at 0.24 kPa towards that of a quiescent fibroblast at 13 kPa [18]. Hybrid GelMA/HAMA hydrogels with compressive moduli in the range of 1–3 kPa induced differential synthesis of ECM components and myofibrogenic/osteogenic markers by VICs under media stimulation [11]. However, with few exceptions [10,15], these studies did not specifically match the mechanical properties of their hydrogels to those directly measured from human tissue; instead, they performed comparative high/low analyses. Absolute magnitude of stiffness is likely important to modeling disease; specific stiffness thresholds have been identified for phenotypic transitions (e.g., myofibrogenic, osteogenic, chondrogenic) of VICs [10] and other relevant cell types such as mesenchymal stem cells [8].

Here, we used nanoindentation to directly mimic the compressive moduli of our 3D hydrogel system to that of native human AV layers. We found that, under basal conditions, both fibrosa-like and spongiosa-like stiffnesses of our hydrogel compositions maintained VICs as quiescent fibroblasts. Meanwhile, under osteogenic media stimulation, naïve non-diseased human VICs responded to layer-specific stiffnesses by preferentially producing microcalcifications, secreting collagen, and synthesizing MMP-9 within hydrogels that mimicked the biomechanics of the most disease-prone fibrosa layer of the human AV. Consistent with rarely observed development of CAVD within the spongiosa, S-like hydrogels also exhibited negligible increases in calcification and low collagen production. These *in vitro* phenotypes replicated key pathways involved in the progression of this disease *in vivo*: nano- and microcalcifications began to accumulate early in the diseased fibrosa [7,41], eventually forming large macro-scale calcific nodules that inhibited leaflet opening/closure. Fibrotic collagen accumulation is also a hallmark of CAVD [55], and sclerotic changes in the valve leaflets are likely to mediate stiffness increases that further drive pro-myofibro/osteogenic differentiation. In addition, matrix metalloproteinases (e.g., MMP-9) upregulated in CAVD were also found to be increased in our 3D model, suggesting a sequential remodeling of fibrotic ECM [43,56]. In total, our GelMA/HAMA scaffolds were bioactive, allowing us to model VIC ECM remodeling.

One key advantage of bioprinting is the spatial control over hydrogel composition and, accordingly, the direction of biomechanics and cellular responses. Our application of this approach offers the benefit of bioprinting multiple mechanically distinct layers while maintaining a constant hydrogel composition, thereby controlling for any associations between GelMA/HAMA pre-polymer concentrations and VIC responses. This method also simplifies printing, as only a single bioprinter extruder is required to print multiple layers with different biomechanics. The tradeoff necessitated by this approach is differential UV exposure

between layers, and resultant differences in hydrogel crosslinking, which has been shown to modulate cellular responses in other tissue types [57]. Importantly, the wavelength of UV light (365 nm) and the power output (2.5 mW/cm²) we utilized herein produced negligible levels of apoptosis in our encapsulated VICs (<~5% after short or long-term culture) and are well-documented to be compatible with VIC viability and quiescence/myofibrogenic/osteogenic responses, depending upon the type of exogenous stimulation [19,20]. If disparities in UV dosage are a concern for future applications of this approach, we describe here an alternative formulation of 6.67% GelMA/1% HAMA (Table S2) that matches the higher fibrosa stiffness while requiring only 30 s of UV exposure (consistent with the 5% GelMA/1% HAMA/30 s UV we utilized for the S-like layer). The use of sacrificial molds enabled us to have consistent and highly customizable control over hydrogel size (i.e., not limited to the standard well plate sizes), negated any meniscus formation, and allowed for free-floating hydrogels. The latter ensured hydrogels could be easily manipulated for biomechanical testing, culture under complex conditions (e.g., stretch/shear bioreactors), confocal imaging, and histopathological sectioning. Nutrient and oxygen diffusion can also occur via all surfaces of the hydrogel. We also demonstrated that individual hydrogel layers with different mechanical properties could be sequentially 3D-bioprinted into complex multilayered constructs while maintaining their unique individual biomechanical properties. Such integrated hydrogel models hold promise for future studies of layer-layer interactions/signaling; the use of bioprinting described herein promises to enable automated multi-well fabrication of hydrogel arrays suitable for higher experimental throughput, testing under hemodynamic loading, and drug target screening. Beyond their compatibility with such pharmaceutical technologies, this “organ-on-a-chip”-like approach also brings us a step closer to non-animal alternatives for preclinical research in CAVD [58].

CONCLUSIONS

In summary, we demonstrate the bioprinting process of a 3D *in vitro* model of human CAVD using specific concentrations of GelMA/HAMA hydrogels that enabled us to mimic the ECM of native tissue and maintain VIC quiescence under basal conditions. The present study is the first to quantify compressive mechanical properties of each layer of the human AV and recapitulate those layer-specific biomechanics *in vitro*. This work also found that induction of nano- and microcalcification and pathological differentiation in naïve, non-diseased VICs can be driven by layer-specific mechanical properties matching those of the disease-prone fibrosa layer of the human AV. Together, these findings establish a novel 3D model for the further study of valvular mechanobiology and are an important step towards high-throughput screening of drug targets for CAVD in a biologically-relevant model of disease. Broadly, we present a generalizable strategy for matching tissue mechanical properties with scalable 3D-bioprinting

of *in vitro* models in tissues with complex ECM composition and mechanosensitive resident cell population(s).

Author Contributions

D.C.v.d.V., C.F.T.v.d.V., M.C.B., and E.A. conceived and designed the experiments; D.C.v.d.V., C.F.T.v.d.V., J.M.G., P.-J.W., O.S.F., J.L.A., and F.B. performed the experiments; D.C.v.d.V., C.F.T.v.d.V., M.C.B., P.-J.W., L.H.L., J.R.W. and A.H.H. analyzed the data; M.W.T., O.S.F., J.L.A., and C.V.C.B. contributed reagents and materials; D.J.M. contributed analysis tools; S.C.B. and J.H. provided tissue and cells; M.C.B., D.C.v.d.V., and C.F.T.v.d.V. wrote the manuscript; M.C.B., M.W.T., A.v.M., J.H., J.P.G.S., R.L., M.A. and E.A. provided support and critically reviewed the manuscript.

Funding

This research was funded by the National Institutes of Health (NIH) R01 grants R01HL114805, R01HL136431 and R01HL109889 (E.A.); the NIH/National Institute of Dental and Craniofacial Research (NIDCR) R01 grant DE013033 (D.M.); the Netherlands CardioVascular Research Initiative (CVON: The Dutch Heart Foundation, Dutch Federation of University Medical Centers, the Netherlands Organization for Health Research and Development, and the Royal Netherlands Academy of Science) and Vrienden UMC Utrecht (C.V., J.S.); an unrestricted grant from CELLINK to Vrienden UMC Utrecht (C.V., J.S.); the Dutch Ministry of Education, Culture, and Science Gravitation Program grant 024.003.013 (C.V.C.B.); the Harvard Catalyst Advanced Microscopy Pilot grants (C.V., M.B., E.A.); and the NIH Ruth L. Kirschstein National Research Service Award F32HL122009 (M.W.T.). This work was conducted with support from Harvard Catalyst|The Harvard Clinical and Translational Science Center (National Center for Advancing Translational Sciences, National Institutes of Health Award UL1 TR001102) and financial contributions from Harvard University and its affiliated academic healthcare centers. This work was performed in part at Harvard University's Center for Nanoscale Systems (CNS), a member of the National Nanotechnology Coordinated Infrastructure Network (NNCI), which is supported by the National Science Foundation under NSF award No. 1541959. We thank the Harvard Center for Biological Imaging for infrastructure and support.

Conflicts of Interest

The authors declare no conflict of interest.

SUPPLEMENTARY MATERIALS

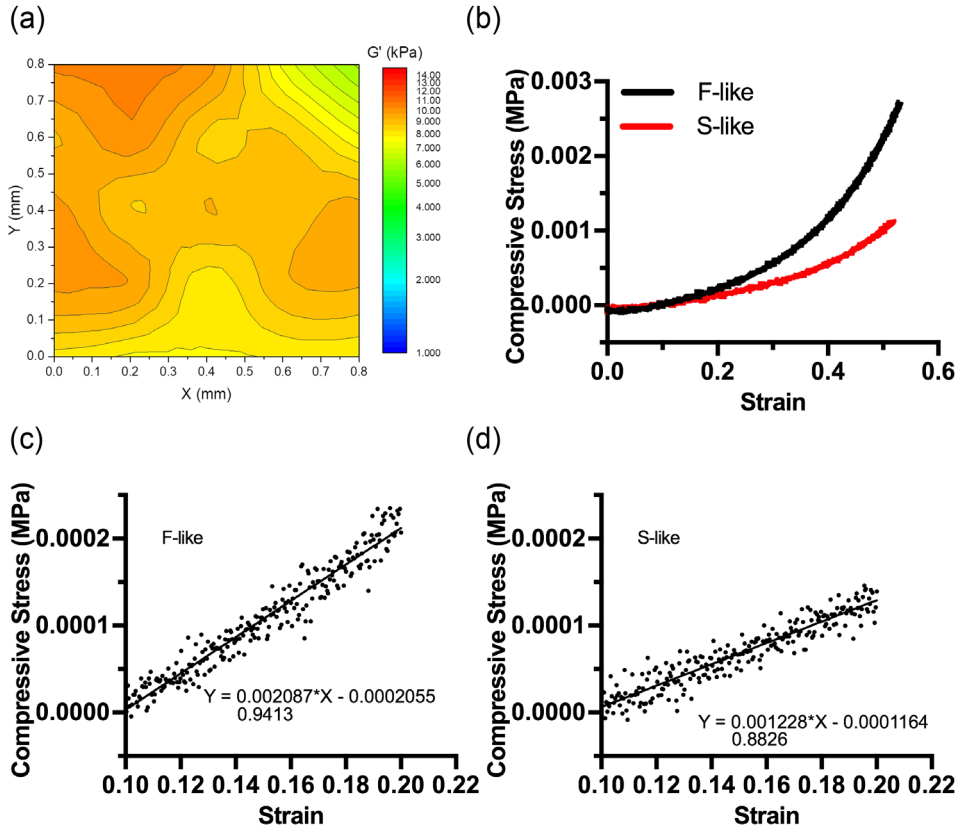
Table S1. Compressive Young's modulus (E), Storage modulus (G'), Loss modulus (G''), Complex modulus (G^*), and $\tan \delta$ of all valve layer samples.

Layer	E (kPa)		G' (kPa)		G'' (kPa)		G^* (kPa)		$\tan \delta$	
	Median	Range	Median	Range	Median	Range	Median	Range	Median	Range
Whole Valve	26.7	22.2-43.2	8.2	7.1-12.6	3.0	2.2-6.7	8.9	7.8-14.8	0.35	0.29-0.48
Fibrosa	37.1	20.-56.7	11.2	5.4-18.0	4.4	2.8-6.3	12.4	6.8-18.9	0.42	0.25-0.75
Spongiosa	15.4	12.8-26.8	4.7	3.9-8.5	2.0	1.9-2.9	5.1	4.3-8.9	0.43	0.33-0.49
Ventricularis	26.9	16.6-33.5	8.7	5.4-13.2	3.4	2.0-4.0	9.0	1.9-11.2	0.39	0.38-0.73
Calcification	670.1	259.5-1080.7	212	78.6-345.3	69.2	36.2-102.1	223.4	86.5-360.2	0.32	0.29-0.36

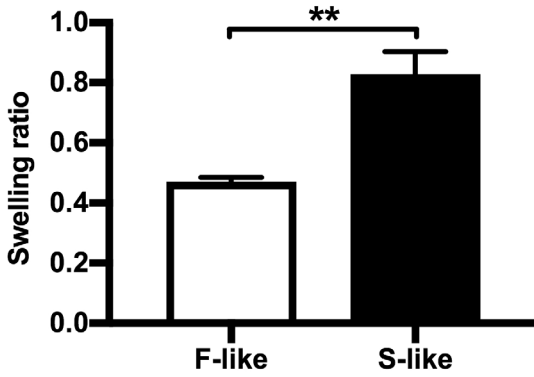
Table S2. Compressive Young's modulus (E), Storage modulus (G'), Loss modulus (G''), Complex modulus (G^*), and $\tan \delta$ of samples with different hydrogel formulations.

Cross-linking time (s)	GelMA %1	E (kPa)		G' (kPa)		G'' (kPa)		G^* (kPa)		$\tan \delta$	
		Median	Range	Median	Range	Median	Range	Median	Range	Median	Range
30	5	21.8	15.0 - 26.6	7.2	4.6 - 8.8	0.6	0.4 - 1.9	7.3	5.0 - 8.9	0.08	0.06-0.42
		38.6	23.6 -60.1	10.5	7.8 -20.0	0.9	0.4 -1.9	10.7	7.9 -20.0	0.09	0.04-0.15
30	8.33	50.2	38.2 -54.1	16.7	12.7 -18.0	1.3	0.6 -2.0	16.7	12.7 -18.0	0.08	0.05-0.11
		49.1	28.3 -76.4	15.9	9.4 -25.5	1.7	0.8 -4.0	16.4	9.4 -25.5	0.13	0.09-0.24
90	5	38.5	33.3 -64.9	12.8	11.1 -21.6	0.9	0.8 -1.0	12.8	11.1 -21.6	0.06	0.05-0.09
		50.4	29.3 -70.2	16.8	8.9 -23.3	2.3	1.3 -4.4	16.8	9.8 -23.4	0.12	0.08-0.49
90	8.33	53	42.2 -63.1	17.2	13.0 -19.4	3.6	1.8 -9.7	17.7	14.1 -21.0	0.26	0.08-0.50
		53.7	34.8 -77.8	16.8	9.2 -25.9	3.5	1.6 -7.1	17.9	11.6 -25.9	0.26	0.06-0.78

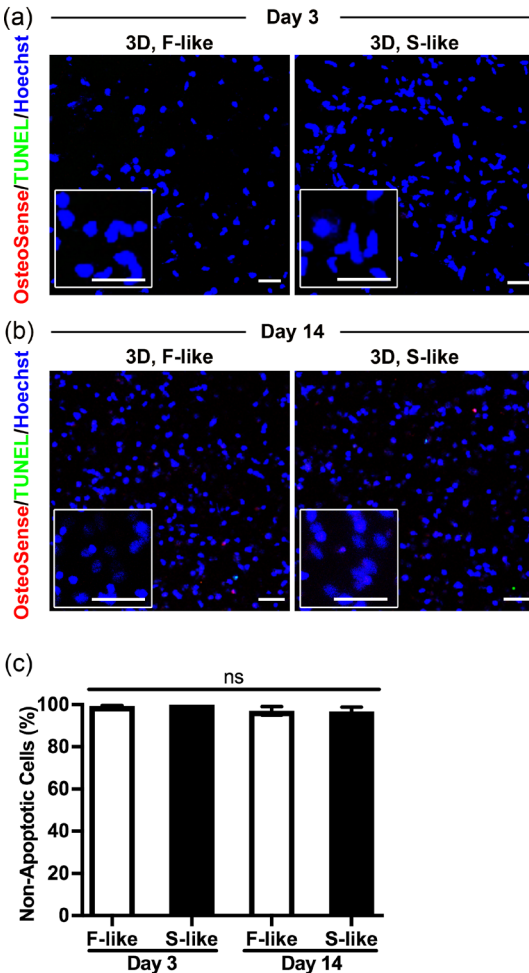
†All hydrogels contain 1% HAMA in addition to the stated % of GelMA



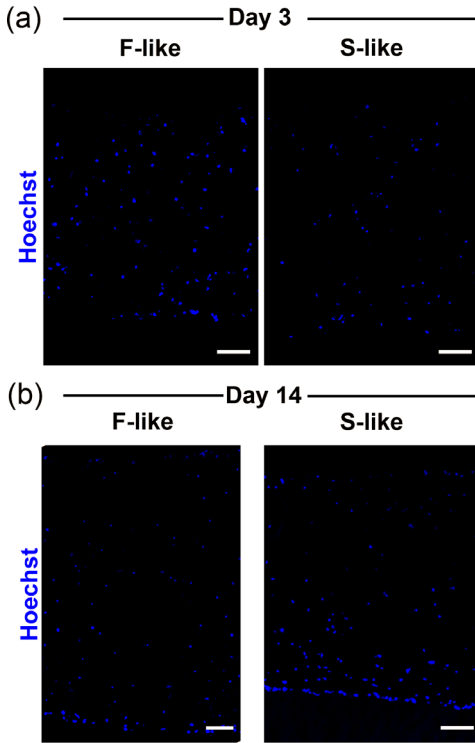
Supplemental Figure 1. Mechanical testing of aortic valve tissue and GelMA/HAMA hydrogels demonstrated the validity of bulk nanoindentation measurements: (a) Heat map of storage moduli (G') generated from 9 nanoindentations performed across the surface of a valve leaflet layer demonstrated uniformity of nanoindentation-measured G' values, (b-d) Stress/strain curves generated by unconfined compression testing of F-like and S-like hydrogels showed that the modulus of F-like hydrogels was $\sim 2x$ that of S-like hydrogels, consistent with moduli measured by nanoindentation. Parts c and d are magnification of the linear region of the loading curves in part b. Calculation of moduli by linear regression in these regions found a $\sim 2x$ increase in loading curve slope between F-like and S-like hydrogels.



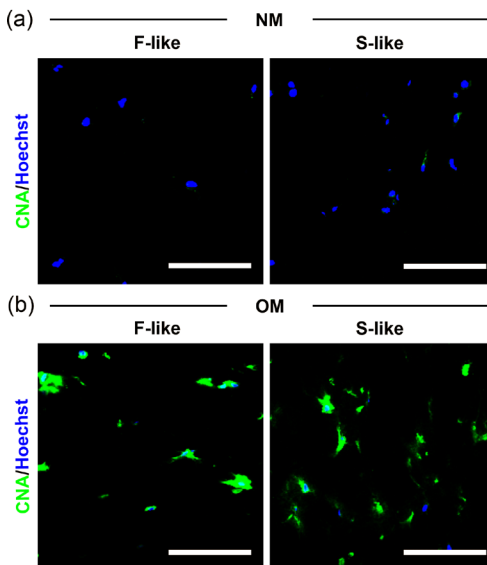
Supplemental Figure 2. 24-hour hydrogel swelling ratios: There was a significant increase in the swelling ratio of acellular S-like hydrogels vs. those of F-like hydrogels after 24 hours in PBS at room temperature. Swelling ratio = (weight_{24hr} - weight_{0hr})/weight_{24hr}; n = 4 samples per condition, ** p < 0.01.



Supplemental Figure 3. Low levels of short- or long-term apoptotic cell death in 3D-bioprinted hydrogels, green = TUNEL apoptosis assay, blue = Hoechst nuclear stain: (a-c) VICs isolated from non-diseased human AV and cultured in NM showed negligible levels of apoptosis at 3 (a) or 14 (b) days after bioprinting. There were no significant differences in apoptosis between F-like or S-like hydrogels, nor between the day 3 and day 14 time points. n = 3 samples per condition (3 images per sample); scale bar = 50 μm. Note: Part b and associated quantification data is duplicated from Figure 5a, to enable direct comparison here.



Supplemental Figure 4. Uniformity of encapsulated VIC distributions in 3D-bioprinted hydrogels, blue = Hoechst nuclear stain; (a/b) Representative cross-sectional images of cell distribution in F-like and S-like hydrogels after 3 (a) and 14 (b) days in NM culture demonstrated evenly distributed initial VIC seeding was maintained over long-term culture of hydrogels; scale bar = 100 μ m.



Supplemental Figure 5. OM stimulation induced marked VIC collagen secretion after 28 days in hydrogel culture: (a,b) VICs isolated from non-diseased human AV and exposed to OM (and not NM) for 28 days stimulated substantial production of collagen, as shown by representative images of collagen-binding probe (CNA35) fluorescence (green); scale bar = 100 μ m.

REFERENCES

1. Messika-Zeitoun D., Bielak L.F., Peyser P.A., Sheedy P.F., Turner S.T., Nkomo V.T., Breen J.F., Maalouf J., Scott C., Tajik A.J., et al. Aortic valve calcification: Determinants and progression in the population. *Arterioscler. Thromb. Vasc. Biol.* 2007;27:642–648. doi: 10.1161/01.ATV.0000255952.47980.c2. [PubMed] [CrossRef] [Google Scholar]
2. Aikawa E., Libby P. A rock and a hard place: Chiseling away at the multiple mechanisms of aortic stenosis. *Circulation.* 2017;135:1951–1955. doi: 10.1161/CIRCULATIONAHA.117.027776. [PMC free article] [PubMed] [CrossRef] [Google Scholar]
3. Hutcheson J.D., Blaser M.C., Aikawa E. Giving calcification its due: Recognition of a diverse disease: A first attempt to standardize the field. *Circ. Res.* 2017;120:270–273. doi: 10.1161/CIRCRESAHA.116.310060. [PMC free article] [PubMed] [CrossRef] [Google Scholar]
4. Hutcheson J.D., Goettsch C., Bertazzo S., Maldonado N., Ruiz J.L., Goh W., Yabusaki K., Faits T., Bouten C., Franck G., et al. Genesis and growth of extracellular-vesicle-derived microcalcification in atherosclerotic plaques. *Nat. Mater.* 2016;15:335–343. doi: 10.1038/nmat4519. [PMC free article] [PubMed] [CrossRef] [Google Scholar]
5. Yutzy K.E., Demer L.L., Body S.C., Huggins G.S., Towler D.A., Giachelli C.M., Hofmann-Bowman M.A., Mortlock D.P., Rogers M.B., Sadeghi M.M., et al. Calcific aortic valve disease: A consensus summary from the alliance of investigators on calcific aortic valve disease. *Arterioscler. Thromb. Vasc. Biol.* 2014;34:2387–2393. doi: 10.1161/ATVBAHA.114.302523. [PMC free article] [PubMed] [CrossRef] [Google Scholar]
6. Otto C.M., Kuusisto J., Reichenbach D.D., Gown A.M., O'Brien K.D. Characterization of the early lesion of 'degenerative' valvular aortic stenosis. Histological and immunohistochemical studies. *Circulation.* 1994;90:844–853. doi: 10.1161/01.CIR.90.2.844. [PubMed] [CrossRef] [Google Scholar]
7. Yabusaki K., Hutcheson J.D., Vyas P., Bertazzo S., Body S.C., Aikawa M., Aikawa E. Quantification of calcified particles in human valve tissue reveals asymmetry of calcific aortic valve disease development. *Front. Cardiovasc. Med.* 2016;3:44. doi: 10.3389/fcvm.2016.00044. [PMC free article] [PubMed] [CrossRef] [Google Scholar]
8. Engler A.J., Sen S., Sweeney H.L., Discher D.E. Matrix elasticity directs stem cell lineage specification. *Cell.* 2006;126:677–689. doi: 10.1016/j.cell.2006.06.044. [PubMed] [CrossRef] [Google Scholar]
9. Yip C.Y., Chen J.H., Zhao R., Simmons C.A. Calcification by valve interstitial cells is regulated by the stiffness of the extracellular matrix. *Arterioscler. Thromb. Vasc. Biol.* 2009;29:936–942. doi: 10.1161/ATVBAHA.108.182394. [PubMed] [CrossRef] [Google Scholar]
10. Chen J.H., Chen W.-L., Sider K., Yip C.Y., Simmons C.A. Beta-catenin mediates mechanically-regulated, tgf-beta1-induced myofibroblast differentiation of aortic valve interstitial cells. *Arterioscler. Thromb. Vasc. Biol.* 2011;31:590–597. doi: 10.1161/ATVBAHA.110.220061. [PubMed] [CrossRef] [Google Scholar]
11. Duan B., Yin Z., Hockaday Kang L., Magin R.L., Butcher J.T. Active tissue stiffness modulation controls valve interstitial cell phenotype and osteogenic potential in 3d culture. *Acta Biomater.* 2016;36:42–54. doi: 10.1016/j.actbio.2016.03.007. [PMC free article] [PubMed] [CrossRef] [Google Scholar]
12. Balguid A., Rubbens M.P., Mol A., Bank R.A., Bogers A.J., van Kats J.P., de Mol B.A., Baaijens F.P., Bouten C.V. The role of collagen cross-links in biomechanical behavior of human aortic heart valve leaflets—relevance for tissue engineering. *Tissue Eng.* 2007;13:1501–1511. doi: 10.1089/ten.2006.0279. [PubMed] [CrossRef] [Google Scholar]
13. Stella J.A., Sacks M.S. On the biaxial mechanical properties of the layers of the aortic valve leaflet. *J. Biomech. Eng.* 2007;129:757–766. doi: 10.1115/1.2768111. [PubMed] [CrossRef] [Google Scholar]
14. Vesely I., Noseworthy R. Micromechanics of the fibrosa and the ventricularis in aortic valve leaflets. *J. Biomech.* 1992;25:101–113. doi: 10.1016/0021-9290(92)90249-Z. [PubMed] [CrossRef] [Google Scholar]
15. Hinderer S., Seifert J., Votteler M., Shen N., Rheinlaender J., Schaffer T.E., Schenke-Layland K. Engineering of a bio-functionalized hybrid off-the-shelf heart valve. *Biomaterials.* 2014;35:2130–2139. doi: 10.1016/j.biomaterials.2013.10.080. [PubMed] [CrossRef] [Google Scholar]

16. Blaser M.C., Wei K., Adams R.L., Zhou Y.Q., Caruso L.L., Mirzaei Z., Lam A., Tam R.K., Zhang H., Heximer S.P., et al. Deficiency of natriuretic peptide receptor 2 promotes bicuspid aortic valves, aortic valve disease, left ventricular dysfunction, and ascending aortic dilatations in mice. *Circ. Res.* 2018;122:405–416. doi: 10.1161/CIRCRESAHA.117.311194. [PubMed] [CrossRef] [Google Scholar]
17. Schlotter F., Halu A., Goto S., Blaser M.C., Body S.C., Lee L.H., Higashi H., DeLaughter D.M., Hutcheson J.D., Vyas P., et al. Spatiotemporal multi-omics mapping generates a molecular atlas of the aortic valve and reveals networks driving disease. *Circulation.* 2018;137 doi: 10.1161/CIRCULATIONAHA.117.032291. [PMC free article] [PubMed] [CrossRef] [Google Scholar]
18. Mabry K.M., Lawrence R.L., Anseth K.S. Dynamic stiffening of poly(ethylene glycol)-based hydrogels to direct valvular interstitial cell phenotype in a three-dimensional environment. *Biomaterials.* 2015;49:47–56. doi: 10.1016/j.biomaterials.2015.01.047. [PMC free article] [PubMed] [CrossRef] [Google Scholar]
19. Hjortnaes J., Camci-Unal G., Hutcheson J.D., Jung S.M., Schoen F.J., Kluin J., Aikawa E., Khademhosseini A. Directing valvular interstitial cell myofibroblast-like differentiation in a hybrid hydrogel platform. *Adv. Healthc. Mater.* 2015;4:121–130. doi: 10.1002/adhm.201400029. [PMC free article] [PubMed] [CrossRef] [Google Scholar]
20. Hjortnaes J., Goetsch C., Hutcheson J.D., Camci-Unal G., Lax L., Scherer K., Body S., Schoen F.J., Kluin J., Khademhosseini A., et al. Simulation of early calcific aortic valve disease in a 3d platform: A role for myofibroblast differentiation. *J. Mol. Cell. Cardiol.* 2016;94:13–20. doi: 10.1016/j.yjmcc.2016.03.004. [PMC free article] [PubMed] [CrossRef] [Google Scholar]
21. Murphy S.V., Atala A. 3d bioprinting of tissues and organs. *Nat. Biotechnol.* 2014;32:773–785. doi: 10.1038/nbt.2958. [PubMed] [CrossRef] [Google Scholar]
22. van der Ven C.F., Wu P.J., Tibbitt M.W., van Mil A., Sluijter J.P., Langer R., Aikawa E. In vitro 3d model and mirna drug delivery to target calcific aortic valve disease. *Clin. Sci.* 2017;131:181–195. doi: 10.1042/CS20160378. [PMC free article] [PubMed] [CrossRef] [Google Scholar]
23. Xu F., Celli J., Rizvi I., Moon S., Hasan T., Demirci U. A three-dimensional *in vitro* ovarian cancer coculture model using a high-throughput cell patterning platform. *Biotechnol. J.* 2011;6:204–212. doi: 10.1002/biot.201000340. [PMC free article] [PubMed] [CrossRef] [Google Scholar]
24. Norotte C., Marga F.S., Niklason L.E., Forgacs G. Scaffold-free vascular tissue engineering using bioprinting. *Biomaterials.* 2009;30:5910–5917. doi: 10.1016/j.biomaterials.2009.06.034. [PMC free article] [PubMed] [CrossRef] [Google Scholar]
25. Flores R.L., Liss H., Raffaelli S., Humayun A., Khouri K.S., Coelho P.G., Witek L. The technique for 3d printing patient-specific models for auricular reconstruction. *J. Craniomaxillofac. Surg.* 2017;45:937–943. doi: 10.1016/j.jcms.2017.03.022. [PubMed] [CrossRef] [Google Scholar]
26. Bhora F.Y., Lewis E.E., Rehmani S.S., Ayub A., Raad W., Al-Ayoubi A.M., Lebovics R.S. Circumferential three-dimensional-printed tracheal grafts: Research model feasibility and early results. *Ann. Thorac. Surg.* 2017;104:958–963. doi: 10.1016/j.athoracsur.2017.03.064. [PubMed] [CrossRef] [Google Scholar]
27. Levato R., Webb W.R., Otto I.A., Mensinga A., Zhang Y., van Rijen M., van Weeren R., Khan I.M., Malda J. The bio in the ink: Cartilage regeneration with bioprintable hydrogels and articular cartilage-derived progenitor cells. *Acta Biomater.* 2017;61:41–53. doi: 10.1016/j.actbio.2017.08.005. [PubMed] [CrossRef] [Google Scholar]
28. Duan B., Hockaday L.A., Kang K.H., Butcher J.T. 3D bioprinting of heterogeneous aortic valve conduits with alginate/gelatin hydrogels. *J. Biomed. Mater. Res. Part A.* 2013;101:1255–1264. doi: 10.1002/jbm.a.34420. [PMC free article] [PubMed] [CrossRef] [Google Scholar]
29. Qian Z., Wang K., Liu S., Zhou X., Rajagopal V., Meduri C., Kauten J.R., Chang Y.H., Wu C., Zhang C., et al. Quantitative prediction of paravalvular leak in transcatheter aortic valve replacement based on tissue-mimicking 3d printing. *JACC. Cardiovasc. Imaging.* 2017;10:719–731. doi: 10.1016/j.jcmg.2017.04.005. [PubMed] [CrossRef] [Google Scholar]

30. Nichol J.W., Koshy S.T., Bae H., Hwang C.M., Yamanlar S., Khademhosseini A. Cell-laden microengineered gelatin methacrylate hydrogels. *Biomaterials*. 2010;31:5536–5544. doi: 10.1016/j.biomaterials.2010.03.064. [PMC free article] [PubMed] [CrossRef] [Google Scholar]
31. Burdick J.A., Chung C., Jia X., Randolph M.A., Langer R. Controlled degradation and mechanical behavior of photopolymerized hyaluronic acid networks. *Biomacromolecules*. 2005;6:386–391. doi: 10.1021/bm049508a. [PMC free article] [PubMed] [CrossRef] [Google Scholar]
32. Akhtar R., Schwarzer N., Sherratt M.J., Watson R.E., Graham H.K., Trafford A.W., Mummery P.M., Derby B. Nanoindentation of histological specimens: Mapping the elastic properties of soft tissues. *J. Mater. Res*. 2009;24:638–646. doi: 10.1557/jmr.2009.0130. [PMC free article] [PubMed] [CrossRef] [Google Scholar]
33. Akhtar R., Draper E.R., Adams D.J., Pfaff H. *Complex Shear Modulus of Hydrogels Using a Dynamic Nanoindentation Method*. Springer International Publishing; Cham, Switzerland: 2016. pp. 141–145. [Google Scholar]
34. Cohen S.R., Kalfon-Cohen E. Dynamic nanoindentation by instrumented nanoindentation and force microscopy: A comparative review. *Beilstein J. Nanotechnol*. 2013;4:815–833. doi: 10.3762/bjnano.4.93. [PMC free article] [PubMed] [CrossRef] [Google Scholar]
35. Choi A.P.C., Zheng Y.P. Estimation of young's modulus and poisson's ratio of soft tissue from indentation using two different-sized indentors: Finite element analysis of the finite deformation effect. *Med. Biol. Eng. Comput*. 2005;43:258–264. doi: 10.1007/BF02345964. [PubMed] [CrossRef] [Google Scholar]
36. Hamid M.S., Sabbah H.N., Stein P.D. Vibrational analysis of bioprosthetic heart valve leaflets using numerical models: Effects of leaflet stiffening, calcification, and perforation. *Circ. Res*. 1987;61:687–694. doi: 10.1161/01.RES.61.5.687. [PubMed] [CrossRef] [Google Scholar]
37. Riem Vis P.W., Bouten C.V., Sluijter J.P., Pasterkamp G., van Herwerden L.A., Kluijn J. Platelet-lysate as an autologous alternative for fetal bovine serum in cardiovascular tissue engineering. *Tissue Eng. Part A*. 2010;16:1317–1327. [PubMed] [Google Scholar]
38. Aper S.J., van Spreeuwel A.C., van Turnhout M.C., van der Linden A.J., Pieters P.A., van der Zon N.L., de la Rangelje S.L., Bouten C.V., Merckx M. Colorful protein-based fluorescent probes for collagen imaging. *PLoS ONE*. 2014;9:e114983. doi: 10.1371/journal.pone.0114983. [PMC free article] [PubMed] [CrossRef] [Google Scholar]
39. Thubrikar M. *The Aortic Valve*. CRC Press, Inc.; Boca Raton, FL, USA: 1990. [Google Scholar]
40. Schmidt M., Rodler N., Miesbauer O., Rojahn M., Vogel T., Dörfler R., Kucukpinar E., Langowski H.-C. Adhesion and barrier performance of novel barrier adhesives used in multilayered high-barrier laminates. *J. Adhes. Sci. Technol*. 2012;26:2405a2436. doi: 10.1163/156856111X599535. [CrossRef] [Google Scholar]
41. Aikawa E., Nahrendorf M., Sosnovik D., Lok V.M., Jaffer F.A., Aikawa M., Weissleder R. Multimodality molecular imaging identifies proteolytic and osteogenic activities in early aortic valve disease. *Circulation*. 2007;115:377–386. doi: 10.1161/CIRCULATIONAHA.106.654913. [PubMed] [CrossRef] [Google Scholar]
42. Aikawa E., Nahrendorf M., Figueiredo J.L., Swirski F.K., Shtatland T., Kohler R.H., Jaffer F.A., Aikawa M., Weissleder R. Osteogenesis associates with inflammation in early-stage atherosclerosis evaluated by molecular imaging *in vivo*. *Circulation*. 2007;116:2841–2850. doi: 10.1161/CIRCULATIONAHA.107.732867. [PubMed] [CrossRef] [Google Scholar]
43. Satta J., Oiva J., Salo T., Eriksen H., Ohtonen P., Biancari F., Juvonen T.S., Soini Y. Evidence for an altered balance between matrix metalloproteinase-9 and its inhibitors in calcific aortic stenosis. *Ann. Thorac. Surg*. 2003;76:681–688. doi: 10.1016/S0003-4975(03)00529-0. [PubMed] [CrossRef] [Google Scholar]
44. Yip C.Y., Simmons C.A. The aortic valve microenvironment and its role in calcific aortic valve disease. *Cardiovasc. Pathol*. 2011;20:177–182. doi: 10.1016/j.carpath.2010.12.001. [PubMed] [CrossRef] [Google Scholar]
45. Yap C.H., Kim H.S., Balachandran K., Weiler M., Haj-Ali R., Yoganathan A.P. Dynamic deformation characteristics of porcine aortic valve leaflet under normal and hypertensive conditions. *Am. J. Physiol. Heart Circ. Physiol*. 2010;298:H395–H405. doi: 10.1152/ajpheart.00040.2009. [PubMed] [CrossRef] [Google Scholar]

46. Szeto K., Pastuszko P., del Alamo J.C., Lasheras J., Nigam V. Bicuspid aortic valves experience increased strain as compared to tricuspid aortic valves. *World J. Pediatr. Congenit. Heart Surg.* 2013;4:362–366. doi: 10.1177/2150135113501901. [PMC free article] [PubMed] [CrossRef] [Google Scholar]
47. Sewell-Loftin M.K., Brown C.B., Baldwin H.S., Merryman W.D. A novel technique for quantifying mouse heart valve leaflet stiffness with atomic force microscopy. *J. Heart Valve Dis.* 2012;21:513–520. [PMC free article] [PubMed] [Google Scholar]
48. Chen J.H., Simmons C.A. Cell-matrix interactions in the pathobiology of calcific aortic valve disease: Critical roles for matricellular, matricrine, and matrix mechanics cues. *Circ. Res.* 2011;108:1510–1524. doi: 10.1161/CIRCRESAHA.110.234237. [PubMed] [CrossRef] [Google Scholar]
49. Sider K.L., Blaser M.C., Simmons C.A. Animal models of calcific aortic valve disease. *Int. J. Inflamm.* 2011;2011:364310. doi: 10.4061/2011/364310. [PMC free article] [PubMed] [CrossRef] [Google Scholar]
50. Sim E.K., Muskawad S., Lim C.S., Yeo J.H., Lim K.H., Grignani R.T., Durrani A., Lau G., Duran C. Comparison of human and porcine aortic valves. *Clin. Anat.* 2003;16:193–196. doi: 10.1002/ca.10149. [PubMed] [CrossRef] [Google Scholar]
51. Sider K.L., Zhu C., Kwong A.V., Mirzaei Z., de Lange C.F., Simmons C.A. Evaluation of a porcine model of early aortic valve sclerosis. *Cardiovasc. Pathol.* 2014;23:289–297. doi: 10.1016/j.carpath.2014.05.004. [PubMed] [CrossRef] [Google Scholar]
52. van Geemen D., Soares A.L., Oomen P.J., Driessen-Mol A., Janssen-van den Broek M.W., van den Bogaerd A.J., Bogers A.J., Goumans M.J., Baaijens F.P., Bouten C.V. Age-dependent changes in geometry, tissue composition and mechanical properties of fetal to adult cryopreserved human heart valves. *PLoS ONE.* 2016;11:e0149020. doi: 10.1371/journal.pone.0149020. [PMC free article] [PubMed] [CrossRef] [Google Scholar]
53. Riedl A., Schleder M., Pudelko K., Stadler M., Walter S., Unterleuthner D., Unger C., Kramer N., Hengstschlager M., Kenner L., et al. Comparison of cancer cells in 2d vs 3d culture reveals differences in akt-mTOR-s6k signaling and drug responses. *J. Cell Sci.* 2017;130:203–218. doi: 10.1242/jcs.188102. [PubMed] [CrossRef] [Google Scholar]
54. Mabry K.M., Payne S.Z., Anseth K.S. Microarray analyses to quantify advantages of 2d and 3d hydrogel culture systems in maintaining the native valvular interstitial cell phenotype. *Biomaterials.* 2016;74:31–41. doi: 10.1016/j.biomaterials.2015.09.035. [PMC free article] [PubMed] [CrossRef] [Google Scholar]
55. Simard L., Cote N., Dagenais F., Mathieu P., Couture C., Trahan S., Bosse Y., Mohammadi S., Page S., Joubert P., et al. Sex-related discordance between aortic valve calcification and hemodynamic severity of aortic stenosis: Is valvular fibrosis the explanation? *Circ. Res.* 2017;120:681–691. doi: 10.1161/CIRCRESAHA.116.309306. [PubMed] [CrossRef] [Google Scholar]
56. Balachandran K., Sucusky P., Jo H., Yoganathan A.P. Elevated cyclic stretch alters matrix remodeling in aortic valve cusps: Implications for degenerative aortic valve disease. *Am. J. Physiol. Heart Circ. Physiol.* 2009;296:H756–H764. doi: 10.1152/ajpheart.00900.2008. [PubMed] [CrossRef] [Google Scholar]
57. Bryant S.J., Chowdhury T.T., Lee D.A., Bader D.L., Anseth K.S. Crosslinking density influences chondrocyte metabolism in dynamically loaded photocrosslinked poly(ethylene glycol) hydrogels. *Ann. Biomed. Eng.* 2004;32:407–417. doi: 10.1023/B:ABME.0000017535.00602.ca. [PubMed] [CrossRef] [Google Scholar]
58. Otto I.A., Breugem C.C., Malda J., Bredenoord A.L. Ethical considerations in the translation of regenerative biofabrication technologies into clinic and society. *Biofabrication.* 2016;8:042001. doi: 10.1088/1758-5090/8/4/042001. [PubMed] [CrossRef] [Google Scholar]

Chapter 3

MicroRNA-214 attenuates formation of microcalcifications in a three-dimensional model of human calcific aortic valve disease

Casper F.T. van der Ven
Klaske Siegersma
Jesper Hjortnaes
Alain van Mil
Pieter A. Doevendans
Joost P.G. Sluijter

ABSTRACT

Aortic valve disease is a major contributor to cardiovascular diseases. Besides aortic valve replacement interventions, there are no drug-based treatments. Microarray studies identified microRNA-214 (miR-214) as an accelerant in inflammatory reactions in human aortic valve interstitial cells (haVIC). Traditionally, *in vitro* these findings would be validated in a 2-dimensional (2D) cell culture system. However, haVICs are mechanosensitive cells and are greatly affected by substrate stiffness. Therefore, we previously developed a 3-dimensional (3D) model of calcific aortic valve disease that better mimics the aortic valve leaflet stiffness, providing an environment that closely resembles the native extracellular matrix mechanical properties. In this study, we modulated miR-214 levels in haVICs in 3D-bioprinted constructs to evaluate its role in the formation of microcalcifications. Exposing haVICs to osteogenic factors resulted in the formation of microcalcifications. Increasing miR-214 levels in de-stimulated 3D constructs resulted in a reduction of the number of microcalcifications.

Keywords: aortic valve disease, calcification, 3D model, microRNA (miRNA)

INTRODUCTION

As the aged population is expanding rapidly, incidence of calcific aortic valve disease (CAVD) is increasing accordingly [1]. Consequently, it is taking a more prominent role in contemporary cardiology. Recent research into the pathobiology of the disease has uncovered multiple active biological mechanisms that underlie non-rheumatic aortic stenosis, making the label 'degenerative' aortic stenosis a misnomer [2].

The native, healthy aortic valve (AV) facilitates unidirectional blood flow from the left ventricle into the systemic circulation. The AV is made up of three distinct layers: the elastin-rich ventricularis layer facing the ventricle providing the elasticity for extension and recoil, the collagen-rich fibrosa layer on the aortic side giving the valve its tensile strength, and the glycosaminoglycan-rich spongiosa layer acting as a bearing surface between the two. These three layers house the valve interstitial cells (VIC) that maintain the extra-cellular matrix (ECM) and are lined with a monolayer of valve endothelial cells (VEC) on the blood-contacting surfaces [3]. In CAVD, calcifications develop primarily in the fibrosa [4]. Pathological ECM remodelling and calcification in the fibrosa layer is a hallmark of CAVD [5]. Whereas VICs normally reside in a quiescent state, VICs differentiate into an osteoblast-like phenotype as the disease progresses, depositing calcium minerals in the ECM [6].

Recently, it was discovered that miR-214 accelerates inflammatory reactions in haVICs, thereby stimulating calcification. microRNAs are short, single-stranded RNA molecules that regulate post-transcriptional gene expression. Patients with aortic stenosis display higher blood and AV tissue levels of miRNA-214 as compared to healthy valves from control patients. In 2 dimensional (2D) cultured haVICs, overexpression of miRNA-214 *in vitro* resulted in increased production of pro-inflammatory mediators ICAM-1, IL-6, IL-8, and MCP-1, through MyD88/NF- κ B signalling. Additionally, stimulated MyD88/NF- κ B signalling increased known calcification markers Runx2, Msx2, and BMP2 [7]. Furthermore, co-culture of M1 macrophages with VICs resulted in decreased expression levels of TWIST1, a direct target of miRNA-214, and increased calcification [8]. miRNA-214 inhibition reduced calcification, and knockdown of TWIST1 reversed the effect of miRNA-214 inhibition, indicating a mediating role of TWIST1 in macrophage induced calcification in VICs via miRNA-214, probably via delivery of miRNA-214 in M1 macrophage-derived microvesicles. Knockdown of miRNA-214 in ApoE^{-/-} mice on a high cholesterol diet reduces AV calcification [8]. Contrastingly, in several other studies, miRNA-214 was downregulated in calcified human AV tissue compared to healthy AV tissue [9-11]. These findings were, however, not confirmed by *in vitro* follow-up studies. Thus, in this paper we aim to clarify the role of miR-214 in aortic stenosis.

It has previously been demonstrated that human aortic VICs behave differently in traditional 2D *in vitro* cell culture settings than in native AV tissue. On 2D tissue culture polystyrene, quiescent porcine aortic VICs spontaneously become activated myofibroblast-like cells [Hjortnaes et al 2015], whereas in 3D porcine aortic VICs remain quiescent. Recently non-diseased human aortic VICs were shown to maintain better a quiescent state, yet could become activated by osteogenic stimulation in a 3D bioprinted human CAVD model [12]. 3D *in vitro* models better replicate cell/tissue organisation and the stiffness of native ECM environment of the AV leaflets and are thus a more accurate representation of aortic valve disease progression.

Hence, this research aims to further investigate the role of miRNA-214 in aortic stenosis. Using the aforementioned 3D model of human CAVD to create a more accurate representation of valve disease, the effects of stimulating and inhibiting miRNA-214 levels on calcification are assessed to clarify the role of miR-214 in aortic stenosis.

METHODS

Aortic Valve Harvest, VIC Isolation, Culture, and Encapsulation

All AV tissue is anonymously derived from hearts explanted at the University Medical Center in Utrecht. These tissues are cleared for use in research projects by a general hospital waiver, approved by the authorized local Medical Ethics Review Committee (Medisch Ethische Toetsingscommissie, METC, Utrecht, Netherlands). As such, no individual informed consent from the patient was necessary.

Diseased AV leaflets were obtained from patients undergoing valve replacement surgery at University Medical Center Utrecht (Utrecht, the Netherlands) as a result of AV calcific stenosis. Leaflets were obtained and processed in accordance with protocols approved by the METC. After the excision, leaflets were kept in Dulbecco's Modified Eagle's Medium (DMEM, Gibco, Thermo Fisher Scientific NL) for a maximum of 1h. Two of the 5 excised AVs were excluded from further experiments due to necrosis. VICs were isolated as previously described [13]. Briefly, CAVD AV leaflets were cut into 5 mm x 5 mm pieces, incubated in 10 mL collagenase (Roche 10103586001) solution at 37 °C, 5% CO₂ for 12 h, and homogenized with a serological pipette. The digested tissue was centrifuged, the supernatant aspirated, and the pellet resuspended in 5 mL VIC cell culture media. The cells were then centrifuged a second time, resuspended in 10 mL VIC cell culture media, and plated in a T75 culture flask. VIC cell culture media, or normal media (NM) (DMEM, Gibco, Thermo Fisher Scientific NL) was supplemented with 10% foetal bovine serum (FBS, Producer) and 1% Penicillin/Streptomycin (P/S, Gibco, Thermo Fisher Scientific NL). Media was replenished every 48 h. VICs of passage five were used for further experiments. VICs were incorporated

in hydrogel pre-polymers by mixing VICs and media (to a final in-gel concentration of 10×10^6 cells/mL) with a 10 wt % GelMA, 3 wt % HAMA, and 5 wt % lithium phenyl-2,4,6-trimethylbenzoylphosphinate (LAP) solution at 37 °C to form a 5% GelMA, 1% HAMA, and 0.3% LAP hydrogel. One day after printing, hydrogels were switched to normal media (10% FBS, 1% P/S) or osteogenic media (OM; NM supplemented with 10 nM dexamethasone, 10 ng/mL ascorbic acid, and 10 mM β -glycerolphosphate) as previously described [14] for up to 14 days or 21 days. Media was changed every 48 h for all cell-laden constructs.

GelMA/HAMA synthesis

GelMA and HAMA were prepared as described previously [15,16]. In brief, gelatine (20.0 g) from porcine skin (Sigma-Aldrich, St. Louis, MO, USA, G2500) was suspended in deionized water (200 mL) in a 500-mL round bottom flask with moderate stirring for 1 h. The mixture was heated to 50 °C and was stirred until gelatine was completely dissolved. Methacrylic anhydride (12.0 g) (Sigma-Aldrich, 276685) was then added to the flask, and the mixture was stirred at 50 °C for 1.5 h. The product was transferred to 50 mL conical tubes and centrifuged at 3500 \times g for 5 min. The supernatant was decanted into a beaker, leaving behind an opaque solid at the bottom of the conical tubes. The supernatant was then diluted with two volumes of 40 °C deionized water and was transferred to dialysis tubing (10 kDa MWCO, SpectraPor 7, Spectrum Laboratories, Rancho Dominguez, CA, USA, 123120). This tubing (containing the GelMA supernatant) was dialyzed against 3500 mL of deionized water at 40 °C for seven days, with the water changed twice per day. The contents of the dialysis tubing were then transferred to a beaker and pH adjusted to 7.4 using a 1 M solution of NaHCO_3 . The solution was sterile filtered with a 0.2 μm vacuum filtration unit and a polyethersulfone (PES) membrane, transferred to 50 mL conical tubes, snap frozen on liquid nitrogen, and lyophilized until complete dryness (approximately 10–14 days) to produce GelMA as a white solid powder.

For HAMA synthesis, sodium hyaluronate (1.0 g) (Lifecore Biomedical, Chaska, MN, USA, HA40K) was dissolved in 1X phosphate-buffered saline (PBS) (100 mL) in a 250 mL round bottom flask and cooled to 4 °C. Methacrylic anhydride (1.0 mL) was added and stirred at 4 °C for 24 h; pH was maintained between 8.0 and 10.0 at the beginning, middle, and end of the reaction period using aliquots of 5 M NaOH. After 24 h the reaction was transferred to 50 mL conical tubes, centrifuged at 3500 \times g for 5 min, and the supernatant was decanted into dialysis tubing (10 kDa MWCO, SpectraPor 7). The tubing containing the HAMA solution was dialyzed against 3500 mL of deionized water at 4 °C for seven days, with the water changed twice per day. Tubing contents were transferred to a beaker and the pH adjusted to 7.4 using a 1 M solution of NaHCO_3 . The solution was sterile filtered with a 0.2 μm vacuum filtration unit with a PES membrane, transferred to 50 mL conical tubes, snap frozen on liquid nitrogen, and lyophilized until complete dryness (approximately 10–14 days) to produce HAMA as a white solid powder.

Pre-polymer solutions were mixed prior to printing. Measured weights of lyophilized GelMA, lyophilized HAMA, and LAP (Sigma-Aldrich, Atlanta, GA, USA) were dissolved in PBS at 80 °C to form 10 wt %, 3 wt %, and 5 wt % solutions, respectively. GelMA solution sonicated at 37 °C, and the pH of HAMA was adjusted to 7.5 using 1 M NaOH. Solutions were reheated to 80 °C for 20 min and sterile-filtered using a 0.2 µm syringe filter. Final solutions were stored at 4 °C and warmed to 37 °C prior to each experiment. For the fabrication of hybrid hydrogels, the 10 wt % GelMA, 3 wt % HAMA, and 5 wt % LAP solutions were mixed in PBS at 37 °C. This yielded hybrid hydrogel pre-polymer solutions with concentrations of 0.3% (v/v) LAP, 1% (v/v) HAMA, and 5% (v/v) GelMA.

3D CAVD model printing and crosslinking

Constructs were fabricated on T = -3 days to -1 day using the previously described 3D bioprinting protocols [12]. Briefly, constructs were designed in Tinkercad (AutoDesk, Inc., San Rafael, CA, USA), and encoded using Repetier-Host (version 2.0.0; Hot-World GmbH & Co. KG, Willich, Germany), and Sublime Text 3 (Sublime HQ, Pty Ltd., Darlinghurst, NSW, Australia). 3D-bioprinting was performed using the Inkredible+ (CELLINK, Cambridge, MA, USA). Pluronic gel (Pluronic F-127; Allevi, Philadelphia, PA, USA) was printed as a cylindrical mould (outer diameter = 9.0 mm, inner diameter = 8.6 mm, height = 1.5 mm) using a stainless steel needle nozzle (JG27-0.25HPX; Jensen Global Inc., Santa Barbara, CA, USA) at a fill density of 95%, layer height of 0.1 mm, printing speed of 4mm/s, and printing pressure of 300 kPa.

The second extruder was filled with the required hydrogel pre-polymer compositions and heated to 37 °C. A hydrogel disc was then printed inside the mould from the second extruder using a 23 G stainless steel nozzle (Fisnar 5901005, Ellsworth Adhesives, Germantown, WI, USA) by opening the valve of the second extruder for 40 ms at 7-10 kPa. Crosslinking the pre-polymers for 30 s with 365 nm UV light produced 8.6 mm × 1.0 mm hydrogel discs. The UV light was calibrated to an intensity of 2.5 mW/cm² using a radiometer (85009, Sper Scientific Direct, Scottsdale, AZ, USA). After printing, the Pluronic gel was dissolved by washing in 37 °C PBS. Constructs were transferred to 24 well tissue culture plates and 1 mL NM was added.

miRNA transfection

Cell-laden constructs were transfected on day 1 and day 7 with 50 nM hsa-miRNA-214-mimic, hsa-miRNA-214-inhibitor, miRNA Mimic Negative Control #1, or miRNA Inhibitor Negative Control #1 (Thermo Scientific mirVana 4464066, 4464084, 4464058, 4464076), respectively, using LipoFectamine RNAiMAX (Thermo Fisher Scientific 13778150) according to manufacturer's protocol, and incubated at 37 C, 5% CO₂ for 6 h prior to supplementing with 1 mL NM.

Calcification and Apoptosis Assays

A near infrared fluorescence (NIRF) imaging agent (OsteoSense 680EX; PerkinElmer, Waltham, MA, USA) was used to visualize nano- and microcalcification. OsteoSense 680EX was added to the cell culture media at a 1:100 dilution and cells were incubated overnight at 37 °C, 5% CO₂ for 12 h prior to imaging. Apoptosis was assessed by Click-iT TUNEL (Thermo Fisher Scientific, Waltham, MA, USA) assays according to the manufacturer's instructions. Confocal imaging (Leica SP8) was performed as follows: three hydrogels per condition were imaged as z-stacks (10 μm/slice) per hydrogel. Z-stacks were analysed using our Python script.

Automatic 3D-image analysis

Automatic analysis of the 3D microscopic samples was performed to extract the quantity of haVIC nuclei, and the quantity and size of calcified nodules in the constructs. A Gaussian filter was used to remove background noise from the image stacks. With a grid-search the optimal values for the Gaussian filter and threshold were determined (Supplementary Figure 2). The cell count in the image analysis was compared with the number of cells present in the sample (1.0×10^7 cells / mL) to define the optimal threshold for segmentation of cell nuclei and the optimal smoothing value for Gaussian filtering. After filtering, a watershed [17] segmentation was performed to separate touching cells. Connected components [18] were used to determine the number of cells and the number of calcified nodules in the sample. Image analysis was performed in Python [19] with the scikit-image package [20]. Code is available upon request.

Initially, conforming to previous studies [12], maximum intensity projections of Z-stacks were created and microcalcifications were quantified using ImageJ. Briefly, the positive stain area was quantified in the compressed maximum intensity projections in individual channels after setting uniform thresholds across all donors (n = 3). Using maximum, or average, intensity projections can result in loss of three-dimensional data that is present in the Z-stacks.

Thus, to improve the quantification method and extract more accurate information, a connected component analysis was tailored specifically to this data set using Python scripts for automatic 3D image analysis. Connected component analysis allows the identification and quantification of particles that are physically above each other (different z-coordinates, same x- and y- coordinates) that would be lost in the compression used in maximum intensity projections (Supplementary Figure 1). This results in more accurate quantification of cells and microcalcifications. Using ImageJ quantification on maximum intensity projections yielded approximately 1.0×10^3 nuclei per construct, whereas connected component analysis more accurately determined the quantity of nuclei at around 1.0×10^4 nuclei per construct, confirming the final cell concentration of 1.0×10^7 cells/ml.

Statistics

Outliers were removed from raw data using the ROUT method ($Q = 5\%$) prior to calculating relative calcification levels. One-way ANOVA with Brown-Forsythe and Bartlett's tests were used as appropriate to evaluate statistically significant differences in multiple group comparisons (GraphPad Prism 8, GraphPad Software LLC, La Jolla, CA, USA).

RESULTS

Osteogenic stimulation increases calcification in haVICs in a 3D human CAVD model

To validate our 3D-bioprinted constructs and the calcifying abilities of the haVICs, we exposed haVIC laden 3D constructs to osteogenic media (OM) stimulation. After 14 days, compared to constructs cultured in normal media (NM), we observed a significant increase in microcalcifications (5-fold) (Figure 1a,b). Cell viability remained high across all conditions ($>98\%$) (Figure 1c). The absence of apoptotic cell death across all conditions confirmed that apoptosis did not cause, or drive, calcification in the groups exposed to osteogenic media.

Fluorescently labelled miRNAs infiltrate haVICs in a 3D human CAVD model

Next, to validate the potential of miRNA intervention in our cell-loaded constructs and thereby eliminate poor infiltration of the miRNA-214 precursors and inhibitors, transfection of haVICs was visualized in the 3D CAVD model. Hsa-miRNA-214-mimic labelled with a Cy5.5 fluorescent probe was complexed with LipoFectamine and added to day 1 constructs. Upon addition of Hoechst nuclear stain and CellTracker Green, we observed that the miRNA-mimics infiltrated the haVICs (Figure 1d).

miRNA-214 reduced osteogenic media-induced microcalcifications in a 3D human CAVD model

To assess the effects of miR-214 modulation on the formation of microcalcifications, haVICs from three different donors in 3D constructs were exposed to either NM or OM for 14 days, and transfected on days 1 and 7 with miRNA-214-mimic, miRNA-214 anti-miR, and their respective controls. This data shows that exposure to OM in the 3D CAVD model results in a 5.3-fold increase in the formation of microcalcifications in haVICs (Figure 2 D). In NM, neither stimulation nor inhibition of miRNA-214 has a significant effect on the formation of microcalcifications. The addition of miRNA-214 attenuates the effects of OM, restoring calcification to levels equivalent to the NM untreated groups. The addition of anti-miRNA-214 seems not to affect the calcification.

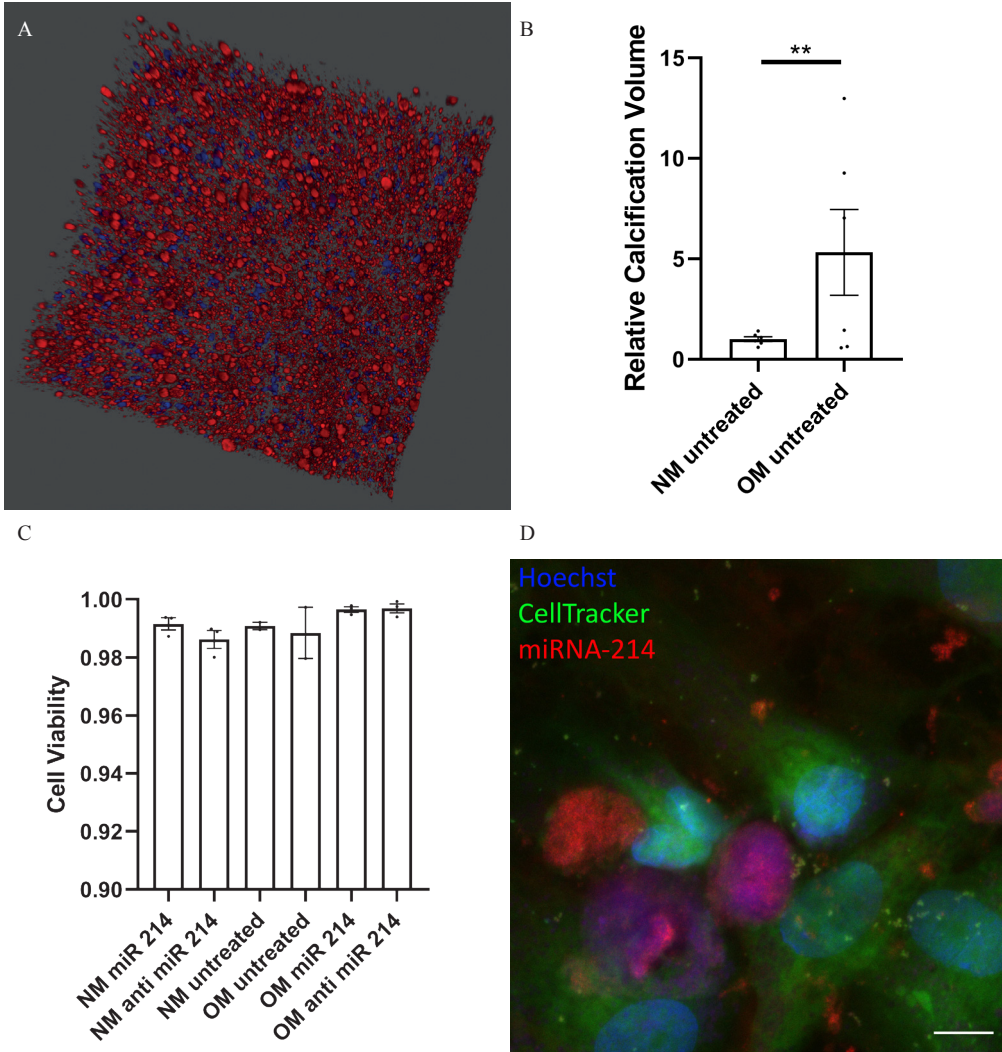


Figure 1 – (a) 3D visualization (1162.5 μm x 1162.5 μm x 400 μm) of microcalcifications (red, near infra-red calcification marker OsteoSense 680EX) in a 3D bioprinted calcific aortic valve disease (CAVD) with human aortic valve interstitial cells (haVICs, blue, Hoechst nuclear stain). (b) Exposure to osteogenic media (OM) compared to normal media (NM) results in a five-fold increase in microcalcifications in CAVD constructs, as quantified by automated analysis based on connected component analysis in Python. (c) TUNEL assay demonstrates high cell viability (>98%) across all groups. (d) Cy5.5-labelled miRNA-214 mimics (red) infiltrate haVICs in the 3D constructs. Nuclei are labelled with Hoechst (blue) and cells with CellTracker Green Dye (green). Mean \pm SEM (* $p < 0.05$; ** $p < 0.01$). Scale bar 10 μm .

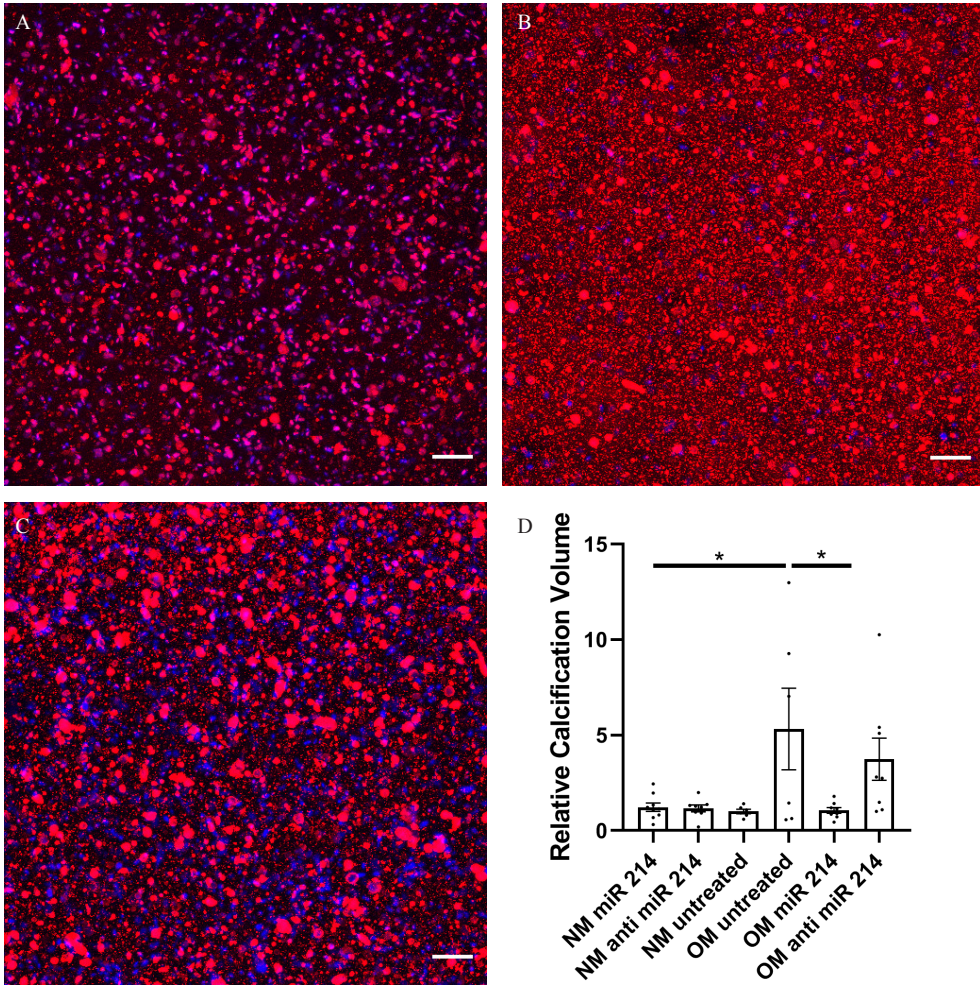


Figure 2-Calcification levels in 3D bioprinted VIC-laden constructs. Constructs from 3 different donors with 3 biological replicates per group were exposed to normal media (NM) and osteogenic media (OM) and transfected with miR-214 mimic or inhibitor. Microcalcifications are visualized with infra-red fluorescent calcium marker OsteoSense 608EX (Red) and haVICs are quantified based on nuclear staining Hoechst (Blue). Representative images of (a) NM untreated, (b) OM untreated and (c) OM transfected with miR-214. Scale bars are 100 μ m. (d) Calcification levels as assessed by near infra-red fluorescent calcium marker OsteoSense 608EX (Red) are presented as the relative calcification controlled for cell count as assessed by Hoechst (Blue), normalized to the normal media untreated group and respective transfection controls. Mean \pm SEM (* $p < 0.05$; ** $p < 0.01$).

DISCUSSION

In this study, haVICs from CAVD patients were isolated after aortic valve replacement surgery and cultured in 3D constructs. Cells were exposed to normal cell culture media (NM) or media supplemented with osteogenic factors (OM) for 14 days to induce osteogenic differentiation

and stimulate the production of microcalcifications. In these 14 days, the cells were transfected on days 1 and 7 with miRNA-214 mimic, anti-miRNA-214, miRNA mimic negative control #1, or miRNA inhibitor negative control #1, to assess the role of miRNA-214 in the calcification process. Microcalcifications were quantified with a connected components analysis optimized for these 3D constructs using a tailored Python script. Our results showed that exposure to OM increases the formation of microcalcifications in haVICs after 14 days, and that introducing miRNA-214 precursor halted the formation of microcalcifications.

Role of miRNA-214 in AV disease is conflicting

Previous research has shown mixed outcomes regarding the role of miR-214 in AV disease. Zheng et al. showed that, compared to non-calcified/healthy controls, AV tissue and blood samples from CAVD patients, overexpressed TLR-4, MyD88, and NF- κ B. They demonstrated increased miRNA-214 levels and mRNA levels of TLR-4, MyD88, and NF- κ B in the blood and tissue samples of CAVD patients, based on only 8 samples in each group. These findings were then validated in 2D *in vitro* follow up experiments, confirming that increasing miRNA-214 resulted in increased calcification [7].

In contrast to the findings by Zheng et al, in multiple other studies, miRNA-214 was downregulated in calcified human AV tissue compared to healthy AV tissue [9-11], ranging from 4-16 samples per group. These results were, however, not validated by detailed *in vitro* follow-up studies. This provided the basis to study miRNA-214 manipulation in a 3D valve disease model, to clarify the role of miRNA-214 in CAVD using a model that more accurately represents the native haVIC ECM. The results of our 3D *in vitro* transfection experiments tend to support the hypothesis that miRNA-214 can reduce the production of microcalcifications in haVICs.

However, a limitation of our 3D experiments is the inconsistency in calcification levels observed in the OM groups transfected with miRNA Inhibitor Negative Control #1 (Supplementary Figure 3). The calcification measured in the OM anti-miRNA negative control group is 18-19 fold higher than the NM untreated group in 2 valves, whereas a proper functioning negative control anti-miRNA should display consistency. To compensate, we normalized OM anti-miR-214 values to the NM miRNA Inhibitor Negative Control #1 values, which were stable across all donors and displayed less variation (mean = 0.733, SEM = 0.185).

Despite the similarity in the methods employed in the experiments conducted by Zheng et al. and the experiments described in our paper (transfection protocol, dose, agent, calcification readout), miRNA-214 stimulation seems to have the opposite effect [7]. The main difference is that Zheng et al. used haVICs from non-diseased valves in a 2D cell culture setting, while we used haVICs from CAVD patients in a 3D *in vitro* model. Therefore, repeating these

experiments in 3D with non-diseased haVICs would be a more optimal experimental setting to show superiority of a 3D system. In addition, miRNA-214 levels should be measured in these follow-up experiments during osteogenesis and before and after transfection to be able to quantify its role more accurately.

Limitations of using haVICs from patients undergoing AVR surgery

In this study, all AV donors underwent the same surgical procedure, though the pathobiology of CAVD could have been different between donors. As CAVD is a multifactorial disease, different pathways could have been the predominant drivers of calcification in the different donors [2]. The role of miRNA-214 in the inflammatory/oxidative-stress driven pathway is not clear, and in the hyperphosphatemia pathway underreported. This difference in pathobiology could explain the differences observed in the results between the constructs with haVICs from the different donors (Supplementary Figure 4). The multifactorial disease mechanism combined with the limited number of AVs ($n = 3$) reduced the power of this study to draw strong conclusions. Ideally, a sufficient number of AVs from both male and female donors is used to first identify differences in disease development (between the sexes) and then validate these findings.

Additionally, porcine aortic VICs were previously shown to produce calcific nodules in a 3D hydrogel model only at day 21 [21]. These results were obtained in a 3D hydrogel model with different mechanical properties, specifically with a lower compressive modulus of approximately 5 kPa. It has since been demonstrated that human AVs have higher compressive moduli [12], and that haVICs from non-diseased AVs produce calcific nodules in a 3D hydrogel model that accurately mimics these mechanical properties as a result of osteogenic stimulation after 14 days already. Here, we show that haVICs from CAVD patients in a 3D construct, according to our previously published protocol [12], develop microcalcifications after 14 of osteogenic stimulation.

Non-diseased human AV tissue is increasingly difficult to obtain, because early/non-diseased human tissue is seldom subject to surgical replacement. Arguably, AVs from patients undergoing heart transplantation surgery could be harvested for research, provided that the pathology requiring transplantation has not affected the AV. The use of non-diseased haVICs in the 3D CAVD model would allow more accurate investigation of the effect of miRNA-214 in the development of CAVD, as the control group would be a healthy control and the formation of microcalcifications is stimulated only through supplementing the cell culture media with osteogenic factors.

Simplification of AV pathobiology associated with the use of *in vitro* models

Despite the improved mechanical properties and more accurate representation of ECM and tissue organisation of the 3D CAVD model, more advanced models that replicate more facets of CAVD pathobiology could be developed. First, the dynamic environment of the AV could be replicated by applying stretch and shear forces on the model. HaVICs populate a dynamic environment and are continuously subjected to mechanical stresses. Porcine AVs, paVICs, and paVECs have been subjected to stress to study the effect of a dynamic environment on calcification [22,23]. Stretch and shear forces contribute to CAVD pathogenesis [24-26], and endoplasmic reticulum stress via the PERK-eIF2 α -ATF4 signalling pathway has been shown to play a role in AV calcification in animals [27, 28], and in vascular calcification [29]. ATF4 is a known target of miRNA-214, and high levels of miRNA-214 inhibit bone formation in human femurs through inhibition of osteoblast formation, which was identified in human osteoporotic bone specimens [30]. Adding the dimension of mechanical stress to the 3D human CAVD model would be of interest.

Of note, porcine models of AV disease are often used as a model for human CAVD, as a result of the similarities between human AVs and porcine AVs, including the tri-layered structure [31]. There are however considerable differences in ECM composition and disease progression, for the human AV calcifies more easily than the porcine AV [32,33]. Therefore, inter-special differences are likely to exist. Thus, *in vitro* models based on human VICs rather than porcine VICs will more accurately represent CAVD characteristics.

Second, including other cell types native to the AV would improve the accuracy of a 3D *in vitro* model. Human aortic valve endothelial cells (haVECs) line the AV to protect against high shear in a high stress environment [34]. It was previously shown that the haVECs can differentiate into osteoblasts via osteogenesis, preceded by endothelial-to-mesenchymal-transition, which can be inhibited by haVICs [35]. Adding haVECs to the 3D CAVD model would create an opportunity to study VIC-VEC interaction. Furthermore, as introduced previously, immune cells infiltrate the AV during pro-inflammatory stages of CAVD [36,37]. When non-diseased haVICs and haVECs would be used to establish a 3D CAVD model, co-culture with macrophages and CD8⁺ T lymphocytes would yield a model that more accurately represents early, pro-inflammatory stages of AV calcification. The aforementioned studies that quantified miR-214 levels in AV tissue did not specify which cell types in the AV expressed miR-214 differentially [7, 9-11]. Thus, assessing miR-214 expression levels in the different cell types present in diseased AV tissue would improve our understanding of its role in CAVD.

Furthermore, variation in calcifying capacity between donors ($n = 9$) and between passages has been observed previously [38]. Two types of calcifying media were tested in 2D culture over 4 passages. haVICs stimulated with OM (containing organic phosphate) calcified less easily after multiple passages compared to haVICs cultured in pro-calcifying media (normal media supplemented with L-ascorbic acid and inorganic phosphate). We observed fewer microcalcifications in the group treated with OM in one of our donors (Supplementary Figure 3), yet overall, in these experiments and in previous experiments [12], haVICs form significantly more microcalcifications after exposure to OM in 3D culture. This requires further investigations, and, for ease of comparison, the field would benefit from a more uniform approach in cell culture practice and stimulation of calcification.

CONCLUSION

In line with previous studies [9-11], our data shows that miR-214 reduces the formation of microcalcifications *in vitro*. The role of miR-214 in CAVD is complex, and contradictory results are evidence for multiple pathways active in this disease. Further research into the pathobiology is required, which would benefit from a more uniform approach and larger sample sizes. For a disease that currently affects a quarter million people annually, screenings ought to be performed with sufficient samples to accurately reflect the patient population to differentiate between the different pathologies leading to CAVD [2]. Furthermore, the multiple cell types present in the native AV must be sorted and miR-214 expression levels must be assessed in each cell type separately to fully understand the role of miR-214 in CAVD. Most importantly, due to the mechano-sensitive nature of haVICs, 3D *in vitro* models that accurately mimic the native AV ECM are essential to study haVIC behaviour and pathology.

SUPPLEMENTARY FIGURES

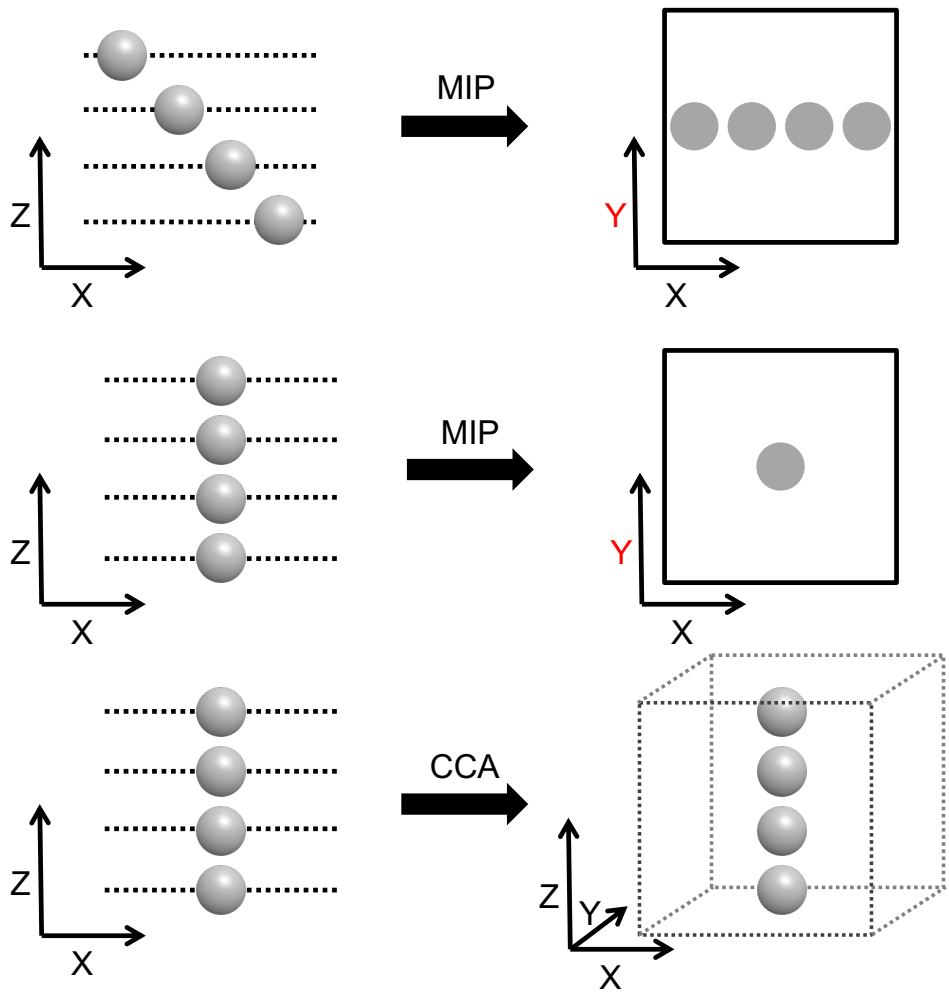


Figure 1 – Illustration comparing Maximum Intensity Projections (MIP) to Connected Component Analysis (CCA). Grey spheres represent calcific nodules. 3-dimensional data about particles aligned in the Z direction is lost in MIPs. CCA preserves this data.

Threshold/Gaussian	0.0	0.0 w/w	0.2	0.2 w/w	0.4	0.4 w/w	0.6	0.6 w/w	0.8	0.8 w/w	1.0	1.0 w/w
20		0	0	0	0	0	0	0	6	0	0	0
22		0	0	0	7	0	0	0	2	0	0	0
24		0	0	6	21	0	2	0	1	0	0	0
26		2	0	14	22	2	4	0	0	0	0	0
28		6	0	23	2	19	10	0	0	0	0	0
30		13	1	21	5	13	16	0	0	0	0	0
32		23	2	22	11	6	22	0	0	0	0	0
34		22	3	16	17	5	22	0	0	0	0	0
36		25	10	13	22	1	23	0	0	0	0	0
38		22	15	10	21	0	24	0	0	0	0	0
40		18	19	8	20	0	22	0	0	0	0	0
42		12	27	5	23	0	21	0	0	0	0	0
44		10	22	4	23	0	19	0	0	0	0	0

Figure 2 – Gaussian filter and threshold parameters were determined by a gridsearch in the connected component analysis. 28 Z-stacks were analysed, the detection range was set from 8000 to 12000 nuclei, corresponding to the final concentration of cells in the constructs. The settings corresponding to the highlighted cell identified the correct number of nuclei in most constructs, and were used for analysis.

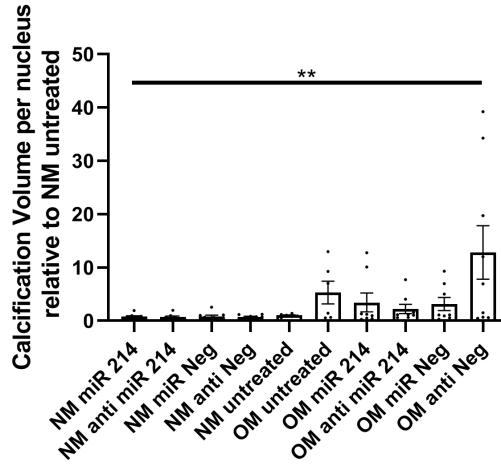


Figure 3 – Average calcification levels in 3D bioprinted VIC-laden constructs from 3 different donors with 3 biological replicates per group presented as the relative calcification controlled for cell number, normalized to the normal media untreated group. Outliers were removed from raw data using the ROUT method (Q = 5%) prior to calculating relative calcification levels. One-way ANOVA with Brown-Forsythe test were used as appropriate to evaluate statistically significant differences, mean ± SEM (* p < 0.05; ** p < 0.01).

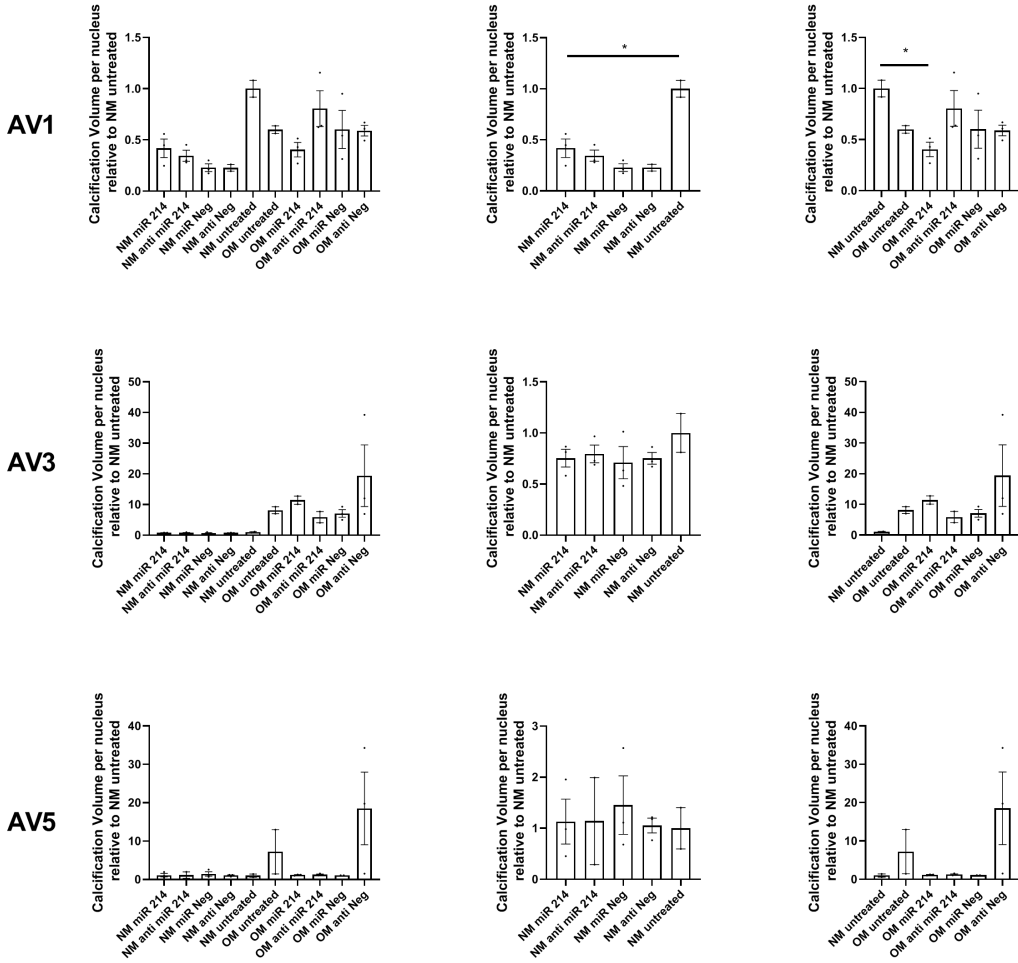


Figure 4 - Calcification levels in 3D bioprinted VIC-laden constructs per donor with 3 biological replicates per group presented as the relative calcification controlled for cell number, normalized to the normal media untreated group. Mean \pm SEM (* $p < 0.05$; ** $p < 0.01$).

REFERENCES

1. Coffey, S. Cox, B. Williams, M.J. The prevalence, incidence, progression, and risks of aortic valve sclerosis: a systematic review and meta-analysis. *J Am Coll Cardiol.* 2014, 63, 2852-2861. [CrossRef] [PubMed]
2. Aikawa, E. Libby, P. A Rock and a Hard Place: Chiseling Away at the Multiple Mechanisms of Aortic Stenosis. *Circulation.* 2017, 135, 1951-1955. [CrossRef] [PubMed]
3. Aikawa, E. Whittaker, P. Farber, M. Mendelson, K. Padera, R.F. Aikawa, M. Schoen, F.J. Human semilunar cardiac valve remodeling by activated cells from fetus to adult: implications for postnatal adaptation, pathology, and tissue engineering. *Circulation.* 2006, 113, 1344-1352. [CrossRef] [PubMed]
4. Yabusaki, K. Hutcheson, J.D. Vyas, P. Bertazzo, S. Body, S.C. Aikawa, M. Aikawa, E. Quantification of calcified particles in human valve tissue reveals asymmetry of calcific aortic valve disease development. *Front. Cardiovasc. Med.* 2016, 3, 44. [CrossRef] [PubMed]
5. Chen, J.H. Simmons, C.A. Cell-matrix interactions in the pathobiology of calcific aortic valve disease: critical roles for matricellular, matricrine, and matrix mechanics cues. *Circ. Res.* 2011, 108, 1510-1524. [CrossRef] [PubMed]
6. Hjortnaes, J. Camci-Unal, G. Hutcheson, J.D. Jung, S.M. Schoen, F.J. Kluin, J. Aikawa, E. Khademhosseini, A. Directing valvular interstitial cell myofibroblast-like differentiation in a hybrid hydrogel platform. *Adv Healthc Mater.* 2015, 4, 121-130. [CrossRef] [PubMed]
7. Zheng, D. Zang, Y. Xu, H. Wang, Y. Cao, X. Wang, T. Pan, M. Shi, J. Li, X. MicroRNA-214 promotes the calcification of human aortic valve interstitial cells through the acceleration of inflammatory reactions with activated MyD88/NF- κ B signaling. *Clin Res Cardiol.* 2018, 108, 691-702. [CrossRef] [PubMed]
8. Li, X.F. Wang, Y. Zheng, D.D. Xu, H.X. Wang, T. Pan, M. Shi, J.H. Zhu, J.H. M1 macrophages promote aortic valve calcification mediated by microRNA-214/TWIST1 pathway in valvular interstitial cells. *Am J Transl Res.* 2016, 8, 5773-5783. [CrossRef] [PubMed]
9. Song, R. Fullerton, D.A. Ao, L. Zhao, K.S. Reece, T.B. Cleveland, J.C. Meng, X. Altered microRNA expression is responsible for the pro-osteogenic phenotype of interstitial cells in calcified human aortic valves. *J. Am. Heart Assoc.* 2017, 6. [CrossRef] [PubMed]
10. H. Shi, J. Li, B. Zhou, Q. Kong, X. Bei, Y. MicroRNA Expression Signature in Human Calcific Aortic Valve Disease. *Biomed Res Int.* 2017, 4820275. [CrossRef] [PubMed]
11. Coffey, S. Williams, M.J. Phillips, L.V. Galvin, I.F. Bunton, R.W. Jones, G.T. Integrated microRNA and messenger RNA analysis in aortic stenosis. *Sci Rep.* 2016, 6, 36904. [CrossRef] [PubMed]
12. van der Valk, D.C. van der Ven, C.F.T. Blaser, M.C. Grolman, J.M. Wu, P.J. Fenton, O.S. Lee, L.H. Tibbitt, M.W. Andresen, J.L. Wen, J.R. Ha, A.H. Buffolo, F. van Mil, A. Bouten, C.V.C. Body, S.C. Mooney, D.J. Sluijter, J.P.G. Aikawa, M. Hjortnaes, J. Langer, R. Aikawa, E. Engineering a 3D-Bioprinted Model of Human Heart Valve Disease Using Nanoindentation-Based Biomechanics. *Nanomaterials.* 2018, 8, 296. [CrossRef] [PubMed]
13. Gould, R.A. Butcher, J.T. Isolation of valvular endothelial cells. *J Vis Exp.* 2010, 46. [CrossRef] [PubMed]
14. Hutcheson, J.D. Goettsch, C. Bertazzo, S. Maldonado, N. Ruiz, J.L. Goh, W. Yabusaki, K. Faits, T. Bouten, C. Franck, G. Quillard, T. Libby, P. Aikawa, M. Weinbaum, S. Aikawa, E. Genesis and growth of extracellular-vesicle-derived microcalcification in atherosclerotic plaques. *Nat. Mater.* 2016, 15, 335-343. [CrossRef] [PubMed]
15. Nichol, J.W. Koshy, S.T. Bae, H. Hwang, C.M. Yamanlar, S. Khademhosseini, A. Cell-laden microengineered gelatin methacrylate hydrogels. *Biomaterials* 2010, 31, 5536-5544. [CrossRef] [PubMed]
16. Burdick, J.A. Chung, C. Jia, X. Randolph, M.A. Langer, R. Controlled degradation and mechanical behavior of photopolymerized hyaluronic acid networks. *Biomacromolecules* 2005, 6, 386-391. [CrossRef] [PubMed]
17. Bengtsson, E. Wählby, C. Lindblad, J. Robust Cell Image Segmentation Methods. *Pattern Recognition and Image Analysis.* 2004, 14, 157-167. [Google Scholar]
18. Rosenfeld, A. Pfälz, J. L. Sequential Operations in Digital Picture Processing. *J Ass Comp Machinery.* 1966, 13, 471-494.

19. Van Rossum, G. Python Tutorial Release 3.5.1. Python Software Foundation. 2016. <https://www.python.org/>
20. van der Walt, S. Schönberger, J. L. Nunez-Iglesias, J. Boulogne, F. Warner, J. D. Yager, N. Gouillart, E. Yu, T. and the scikit-image contributors. Scikit-image: image processing in Python. *PeerJ*. 2014, 2, e453. [CrossRef] [PubMed]
21. Rabkin, E. Aikawa, M. Stone, J.R. Fukumoto, Y. Libby, P. Schoen, F.J. Activated interstitial myofibroblasts express catabolic enzymes and mediate matrix remodeling in myxomatous heart valves. *Circulation*. 2001, 104, 2525-2532. [CrossRef] [PubMed]
22. Sucusky, P. Padala, M. Elhammali, A. Balachandran, K. Jo, H. Yoganathan, A.P. Design of an *ex vivo* culture system to investigate the effects of shear stress on cardiovascular tissue. *J Biomech Eng*. 2008, 130, 035001. [CrossRef] [PubMed]
23. Balachandran, K. Konduri, S. Sucusky, P. Jo, H. Yoganathan, A.P. An *ex vivo* study of the biological properties of porcine aortic valves in response to circumferential cyclic stretch. *Ann Biomed Eng*. 2006, 34, 1655-65. [CrossRef] [PubMed]
24. Balachandran, K. Sucusky, P. Yoganathan, A.P. Hemodynamics and mechanobiology of aortic valve inflammation and calcification. *Int. J. Inflamm*. 2011, 2011, 263870. [CrossRef] [PubMed]
25. Arjunon, S. Rathan, S. Jo, H. Yoganathan, A.P. Aortic valve: mechanical environment and mechanobiology. *Ann. Biomed. Eng*. 2013, 41, 1331–1346. [CrossRef] [PubMed]
26. Gould, S.T. Srigunapalan, S. Simmons, C.A. Anseth, K.S. Hemodynamic and cellular response feedback in calcific aortic valve disease. *Circ. Res*. 2013, 113, 186–197. [CrossRef] [PubMed]
27. Cai, Z. Li, F. Gong, W. Liu, W. Duan, Q. Chen, C. Ni, L. Xia, Y. Cianflone, K. Dong, N. Wang, D.W. Endoplasmic reticulum stress participates in aortic valve calcification in hypercholesterolemic animals. *Arterioscler. Thromb. Vasc. Biol*. 2013, 33, 2345–2354. [CrossRef] [PubMed]
28. Wang, B. Cai, Z. Liu, B. Liu, Z. Zhou, X. N. Dong, N. Li, F. RAGE deficiency alleviates aortic valve calcification in ApoE^{-/-} mice via the inhibition of endoplasmic reticulum stress. *Biochim. Biophys. Acta Mol. Basis Dis*. 2017, 1863, 781–792. [CrossRef] [PubMed]
29. Duan, X. Chang, J. Zhang, J. Zhang, B. Li, Y. Teng, X. Zhu, Y. Du, J. Tang, C. Q. Y. Activating transcription factor 4 is involved in endoplasmic reticulum stress-mediated apoptosis contributing to vascular calcification. *Apoptosis*. 2013, 18, 1132-1144. [CrossRef] [PubMed]
30. Wang, X. Guo, B. Li, Q. Peng, J. Yang, Z. Wang, A. Li, D. Hou, Z. Lv, K. Kan, G. Cao, H. Wu, H. Song, J. Pan, X. Sun, Q. Ling, S. Li, Y. Zhu, M. Zhang, P. Peng, S. Xie, X. Tang, T. Hong, A. Bian, Z. Bai, Y. Lu, A. Li, Y. He, F. Zhang, G. Li, Y. miR-214 targets ATF4 to inhibit bone formation. *Nat Med*. 2013, 19, 93-100. [CrossRef] [PubMed]
31. Sider, K.L. Blaser, M.C. Simmons, C.A. Animal models of calcific aortic valve disease. *Int. J. Inflamm*. 2011, 2011, 364310. [CrossRef] [PubMed]
32. Sim, E.K. Muskawad, S. Lim, C.S. Yeo, J.H. Lim, K.H. Grignani, R.T. Durrani, A. Lau, G. Duran, C. Comparison of human and porcine aortic valves. *Clin. Anat*. 2003, 16, 193–196. [CrossRef] [PubMed]
33. Sider, K.L. Zhu, C. Kwong, A.V. Mirzaei, Z. de Lange, C.F. Simmons, C.A. Evaluation of a porcine model of early aortic valve sclerosis. *Cardiovasc. Pathol*. 2014, 23, 289–297. [CrossRef] [PubMed]
34. Butcher, J. T. Nerem, R.M. Valvular Endothelial Cells Regulate the Phenotype of Interstitial Cells in Culture: Effects of Steady Shear Stress. *Tissue Engineering*. 2006, 12, 905-915. [CrossRef] [PubMed]
35. Hjortnaes, J. Shapero, K. Goetsch, C. Hutcheson, J.D. Keegan, J. Kluin, J. Mayer, J.E. Bischoff, J. Aikawa, E. Valvular interstitial cells suppress calcification of valvular endothelial cells. *Atherosclerosis*. 2015, 242, 251-260. [CrossRef] [PubMed]
36. Aikawa, E. Nahrendorf, M. Figueiredo, J.L. Swirski, F.K. Shtatland, T. Kohler, R.H. Jaffer, F.A. Aikawa, M. Weissleder, R. Osteogenesis associates with inflammation in early-stage atherosclerosis evaluated by molecular imaging *in vivo*. *Circulation*. 2007, 116, 2841–2850. [CrossRef] [PubMed]

37. Nagy, E. Lei, Y. Martínez-Martínez, E. Body, S.C. Schlotter, F. Creager, M. Assmann, A. Khabbaz, K. Libby, P. Hansson, G.K. Aikawa, E. Interferon- γ released by activated CD8⁺ T-lymphocytes impairs the calcium resorption potential of osteoclasts in calcified human aortic valves. *Am J Path.* 2017, 187, 1413-1425. [CrossRef] [PubMed]
38. Goto, S. Rogers, M.A. Blaser, M.C. Higashi, H. Lee, L.H. Schlotter, F. Body, S.C. Aikawa, M. Singh, S.A. Aikawa, E. Standardization of Human Calcific Aortic Valve Disease *in vitro* Modeling Reveals Passage-Dependent Calcification. *Front Cardiovasc Med.* 2019, 6, 49. [CrossRef] [PubMed]

Chapter 4

Controlled delivery of gold nanoparticle-coupled miRNA therapeutics via an injectable self-healing hydrogel

Casper F.T. van der Ven
Mark W. Tibbitt
João Conde
Alain van Mil
Jesper Hjortnaes
Pieter A.F.M. Doevendans
Joost P.G. Sluijter
Elena Aikawa
Robert Langer

ABSTRACT

Differential expression of microRNAs (miRNAs) plays a role in many diseases, including cancer and cardiovascular diseases. Potentially, miRNAs could be targeted with miRNA-therapeutics. Sustained delivery of these therapeutics remains challenging. This study couples miR-mimics to PEG-peptide gold nanoparticles (AuNP) and loads these AuNP-miRNAs in an injectable, shear thinning, self-assembling polymer-nanoparticle (PNP) hydrogel drug delivery platform to improve delivery. Spherical AuNPs coated with fluorescently labelled miR-214 are loaded into an HPMC-PEG-*b*-PLA PNP hydrogel. Release of AuNP/miRNAs is quantified, AuNP-miR-214 functionality is shown *in vitro* in HEK293 cells, and AuNP-miRNAs are tracked in a 3D bioprinted human model of calcific aortic valve disease (CAVD). Lastly, biodistribution of PNP-AuNP-miR-67 is assessed after subcutaneous injection in C57BL/6 mice. AuNP-miRNA release from the PNP hydrogel *in vitro* demonstrates a linear pattern over 5 days up to 20%. AuNP-miR-214 transfection in HEK293 results in 33% decrease of Luciferase reporter activity. In the CAVD model, AuNP-miR-214 are tracked into the cytoplasm of human aortic valve interstitial cells. Lastly, 11 days after subcutaneous injection, AuNP-miR-67 predominantly clears via the liver and kidneys, and fluorescence levels are again comparable to control animals. Thus, the PNP-AuNP-miRNA drug delivery platform provides linear release of functional miRNAs *in vitro* and has potential for *in vivo* applications.

Keywords: drug delivery, hydrogels, nanoparticles, microRNA, calcific aortic valve disease, bioprinting, 3D printing

INTRODUCTION

Since their discovery, microRNAs (miRNAs) have become a focus of (bio)medical research. The research community has elucidated the role of miRNAs in the etiology and progression of various diseases, including cardiovascular disease [1,2,3], cancer [4,5], and hepatitis C [6]. The discovery of their central role in several pathological conditions has provided the basis for using miRNAs in the treatment of these diseases. For example, miR-34 has been tested in phase I trials to treat multiple types of cancer (ClinicalTrials.gov: NCT01829971, NCT02862145) and miR-122 has been explored for the treatment of hepatitis C [6]. The latter successfully completed phase II, whereas the former two trials were terminated prematurely due to serious adverse events, including enterocolitis, hypoxia/systemic inflammatory response syndrome, colitis/pneumonitis, hepatic failure, and cytokine release syndrome/respiratory failure that could be attributed to the treatment [7]. The mixed outcomes of these trials highlight the potential of miRNA therapeutics and the present challenge in their successful delivery to the targeted cells and tissues.

Prior to clinical testing and application, there are several hurdles for RNA therapeutics to overcome regarding their delivery, retention, stability, and degradation. To prevent endosomal degradation, miRNAs were functionalized with fusogenic pH-sensitive peptides that enabled endosomal escape [8]. When miRNAs are injected directly, washout is high and retention is low [9]. Carrier vehicles and modifications have been explored to reduce the washout and improve the delivery of miRNAs. We previously described non-viral vectors to improve delivery, including lipids [10], microbubbles [11], polymers [12], and inorganic materials [13], as well as modifications to improve both biostability and binding stability [14]. Injectable hydrogels are promising candidates to improve and localize the delivery of therapeutic miRNA molecules while allowing minimally invasive application.

Injectable hydrogels have been designed with natural or synthetic polymers, including ECM [15], collagen, fibrin, alginate, functionalized poly(ethylene glycol) (PEG), or poly(*N*-isopropylacrylamide) (pNIPAM) [16]. Traditionally, hydrogels have been based on covalent cross-linking methods that require initiation by temperature [17], light [18], or a change in pH [19,20,21]. For biomedical applications, including drug delivery, these covalent cross-linking methods can provide an additional hurdle, as the cross-linking reaction is not instantaneous, and drugs can be lost during network formation. Additionally, for some materials it requires an external stimulus or an instrument, such as a UV light source. To simplify the application of hydrogels and avoid the challenges associated with covalent cross-linking, non-covalent cross-linking allows for spontaneous gel formation without an external trigger. In addition, non-covalent hydrogels often exhibit shear-thinning (the ability to flow upon application of stress) and self-healing (reformation of the gel upon relaxation

of the external stress) properties. Shear-thinning facilitates injection and minimally invasive delivery, thus improving clinical application.

Injectable hydrogels have been developed using leucine zipper domains [22], dock-and-lock proteins [23], and host-guest interactions [24]. A pH cross-linkable hydrogel was developed for miRNA delivery based on non-covalent ureido-pyrimidinone (UPy) cross-linking. Near complete release of miRNA molecules from UPy gels was achieved after two days [21]. This release could be extended by modification of the miRNA molecules with cholesterol groups. We recently developed a class of shear-thinning and self-healing hydrogels based on polymer–nanoparticle (PNP) interactions [25,26]. These properties arise from the reversible, non-covalent interactions between the polymer and the nanoparticles within the gel, employing a hydroxypropylmethylcellulose derivative (HPMC-C₁₂) and core-shell nanoparticles [poly(ethylene glycol)-*block*-poly(lactic acid) (PEG-*b*-PLA) nanoparticles].

This research set out to improve both the biostability and the delivery of miRNA. In order to improve biostability and reduce degradation the miRNA molecules were attached to gold nanospheres (AuNP) that were functionalized with poly(ethylene-glycol) (PEG) [13,27,28,29]. In addition, influenza hemagglutinin (HA1) peptide was added to stimulate endosomal escape intracellularly by destabilizing the endosomal membrane.

These functionalized AuNP (AuNP-miR) were loaded into a biocompatible, shear-thinning, and self-healing injectable hydrogel, based on the PNP gel platform, in order to improve minimally invasive, local, and sustained delivery. This research shows (1) linear release of AuNP-miRs from the PNP hydrogel over multiple days, and (2) that AuNP-miRs retain functionality *in vitro*. Additionally, it shows that (3) AuNP-miRs retain functionality by employing an *in vitro* miRNA reporter assay and a complex model system, specifically in a 3D *in vitro* model of human calcific aortic valve disease. [30] Lastly, it shows (4) the biodistribution of AuNP-miRs after subcutaneous injection *in vivo*. Together, this data demonstrates an innovative approach to achieve controlled release of functional miRNA from an injectable, self-healing PNP hydrogel.

RESULTS & DISCUSSION

Production of AuNP-miR-loaded PNP hydrogels

To engineer an injectable biomaterial for controlled release of miRNAs, we prepared AuNP-miRNAs within PNP hydrogel formulations. We synthesized the PNP hydrogel components and functionalized the AuNPs with PEG, miR-67 or miR-214, and HA1-peptide (**Figure S1**). The HA1 peptide, a fusogenic peptide (influenza hemagglutinin HA1 peptide, N-YPYDVPDYA-C23)

was used to increase miRNA uptake by destabilizing the endosomal membrane stimulating endosomal discharge by a pH-responsive machinery [13]. This peptide was functionalized on the surface of the AuNPs via carbodiimide chemistry assisted by N-hydroxysuccinimide using an EDC/NHS coupling reaction between the carboxylated PEG spacer and the amine terminal group of the peptide. HPMC-C₁₂ and PEG-*b*-PLA polymers were synthesized as previously described [25]. PEG-*b*-PLA polymers were formulated into NPs via nanoprecipitation and characterized by dynamic light scattering (DLS). PEG-*b*-PLA NPs with a diameter (Dh) of ~88 nm and dispersity (*D*) of 0.12 were used to formulate the PNP hydrogel. Based on prior work, NPs of this diameter form gels by enabling polymer bridging over several NPs in contrast to polymer wrapping around single NPs [31]. PNP hydrogels were formulated at 1 wt % HPMC-C₁₂ and 10 wt % PEG-*b*-PLA NPs (Figure 1a).

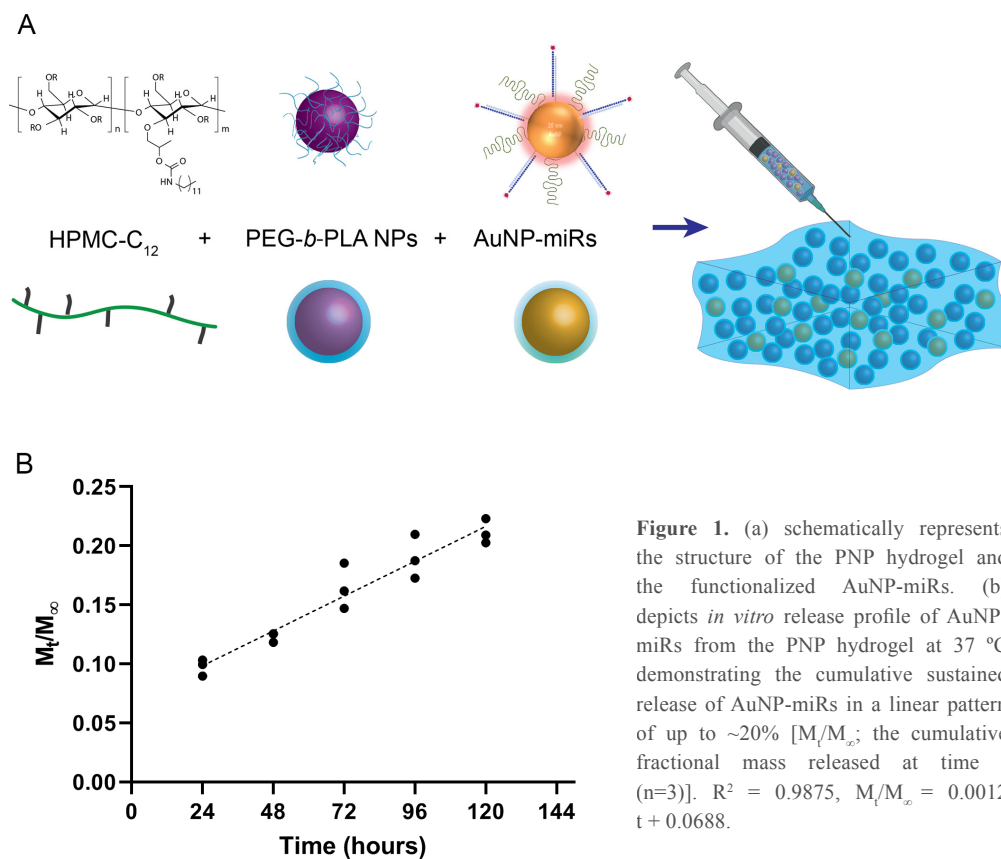


Figure 1. (a) schematically represents the structure of the PNP hydrogel and the functionalized AuNP-miRs. (b) depicts *in vitro* release profile of AuNP-miRs from the PNP hydrogel at 37 °C demonstrating the cumulative sustained release of AuNP-miRs in a linear pattern of up to ~20% [M_t/M_∞ ; the cumulative fractional mass released at time t ($n=3$)]. $R^2 = 0.9875$, $M_t/M_\infty = 0.0012 t + 0.0688$.

Linear release of AuNP-miRs from PNP hydrogels

To monitor the release of AuNP-miRs from the PNP hydrogels, non-modified AuNPs and AuNP-miR-67 were loaded into the PNP hydrogel in a 1:1:1 ratio (PEG-*b*-PLA:HPMC-C₁₂:AuNP; final concentration AuNP-miR-67 0.34 nM) and incubated at 37 °C, 5% CO₂. The supernatant was collected and replaced at 24 h intervals to quantify the concentration of AuNPs in the supernatant based on a calibrated absorbance measurement (**Figure S2**). Sustained linear release of AuNP-miR-67 was observed up to ~20 % of the loaded AuNPs over the course of 5 days (**Figure 1b**), demonstrating extended release compared to other hydrogel-based drug-delivery systems [14,20,31,32,33]. Following an initial burst release of ~10% of the loaded AuNP over the first 24 h, ~3% of the loaded AuNP were released per day over the course of 5 days. The observed linear release was consistent with an erosion-based release that has been observed for NP release from PNP hydrogels [25].

AuNP-miR-214 demonstrates *in vitro* mRNA targeting activity

Next, we verified the mRNA targeting capacity of miR-214 after conjugation to the AuNPs. HEK293 cells were transfected with a miR-214 target luciferase reporter [34] and incubated with AuNP-miR-214s. Compared to a non-transfected control and an inactive AuNP-miR-67 control, AuNP-miR-214 significantly reduced the Luciferase signal (~42%) after 48 h, demonstrating preserved miR-214 bioactivity after coupling to the AuNP (**Figure 2**). As a positive control, transfection with unmodified miR-214 mimics using Lipofectamine resulted in a knockdown of ~67% relative to the control groups. The higher transfection efficiency of Lipofectamine compared to AuNP-miR-214 is expected, considering the thorough optimization of commercially available Lipofectamine.

Suppression of a target gene up to 90% has been observed for small interfering RNA (siRNA) released from alginate or collagen hydrogels in a green fluorescent protein (GFP) expressing HEK293 cell line [33], though over a longer time scale of 6 days. 80% knockdown of GFP signal was achieved with miRNA released from a PEG hydrogel over a period of 42 days [35]. This suggests that an extended testing period for AuNP-miR-214 should be considered for translational use.

AuNP-miR-67 infiltrate haVICs in a 3D bioprinted *in vitro* CAVD model

In order to test AuNP-miR uptake in a more complex tissue model, we tracked fluorescently labelled AuNP-miR-67 in a 3D model of CAVD. Cy5.5-labelled AuNP-miR-67 were added to the cell culture media of a 3D bioprinted model of CAVD containing human aortic valve interstitial cells (haVICs) [30]. In this model, VICs cultured in NM maintain a quiescent phenotype and VICs exposed to OM produce microcalcifications (**Figure S3**). Labeling nuclei with Hoechst (blue), cytoplasm with CellTracker Green (green), and lysosomes with

LysoTracker Red (red) aided in demonstrating that AuNP-miR-67 (white) were taken up by the cells in lysosomes (**Figure 3a**), indicated by co-localization (pink arrows) of CellTracker Red and the Cy5.5-labelled AuNP-miR-67 (**Figure 3b**). We hypothesize that AuNP-miRs are taken up via endocytosis, indicated by co-localization (pink arrows) of CellTracker Red and white AuNP-miR-67, and that they can escape the lysosomes, indicated by the presence of both lysosomes (red arrows) and AuNP-miRs (white arrows).

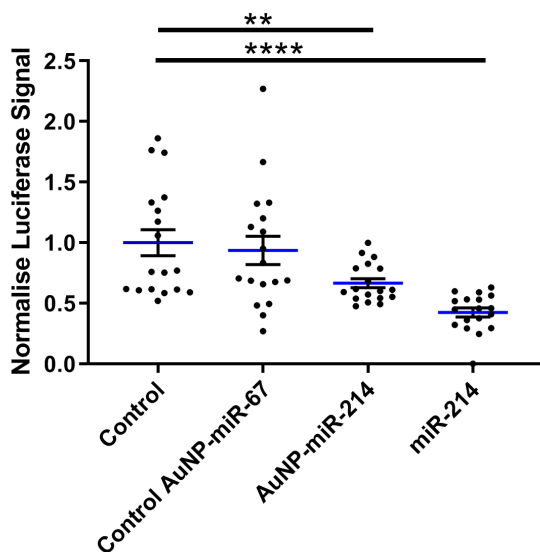


Figure 2. AuNP-miR-214 significantly reduces Luciferase activity. AuNP-miR-214 were added to HEK293 cells introduced to the pMIR-REPORT-QKI-3' UTR Luciferase vector *in vitro*. Compared to an untransfected control and an inactive control AuNP-miR-67, AuNP-miR-214 suppresses the Luciferase signal (~42%) after 48 h. Transfection with miR-214 mimic using Lipofectamine results in knockdown of ~67% relative to the control groups, compared to ~42% in the AuNP-miR-214 transfection. Mean \pm SEM; * $p < 0.05$, ** $p < 0.01$, **** $p < 0.0001$; $n = 6$, experiment conducted in triplicate.

AuNP-miR-214 increase alkaline phosphatase expression in a 3D CAVD model

Additionally, we employed the 3D bioprinted *in vitro* human CAVD model to test AuNP-miR-214 functionality [30]. Osteogenic medium (OM) has been shown to stimulate the formation of calcium minerals through osteogenic differentiation of haVICs [30]. miR-214 was found to increase calcification of haVICs *in vitro* in traditional 2D cell culture [37]. Here, we demonstrate that compared to non-transfected controls 30 nM AuNP-miR-214 transfection significantly increased ALP activity, a phospholytic enzyme associated with early calcification in CAVD [38], in haVICs within a 3D-bioprinted *in vitro* model of human CAVD cultured in normal medium (NM) (**Figure 4**). Compared to NM, OM increased ALP activity (left column), confirming earlier results [39]. Compared to NM, addition of AuNP-miR-214 significantly

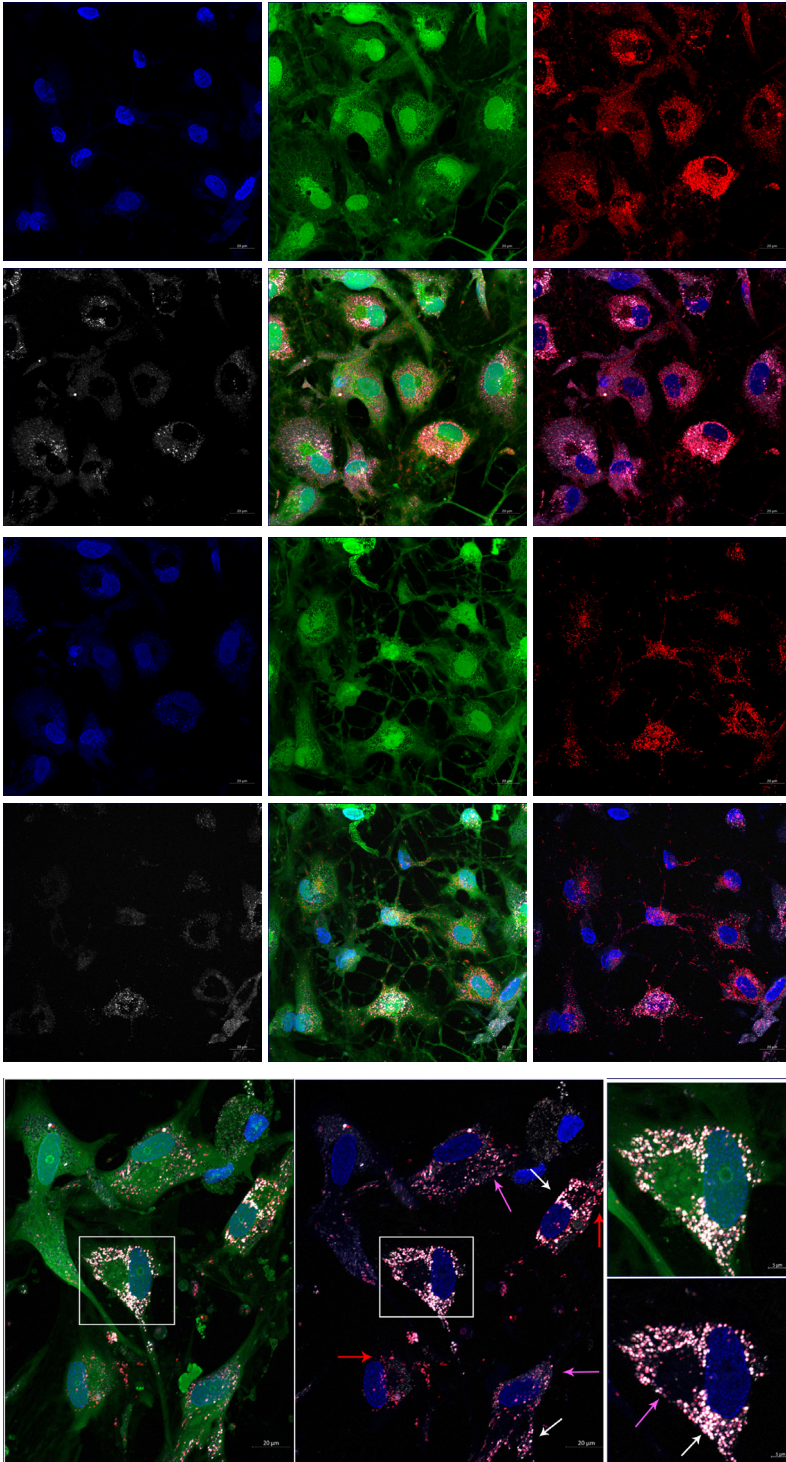
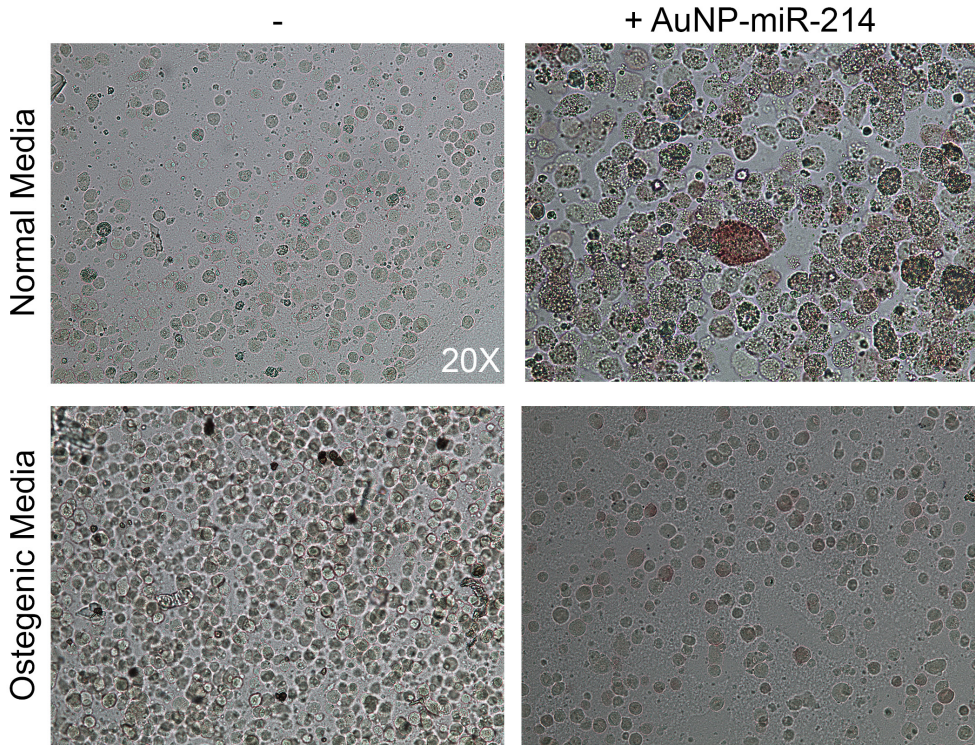


Figure 3. Infiltration of AuNP-miR-67 into human aortic valve interstitial cells (haVICs) in a 3D bioprinted model of calcific aortic valve disease (CAVD). Nuclei were labelled with Hoechst (blue), haVICs were labelled with CellTracker Green (green), and lysosomes were labelled with LysoTracker Red (red). Co-localization of lysosomes (red) and Cy5.5-labelled AuNP-miR-67 (white) demonstrated that AuNP-miRs were taken up by the cells in lysosomes. (scale bar = 20 µm, scale bar insert = 5 µm, t = 48 h, n = 3).



4

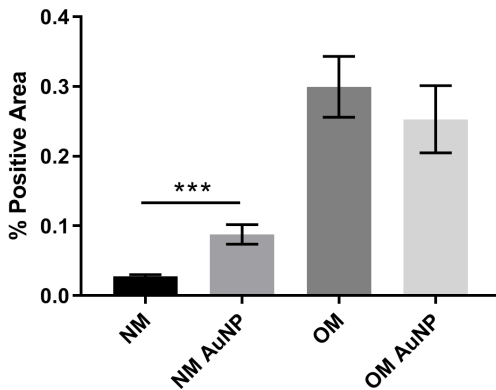


Figure 4. AuNP-miR-214 increase alkaline phosphatase expression (red) after 48 h in human aortic valve interstitial cells (haVICs) comparable to osteogenic stimulation in 3D human calcific aortic valve disease model. Brightfield microscopy, mean \pm SEM, *** $p < 0.001$, $n = 3$, 20X magnification.

increased ALP activity (**Figure 4a** top row; **Figure 4b**). The difference between the effect of AuNP-miR-214 and OM on haVICs was likely due to the relatively low concentration of AuNP-miR-214 and the prolonged exposure to OM. These findings further support a role for miR-214 in the development of CAVD by stimulating ALP and encourage further investigation.

The involvement of miR-214 in CAVD is a relatively recent discovery, and its precise role in CAVD requires further clarification. miR-214 involvement in CAVD was first identified in porcine AV endothelial cells (paVECs) [40]. Specifically, micro-array analysis and *ex vivo* validation of healthy ventricular and aortic paVECs RNA yielded differential expression levels of miR-214 as a result of oscillatory shear due to disturbed blood flow. Compared to the ventricularis side, increased expression of miR-214 in the fibrosa side of pAVs resulted in thickening and calcification. Later, in a comparison between valves of healthy controls and patients with calcific aortic stenosis, miR-214 was increased in CAVD patients and osteocalcin, osteopontin, Runx2, and osterix were identified and validated as its targets [41]. Furthermore, in excised AVs from patients with CAVD, increased miR-214 expression was found to play a role in suppressing the apoptosis repressor with caspase recruitment domain ARC [42]. In addition, it was demonstrated that miR-214 stimulates the formation of calcific nodules in haVICs *in vitro* via the MyD88/NF- κ B inflammatory pathway [37]. Contradictory to the aforementioned results, in larger micro-array studies miR-214 was found low in valves from patients with CAVD compared to non-diseased control valves [43,44,45]. Furthermore, dynamic stretch on porcine AVs *ex vivo* demonstrated that miR-214 was significantly downregulated during late stage calcification, and addition of miR-214 mimic in static stretch conditions resulted in lower levels of calcification. Therefore, the role of miR-214 in the development of CAVD is complex and needs to be further elucidated [46].

AuNPs subcutaneous implantation in PNP hydrogels

We further investigated the biodistribution of AuNP-miRs following delivery from the PNP hydrogel *in vivo*. In general, parenteral administration of therapeutics or drug delivery systems via injection can be achieved easily and in a minimally invasive manner. However, traditional intravenous injections result in relatively short residence time in the body. On the other hand, surgical implantation of a material-based controlled release system provides longer-lasting effects but is more invasive. Injectable hydrogels with controlled release provide an attractive method to administer drugs locally, in a minimally invasive manner, and with extended biological effect. For example, hyaluronic acid-based PNP hydrogels were recently administered to cardiac tissue via catheter-based delivery [47]. Therefore, we employed AuNP-miR-loaded PNP hydrogels for administration of an AuNP-miR releasing depot following minimally invasive subcutaneous injection. AuNP-miR-67-loaded PNP hydrogel was injected subcutaneously in nine C57BL/6 mice to assess biodistribution. To monitor the biodistribution of the AuNP-miR, fluorescent signals of the Cy5.5 labelled miR-

67 were measured in the lungs, liver, spleen, kidney, and skin surrounding the injection site in three adult male wildtype C57BL/6 mice on days 1, 4, and 11 after injection (**Figure 5**). Three additional animals were injected with unloaded PNP hydrogel as negative control and aforementioned tissues were harvested and monitored on day 11. Image quantification of the fluorescent signal of the labelled AuNP-miR-67 demonstrated accumulation in the lungs, spleen, liver and kidney on day 1 and suggests clearance via the liver and kidney by day 11, as demonstrated by decreasing fluorescence that approached the values of control animals.

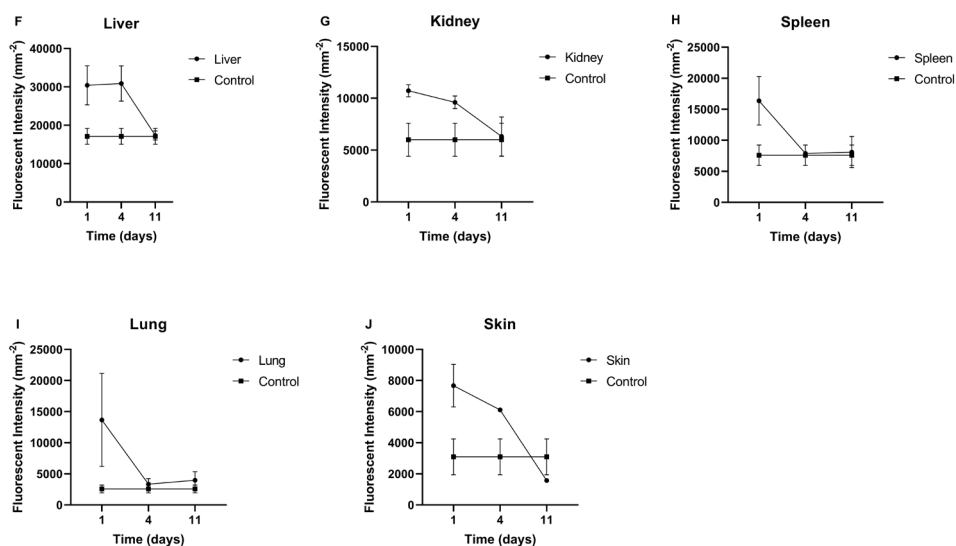


Figure 5. To assess biodistribution of AuNP-miR-67 $n = 9$ C57BL/6 mice were injected subcutaneously with PNP-AuNP-miR-67. (a-e) Fluorescent signals of the Cy5.5 labelled AuNP-miR-67 were measured in the lungs, liver, spleen, kidney, and skin surrounding the injection site in $n = 3$ animals on days 1, 4, and 11 after injection. $N = 3$ mice were injected with unloaded PNP hydrogel as a control and aforementioned tissues were harvested on day 11. Intensity of the fluorescent signal of labelled AuNP-miR-67 demonstrates accumulation in the lungs, spleen, liver and kidney on day 1 and clearance via the kidneys after 11 days, as demonstrated by decreasing fluorescent signal comparable to control animals. (f-k) Quantified fluorescent signal in liver, kidney, lung, spleen, and skin surrounding the injection site on days 1, 4, and 11 demonstrates clearance over 11 days. $N = 3$ animals per time point. Mean \pm SEM.

MATERIAL & METHODS

PNP Hydrogel Synthesis

PNP hydrogels were synthesized as previously described [25]. In short:

HPMC-C₁₂ Synthesis

Briefly, hydroxypropylmethylcellulose (HPMC; Sigma h7509-100G; 1.0 g) was dissolved in N-methylpyrrolidone (NMP; 45 mL) by magnetic stirring at 80 °C for 1 h. After cooling the solution to room temperature, a solution of 1-dodecylisocyanate (Sigma 389064-5G; 0.5 mmol) and triethylamine (2 drops) were dissolved in N-methylpyrrolidone (Sigma PHR1352-2G; 5 mL) and added to the reaction mixture. The mixture was stirred at room temperature for 16 h. This solution was then precipitated from acetone and filtered to recover the polymer, which was dried under vacuum at room temperature for 24 h and weighed, yielding the functionalized HPMC-C₁₂ as a white amorphous powder (0.96 g, 87%).

PEG-block-PLA synthesis

PEG (Sigma 373001-250G; 0.25 g, 4.1 mmol) and 1,8-diazabicycloundec-7-ene (DBU; Sigma 139009-25G; 10.6 mg, 10 mL, 1.0 mol% relative to LA) were dissolved in dichloromethane (DCM; 1.0 mL). LA (Sigma 767344-5G; 1.0 g, 6.9 mmol) was dissolved in DCM (3.0 mL) with mild heating. The LA solution was then added rapidly to the PEG/DBU solution and stirred rapidly for 10 min. Acetone (7.0 mL) addition then quenched the reaction and the PEG-*b*-PLA copolymer was precipitated from cold diethyl ether, filtered for collection, and lyophilized to yield a white amorphous polymer (1.15 g, 92%). GPC (THF): Mn (\bar{D}): 25 kDa (1.09).

PEG-block-PLA NP preparation.

A solution of PEG-*b*-PLA in DMSO (40 mg mL⁻¹) was added dropwise to water (10 v/v) under a high stir rate. NPs were purified by ultracentrifugation over a filter (molecular weight cut-off of 10 kDa; Millipore Amicon Ultra-15) and resuspended in water to a final concentration of 150 mg mL⁻¹. NP size and dispersity were characterized by DLS.

PNP hydrogel preparation.

PNP gels were prepared by first dissolving the HPMC-C₁₂ polymer in water (3 wt%, 30 mg mL⁻¹) with stirring and mild heating. NPs were concentrated to 15 wt% solutions. HPMC-C₁₂ polymer solution (100 mg) and NP solution (200 mL) were then combined and mixed well by alternately vortex and centrifugation (to remove air bubbles arising from mixing).

AuNP-miR Synthesis

AuNP-miRs were synthesized as previously described. [13] In summary:

Functionalization of AuNP with PEG

Briefly, bare AuNP (20 nm gold nanospheres from Cytodiagnostics Inc. G-20-1000; 10 nm) dispersed in aqueous solution of 18 MEG DI Water were mixed with a commercial hetero-functional PEG (α -Mercapto- ω -carboxy PEG solution, HS-C₂H₄-CONH-PEG-O-C₃H₆-COOH, MW. 3.5 kDa, Sigma 712515-100MG; 0.006 mg mL⁻¹) in an aqueous solution of SDS (0.08%). Centrifugation (20,000×g, 30 min, 4 °C) removed excess PEG, which was quantified by the Ellman's Assay. The excess of thiolated chains in the supernatant was quantified by interpolating a calibration curve set by reacting α -Mercapto- ω -carboxy PEG solution (200 μ L) in phosphate buffer (100 μ L, 0.5 M, pH 7) with 5,5'-dithio-bis(2-nitrobenzoic) acid (DTNB, 7 μ L, 5 mg mL⁻¹) in phosphate buffer (0.5 M, pH 7) and measuring the absorbance at 412 nm after 10 min reaction. The linear range for the PEG chain obtained by this method is 0-0.1 mg mL⁻¹ (Abs at 412nm = 8.0353 \times [PEG, mg mL⁻¹] + 0.0486). The number of exchanged chains is given by the difference between the amount determined by this assay and the initial amount incubated with the AuNP. There is a point at which the AuNP becomes saturated with a thiolated layer and is not able to take up more thiolated chains - maximum coverage per AuNP, which was 0.03 mg mL⁻¹ of PEG for these AuNP. The AuNP were functionalized with 50% PEG layer in order to leave space for binding the thiolated miRNAs and HA1 peptide (Figure S1).

Functionalization of AuNP with miRNA molecules

AuNP were functionalised with Cy5.5-labelled miRNA against hsa-miR-214-3p (ACAGCAGGCACAGACAGGCAGU) or cel-miR-67-5p (CGCUCAUUCUGCCGGUU-GUUAUG). Cel-miR-67 was used as a negative control as it has minimal sequence identity with murine or human miRNAs and it is not naturally present in human cells; thus, it should not have any biological effect. Briefly, thiolated miRNA (Thermo Scientific Dharmacon) was dissolved in DTT (1 mL, 0.1 M), extracted three times with ethyl acetate, and further purified through a desalting NAP-5 column (Pharmacia Biotech) according to the manufacturer's instructions. The miRNA was only resuspended in DEPC-water and incubated immediately with AuNP previously functionalized with PEG. The purified thiolated miRNAs (10 μ M) were incubated with RNase-free solution of the PEG-AuNP (10 nm) containing 0.08% SDS. Subsequently, the salt concentration was increased from 0.05 to 0.3 M NaCl with brief ultrasonication following each addition to increase the coverage of oligonucleotides on the AuNP surface. After functionalization at 4 °C for 16 h, the particles were purified by centrifugation (20,000×g, 20 min, 4 °C), and re-suspended in DEPC-water. This procedure was repeated 3 times. The number of miRNA per AuNP was determined by quantification of the excess miRNA oligos in the supernatants collected during synthesis via the emission spectra of Cy5.5 (excitation/emission, 688 nm / 707 nm) dye in a microplate reader (Varioskan Flash Multimode Reader; Thermo Scientific). All nanoparticle samples and standard solutions of the thiolated-miRNAs were kept at the same pH and ionic strength for all measurements. Fluorescence emission was

converted to molar concentrations by interpolation from a standard linear calibration curve prepared with known concentrations of miRNA (**Figure S4**).

HA1 peptide functionalization

The HA1 (N-YPYDVDPDYA-C) peptide was coupled to the functionalized AuNP using carbodiimide chemistry assisted by N-hydroxysuccinimide using an EDC/NHS coupling reaction between the carboxylated PEG spacer and the amine terminal group of the peptide. HA1 peptide, which is used to enhance the miRNA uptake, was functionalized on the AuNP after miRNA functionalization. Briefly, 10 nM of NPs-PEG, 1.98 mg mL⁻¹ N-hydroxysulfosuccinimide (sulfo-NHS, Sigma) and 500 µg mL⁻¹ EDC (1-Ethyl-3-(3-dimethylaminopropyl)carbodiimide, Sigma) were incubated in 10 mM MES (2-(N-morpholino)ethanesulfonic acid, Sigma) at pH 6.2 and allowed to react for 30 min to activate the carboxylic groups. After this, activated AuNP were washed once with 10 mM MES, pH 6.2 and used immediately. HA1 was added to the mixture (final concentration 3 µg mL⁻¹) and allowed to react for 16 h at 25 °C. After this period, the AuNP were centrifuged at 20,000× g for 30 min at 4 °C and washed three times with Milli-Q water.

HA1 quantification was performed with the Pierce® BCA Protein Assay kit (Thermo Scientific) according to manufacturer's instructions. Briefly, each standard (0.025 mL) and unknown sample (the supernatants; 0.025 mL) was mixed with the BCA™ Working Reagent (50:1, BCA reagent A:BCA reagent B; 0.2 mL) to each tube. The reaction mixture was incubated at 60 °C for 30 min. After incubation, the tubes were cooled down to room temperature and the absorbance measured at 562 nm. The standard curve was used to determine the HA1 concentration of each unknown sample (supernatant). The calibration curve for a working range (0–125 µg mL⁻¹) is given by the following equation $\text{Abs } 562 \text{ nm} = 0.0036 \times [\text{HA1 peptide, } \mu\text{g mL}^{-1}] + 0.8016$, $R^2 = 0.9939$ for HA1 peptide (Figure S4).

Release of AuNP-miRs from PNP Hydrogel

AuNP-miR-214 were loaded into PNP hydrogels and incubated at 37 °C, 5% CO₂ with MilliQ water in 1.5 mL Eppendorf tubes. Supernatant was collected at regular 24 h intervals and the absorbance of the supernatant was measured at 524 nm on a Tecan Infinite 200 (Tecan Group Ltd. Männedorf, Switzerland) plate reader from 400 nm to 700 nm. The calibration curve based on a standard series of AuNP and AuNP-miRs (0.0 - 1.0 nM) is given by the following equations: $\text{Abs } 524 \text{ nm} = 0.299 \times [\text{AuNP}] + 0.0044$, $R^2 = 0.9984$, and $\text{Abs } 524 \text{ nm} = 1.4239 \times [\text{AuNP-miRs}] - 0.0048$, $R^2 = 0.9986$, respectively.

HEK293 Cell Culture

Human embryonic kidney 293 (HEK293) cells were cultured in Dulbecco's Modified Eagle's Medium (DMEM; ThermoFisher Gibco, supplemented with 10% FBS (ThermoFischer Gibco),

1% Pen/Strep (ThermoFisher Gibco 15070063), 1% Non-Essential Amino Acids NEAA (ThermoFisher Gibco 11140050), 1% Sodium Pyruvate (ThermoFisher Gibco, 11360070), on 2% gelatin coated until confluent. For experiments, cells were seeded at 25,000 cells per well in media (100 μ L) in a 96 well plate.

Luciferase/beta-Galactosidase cell transfection and reporter assay

Cells were transfected at 60-70% confluence with Luciferase and beta-Galactose (β -Gal) pMIR-REPORT vectors as previously described [34]. Briefly, the conserved miR-214-binding sequences in the Quaking (QKI) 3' untranslated region (UTR) were cloned into the pMIR-REPORT Luciferase vector (Ambion).

To assess the suppression efficiency of AuNP-miR-214, HEK293 cells were co-transfected with pMIR-REPORT-QKI-3' UTR Luciferase vector (100 ng) and a pMIR-REPORT β -Gal control plasmid (100 ng) in OptiMEM for 4 h to evaluate transfection efficiency. Subsequently, pre-miR-214 (60 nm) was delivered using Lipofectamine 3000 (ThermoFisher, L3000015). AuNP-miR-214 and AuNP-miR-67, as a scramble control microRNA, were added directly to the OptiMEM. Luciferase and β -Gal activity was assessed after 48 h with the Steady-Glo Luciferase Assay Kit (Promega E2520) and β -Gal assay buffer (200 mM sodium phosphate, 2 mM magnesium chloride, 100 mM beta-mercaptoethanol, 1.33 mg mL⁻¹ ortho-Nitrophenyl- β -galactoside (ONPG) in water), respectively. Luciferase activity was assessed by measuring luminescence and β -Gal activity was determined by measuring absorbance at 405 nm and 570 nm. Six biological replicates were transfected per conditions. Experiments were conducted in triplicate.

3D Calcific Aortic Valve Disease (CAVD) Model

A 3D *in vitro* model of human CAVD was employed to image AuNP-miRs uptake into cells. We previously published a detailed description and validation of this model [30]. Briefly, human aortic valves were obtained from patients undergoing valve replacement surgery at Brigham and Women's Hospital (Boston, MA, USA) as a result of aortic valve (AV) calcific stenosis. Leaflets were obtained and utilized in accordance with protocols approved by the Institutional Review Board (IRB protocol #2011P001703/PHS). Valvular interstitial cells (VICs) were isolated as previously described [46]. In short, CAVD AV leaflets were cut into 5 mm x 5 mm pieces, incubated in collagenase (Roche 10103586001; 10 mL) solution at 37 °C, 5% CO₂ for 12 h, and homogenized with a serological pipette. The digested tissue was centrifuged, the supernatant aspirated, and the pellet resuspended in VIC cell culture media [DMEM supplemented with 10% FBS (ThermoFisher, Gibco) and 1% P/S (ThermoFisher, Gibco); 5 mL]. The cells were then centrifuged a second time, resuspended in VIC cell culture media (10 mL), and plated in a T75 culture flask. Media was replenished every 48 h. VICs of passage five were used for further experiments. VICs were incorporated in hydrogel pre-

polymers by mixing VICs and media (to a final concentration of 10×10^6 cells mL^{-1} in the gel) with a GelMA (10 wt %), HAMA (3 wt %), and LAP solution (5 wt %) at 37 °C to form a GelMA (5%), HAMA (1%), and LAP (0.3%) hydrogel. GelMA and HAMA were synthesized as previously described [49,50].

Constructs were designed in Tinkercad (AutoDesk, Inc., San Rafael, CA, USA), and encoded using Repetier-Host (version 2.0.0; Hot-World GmbH & Co. KG, Willich, Germany), and Sublime Text 3 (Sublime HQ, Pty Ltd., Darlinghurst, NSW, Australia). 3D bioprinting was performed using the Inkredible+ (Cellink, Cambridge, MA, USA). Pluronic gel (Pluronic F-127; Allevi, Philadelphia, PA, USA) was printed as a cylindrical mold (outer diameter = 9.0 mm, inner diameter = 8.6 mm, height = 1.5 mm) using a stainless steel needle nozzle (JG27-0.25HPX; Jensen Global Inc., Santa Barbara, CA, USA) at a fill density of 95%, layer height of 0.1 mm, printing speed of 4mm/s, and printing pressure of 320 kPa. The second extruder was filled with the required hydrogel pre-polymer compositions and heated to 37 °C. A hydrogel disc was then printed inside the mold from the second extruder using a 23 g stainless steel nozzle (Fisnar 5901005, Ellsworth Adhesives, Germantown, WI, USA) by opening the valve of the second extruder for 40 ms at 15–20 kPa. Cross-linking the pre-polymers for 90 s with 365 nm UV light produced 8.6 mm x 1.0 mm hydrogel discs. The UV light was calibrated to an intensity of 2.5 mW/cm^2 using a radiometer (85009, Sper Scientific Direct, Scottsdale, AZ, USA). After printing, the Pluronic gel was dissolved by washing in cold PBS. One day after printing, hydrogels were switched to normal media (NM; 10% FBS, 1% P/S) or osteogenic media (NM supplemented with 10 nM dexamethasone, 10 ng mL^{-1} ascorbic acid, and 10 mM β -glycerolphosphate) as previously described [51], for up to 14 days. Media was changed every 48 h for all constructs. Cells were transfected with miR-214 (30 nM) by addition of AuNP-miR-214 to the cell culture media 48 h prior to imaging.

CellTracker/LysoTracker and confocal imaging

To trace the AuNP-miRs into the cells in the 3D CAVD model LysoTracker Red (ThermoFisher, L7528; 50 nm), CellTracker Green (ThermoFisher, C2925; 10 nm) dyes, and Hoechst 33342 (ThermoFisher, H1399) were added according to the manufacturer's protocol. CellTracker Green was incubated overnight at 37 °C, 5% CO_2 , LysoTracker Red was incubated for 1 h at 37 °C, 5% CO_2 , Hoechst (1:5000) was added and incubated for 30 min at 37 °C, 5% CO_2 , prior to imaging. Z-stack images of the constructs were taken on a ZEISS LSM 880 Confocal Microscope with AiryScan.

Animal Procedures

All animal procedures were performed according to MIT Animal Care and Use Committee approved protocols. Adult male C57BL/6 mice were injected subcutaneously on the back with PNP-AuNP-miR-67 gels (100 μL ; HPMC- C_{12} 1 wt %; PEG-*b*-PLA NPs 10 wt %; AuNP-

miR-67 85 nm) using a 26G syringe. At 1, 4, and 11 days following injection 3 animals per time point were sacrificed and lung, spleen, liver, kidneys and the tissue surrounding the injection site were harvested, flash-frozen, and stored until further analysis. Fluorescence reflectance of tissues was measured using a Kodak Image Station 4000mm Pro.

Statistics

Quantitative data is given as mean \pm standard error. The number of independent experiments is given as n. Statistical analyses were performed with GraphPad Prism 7 (GraphPad Software, La Jolla, CA, USA), Student's *t*-tests were performed for two-group comparisons, and for multiple group comparisons one-way or two-way ANOVA with Tukey's post-hoc HSD tests were used as appropriate. P-values <0.05 were considered statistically significant.

CONCLUSION

In conclusion, our data demonstrate that AuNP-miRs can be delivered via a minimally invasive, injectable self-assembling hydrogel, expressing controlled release. We showed that approximately 20% of AuNP-miRs were released from the PNP hydrogel over 5 days. Additionally, we observed that AuNP-miR-214 remained functional after delivery in both a 2D *in vitro* miR-214 target luciferase reporter assay and in a 3D bioprinted human CAVD model. Furthermore, we demonstrated that AuNP-miRs were cleared after 11 days in mice following subcutaneous injection of the PNP-AuNP-miR hydrogel delivery system. Without any cell-targeting ligands, these subcutaneously administered AuNP-miRs were taken up by the spleen, lungs, and liver, and were disposed via renal excretion. Additional targeting ligands and site-specific delivery could tailor this platform to specific cells or tissues, especially in combination with RNAi molecules adapted to a specific tissue, cell type, or disease.

ACKNOWLEDGEMENTS

This research was funded by the National Institutes of Health (NIH) R01 grants R01HL119798, R01HL136431 and R01HL147095 (E.A.); the National Institutes of Health (to R.L.); the Netherlands CardioVascular Research Initiative (CVON: The Dutch Heart Foundation, Dutch Federation of University Medical Centers, the Netherlands Organization for Health Research and Development, and the Royal Netherlands Academy of Science) and Vrienden UMC Utrecht (C.V., J.S.); an unrestricted grant from CELLINK to Vrienden UMC Utrecht (C.V., J.S.); the Harvard Catalyst Advanced Microscopy Pilot grants (C.V., E.A.); and the NIH Ruth L. Kirschstein National Research Service Award F32HL122009 (M.W.T.). This work was conducted with support from Harvard Catalyst | The Harvard Clinical and Translational

Science Center (National Center for Advancing Translational Sciences, National Institutes of Health Award UL1 TR001102) and financial contributions from Harvard University and its affiliated academic healthcare centers. We thank the Harvard Center for Biological Imaging for infrastructure and support, in particular Dr. D. Richardson and S. Terclavers.

SUPPORTING INFORMATION

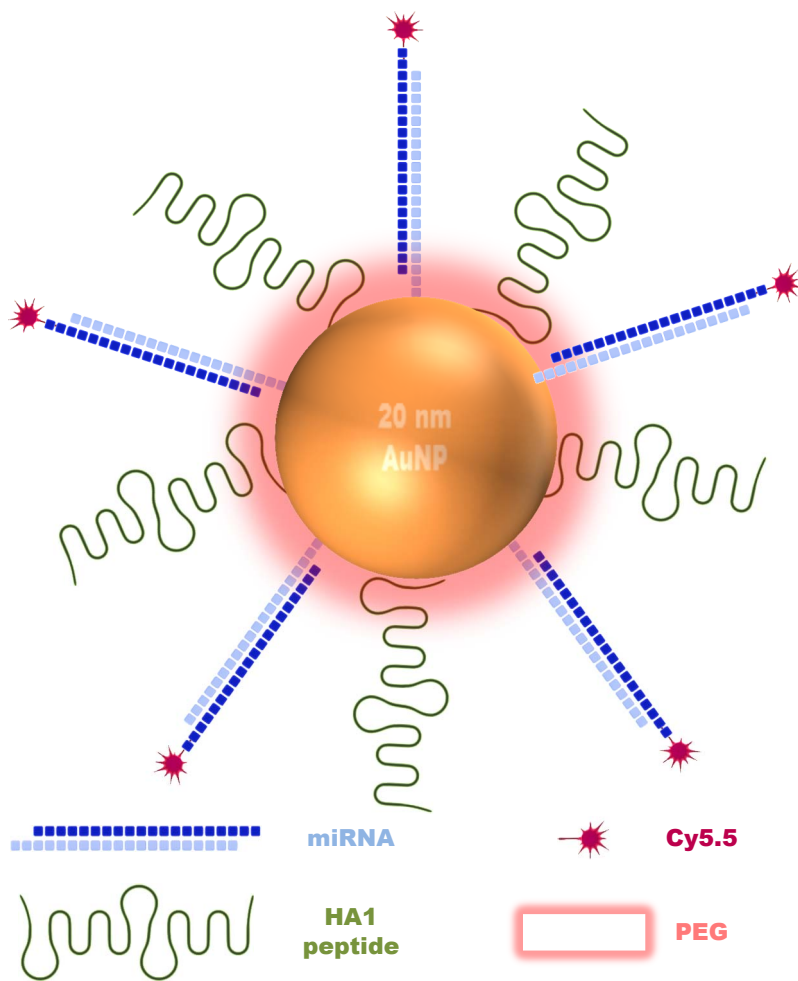


Figure S1. Schematic representation of the functionalization of AuNPs with PEG, Cy5.5, and HA1 peptide.

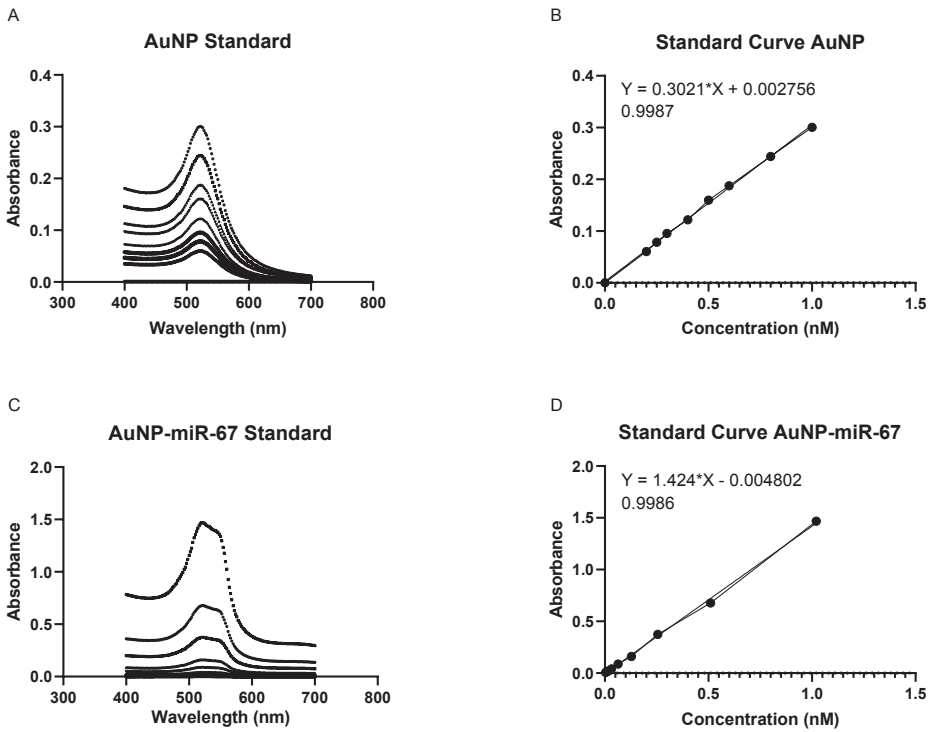


Figure S2. Absorbance spectra and calibration curves at 524 nm of a series of standard dilutions of (a,b) unmodified AuNPs is comparable to those of (c,d) AuNP functionalized with HA1 peptide, PEG, and miR-67/214, and quantifiable.

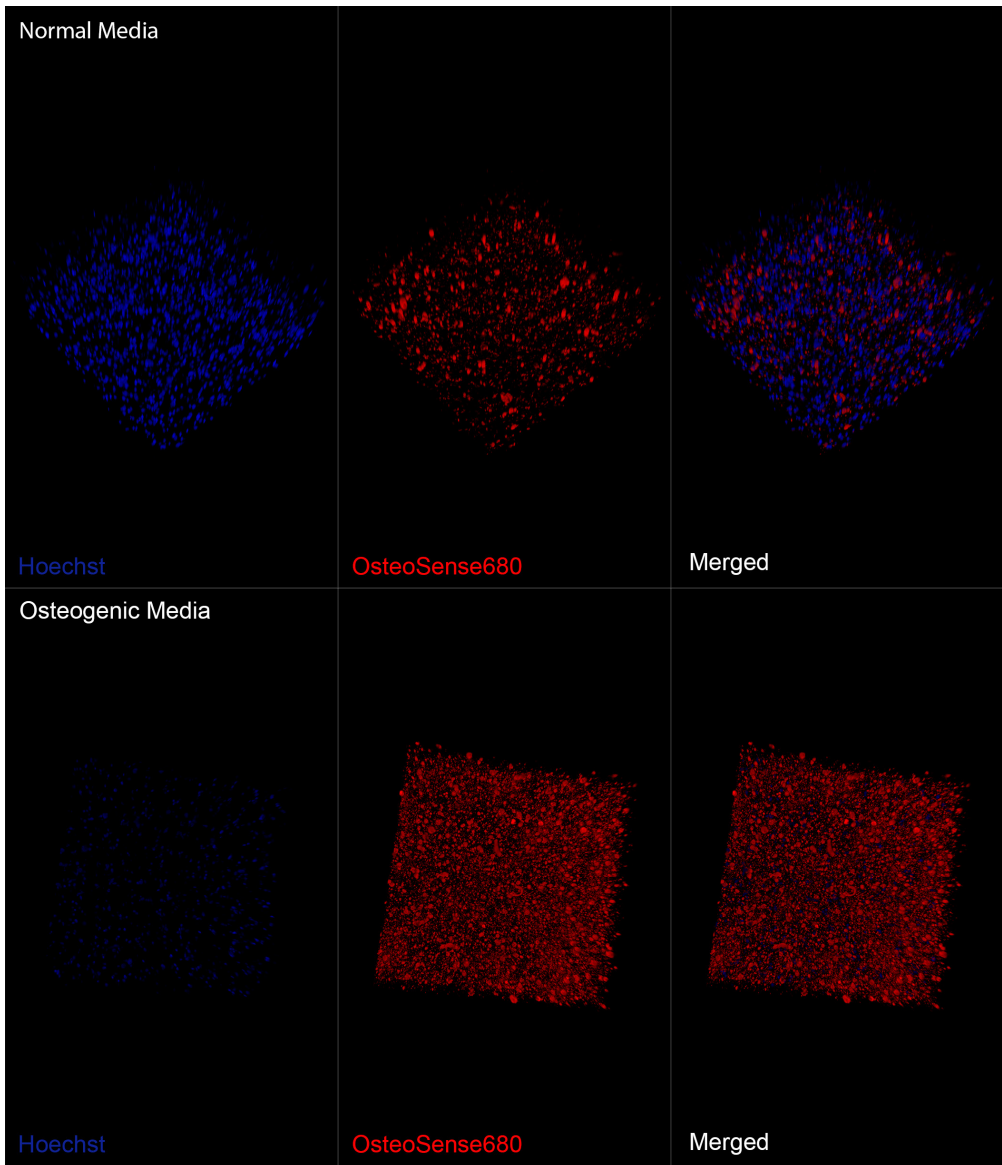


Figure S3. Human aortic valve interstitial cells in an *in vitro* bioprinted 3D Calcific Aortic Valve Disease model produce microcalcifications upon stimulation with osteogenic media (bottom) compared to normal cell culture media (top). Nuclei are stained with Hoechst (blue) and calcification with near-infrared fluorescent mineralization marker OsteoSense680EX (red). 3D render of Z-stacks of confocal images (10X) for Hoechst (left), OsteoSense680EX (middle), and merged (right).

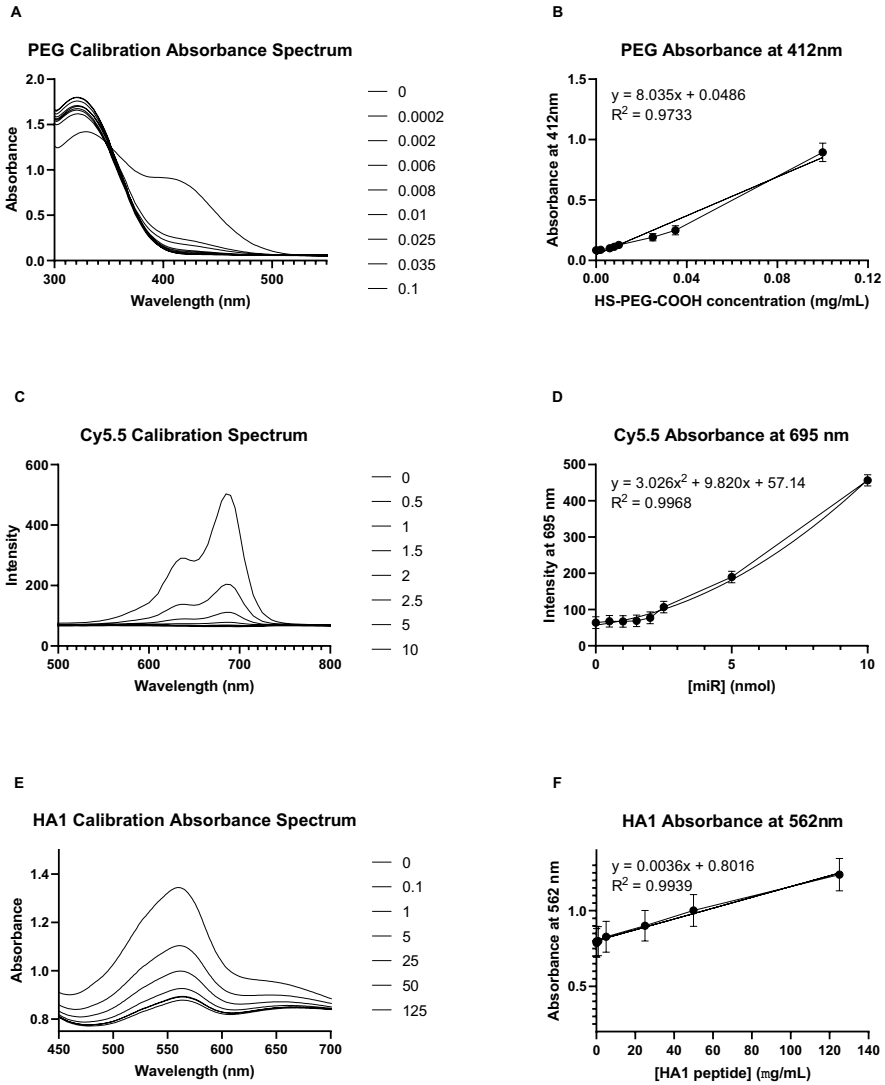


Figure S4. Functionalization of AuNPs with (a,b) PEG, (c,d) Cy5.5, and (e,f) HA1 peptide. Absorbance spectra of the dilution series in the left column and calibration curves in the right column.

REFERENCES

1. A. Eulalio, M. Mano, M. Dal Ferro, L. Zentilin, G. Sinagra, S. Zacchigna, M. Giacca. Functional screening identifies miRNAs inducing cardiac regeneration. *Nature* **2012**, *492*, 376-81 [PubMed] [CrossRef]
2. C. Wahlquist, D. Jeong, A. Rojas-Muñoz, C. Kho, A. Lee, S. Mitsuyama, A. van Mil, W.J. Park, J. P. Sluijter, P. A. Doevendans, R.F. Hajjar, M. Mercola. Inhibition of miR-25 improves cardiac contractility in the failing heart. *Nature* **2014**, *508*, 531. [PubMed] [CrossRef]
3. A. Aguirre, N. Montserrat, S. Zacchigna, E. Nivet, T. Hishida, M. N. Krause, L. Kurian, A. Ocampo, E. Vazquez-Ferrer, C. Rodriguez-Esteban, S. Kumar, J. J. Moresco, J. R. Yates 3rd, J. M. Campistol, I. Sancho-Martinez, M. Giacca, J. C. Izpisua Belmonte. In vivo activation of a conserved microRNA program induces mammalian heart regeneration. *Cell Stem Cell* **2014**, *15*, 589. [PubMed] [CrossRef]
4. H. Hosseini, M. M. S. Obradović, M. Hoffmann, K. L. Harper, M. S. Sosa, M. Werner-Klein, L. K. Nanduri, C. Werno, C. Ehrl, M. Maneck, N. Patwary, G. Haunschild, M. Gužvić, C. Reimelt, M. Grauvogl, N. Eichner, F. Weber, A. D. Hartkopf, F. A. Taran, S.Y. Brucker, T. Fehm, B. Rack, S. Buchholz, R. Spang, G. Meister, J. A. Aguirre-Ghiso, C. A. Klein. Early dissemination seeds metastasis in breast cancer. *Nature* **2016**, *540*, 552. [PubMed] [CrossRef]
5. J. Su, S. M. Morgani, C.J. David, Q. Wang, E. E. Er, Y. H. Huang, H. Basnet, Y. Zou, W. Shu, R. K. Soni, R. C. Hendrickson, A. K. Hadjantonakis, J. Massagué. TGF- β orchestrates fibrogenic and developmental EMTs via the RAS effector RREB1. *Nature* **2020**, *577*, 566. [PubMed] [CrossRef]
6. M. H. van der Ree, J. M. de Vree, F. Stelma, S. Willemse, M. van der Valk, S. Rietdijk, R. Molenkamp, J. Schinkel, A. C. van Nuenen, U. Beuers, S. Hadi, M. Harbers, E. van der Veer, K. Liu, J. Grundy, A. K. Patick, A. Pavlicek, J. Blem, M. Huang, P. Grint, S. Neben, N. W. Gibson, N. A. Kootstra, H. W. Reesink. Safety, tolerability, and antiviral effect of RG-101 in patients with chronic hepatitis C: a phase 1B, double-blind, randomised controlled trial. *Lancet* **2017**, *389*, 709. [PubMed] [CrossRef]
7. D.S. Hong, Y.K. Kang, M. Borad, J. Sachdev, S. Ejadi, H.Y. Lim, A.J. Brenner, K. Park, J.L. Lee, T.Y. Kim, S. Shin, C.R. Becerra, G. Falchook, J. Stoudemire, D. Martin, K. Kelnar, H. Peltier, V. Bonato, A.G. Bader, S. Smith, S. Kim, V. O'Neill, M.S. Beg. Phase 1 study of MRX34, a liposomal miR-34a mimic, in patients with advanced solid tumours. *Br J Cancer* **2020** Apr 2. Epub ahead of print. [PubMed] [CrossRef]
8. S. Oliveira, I. van Rooy, O. Kranenburg, G. Storm, R. M. Schiffelers. Fusogenic peptides enhance endosomal escape improving siRNA-induced silencing of oncogenes. *Int J Pharm* **2007**, *331*, 211. [PubMed] [CrossRef]
9. A. van Mil, P. A. Doevendans, J. P. Sluijter. The potential of modulating small RNA activity *in vivo*. *Mini. Rev. Med. Chem* **2009**, *9*, 235. [PubMed] [CrossRef]
10. O. S. Fenton, K. J. Kauffman, J. C. Kaczmarek, R. L. McClellan, S. Jhunjhunwala, M. W. Tibbitt, M. D. Zeng, E. A. Appel, J. R. Dorkin, F. F. Mir, J. H. Yang, M. A. Oberli, M. W. Heartlein, F. DeRosa, R. Langer, D. G. Anderson. Synthesis and Biological Evaluation of Ionizable Lipid Materials for the In Vivo Delivery of Messenger RNA to B Lymphocytes. *Adv. Mater* **2017**, *29*. [PubMed] [CrossRef]
11. R.F. Kwekkeboom, J. P. Sluijter, B. J. van Middelaar, C. H. Metz, M. A. Brans, O. Kamp, W. J. Paulus, R. J. Musters. Increased local delivery of antagomir therapeutics to the rodent myocardium using ultrasound and microbubbles. *J Control Release* **2016**, *222*, 18. [PubMed] [CrossRef]
12. A. Kargaard, J. P. G. Sluijter, B. Klumperman. Polymeric siRNA gene delivery - transfection efficiency versus cytotoxicity. *J Control Release* **2019**, *316*, 263. [PubMed] [CrossRef]
13. J. Conde, N. Oliva, Y. Zhang, N. Artzi. Local triple-combination therapy results in tumour regression and prevents recurrence in a colon cancer model. *Nat. Mater* **2016**, *15*, 1128. [PubMed] [CrossRef]
14. C. F. T. van der Ven, P. J. Wu, M. W. Tibbitt, A. van Mil, J. P. G. Sluijter, R. Langer, E. Aikawa. In vitro 3D model and miRNA drug delivery to target calcific aortic valve disease. *Cli.Sci* **2017**, *131*, 181. [PubMed] [CrossRef]
15. M. J. Hernandez, R. Gaetani, V. M. Pieters, N. W. Ng, A. E. Chang, T. R. Martin, E. van Ingen, E. A. Mol, J. P. G. Sluijter, K. L. Christman. Decellularized Extracellular Matrix Hydrogels as a Delivery Platform for MicroRNA and Extracellular Vesicle Therapeutics. *Adv Ther (Weinh)* **2018**, *1*. [PubMed] [CrossRef]
16. N. Bayat, Y. Zhang, P. Falabella, R. Menefee, J. J. Whalen, M. S. Humayun, M. E. Thompson. A reversible thermoresponsive sealant for temporary closure of ocular trauma. *Sci Transl Med* **2017**, *9*. [PubMed] [CrossRef]

17. D. Q. Wu, T. Wang, B. Lu, X.D. Xu, S. X. Cheng, X. J. Jiang, X. Z. Zhang, R. X. Zhuo. Fabrication of supramolecular hydrogels for drug delivery and stem cell encapsulation. *Langmuir* 2008, 24, 10306. [PubMed] [CrossRef]
18. J. A. Burdick, K. S. Anseth. Photoencapsulation of osteoblasts in injectable RGD-modified PEG hydrogels for bone tissue engineering. *Biomaterials* 2002, 23, 4315. [PubMed] [CrossRef]
19. Y. S. Pek, A. C. A. Wan, A. Shekaran, L. Zhou, J. Y. A. Ying. A thixotropic nanocomposite gel for three-dimensional cell culture. *Nat. Nanotechnol* 2008, 3, 671. [PubMed] [CrossRef]
20. M. M. Bastings, S. Koudstaal, R. E. Kieltyka, Y. Nakano, A. C. Pape, D. A. Feyen, F. J. van Slochteren, P. A. Doevendans, J. P. Sluijter, E. W. Meijer, S. A. Chamuleau, P. Y. Dankers. A fast pH-switchable and self-healing supramolecular hydrogel carrier for guided, local catheter injection in the infarcted myocardium. *Adv Healthc Mater* 2014, 3, 70. [PubMed] [CrossRef]
21. M. H. Bakker, E. van Rooij, P. Y. W. Dankers. Controlled Release of RNAi Molecules by Tunable Supramolecular Hydrogel Carriers. *Chem. Asian. J* 2018, 13, 3501. [PubMed] [CrossRef]
22. W. A. Petka, J. L. Harden, K. P. McGrath, D. Wirtz, D. A. Tirrell. Reversible hydrogels from self-assembling artificial proteins. *Science* 1998, 281, 389. [PubMed] [CrossRef]
23. H. D. Lu, M. B. Charati, I. L. Kim, J. A. Burdick. Injectable shear-thinning hydrogels engineered with a self-assembling Dock-and-Lock mechanism. *Biomaterials* 2012, 33, 2145. [PubMed] [CrossRef]
24. C. B. Rodell, A. Kaminski, J. A. Burdick. Rational design of network properties in guest-host assembled and shear-thinning hyaluronic acid hydrogels. *Biomacromolecules* 2013, 14, 4125. [PubMed] [CrossRef]
25. E. A. Appel, M. W. Tibbitt, M. J. Webber, B. A. Mattix, O. Veiseh, R. Langer. Self-assembled hydrogels utilizing polymer-nanoparticle interactions. *Nat. Comm* 2015, 6, 6295. [PubMed] [CrossRef]
26. O. S. Fenton, M. W. Tibbitt, E. A. Appel, S. Jhunjhunwala, M. J. Webber, R. Langer. Injectable Polymer–Nanoparticle Hydrogels for Local Immune Cell Recruitment. *Biomacromolecules* 2019, 20, 4430. [PubMed] [CrossRef]
27. A. Gilam, J. Conde, D. Weissglas-Volkov, N. Oliva, E. Friedman, N. Artzi, N. Shomron. Local microRNA delivery targets Palladin and prevents metastatic breast cancer. *Nat Commun* 2016, 7, 12868. [PubMed] [CrossRef]
28. J. Conde, N. Oliva, N. Artzi. Implantable hydrogel embedded dark-gold nanoswitch as a theranostic probe to sense and overcome cancer multidrug resistance. *Proc Natl Acad Sci U S A.* 2015, 112, E1278-87. [PubMed] [CrossRef]
29. J. Conde, A. Ambrosone, V. Sanz, Y. Hernández, V. Marchesano, F. Tian, H. Child, C.C. Berry, M.R. Ibarra, P.V. Baptista, C. Tortiglione, J.M. de la Fuente. Design of multifunctional gold nanoparticles for *in vitro* and *in vivo* gene silencing. *ACS Nano* 2012, 6, 8316-24. [PubMed] [CrossRef]
30. D. C. van der Valk, C. F.T. van der Ven, M. C. Blaser, J. M. Grolman, P. J. Wu, O. S. Fenton, L. H. Lee, M. W. Tibbitt, J. L. Andresen, J. R. Wen, A. H. Ha, F. Buffolo, A. van Mil, C. V. C. Bouten, S.C. Body, D. J. Mooney, J. P. G. Sluijter, M. Aikawa, J. Hjortnaes, R. Langer, E. Aikawa. Engineering a 3D-Bioprinted model of human heart valve disease using nanoindentation-based biomechanics. *Nanomaterials* 2018, 8, 296. [PubMed] [CrossRef]
31. E. A. Appel, M. W. Tibbitt, J. M. Greer, O. S. Fenton, K. Kreuels, D. G. Anderson, R. Langer. Exploiting Electrostatic Interactions in Polymer–Nanoparticle Hydrogels. *ACS Macro Lett* 2015, 4, 848. [CrossRef]
32. E. A. Mol, Z. Lei, M. T. Roefs, M. H. Bakker, M. J. Goumans, P. A. Doevendans, P. Y. W. Dankers, P. Vader, J. P. G. Sluijter. Injectable Supramolecular Ureidopyrimidinone Hydrogels Provide Sustained Release of Extracellular Vesicle Therapeutics. *Adv. Healthc. Mater.* 2019, 8. [PubMed] [CrossRef]
33. M. D. Krebs, O. Jeon, E. Alsborg. Localized and sustained delivery of silencing RNA from macroscopic biopolymer hydrogels. *J. Am. Chem. Soc.* 2009, 131, 9204. [PubMed] [CrossRef]
34. A. Van Mil, S. Grundmann, M. J. Goumans, Z. Lei, M. I. Oerlemans, S. Jaksani, P. A. Doevendans, J. P. Sluijter. MicroRNA-214 inhibits angiogenesis by targeting Quaking and reducing angiogenic growth factor release. *Cardiovasc. Res* 2012, 93, 655. [PubMed] [CrossRef]
35. N. Segovia, M. Pont, N. Oliva, V. Ramos, S. Borrós, N. Artzi. Hydrogel doped with nanoparticles for local sustained release of siRNA in breast cancer. *Adv Healthc Mater* 2015, 4, 271. [PubMed] [CrossRef]

36. M. K. Nguyen, O. Jeon, M. D. Krebs, D. Schapira, E. Alsberg. Sustained localized presentation of RNA interfering molecules from *in situ* forming hydrogels to guide stem cell osteogenic differentiation. *Biomaterials* 2014, 35, 6278. [PubMed] [CrossRef]
37. D. Zheng, Y. Zang, H. Xu, Y. Wang, X. Cao, T. Wang, M. Pan, J. Shi, X. Li. MicroRNA-214 promotes the calcification of human aortic valve interstitial cells through the acceleration of inflammatory reactions with activated MyD88/NF- κ B signaling. *Clin Res Cardiol.* 2019, 108, 691. [PubMed] [CrossRef]
38. E. Aikawa, M. Nahrendorf, D. Sosnovik, V. M. Lok, F. A. Jaffer, M. Aikawa, R. Weissleder. Multimodality molecular imaging identifies proteolytic and osteogenic activities in early aortic valve disease. *Circulation* 2007, 115, 377. [PubMed] [CrossRef]
39. J. Hjortnaes, C. Goettsch, J. D. Hutcheson, G. Camci-Unal, L. Lax, K. Scherer, S. Body, F. J. Schoen, J. Kluin, A. Khademhosseini, E. Aikawa. Simulation of early calcific aortic valve disease in a 3D platform: A role for myofibroblast differentiation. *J Mol Cell Cardiol* 2016, 94, 13. [PubMed] [CrossRef]
40. S. Rathan, C.J. Ankeny, S. Arjunon, Z. Ferdous, S. Kumar, J. Fernandez Esmerats, J. M. Heath, R. M. Nerem, A. P. Yoganathan, H. Jo. Identification of side- and shear-dependent microRNAs regulating porcine aortic valve pathogenesis. *Sci Rep* 2016, 6, 25397. [PubMed] [CrossRef]
41. H.X. Xu, Y. Wang, D. D. Zheng, T. Wang, M. Pan, J. H. Shi, J.H. Zhu, X. F. Li. Differential Expression of MicroRNAs in Calcific Aortic Stenosis. *Clin Lab* 2017, 63, 1163. [PubMed] [CrossRef]
42. M. I. Jan, R. A. Khan, T. Ali, M. Bilal, L. Bo, A. Sajid, A. Malik, N. Urehman, N. Waseem, J. Nawab, M. Ali, A. Majeed, H. Ahmad, S. Aslam, S. Hamera, A. Sultan, M. Aneesa, Q. Javed, I. Murtaza. Interplay of mitochondria apoptosis regulatory factors and microRNAs in valvular heart disease. *Arch Biochem Biophys* 2017, 633, 50. [PubMed] [CrossRef]
43. S. Coffey, M. J. Williams, L. V. Phillips, I. F. Galvin, R. W. Bunton, G. T. Jones. Integrated microRNA and messenger RNA analysis in aortic stenosis. *Sci Rep* 2016, 6, 36904. [PubMed] [CrossRef]
44. R. Song, D. A. Fullerton, L. Ao, K. S. Zhao, T. B. Reece, J. C. Jr. Cleveland, X. Meng. Altered MicroRNA Expression Is Responsible for the Pro-Osteogenic Phenotype of Interstitial Cells in Calcified Human Aortic Valves. *J Am Heart Assoc* 2017, 6, e005364. [PubMed] [CrossRef]
45. H. Wang, J. Shi, B. Li, Q. Zhou, X. Kong, Y. Bei. MicroRNA Expression Signature in Human Calcific Aortic Valve Disease. *Biomed Res Int* 2017, 2017, 4820275. [PubMed] [CrossRef]
46. E. Aikawa, P. A. Libby. A Rock and a Hard Place: Chiseling Away at the Multiple Mechanisms of Aortic Stenosis. *Circulation.* 2017, 135, 1951. [PubMed] [CrossRef]
47. A. N. Steele, L. M. Stapleton, J. M. Farry, H. J. Lucian, M. J. Paulsen, A. Eskandari, C. E. Hironaka, A. D. Thakore, H. Wang, A. C. Yu, D. Chan, E. A. Appel, Y. J. Woo. A Biocompatible Therapeutic Catheter-Deliverable Hydrogel for In Situ Tissue Engineering. *Adv Healthc Mater* 2019, 8. [PubMed] [CrossRef]
48. R. A. Gould, J. T. Butcher. Isolation of valvular endothelial cells. *J Vis. Exp.* 2010, 44. [PubMed] [CrossRef]
49. J. W. Nichol, S. T. Koshy, H. Bae, C. M. Hwang, S. Yamanlar, A. Khademhosseini. Cell-laden microengineered gelatin methacrylate hydrogels. *Biomaterials* 2010, 31, 5536. [PubMed] [CrossRef]
50. J. A. Burdick, C. Chung, X. Jia, M. A. Randolph, R. Langer. Controlled degradation and mechanical behavior of photopolymerized hyaluronic acid networks. *Biomacromolecules* 2005, 6, 386. [PubMed] [CrossRef]
51. J. D. Hutcheson, C. Goettsch, S. Bertazzo, N. Maldonado, J. L. Ruiz, W. Goh, K. Yabusaki, T. Faits, C. Bouten, G. Franck. Genesis and growth of extracellular-vesicle-derived microcalcification in atherosclerotic plaques. *Nat. Mater* 2016, 15, 335. [PubMed] [CrossRef]

Chapter 5

Non-coding RNAs in cardiac regeneration

Casper F.T. van der Ven
Benjamin C.R. Hogewoning
Alain van Mil
Joost P.G. Sluijter

INTRODUCTION

Cardiovascular disease is a leading cause of death worldwide, and with the dramatically increasing numbers of heart failure patients in the next ten years, mortality will only increase [1]. For patients with end-stage heart failure, heart transplantation is the sole option. Regrettably, the number of available donor hearts is drastically lower than the number of patients waiting for heart transplantation. Despite evidence of cardiomyocyte renewal in adult human hearts, regeneration of functional myocardium after injury can be neglected. The limited regenerative capacity due to inadequate proliferation of existing cardiomyocytes is insufficient to repopulate areas of lost myocardium [2]. As a solution, the hypothesis that adult stem cells could be employed to generate functional cardiomyocytes was proposed. One of the early studies that supported this hypothesis involved direct injection of hematopoietic c-kit-positive cells derived from bone marrow into the infarcted heart [3]. However, in sharp contrast, more recent evidence emerged demonstrating that these hematopoietic stem cells only differentiate into cells down the hematopoietic lineage rather than into cardiomyocytes [4,5], and the focus shifted towards stem cells residing in the heart, called cardiac progenitor cells. These CPCs were extracted and injected into the myocardium to regenerate the heart [6]. In recent years, over 80 pre-clinical studies employing cardiac stem cells *in vivo* in large and small animals to evaluate the effect on functional parameters were systematically reviewed, identifying differences between large and small animals [7]. Despite the positive outcome of these stem cell therapies on functional parameters, c-kit-positive cardiac progenitor cells were shown to contribute minimally to the generation of functional cardiomyocytes [8,9]. This heavily debated topic is summarized concisely by van Berlo and Molkentin [10]. Recently, single-cell sequencing and genetic lineage tracing of proliferative cells in the murine heart in both homeostatic and regenerating conditions did not yield a quiescent cardiac stem cell population or other cell types that support transdifferentiation into cardiomyocytes, nor did it support proliferation of cardiac myocytes [11,12]. Now, the focus is shifting towards exploiting the limited regenerative capacity of the cardiomyocytes themselves, by re-activating proliferation of existing cardiomyocytes through dedifferentiation, reentry into the cell cycle, and cytokinesis. This process is the new focus of research to promote cardiac regeneration, and can be controlled on multiple levels, including cell-cycle manipulation, reprogramming, small molecules, extra-cellular matrix (ECM), proteins, and RNA regulation [13].

Cardiac neovascularization, the formation of new blood vessels in the heart, is an essential part of cardiac regeneration. Neovascularization is distinct from vasculogenesis, which is considered *de novo* primitive vascular network formation, and occurs when angioblast precursors differentiate into endothelial cells in the developmental stages [14]. Angiogenesis is the formation of a new blood vessel from existing blood vessels. In the past the focus has been on mechanisms influencing the inhibition of angiogenesis, relating to its role in

the spread of tumors [15]. However, there has been a growing interest in tackling ischemic disorders by promoting neovascularization in an attempt to regenerate tissues [16].

This chapter will focus on findings regarding the role of non-coding RNAs in cardiac regeneration. Cardiac regeneration is defined as the repair of cardiac tissue, which in turn enhances or restores the functional capabilities of the heart. Studying the role of these non-coding RNAs in species with inherent cardiac regenerative capacity uncovers and helps to understand the mechanisms that drive cardiac regeneration, such as cardiomyocyte proliferation and neovascularization. First, we elaborate on the regenerative capacity in lower vertebrates and rodents and their role as scientific models, then we elucidate the role of non-coding RNAs in cardiomyocyte proliferation and neovascularization.

CARDIAC REGENERATION IN VARIOUS SCIENTIFIC MODEL SPECIES

5

Regenerative capacity varies between species. Lower vertebrate species have a high regenerative capacity throughout life, whereas in higher vertebrate species this regenerative capacity decreases after birth. Teleost fish like zebrafish and urodeles like newts or axolotls display robust cardiac regeneration, making them excellent model systems to study the underlying processes for cardiac regeneration. In zebrafish, after apical resection, bleeding is halted by blood clotting in the wound. Then fibrin is deposited, and where mammalian hearts become fibrotic through collagen deposition and scarring, the zebrafish heart replaces lost myocardium by proliferation of cardiomyocytes [17,18]. Cardiomyocyte proliferation is highest two weeks after injury, and two months after injury the majority of the lost myocardium has been renewed and cardiac output restored [18,19]. By employing Cre-based genetic fate mapping it was shown that resident cardiomyocytes dedifferentiate, proliferate, and mature similar to the developmental program to replace the lost myocardium, indicating that stem cells are not the source of regenerated myocardium [20,21]. Similarly, in urodeles complete regeneration without scarring was observed two to three months after the injury [22], and it was demonstrated that sarcomeric gene expression is downregulated during regeneration which supports the notion that adult cardiomyocytes can generate more cardiomyocytes via dedifferentiation, proliferation, and redifferentiation. This concept is known as the dedifferentiation hypothesis [23,24]. A concise recapitulation of the evolution of the scientific view on cardiomyocyte proliferation was published by Yutzey [25].

Rodent models like mice and rats display full growth and regeneration before and shortly after birth, yet have a reduced cardiac regenerative capacity as adult mammals [19]. Thus, neonatal rodents are excellent models for studying the mechanisms, and adult rodents are a

suitable model to test stimulation of regeneration. To study the regenerative capacity of the fetal mice heart, an X-linked mutation, deadly to cardiomyocytes was introduced in female embryos. Due to random X inactivation half of the cardiomyocytes were lost, though at birth the hearts were fully functional. The fetal hearts compensated for the effective loss of 50% of cardiomyocytes by increased proliferation of the healthy cardiac cells [26]. High regenerative capacity in neonatal mice hearts has been demonstrated in multiple cardiac damage models: myocardial infarction [27], ventricular resection [28], cryoinfarction [29,30], and clamping [31]. The human heart can also fully recover from injury as demonstrated in a case study of myocardial infarction in neonatal humans as a result of coronary artery occlusion. The infants fully recovered from the ischemic injury [32].

NON-CODING RNA IN CARDIOMYOCYTE PROLIFERATION

In contrast to the aforementioned lower vertebrate species, cardiomyocyte proliferation in adult mammals is, though present [2], insufficient to replenish lost cardiomyocytes due to injury. The proliferative state of cardiomyocytes as observed in embryonic stages of development quickly diminishes as the cells differentiate into the mature phenotype characterized by binucleation and hypertrophy. This development and maturation is regulated by many different factors. The capability of mature cardiomyocytes to again become proliferative is small [33,34,35]. Consequently, after the significant loss of cardiomyocytes as seen in ischemic injury, the heart cannot replace the lost cardiomyocytes and regenerate the myocardium. To enhance the regenerative capacity of the heart, understanding the mechanisms underlying the development and proliferation of cardiomyocytes is essential. Recently, non-coding RNAs have been shown to play an important role in regulating cardiomyocyte proliferation. These non-coding RNAs and their effect on cardiomyocyte proliferation are listed in Table 1. Here, we aim to highlight the discoveries of these non-coding RNAs and their role, organized per non-coding RNA class. At the time of writing the knowledge on the role of non-coding RNA in cardiac regeneration is limited to microRNAs (miRNAs) and long non-coding RNAs (lncRNAs). Other non-coding RNAs such as circular RNA, PIWI-interacting RNAs, or small inhibitory RNAs are not covered, as their roles in cardiac regeneration are still to be uncovered.

MicroRNA

With their function as post-transcriptional regulators and their broad spectrum of targets due to partially complementary binding, miRNAs are potential candidates to regulate cardiomyocyte proliferation. Both the aforementioned models, fish and rodent, are widely used to study the involvement of miRNAs in cardiac regeneration, and cardiomyocyte proliferation specifically. A common approach to identify miRNAs that could potentially regulate cardiomyocyte

regeneration is to compare miRNA expression levels in different stages of development in prenatal and postnatal rodent hearts. Candidate miRNAs are then validated in one or multiple *in vivo* models of cardiac injury in either or both neonatal and adult rodents. Oftentimes, a model of cardiac injury is employed to replicate the disease as observed in humans. These models are based on either surgical induction, via ischemia or ischemia/reperfusion, or on genetic induction of heart failure (HF). Here, the role of the different miRNAs in cardiomyocyte proliferation is illustrated per disease model.

Surgical cardiac injury models

Through ligation of the left anterior descending coronary artery (LAD), ischemia is induced in the left ventricle, inducing a myocardial infarction (MI), thereby resulting in a loss of cardiomyocytes [36]. The following miRNAs were found to play a role in increasing the regenerative capacity of the heart using this approach.

Initially miR-99/100 and Let-7a/c were identified as key players in cardiomyocyte dedifferentiation in a cardiac apical resection model in zebrafish that naturally regenerate. They were both validated in mice subjected to LAD ligation causing MI. Blocking these miRNAs increased expression of their target proteins farnesyl transferase-beta (FNTB) and SWI/SNF-related matrix associated actin-dependent regulator of chromatin-subfamily A, number 5 (SMARCA5). Upon blocking, increased left ventricular ejection fraction and fractional shortening indicated functional improvements. The resulting cardiac regeneration, induced via dedifferentiation and proliferation of cardiomyocytes, and improved functional effects in both species proved that this mechanism is conserved between species [37].

Over-expression of miR-128 in cardiomyocytes in a neonatal apical resection model, suppressed cardiomyocyte proliferation and hampering cardiac function, thereby inhibiting cardiac regeneration, which can be observed after apical resection in untreated neonatal mice. Additionally, the role of miR-128 in cardiac regeneration was validated by deletion in cardiomyocytes in adult mice demonstrating improved cardiomyocyte proliferation after myocardial infarction induced by permanent LAD ligation. By deleting miR-128 the expression of SUZ12, a chromatin modifier, was enhanced. This in turn suppressed cyclin-dependent kinase inhibitor p27 and activated cell cycle regulators Cyclin E and cyclin dependent kinase 2 (CDK2), promoting cell cycle re-entry in adult cardiomyocytes. Additionally, increased levels of GATA4 were observed, indicative of dedifferentiated cardiomyocytes [38].

In neonatal mice, miR-34a levels were found to be low and in adult mice, miR-34a levels were high, even after cardiac injury. Increasing miR-34a expression levels in neonatal mice resulted in a decreased regenerative capacity and hampered recovery. Inhibiting miR-34a in adult mice hearts after inducing MI increased the regenerative capacity and improved cardiac function,

reduced adverse remodeling, decreased fibrosis, and increased cell cycle activity. Further investigation demonstrated that this miR-43a inhibition resulted in higher protein levels of Sirt1, Cyclin D1, and Bcl2. These proteins have been implicated in cellular aging, cell cycle activity, and cell survival. The former was merely protective against cell death, whereas the latter two maintained proliferative and cell cycle capacities [39].

Similarly, the miRNA cluster miR-302-367 was found to be elevated in pre-natal stages compared to post-natal stages. Reactivating the cluster in adult hearts led to cardiomyocyte proliferation, though persistent, prolonged expression resulted in cardiomegaly and ultimately in heart failure. The positive effect of reactivation of the cluster on cardiomyocyte proliferation was confirmed in mice with MI induced by LAD ligation. Transient transfection with the miRNA cluster however prevented the adverse effects of persistent over-expression without compromising the positive effect of increased cardiomyocyte proliferation on the regenerative capacity of the heart. This cluster was found to target components of the Hippo pathway. Specifically, proliferation-associated gene *Ccnd1*, and consequently Cyclin G1, was elevated, and kinases *Mst1* and *Mob1b* were decreased [40]. In a more recent study, miR-302 was injected intramyocardially using a hydrogel delivery system for local and sustained delivery in adult Confetti mice with a MI. Due to the lineage labeling it was possible to distinguish newly generated cardiomyocytes as a result of clonal expansion. In addition, infarcted mice treated with the miR-302 showed comparable cardiac function to non-infarcted mice, as measured by ejection fraction and fractional shortening. Mice treated with miR-302 mimic demonstrated knock-down of *Lats2*, *Mob1*, and *Mst1*, all components of the Hippo signaling pathway, which controls cell proliferation mediated by YAP [41].

Additionally, miR-199a and miR-590 were identified by using a high-throughput functional screening with a whole-genome human miRNA library, and validated *in vivo*. Neonatal rats received injections of one of the two miRNAs complexed with a lipid transfection agent directly in the heart. Four days after treatment the ventricular wall thickness had increased, proliferating cardiomyocytes were found, and no fibrosis was observed. Next, adult mice were treated with AAV9 vectors expressing the two miRNAs after induction of a MI through permanent LAD ligation. Infarct size was significantly reduced in mice treated with miRNAs and cardiac function measured by left ventricular ejection fraction, fractional shortening, and end-systolic anterior wall thickness was preserved [42]. Expanding on these results, miR-199a was overexpressed using AAVs in pigs subjected to MI and reperfusion. Functional parameters improved, such as overall and local contractility. Muscle mass increased while scar tissue decreased, demonstrating that it is possible to regenerate the myocardium in larger mammals by stimulating endogenous repair via cardiomyocyte proliferation [43]. In all, expression of miR-199a and miR-590 after MI reduced infarct size and improved cardiac function by actively stimulating cardiomyocyte proliferation. Both miRs suppressed *Homer1* and *Hopx*,

genes involved in calcium signaling and in regulating proliferation, respectively [42,43]. After inducing MI on day 1 after birth through LAD ligation, the mouse heart recovered fully within three weeks, through proliferation of existing cardiomyocytes. This regenerative response was impaired by over-expression of miR-195, one of the members of the miR-15 family, leading to adverse remodeling as observed in adult mice. Next, in an ischemia-reperfusion model of MI the miR-15 family was inhibited during postnatal development into adulthood. This led to an increase in cardiomyocyte proliferation and improved systolic function. Thus, inhibition of the miR-15 family increases the regenerative capacity [44]. In an earlier study by the same group, miR-195 was shown to directly affect cell cycle genes *Chek1*, *Cdc2a*, *Birc5*, *Nusap1*, and *Spag5*, supposedly increasing mitotic and cell cycle entry, and cell cycle progression. However, of these, *Chek1* is the only gene with a miR-15 binding site that is conserved between mice and humans [45].

Genetic cardiac injury models

When *Dicer*, which is required for pre-miR processing to mature miRNAs, was deleted in the hearts of embryonic mice using Cre recombinase and under the control of the *Nkx2.5* promotor this led to death as a result of heart failure. Thus proper miRNA functioning is required in cardiac development. In the *Dicer* mutant hearts, miR-1 was dysregulated. Using homologous recombination, miR-1-2 was deleted in mouse embryonic stem cells. Heterozygous animals were intercrossed to create offspring lacking miR-1-2. These mice died early, mostly due to ventricular septum defects, and those that survived suffered from cardiac arrhythmias and hyperplasia due to abnormalities in the cardiomyocyte cell cycle. Loss of miR-1-2 resulted in a loss of *lrx5*, leading to abnormal repolarization of cardiomyocytes and consequently cardiac arrhythmias. Furthermore, miR-1-2 mutants were hyperplastic as a result of increased mitotic activity in cardiomyocytes. This indicates a potential role for miR-1-2 in stimulating the regenerative capacity, though the observation in this study may be a result of increased proliferation in the early stages of development rather than in adult animals, for cytokinesis was not observed in adult animals [46].

Another example of complete knockout of a miRNA resulting in abnormal cardiomyocyte proliferation is the double knockout of miRNA-133a-1 and miRNA-133a-2 in mice, targeting Cyclin D2 and serum response factor (SRF). Mice lacking genes for one of the variants were normal, but deletion of both genes led to ventricular septal defects and consequently death in embryonic and neonatal animals, as a result of dysregulated cardiomyocyte proliferation, apoptosis, and abnormal expression of smooth muscle genes in the heart. Mice surviving into adulthood perished from heart failure and sudden death. Thus, miR-133a-1 and -2 are essential for normal cardiac growth and function [47].

Similarly, complete knockout of the miR-17-92 cluster in embryonic, postnatal, and adult mice resulted in smaller hearts and lower proliferation rates in postnatal animals, a reduced number of cardiomyocytes in adult hearts, and decreased cardiac function, demonstrating that this cluster is essential for cardiomyocyte proliferation in embryonic and postnatal hearts. Overexpression of the cluster in a transgenic mouse model demonstrated enlargement of the hearts and thickening of the ventricle walls due to proliferation rather than hypertrophy. Overexpression of miR-17-92 using tamoxifen-inducible Cre recombinase in mice, subjected to MI, attenuated the effects of MI-induced damage and adverse remodeling. miR-17-92 was found to affect phosphatase and tensin homolog (PTEN), and overexpression of PTEN diminished miR-19 (a member of the miR-17-92 cluster) promoted cardiomyocyte proliferation. These results confirmed that the miR-17-92 cluster, and miR-19 specifically, can induce proliferation by suppressing PTEN in cardiomyocytes [48].

Some miRNAs have been validated *in vivo* without cardiac validation. For example, miRNA array on post-natal day 0 and day 10 rat cardiomyocytes revealed upregulated miR-31a levels on day 10. Inhibition of miR-31a on days 0, 1, and 2 resulted in reduced cardiomyocyte proliferation through RhoBTB1, a subfamily of the Rho small GTPases, suggesting that upregulating miR-31 might increase the generative capacity of the heart through stimulating cardiomyocyte proliferation [49].

Overall, evidence that miRNAs can influence cardiomyocyte proliferation is accumulating. Multiple miRNAs have been identified and validated *in vivo*. However, it is not yet fully understood how these miRNAs in turn are regulated, nor is it evident that miRNA are the sole regulatory RNAs in cardiac regeneration. Long non-coding RNAs are emerging as regulators of RNAs (mRNA, miRNA, circRNA) as well as DNA and proteins. Their broad complex roles in gene regulation is a popular current topic, and there is evidence for involvement of several lncRNAs in cardiomyocyte proliferation.

Long non-coding RNA

Long non-coding RNAs are a class of RNA molecules consisting of over 200 nucleotides that can regulate gene expression, both at transcriptional and post-transcriptional level, in a range of cellular processes, including (de)differentiation and proliferation. The research field of lncRNAs is relatively young and only a limited number of lncRNAs have been explored in the context of cardiovascular regeneration. How the lncRNAs listed in Table 1 were identified and how they affect cardiomyocyte proliferation is elaborated on in the following paragraphs.

Three lncRNAs have been identified that influence cardiomyocyte proliferation through affecting cell cycle genes. Endogenous cardiac regeneration-associated regulator (ECRAR) [50], LINC3 (Gas5), and LINC9 (Sghrt) [51] exert their function indirectly on one

or more Cyclin proteins. ECRAR binds to extracellular signal-regulated kinases 1 and 2 (ERK1/2) activating cyclin D1 and cyclin E1, which both activate E2F transcription factor 1 (E2F1). E2F1 can upregulate ECRAR, creating a positive feedback loop that stimulates cell cycle progression, promoting proliferation in cardiomyocytes. Over-expression of ECRAR stimulated cardiomyocyte proliferation *in vivo* in the adult rat heart. To assess the effect of ECRAR over-expression in a disease environment, rats with MI from LAD ligation were injected with Adenovirus-mediated ECRAR. Over-expression of ECRAR led to increased proliferation resulting in cardiomyogenesis. Furthermore, infarct size was significantly smaller in rats that were treated with ECRAR, scar formation measured by fibrotic area was less, and functional parameters were improved, suggesting ECRAR enhances the regenerative capacity of the myocardium. This was confirmed by knockdown of ECRAR in naturally regenerative neonatal rat hearts, preventing recovery after MI. ECRAR showed a 12-fold increased expression from the analysis of four datasets of RNA-sequencing in fetal compared to adult human cardiac tissues. This finding was confirmed in rat fetal hearts, where ECRAR expression is high on embryonic day 12 and decreased after birth [50].

Similarly, nuclear RNA-sequencing of single cardiomyocytes from failing and healthy human heart tissue identified heterogeneity in the transcriptomic stress-response [51]. Key nodal lncRNA surfaced that regulate dedifferentiation and cell cycle genes in certain subsets of cardiomyocytes that can potentially regulate cardiac repair. In the diseased cells of a trans-aortic constriction (TAC) mice model, LINCM3 (*Gas5*) and LINCM9 (*Sghrt*) were upregulated, and LINCM5 was down-regulated compared to sham operated mice. Both *Gas5* and *Sghrt* are part of signaling pathways related to translation, generation of precursor metabolites, oxidative phosphorylation, response to oxidative stress, cell proliferation, and cardiac muscle tissue development. This indicated that both lncRNAs could be the main regulators of other genes within the same gene regulatory network. This hypothesis was tested by knocking down either of these lncRNAs in adult cardiomyocytes from TAC operated mice. Knockdown of *Gas5* down-regulated the expression of *Nppa* (fetal reprogramming), *Dstn* (dedifferentiation marker), *Ccng1* (cell cycle gene, coding for Cyclin G1), and *Ccnd2* (cell cycle gene, coding for Cyclin D2). *Gas5* has previously been shown to accumulate in the heart [52] and regulate apoptosis [53] and proliferation [54] in other cell types. *Sghrt*, at the time of writing, has no previously described function. Suppression of *Sghrt* did not have any significant effects on either *Nppa* or *Dstn*, increased *Ccng1*, and decreased *Ccnd2*. Thus, these experiments demonstrated that both lncRNAs can regulate genes in the same regulatory network at a transcriptional level [51].

Three other lncRNAs have been identified to be involved in cardiomyocyte regeneration, though not through affecting cell cycle genes. CAREL [55], MALAT1 [56], and Sirt1 antisense lncRNA [57] influence cardiomyocyte proliferation through anti-proliferative and pro-

apoptotic pathways, through inhibiting transcription factors in developmental pathways, and through stabilization of mRNA, respectively.

Microarray analysis revealed that lncRNA CAREL was upregulated in postnatal mouse hearts. Over-expression of CAREL in cardiomyocytes of mice diminished their division and proliferation, and the regenerative capacity of neonatal hearts was lost. In contrast, silencing CAREL stimulated cardiac regeneration and promoted cardiac function after injury in both neonatal and adult mice. CAREL binds competitively to the targets of miR-296, *Trip53inp1* and *Itm2a*. In line with previous results, over-expression of miR-296 induced cardiomyocyte proliferation and increased the regenerative capacity. In CAREL transgenic mice, the regenerative capacity was decreased, and could be restored by over-expressing miR-296 [55].

LncRNA MALAT-1 is expressed in adult zebrafish hearts [56]. MALAT-1 knock-out zebrafish showed an enlarged pericardium and other cardiac developmental abnormalities. Cardiac progenitor cell genes *nkx2.5* and *gata4* were upregulated, hinting at a regulatory role for MALAT-1 [56].

Expression patterns of Silent information regulator factor 2 related enzyme 1 (Sirt1) antisense lncRNA are higher in embryonic and neonatal compared to adult mouse hearts [57]. Sirt1 antisense lncRNA can bind Sirt1 messengerRNA, stabilizing it, and enhancing its translation into Sirt1 protein. Isolated neonatal cardiomyocytes were transfected with Sirt1 antisense lncRNA to examine its role in proliferation. Over-expression resulted in higher cell cycle activity, increased mitosis, and a higher cell number, indicating a positive influence on proliferation. In contrast, knocking down Sirt1 antisense lncRNA decreased the number of cardiomyocytes, cell cycle activity, and mitosis, and increased apoptosis. Next, intramyocardial injections of LNA targeting Sirt1 antisense lncRNA resulted in decreased levels of proliferation in neonatal mice. Following these experiments, Sirt1 antisense lncRNA was over-expressed in both healthy and LAD-MI adult mice, leading to increased cardiomyocyte proliferation compared to their respective controls and a higher survival rate in the treated LAD-MI mice compared to untreated mice. In the latter group, cardiac output parameters, left ventricular ejection fraction and fractional shortening, improved, and the infarct size was smaller compared to untreated LAD-MI animals. These outcomes indicate that Sirt1 antisense lncRNA positively affects the regenerative capacity in ischemic adult hearts [57].

In addition to affecting gene expression through the aforementioned mechanisms, lncRNAs can act as sponges to miRNAs. Two lncRNAs have been identified that function thusly in affecting cardiomyocyte proliferation.

Recently, lncRNA [NR_045363](#) was discovered to be mainly expressed in cardiomyocytes compared to non-cardiomyocytes, and more in embryonic mouse hearts than in adult mouse hearts [58]. Over-expression of this lncRNA in neonatal mice cardiomyocytes significantly increased proliferation *in vitro* and *in vivo*. Knockdown in primary embryonic cardiomyocytes led to decreased proliferation. Furthermore, over-expression in mice subjected to MI resulted in significantly ameliorated left ventricular ejection fraction and fractional shortening. Additionally, using EdU staining cardiomyocyte proliferation was shown to have increased in the animals over-expressing NR_045363. In silico target prediction showed miR-216a as a potential targets of NR_045363. Mir-216a is also a target of [LOC101927497](#), the human ortholog of NR_045363. These predictions were validated *in vitro* and it showed that knockdown of NR_045363 led to increased miR-216a expression, and over-expression of NR_045363 resulted in decreased miR-216a expression levels. The researchers concluded that NR_045363 may function as a miRNA sponge for miR-216a, thereby preventing down-regulation of the targets of miR-216a, and consequently promoting proliferation [58].

Interestingly, one lncRNA has been identified that affects one of the cardiomyocyte proliferation-associated miRNAs. Cardiomyocyte regeneration related lncRNA ([CRRL](#)) has been identified from RNA-sequencing data of human fetal and adult heart tissues. CRRL promotes the expression of Hopx, the gene coding for Homeodomain-only protein, by directly binding miR-199a-3p, thereby removing the inhibition of miR-199a-3p on Hopx mRNA expression [59]. Loss of CRRL in adult rats preserved cardiac function and diminished adverse remodeling post infarct. Knockdown of CRRL in neonatal rat cardiomyocytes promoted proliferation *in vitro* and *in vivo* [59]. Thus, downregulation of the Hopx gene by removing the miR-199a-3p sponge CRRL via knockdown has a comparable effect to adding miR-199a as described previously [42].

ncRNA	Target	Effect on Cardiac Function	Species	Reference
Let-7a/c	FNTB, SMARCA5	Negative	Zebrafish	Aguirre 2014 [37]
miR-1-2	Irx5	Positive	Mice	Zhao 2007 [46]
miR-15	Chek1	Negative	Mice	Porrello 2011, Porrello 2013 [44,45]
miR-17-92, miR-19a/b	PTEN	Positive	Mice	Chen 2013 [48]
miR-31a	RhoBTB1	Positive	Rats	Xiao, 2017 [49]
miR-34a	Sirt1, Cyclin D1, Bcl2	Negative	Mice	Yang 2015 [39]
miR-99/100	FNTB, SMARCA5	Negative	Zebrafish	Aguirre 2014 [37]
miR-128	SUZ12, CDK2, Cyclin E, GATA4	Negative	Mice	Huang 2018 [38]
miR-133a-1/2	SRF, Cyclin D2	Positive	Mice	Liu 2008 [47]
miR-195	Chek1	Negative	Mice	Porrello 2013 [44]
miR-199a	Homer1, Hopx	Positive	Mice, Rats	Eulalio 2012 [42]
miR-296	Trip53inp1, Itm2a	Positive	Mice	Cai 2018 [55]
miR-302	Hippo, spec.: Lats2, Mob1, Mst1	Positive	Mice	Tian 2015, Wang 2017 [40,41]
miR-590	Homer1, Hopx	Positive	Mice, Rats	Eulalio 2012 [42]
CAREL	Trip53inp1, Itm2a	Negative	Mice	Cai 2018 [55]
CRRL	miR-199a - Hopx	Negative	Rat	Chen 2018 [59]
ECRAR	ERK1/2, Cyclin D1, Cyclin E1	Positive	Rat	Chen 2019 [50]
LINCM3 (Gas5)	Nppa, Dstan, Cyclin G1, Cyclin D2		Mice	Yin 2014, See 2017 [54,51]
LINCM9 (Sghrt)	Cyclin G1, Cyclin D2		Mice	See 2017 [51]
MALAT-1	Nkx2.5, GATA4	Negative	Zebrafish	Wu 2019 [56]
NR_045363	miR-216a	Positive	Mice	Wang 2019 [58]
Sirt1 antisense lncRNA	Sirt1 mRNA	Positive	Mice	Li 2018 [57]

Table 1 - Overview of identified non-coding RNAs validated *in vivo* for their role in cardiomyocyte proliferation.

NON-CODING RNAs IN NEOVASCULARIZATION

The growth of new blood vessels requires proangiogenic stimuli, including growth factors such as vascular endothelial growth factor (VEGF-A) [60]. Certain non-coding RNAs, for example, have the ability to influence these proangiogenic factors. Therefore, non-coding RNAs have the potential to become a therapeutic tool for treating ischemic cardiac tissue [61].

The following part provides an overview of advances in non-coding RNA research on cardiac regeneration through neovascularization. The non-coding RNAs listed in Table 2 are also shown in Figure 1, to illustrate the pathways they affect, and their effect on cell cycle progression or apoptosis, respectively.

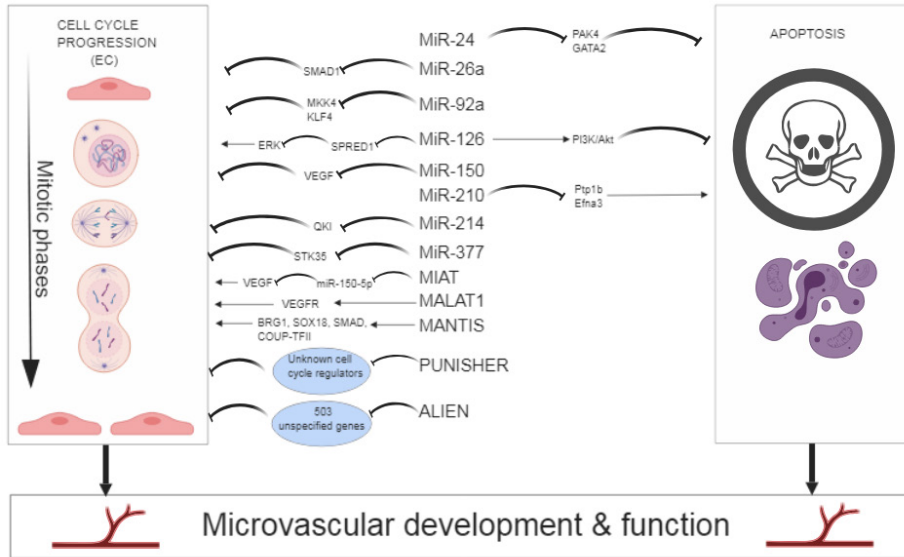


Figure 1 - Schematic representation of non-coding ribonucleic acids (RNA) and their respective targets that affect microvascular development and function through either stimulation (green) or repression (red) of cell cycle progression or apoptosis.

miRNA

The first example of involvement of miRNA in the regulation of neovascularization was shown by Yang [39]. Their discovery demonstrated that knocking out the miRNA processing enzyme Dicer in mice would result in early death during embryonic development, due to impaired angiogenesis [39,62]. Following up on that discovery, numerous studies have shown the critical roles of miRNAs in neovascularization.

Over-expression of miR-210 on MI-injured cardiac tissue, showed an increase in neovascularization and angiogenic processes [63]. MiR-210 is known as a hypoxamiR, a label given to miRNAs that have an important role in hypoxic conditions [64]. Improved contractility in mammalian acute cardiac ischemia (ACI) models was observed when exposed to over-expression of miR-210, through the stimulation of hepatocyte growth factor (HGF) expression as well as the effect of miR-210 on left ventricular (LV) remodeling. This study concluded that through administration of miR-210 agonists, increased micro-vessel density was observed, indicating a potential therapeutic tool for patients with ACI [65].

In mice, miR-92a has been observed to control recovery of ischemic tissue and has been noticed to play a role in angiogenesis. Both *in vitro* and *in vivo*, over-expression of miR-92a in endothelial cells blocked neovascularization. In MI models, miR-92a antagonists demonstrated enhanced angiogenesis and resulted into recovery of the injured tissue. MiR-92a affects numerous proteins that promote angiogenesis, including integrin subunit $\alpha 5$. An abundance of miR-92a in endothelial cell caused a decline in endothelial cell migration, decreased vascular network formation, blocking of sprouting in a 3D neovascularization model, as well as reduced adhesion of the endothelial cell to fibronectin. MiR-92a influences MAP kinase kinase 4 (MKK4) and Kruppel-like factors-4 (KLF4) by targeting integrin subunit alpha-5, thereby inhibiting cell cycle progression in endothelial cells, and consequently the formation of new blood vessels. MiR-92a can therefore be categorized as an anti-angiogenic factor [62,66]. Most of these studies were solely conducted in small animal models, and Hinkel et al. [67] took the next step and tested the efficacy of using the therapeutic potential of miR-92a inhibition in a pre-clinical porcine model of ischemia and reperfusion (I/R). The study showed that by using LNA-modified antisense miR-92a (miR-92a inhibitor), when applied regionally with the use of a catheter, the infarct size could be reduced significantly. This consequence resulted in enhanced cardiac function, as measured by LV ejection fraction and LV end-diastolic pressure. Histochemistry in the models confirmed an increased density of capillaries in the post-ischemic MI porcine hearts [67]. This study indicates that *anti-angiogenic* non-coding RNAs have the potential to be used as therapeutic targets in regenerative blood vessel formation.

MiR-24 is an additional anti-angiogenic miRNA, validated in a MI model in mice. MiR-24 has multiple effects on cardiac vascularization was shown to be upregulated as a consequence of cardiac ischemia. By acting on transcription factor GATA2, usually enriched in EC, as well as affecting PAK4, a p21-activated kinase, miR-24 promotes apoptosis of EC, limits cell sprouting (branching of vessels), and inhibits capillary network formation. Silencing of miR-24-targets as well as over-expression of miR-24, significantly restricted and halted angiogenesis in zebrafish embryos. Complete block of miR-24 decreased the damaged myocardial infarct size in mice, through increased vascularization and reduced apoptosis of the endothelial tissue. This resulted in improved cardiac function and thus miR-24 could be a potential therapeutic candidate for the regeneration of damaged tissue [62,68]. In a mouse LAD-MI model, miR-24 expression showed increased expression levels in ECs. By blocking miR-24 specifically through local delivery of an adenovirus-mediated decoy, angiogenesis and blood perfusion of the myocardial tissue surrounding the infarcted area increased. In addition, there was a reduction in the infarct size, miR-24 induced fibroblast apoptosis, and overall cardiac function improved. Despite these potentially regenerative measures and effects, miR-24 decoy also increased cardiomyocyte apoptosis. *In vitro*, miR-24 inhibition supported endothelial cell survival, proliferation, and blood-vessel forming capabilities. Additionally, it

led to fibroblast apoptosis, which could result in a reduction in scar formation *in vivo*, and CM apoptosis. These results were confirmed *in vivo* 14 days post-MI [69]. Both inhibition [68] and over-expression [70] of miR-24 have yielded positive results in mice with acute MI. Meloni et al. [69] set out to test the results of inhibiting miR-24 on cardiac function in a MI model and observed, 14 days after MI, that cardiac function had improved. These results indicated that the initial positive effect on endothelial cells is stronger than the apoptotic effect in CMs, resulting in a pro-angiogenic response and improved cardiac function two weeks after MI. It must be noted that that extended inhibition of miR-24 could lead to increased apoptosis in CMs and have a destructive effect on cardiac function and infarct size.

Wang et al. [71] discovered the importance of miR-126 in ensuring vascular integrity and function. The observation of mutant mice lacking the gene encoding for miR-126 resulted in dead embryos, or embryos suffering from ruptured blood vessels, hemorrhages and systemic edema. These abnormalities can be linked to reduced pro-angiogenic growth factor signaling, through e.g. VEGF and fibroblast growth factor (FGF). A lack of these angiogenic factors can lead to decreased endothelial cell growth, sprouting, and adhesion. MiR-126 as a pro-angiogenic stimulator is linked to the inhibition of Spred-1, which is an inhibiting regulator of MAP kinase signaling. If Spred-1 is over-expressed, it decreases pro-angiogenic signals by VEGF and FGF. In the absence of miR-126, there is no regulation of Spred-1. The group of mutant animals that survived showed malfunctioning cardiac neovascularization following MI induced by permanent LAD ligation, indicating the essential function of miR-126 [71].

In mice that suffer from ACI and in humans with acute coronary syndromes, increased levels of miR-26a has been observed [72]. Expression of miR-26a resulted in endothelial cell cycle arrest, inhibition of endothelial cell migration, sprouting angiogenesis, and blood vessel network formation in Matrigel. Blocking of miR-26a has the opposite effects. Over-expression of miR-26a *in vivo* in mice inhibited endothelial cell SMAD1 expression. It also resulted into a decrease in exercise-induced angiogenesis. Additionally, miR-26a inhibitor given intravenously resulted in increased levels of SMAD1 expression and readily induced significant levels of angiogenesis within two days. The pathway of miR-26a consists of the inhibition of the bone morphogenic protein/SMAD1 signaling pathway in ECs through directly targeting SMAD1. Through this blockage, Id1 expression is decreased, resulting in increased levels of p21 and p27 (regulators of the cell-cycle). leading to reduced infarct size and damage [72].

MiR-377 was found to play a role in paracrine-mediated angiogenesis [73]. *In vivo* evidence proved that, by knockdown of miR-377, mesenchymal stem cell (MSC) mediated angiogenesis increased, as well as the recovery of cardiac function after MI. Through the transplantation of these MSCs in MI rat hearts, the genetic over-expression of miR-377, its knockdown and

a control were compared. Anti-MiR-377 treated hearts showed most myocardial angiogenesis post-MI. Through computational miRNA prediction analysis, VEGF was determined to be a potential target affected by miR-377. Verification of this assumption was performed through Western Blotting as well as through dual luciferase reporter assay. Wen et al. [73] determined that miR-377 can bind to the VEGF untranslated-region (UTR), resulting in its negative regulation on expression [73]. STK35, also known as CLP36-interacting kinase 1, was found to be one of the top targets for miR-377. Indeed knockdown of STK35 resulted into a decreased angiogenic potential of ECs [74]. Goyal et al. concluded that VEGF stimulation in ECs increased STK35 expression, so targeting STK35 would have an antagonistic effect to VEGF. Subsequent studies have demonstrated that myocardial tissue, derived via human cardiac biopsies from patients that suffered from heart failure (HF), showed a significant increase in miR-377 expression compared to non-failing control hearts [74]. The transplantation of miR-377 knockdown hCD34+ cells into ischemic myocardium enhanced the proangiogenic capabilities of the tissue, stimulating LV remodeling and reducing cardiac fibrosis [75].

Not all miRNAs relevant to angiogenesis have been validated in cardiac disease models. Other models have been employed to demonstrate the role of miRNAs in angiogenesis in other tissues such as the eye, muscle tissue, or cerebral tissue. These miRs could potentially be used to play a therapeutic role in cardiac tissue with regards to cardiac regeneration.

For example, miR-132/212 was knocked out in mice subjected to hind-limb ischemia. These animals displayed slower recovery compared to wild-type animals. These results were validated *in vitro* in a human umbilical vein endothelial cell (HUVEC)/pericyte co-culture by transfection of miR-132 and miR-212i. Addition of these miRs resulted in improved tubule formation, additional junctions, and longer tubule length, whereas inhibiting these miRs resulted in the opposite. By directly inhibiting SPRED1 and RASA1, miR 132/212 modulates the Ras-MAP-kinase pathway and promotes arteriogenesis [76]. MiR-214 has been proven to have an influence on developmental angiogenesis *in vivo* and *in vitro*, as well as in adult angiogenesis of mice. Specifically, van Mil et al. [77] demonstrated that miR-214 directly targets Quaking (QKI), a protein instrumental for vascular development. QKI transcript levels were up-regulated in various tissues of mice transfected with antagomiR-214, and QKI knockdown by siRNA as well as miR-214 over-expression demonstrated abnormal vascular sprouting, confirming its importance on vascular formation. Additionally, the role of miR-214 on developmental angiogenesis was shown as antagomir-mediated miR-214 knockdown enhanced mouse retinal developmental angiogenesis. Mechanistic studies indicated that by silencing miR-214, more potent pro-angiogenic growth factors, such as VEGF-A, were secreted and the pro-angiogenic activity of EC-derived conditioned medium was increased, introducing a new pathway to possibly improve therapeutic vascular growth [77].

Established in the study above as well, miRNA influence on VEGF is a determining factor towards the neovascularization of respective tissues. A study by He et al. [78] demonstrated the regulatory function miR-150 has on post-stroke cerebral ischemia in rats via its interaction with VEGF. Through the upregulation of miR-150, the study resulted into decreased levels of vascular density of near-infarcted zones of the brain after middle cerebral artery occlusion. Additionally, miR-150 was seen to counter-effect tube formation, proliferation and migration of brain microvascular endothelial cells. All these results could be linked to the interaction of miR-150 and VEGF, leading to reduced expression. Using a dual-luciferase assay, VEGF was determined to be a direct target of miR-150 [78].

The aforementioned miRNAs play crucial roles in neovascularization and are consequently potential opportunities for therapy. Naturally, expression of miRNAs can be controlled by lncRNAs as illustrated in the subchapter on cardiomyocyte proliferation. Several lncRNAs have been identified to play a role in regulating neovascularization. These are highlighted in the next section.

LncRNA

LncRNAs have been established as regulators of various mechanisms involving neovascularization. This group of lncRNAs is also known as “Angio-lncRs” [14]. Due to the relative novelty of lncRNAs, lncRNAs that have not been directly validated in cardiac disease models are included in this part if the mechanism plays a role in neovascularization and has the potential to be relevant for cardiac regeneration.

The interplay between previously introduced miR-150 and the lncRNA MIAT was demonstrated with regards to their role in cardiac neovascularization [79]. In cardiac as well as in retinal cells, MIAT functions as a reliever to miR-150-5p repression of the pro-angiogenic growth factor VEGF. By functioning as a sponge to miR-150, it has proven to enhance cardiac hypertrophy in rat derived heart H9c2 cells. MIAT can therefore be labelled as a competitive endogenous RNA. Knockdown of MIAT results in depleted levels of vascular forming networks that result from reduced TNF- α and VEGF. Taken together, this study showed that MIAT functions as an inducer of in pathological angiogenesis [14,79].

In vivo genetic deletion of MALAT1 as well as pharmacological inhibition of MALAT1 reduced vascular growth, indicating its significance in neovascularization. Using a genetic ablation mouse model, Michalik et al. [80] determined that the lack of MALAT1 resulted in lower neonatal retina vascularization and delayed vessel extension, as opposed to wild-type mice from the same litter. Furthermore, pharmacologically inhibiting MALAT1 with GapmeRs in a hind limb ischemia mouse model hampered blood flow recovery and reduced capillary density. MALAT1 controls the transition between proliferative and migratory

phenotypes of ECs, and its silencing through small interfering RNA (siRNA) resulted in the reduction of the number of proliferating ECs. Zhang et al. [81] additionally conducted RNA-immunoprecipitation experiments. These tests demonstrated how MALAT1 has an immediate effect on vascular endothelial growth factor receptor 2 (VEGFR2) to facilitate angiogenesis, indicating that MALAT1 controls intrinsic angiogenesis through direct regulation of VEGFR2. The silencing of MALAT1 reduced tube formation, proliferation as well as cell migration in skeletal muscle microvascular endothelial cell [80,81]. Even though the aforementioned experiments employed the hind limb ischemia model, the results are relevant for cardiac endothelial cells that are in similar pathological remodeling conditions [62].

The lncRNA named MANTIS also affects angiogenesis [82,83]. In particular HUVECs were used in a Matrigel angiogenesis assay in mice. CRISPR/Cas9-facilitated knockout of MANTIS, or silencing through siRNAs or GapmeRs, decreased angiogenic sprouting and tube formation. MANTIS was discovered to target the endothelial genes SOX18, SMAD6, and COUP-TFII, all important pro-angiogenic genes. Silencing of MANTIS using GapmeRs and siRNAs resulted in decreased protein expression of SOX18, SMAD6, and COUP-TFII in coronary artery smooth muscle cells, human aortic smooth muscle cells, and in human aortic ECs. Furthermore, depression of any of these three proteins in a spheroid outgrowth assay resulted in poor endothelial sprouting. MANTIS was found to interact with BRG1, part of an ATP-dependent transcription activator family of proteins [82,83]. MANTIS increases ATP-ase activity of BRG1 by acting as a promoter for BAF155, a subunit of the complex. The BRG1 protein family regulates the alteration and remodeling of the chromatin structure of the genes it acts on, namely SOX18, SMAD6, and COUP-TFII in this particular example. MANTIS can therefore be seen as a promoter of angiogenesis by stimulating transcription of these genes. Leisegang et al. concluded from their data that a decrease in MANTIS levels reduced the endothelial angiogenic function *ex vivo* as well as *in vivo*, opening more doors for the relatively unknown domain of lncRNA influence on angiogenic functions [82].

An antisense lncRNA named PUNISHER was found to have a large effect on neovascularization, as its inhibition led to severe vascular defects with problematic branching and decreased vessel formation [83]. These observations were made with the help of human pluripotent stem cell differentiation models. In zebrafish, PUNISHER supports and maintains EC function, yet its particular mechanism is still unknown.

In addition, knockdown of the lncRNA ALIEN resulted into observed down-regulation of 503 genes that contributed to angiogenesis and blood vessel development [83,84].

ncRNA	Target	Effect on neovascularisation	Species	Reference
miR-24	PAK4, GATA2	Positive	Zebrafish	Fiedler 2011, Meloni 2013 [69,70]
miR-26a	SMAD1	Negative	Mice	Icli 2013 [73]
miR-92a	nMKK4, KLF4	Negative	Mice, Pigs	Bonauer 2009, Hinkel 2013 [67,68]
miR-126	SPRED1, PI3K/Akt	Negative	Mice	Wang 2008 [71]
miR-132/212	SPRED1, RASA1	Positive	Mice	Lei 2015 [77]
miR-150	VEGF	Negative	Rat	He 2016 [79]
miR-210	Ptp1b, Efna3	Negative	Mice	Hu 2010, Arif 2017, Fan 2018 [64,65,66]
miR-214	QKI	Positive	Mice	van Mil 2012 [78]
miR-377	STK35	Positive	Rat	Wen 2014, Fan 2018 [74,66]
ALIEN	503 unspecified genes	Negative		Kurian 2015, Gomes 2017 [85,86]
MALAT1	VEGFR2	Positive	Mice	Michalik 2014, Zhang 2018 [81,82]
MANTIS	BRG1, SOX18, SMAD, COUP-TFII	Positive	Mice	Leisegang 2017 [83]
MIAT	miR-150	Negative	Rat cell (<i>in vitro</i>)	Yan 2015 [80]
PUNISHER	Unknown	Positive	Zebrafish	Kurian 2015 [85]

Table 2 - Overview of identified non-coding ribonucleic acids validated *in vivo* for their role in neovascularization.

DISCUSSION

This chapter outlines various non-coding RNAs, their targets, and their effects on cardiac regeneration. By focusing on cardiomyocyte proliferation and cardiac neovascularization as hallmarks of regeneration, research involving the inhibition or enhanced expression of certain non-coding RNAs that resulted in significant alterations in the regenerative abilities of the heart was used to highlight the role non-coding RNAs can play in cardiac regeneration. These results open doors for new research into potential therapeutics based on the influence of non-coding RNAs on cellular pathways.

For non-coding RNAs to be used clinically several challenges have to be overcome and several requirements have to be met. The non-coding RNAs need to be stable, specific, and with high binding affinity, and they need to be delivered efficiently to the target tissue. Modification of non-coding RNAs to improve stability, specificity, and uptake, as well as delivery strategies are reviewed elsewhere [86,87,88,89]. Briefly, non-coding RNAs are modified with chemical modifications, such as 2' sugar modifications, locked nucleic acids, or phosphodiester and phosphorothioate linkages, to improve stability, specificity, and uptake. Delivery strategies

include (biodegradable) biomaterials, lipid-based vehicles, viruses, exosomes, nanoparticles, microbubbles, and (cationic) polymeric drug delivery devices [90,91]. Their advantages include small size, stability, reduced degradation, improved uptake, and specificity. Local delivery may be facilitated by targeting ligands or localized injections. These strategies need to be investigated in models that allow for inclusion of delivery and surgical practices akin to surgery in humans, and that adequately resemble human pathophysiology. Additional to delivery, bio-distribution and pharmacokinetics/pharmacodynamics of these delivery vehicles need to be characterized. Furthermore, modulation of expression by non-coding RNAs can have profound effects in both the short and the long term. Their targets not only have to be identified and validated in short-term studies, the effect of non-coding RNA modulation also has to be assessed in long-term *in vivo* studies. As illustrated by Tian et al. and Gabisonia et al. [40,43], persistent and uncontrolled expression can result in death. Besides these short and long-term effects, off-target effects have to be identified and investigated, for non-coding RNAs can have multiple targets. Only after these rigorous tests have been performed to a satisfactory level, the safety and efficacy of ncRNA therapeutics can be assessed in humans [92,43]. Therefore, to bring non-coding RNA therapeutics one step closer to clinical applications, research needs to move forward into more representative models of human disease that encompass all aspects of treatment.

ACKNOWLEDGEMENTS

This work was funded by the Netherlands CardioVascular Research Initiative (CVON: The Dutch Heart Foundation, Dutch Federation of University Medical Centers, the Netherlands Organization for Health Research and Development, and the Royal Netherlands Academy of Science) and Vrienden UMC Utrecht (C.V., J.S.); an unrestricted grant from CELLINK to Vrienden UMC Utrecht (C.V., J.S.).

REFERENCES

1. Benjamin, E.J. Muntner, P. Alonso, A. Bittencourt, M.S. Callaway, C.W. Carson, A.P. Chamberlain, A.M. Chang, A.R. Cheng, S. Das, S.R. Delling, F.N. Djousse, L. Elkind, M.S.V. Ferguson, J.F. Fornage, M. Jordan, L.C. Khan, S.S. Kissela, B.M. Knutson, K.L. Kwan, T.W. Lackland, D.T. Lewis, T.T. Lichtman, J.H. Longenecker, C.T. Loop, M.S. Lutsey, P.L. Martin, S.S. Matsushita, K. Moran, A.E. Mussolino, M.E. O'Flaherty, M. Pandey, A. Perak, A.M. Rosamond, W.D. Roth, G.A. Sampson, U.K.A. Satou, G.M. Schroeder, E.B. Shah, S.H. Spartano, N.L. Stokes, A. Tirschwell, D.L. Tsao, C.W. Turakhia, M.P. VanWagner, L.B. Wilkins, J.T. Wong, S.S. Virani, S. S (2019) American Heart Association Council on Epidemiology and Prevention Statistics Committee and Stroke Statistics Subcommittee. Heart disease and stroke statistics-2019 update: a report from the American Heart Association. *Circulation* 139 (10): e56-e528. [PubMed] [CrossRef] [Google Scholar]
2. Bergmann O, Bhardwaj RD, Bernard S, Zdunek S, Barnabé-Heider F, Walsh S, Zupicich J, Alkass K, Buchholz BA, Druid H, Jovinge S, Frisén J. Evidence for cardiomyocyte renewal in humans. *Science*. 2009;324(5923):98–102. [PubMed] [PubMedCentral] [CrossRef] [Google Scholar]
3. Orlic D, Kajstura J, Chimenti S, Jakoniuk I, Anderson SM, Li B, Pickel J, McKay R, Nadal-Ginard B, Bodine DM, Leri A, Anversa P. Bone marrow cells regenerate infarcted myocardium. *Nature*. 2001;410(6829):701–5. [PubMed] [CrossRef] [Google Scholar]
4. Balsam LB, Wagers AJ, Christensen JL, Kofidis T, Weissman IL, Robbins RC. Haematopoietic stem cells adopt mature haematopoietic fates in ischaemic myocardium. *Nature*. 2004;428(6983):668–73. [PubMed] [CrossRef] [Google Scholar]
5. Murry CE, Soonpaa MH, Reinecke H, Nakajima H, Nakajima HO, Rubart M, Pasumarthi KB, Virag JI, Bartelmez SH, Poppa V, Bradford G, Dowell JD, Williams DA, Field LJ. Haematopoietic stem cells do not transdifferentiate into cardiac myocytes in myocardial infarcts. *Nature*. 2004;428:664–8. [PubMed] [CrossRef] [Google Scholar]
6. Beltrami AP, Barlucchi L, Torella D, Baker M, Limana F, Chimenti S, Kasahara H, Rota M, Musso E, Urbaneck K, Leri A, Kajstura J, Nadal-Ginard B, Anversa P. Adult cardiac stem cells are multipotent and support myocardial regeneration. *Cell*. 2003;114(6):763–76. [PubMed] [CrossRef] [Google Scholar]
7. Zwetsloot PP, Végh AM, Jansen of Lorkeers SJ, van Hout GP, Currie GL, Sena ES, Gremmels H, Buikema JW, Goumans MJ, Macleod MR, Doevendans PA, Chamuleau SA, Sluijter JP. Cardiac stem cell treatment in myocardial infarction: a systematic review and meta-analysis of preclinical studies. *Circ Res*. 2016;118(8):1223–32. [PubMed] [CrossRef] [Google Scholar]
8. van Berlo JH, Kanisicak O, Mailliet M, Vagnozzi RJ, Karch J, Lin SC, Middleton RC, Marbán E, Molkentin JD. c-kit+ cells minimally contribute cardiomyocytes to the heart. *Nature*. 2014;509(7500):337–41. [PubMed] [PubMedCentral] [CrossRef] [Google Scholar]
9. Sultana N, Zhang L, Yan J, Chen J, Cai W, Razzaque S, Jeong D, Sheng W, Bu L, Xu M, Huang GY, Hajjar RJ, Zhou B, Moon A, Cai CL. Resident c-kit(+) cells in the heart are not cardiac stem cells. *Nat Commun*. 2015;6:8701. [PubMed] [PubMedCentral] [CrossRef] [Google Scholar]
10. van Berlo JH, Molkentin JD. Most of the dust has settled: cKit+ progenitor cells are an irrelevant source of cardiac myocytes *in vivo*. *Circ Res*. 2016;118(1):17–9. [PubMed] [PubMedCentral] [CrossRef] [Google Scholar]
11. Kretzschmar K, Post Y, Bannier-Hélaouët M, Mattiotti A, Drost J, Basak O, Li VSW, van den Born M, Gunst QD, Versteeg D, Kooijman L, van der Elst S, van Es JH, van Rooij E, van den Hoff MJB, Clevers H. Profiling proliferative cells and their progeny in damaged murine hearts. *Proc Natl Acad Sci*. 2018;115(52):E12245–54. [PubMed] [CrossRef] [Google Scholar]
12. Li Y, He L, Huang X, Bhaloo SI, Zhao H, Zhang S, Pu W, Tian X, Li Y, Liu Q, Yu W, Zhang L, Liu X, Liu K, Tang J, Zhang H, Cai D, Ralf AH, Xu Q, Lui KO, Zhou B. Genetic lineage tracing of nonmyocyte population by dual recombinases. *Circulation*. 2018;138(8):793–805. [CrossRef] [Google Scholar]
13. Bergmann O. Clearing up the mist: cardiomyocyte renewal in human hearts. *Eur Heart J*. 2019;40(13):1037–8. [PubMed] [CrossRef] [Google Scholar]

14. Yu B, Wang S. *Angio-LncRNs: LncRNAs that regulate angiogenesis and vascular disease*. *Theranostics*. 2018;8(13):3654–75. [PubMed] [PubMedCentral] [CrossRef] [Google Scholar]
15. Folkman J. *Tumor angiogenesis*. *Adv Cancer Res*. 1985;43:175–203. [PubMed] [CrossRef] [Google Scholar]
16. Tabibiazar R, Rockson SG. *Angiogenesis and the ischaemic heart*. *Eur Heart J*. 2001;22(11):903–18. [PubMed] [CrossRef] [Google Scholar]
17. Lepilina A, Coon AN, Kikuchi K, Holdway JE, Roberts RW, Burns CG, Poss KDA. *Dynamic epicardial injury response supports progenitor cell activity during zebrafish heart regeneration*. *Cell*. 2006;127(3):607–19. [PubMed] [CrossRef] [Google Scholar]
18. Poss KD, Wilson LG, Keating MT. *Heart regeneration in zebrafish*. *Science*. 2002;298(5601):2188–90. [PubMed] [CrossRef] [Google Scholar]
19. Kikuchi K, Poss KD. *Cardiac regenerative capacity and mechanisms*. *Annu Rev Cell Dev Biol*. 2012;28(1):719–41. [PubMed] [PubMedCentral] [CrossRef] [Google Scholar]
20. Jopling C, Sleep E, Raya M, Martí M, Raya A, Izpisua Belmonte JC. *Zebrafish heart regeneration occurs by cardiomyocyte dedifferentiation and proliferation*. *Nature*. 2010;464(7288):606–9. [PubMed] [PubMedCentral] [CrossRef] [Google Scholar]
21. Kikuchi K, Holdway JE, Werdich AA, Anderson RM, Fang Y, Egnaczyk GF, Evans T, MacRae CA, Stainier DYR, Poss KD. *Primary contribution to zebrafish heart regeneration by gata4+ cardiomyocytes*. *Nature*. 2010;464(7288):601–5. [PubMed] [PubMedCentral] [CrossRef] [Google Scholar]
22. Witman N, Murtuza B, Davis B, Arner A, Morrison JI. *Recapitulation of developmental cardiogenesis governs the morphological and functional regeneration of adult newt hearts following injury*. *Dev Biol*. 2011;354(1):67–76. [PubMed] [CrossRef] [Google Scholar]
23. Laube F, Heister M, Scholz C, Borchardt T, Braun T. *Re-programming of newt cardiomyocytes is induced by tissue regeneration*. *J Cell Sci*. 2006;119(22):4719–29. [PubMed] [CrossRef] [Google Scholar]
24. Wang WE, Li L, Xia X, Fu W, Liao Q, Lan C, Yang D, Chen H, Yue R, Zeng C, Zhou L, Zhou B, Duan DD, Chen X, Houser SR, Zeng C. *Dedifferentiation, proliferation, and redifferentiation of adult mammalian cardiomyocytes after ischemic injury*. *Circulation*. 2017;136(9):834–48. [PubMed] [PubMedCentral] [CrossRef] [Google Scholar]
25. Yutzey K. *Cardiomyocyte proliferation: teaching an old dogma new tricks*. *Circ Res*. 2017;120:627–9. [PubMed] [PubMedCentral] [CrossRef] [Google Scholar]
26. Drenkhahn J-D, Schwarz QP, Gray S, Laskowski A, Kiriazis H, Ming Z, Harvey RP, Du X-J, Thorburn DR, Cox TC. *Compensatory growth of healthy cardiac cells in the presence of diseased cells restores tissue homeostasis during heart development*. *Dev Cell*. 2008;15(4):521–33. [PubMed] [CrossRef] [Google Scholar]
27. Haubner BJ, Adamowicz-Brice M, Khadayate S, Tiefenthaler V, Metzler B, Aitman T, Penninger JM. *Complete cardiac regeneration in a mouse model of myocardial infarction*. *Aging*. 2012;4(12):966–77. [PubMed] [PubMedCentral] [CrossRef] [Google Scholar]
28. Porrello ER, Mahmoud AI, Simpson E, Hill JA, Richardson JA, Olson EN, Sadek HA. *Transient regenerative potential of the neonatal mouse heart*. *Science*. 2011;331(6020):1078–80. [PubMed] [PubMedCentral] [CrossRef] [Google Scholar]
29. Jesty SA, Steffey MA, Lee FK, Breitbart M, Hesse M, Reining S, Lee JC, Doran RM, Nikitin AY, Fleischmann BL, Kotlikoff MI. *c-kit+ precursors support postinfarction myogenesis in the neonatal, but not adult, heart*. *Proc Natl Acad Sci*. 2012;109(33):13380–5. [PubMed] [CrossRef] [Google Scholar]
30. Strungs, E.G. Ongstad, E.L. O’Quinn, M.P. Palatinus, J.A. Jourdan, L.J. Gourdie, R.G (2013) *Cryoinjury models of the adult and neonatal mouse heart for studies of scarring and regeneration*. *Methods Mol Biol* 1037:343–353. [PubMed] [CrossRef] [Google Scholar]
31. Bryant, D.M. O’Meara, C.C. Ho, N.N. Gannon, J. Cai, L. Lee, R.T (2015) *A systematic analysis of neonatal mouse heart regeneration after apical resection*. *J Mol Cell Cardiol* 79:315–318. [PubMed] [CrossRef] [Google Scholar]
32. Haubner BJ, Schneider J, Schweigmann U, Schuetz T, Dichtl W, Velik-Salchner C, Stein JI, Penninger JM. *Functional recovery of a human neonatal heart after severe myocardial infarction*. *Circ Res*. 2016;118(2):16–221. [CrossRef] [Google Scholar]

33. Ahuja P, Sdek P, MacLellan WR. Cardiac myocyte cell cycle control in development, disease, and regeneration. *Physiol Rev.* 2007;87(2):521–44. [PubMed] [PubMedCentral] [CrossRef] [Google Scholar]
34. van Amerongen MJ, Engel FB. Features of CM proliferation and its potential for cardiac regeneration. *J Cell Mol Med.* 2008;12:2233–44. [PubMed] [PubMedCentral] [CrossRef] [Google Scholar]
35. Bicknell KA, Coxon CH, Brooks G. Can the CM cell cycle be reprogrammed? *J Mol Cell Cardiol.* 2007;42(4):706–21. [PubMed] [CrossRef] [Google Scholar]
36. Muthuramu I, Lox M, Jacobs F, De Geest B. Permanent ligation of the left anterior descending coronary artery in mice: a model of post-myocardial infarction remodeling and heart failure. *J Vis Exp.* 2014;94 [Google Scholar]
37. Aguirre A, Montserrat N, Zacchigna S, Nivet E, Hishida T, Krause MN, Kurian L, Ocampo A, Vazquez-Ferrer E, Rodriguez-Esteban C, Kumar S, Moresco JJ, Yates JR III, Campistol JM, Sancho-Martinez I, Giacca M, Izpisua Belmonte JC. In vivo activation of a conserved microRNA program induces mammalian heart regeneration. *Cell Stem Cell.* 2014;15(5):589–604. [PubMed] [PubMedCentral] [CrossRef] [Google Scholar]
38. Huang W, Feng Y, Liang J, Yu H, Wang C, Wang B, Wang M, Jiang L, Meng W, Cai W, Medvedovic M, Chen J, Paul C, Davidson WS, Sadayappan S, Stambrook P, Yu X, Wang Y. Loss of microRNA-128 promotes cardiomyocyte proliferation and heart regeneration. *Nat Commun.* 2018;9(1):700. [PubMed] [PubMedCentral] [CrossRef] [Google Scholar]
39. Yang Y, Cheng HW, Qiu Y, Dupee D, Noonan M, Lin YD, Fisch S, Unno K, Sereti KI, Liao R. MicroRNA-34a plays a key role in cardiac repair and regeneration following myocardial infarction. *Circ Res.* 2015;117(5):450–9. [PubMed] [PubMedCentral] [CrossRef] [Google Scholar]
40. Tian Y, Liu Y, Wang T, Zhou N, Kong J, Chen L, Snitow M, Morley M, Li D, Petrenko N, Zhou S, Lu M, Gao E, Koch WJ, Stewart KM, Morrisey EE. A microRNA-Hippo pathway that promotes cardiomyocyte proliferation and cardiac regeneration in mice. *Sci Transl Med.* 2015;7(279):279–89. [CrossRef] [Google Scholar]
41. Wang LL, Liu Y, Chung JJ, Wang T, Gaffey AC, Lu M, Cavanaugh CA, Zhou S, Kanade R, Atluri P, Morrisey EE, Burdick J. Sustained miRNA delivery from an injectable hydrogel promotes cardiomyocyte proliferation and functional regeneration after ischaemic injury. *Nat Biomed Eng.* 2017;1(12):983–92. [PubMed] [PubMedCentral] [CrossRef] [Google Scholar]
42. Eulalio A, Mano M, Dal Ferro M, Zentilin L, Sinagra G, Zacchigna S, Giacca M. Functional screening identifies miRNAs inducing cardiac regeneration. *Nature.* 2012;492(7429):376–81. [PubMed] [CrossRef] [PubMedCentral] [Google Scholar]
43. Gabisonia K, Prosdocimo G, Aquaro GD, Carlucci L, Zentilin L, Secco I, Ali H, Braga L, Gorgodze N, Bernini F, Burchielli S, Collesi C, Zandonà L, Sinagra G, Piacenti M, Zacchigna S, Bussani R, Recchia FA, Giacca M. MicroRNA therapy stimulates uncontrolled cardiac repair after myocardial infarction in pigs. *Nature.* 2019;569(7756):418. [PubMed] [PubMedCentral] [CrossRef] [Google Scholar]
44. orrello ER, Mahmoud AI, Simpson E, Johnson BA, Grinsfelder D, Canseco D, Mammen PP, Rothmel BA, Olson EN, Sadek HA. Regulation of neonatal and adult mammalian heart regeneration by the miR-15 family. *Proc Natl Acad Sci.* 2013;110(1):187–92. [PubMed] [CrossRef] [PubMedCentral] [Google Scholar]
45. Porrello ER, Johnson BA, Aurora AB, Simpson E, Nam YJ, Matkovich SJ, Dorn GW 2nd, van Rooij E, Olson EN. MiR-15 family regulates postnatal mitotic arrest of cardiomyocytes. *Circ Res.* 2011;109(6):670–9. [PubMed] [PubMedCentral] [CrossRef] [Google Scholar]
46. Zhao Y, Ransom J, Li A, von Vedantham C, Drehle M, Muth AN, Tsuchihashi T, McManus MT, Schwartz RJ, Srivastava D. Dysregulation of cardiogenesis, cardiac conduction, and cell cycle in mice lacking miRNA-1-2. *Cell.* 2007;129(2):303–17. [PubMed] [CrossRef] [PubMedCentral] [Google Scholar]
47. Liu N, Bezprozvannaya S, Williams AH, Qi X, Richardson JA, Bassel-Duby R, Olson EN. MicroRNA-133a regulates cardiomyocyte proliferation and suppresses smooth muscle gene expression in the heart. *Genes Dev.* 2008;22(23):3242–54. [PubMed] [PubMedCentral] [CrossRef] [Google Scholar]
48. Chen J, Huang ZP, Seok HY, Ding J, Kataoka M, Zhang Z, Hu X, Wang G, Lin Z, Wang S, Pu WT, Liao R, Wang DZ. mir-17-92 cluster is required for and sufficient to induce cardiomyocyte proliferation in postnatal and adult hearts. *Circ Res.* 2013;112(12):1557–66. [PubMed] [PubMedCentral] [CrossRef] [Google Scholar]

49. Xiao J, Liu H, Cretoiu D, Toader DO, Suci N, Shi J, Shen S, Bei Y, Sluijter JP, Das S, Kong X, Li X. miR-31a-5p promotes postnatal cardiomyocyte proliferation by targeting RhoBTB1. *Exp Mol Med*. 2017;49(10):e386. [PubMed] [PubMedCentral] [CrossRef] [Google Scholar]
50. Chen Y, Li X, Li B, Wang H, Li M, Huang S, Sun Y, Chen G, Si X, Huang C, Liao W, Liao Y, Bin J. Long non-coding RNA ECRAR triggers post-natal myocardial regeneration by activating ERK1/2 signaling. *Mol Ther*. 2019;27(1):29–45. [PubMed] [CrossRef] [Google Scholar]
51. See K, Tan WLW, Lim EH, Tiang Z, Lee LT, Li PYQ, Luu TDA, Ackers-Johnson M, Foo RS. Single cardiomyocyte nuclear transcriptomes reveal a lincRNA-regulated de-differentiation and cell cycle stress-response *in vivo*. *Nat Commun*. 2017;8(1):225. [PubMed] [PubMedCentral] [CrossRef] [Google Scholar]
52. Coccia EM, et al. Regulation and expression of a growth arrest-specific gene (gas5) during growth, differentiation, and development. *Mol Cell Biol*. 1992;12(8):3514–21. [PubMed] [PubMedCentral] [CrossRef] [Google Scholar]
53. Mourtada-Maarabouni M, Pickard MR, Hedge VL, Farzaneh F, Williams GT. GAS5, a non-protein-coding RNA, controls apoptosis and is downregulated in breast cancer. *Oncogene*. 2009;28(2):195–208. [PubMed] [CrossRef] [Google Scholar]
54. Yin D. Long noncoding RNA GAS5 affects cell proliferation and predicts a poor prognosis in patients with colorectal cancer. *Med Oncol*. 2014;31(11):253. [PubMed] [CrossRef] [Google Scholar]
55. Cai B, Ma W, Ding F, Zhang L, Huang Q, Wang X, Hua B, Xu J, Li J, Bi C, Guo S, Yang F, Han Z, Li Y, Yan G, Yu Y, Bao Z, Yu M, Li F, Tian Y, Pan Z, Yang B. The long noncoding RNA CAREL controls cardiac regeneration. *J Am Coll Cardiol*. 2018;72(5):534–50. [PubMed] [CrossRef] [Google Scholar]
56. Wu M, Zhang S, Chen X, Xu H, Li X. Expression and function of lncRNA MALAT-1 in the embryonic development of zebrafish. *Gene*. 2019;680:65–71. [PubMed] [CrossRef] [Google Scholar]
57. Li B, Hu Y, Li X, Jin G, Chen X, Chen G, Chen Y, Huang S, Liao W, Liao Y, Teng Z, Bin J. Sirt1 antisense long noncoding RNA promotes cardiomyocyte proliferation by enhancing the stability of Sirt1. *J Am Heart Assoc*. 2018;7(21) [Google Scholar]
58. Wang J, Chen X, Shen D, Ge D, Chen J, Pei J, Li Y, Yue Z, Feng J, Chu M, Nie Y. A long non-coding RNA NR_045363 controls cardiomyocyte proliferation and cardiac repair. *J Mol Cell Cardiol*. 2019;127:105–14. [PubMed] [CrossRef] [Google Scholar]
59. Chen G, Li H, Li X, Li B, Zhong L, Huang S, Zheng H, Li M, Jin G, Liao W, Liao Y, Chen Y, Bin J. Loss of long non-coding RNA CRRL promotes cardiomyocyte regeneration and improves cardiac repair by functioning as a competing endogenous RNA. *J Mol Cell Cardiol*. 2018;122:152–64. [PubMed] [CrossRef] [Google Scholar]
60. Adair TH, Montani JP. *Angiogenesis*. San Rafael (CA): Morgan & Claypool Life Sciences Chapter 1, overview of angiogenesis; 2010. [Google Scholar]
61. Choong OK, Lee DS, Chen CY, Hsieh P. The roles of non-coding RNAs in cardiac regenerative medicine. *Non-coding RNA Research*. 2017;2(2):100–10. [PubMed] [PubMedCentral] [CrossRef] [Google Scholar]
62. Juni R, Abreu R, da Costa Martins P. Regulation of microvascularization in heart failure – an endothelial cell, non-coding RNAs and exosome liaison. *Non-coding RNA Research*. 2017;2(1):45–55. [PubMed] [PubMedCentral] [CrossRef] [Google Scholar]
63. Hu S, Huang M, Li Z, Jia F, Ghosh Z, Lijkwan MA, Fasanaro P, Sun N, Wang X, Martelli F, Robbins RC, Wu JC. MicroRNA-210 as a novel therapy for treatment of ischemic heart disease. *Circulation*. 2010;122(11 Suppl):S124–31. [PubMed] [PubMedCentral] [CrossRef] [Google Scholar]
64. Arif M, Pandey R, Alam P, Jiang S, Sadayappan S, Paul A, Ahmed R. MicroRNA-210-mediated proliferation, survival, and angiogenesis promote cardiac repair post myocardial infarction in rodents. *J Mol Med (Berl)*. 2017;95(12):1369–85. [CrossRef] [Google Scholar]
65. Fan ZG, Qu XL, Chu P, Gao YL, Gao XF, Chen SL, Tian NL. MicroRNA-210 promotes angiogenesis in acute myocardial infarction. *Mol Med Rep*. 2018;17(4):5658–65. [PubMed] [PubMedCentral] [Google Scholar]
66. Bonauer A, Carmona G, Iwasaki M, Mione M, Koyanagi M, Fischer A, Burchfield J, Fox H, Doebele C, Ohtani K, et al. MicroRNA-92a controls angiogenesis and functional recovery of ischemic tissues in mice. *Science*. 2009;324(5935):1710–3. [PubMed] [CrossRef] [Google Scholar]

67. Hinkel R, Penzkofer D, Zahlke S, Fischer A, Husada W, Xu QF, Baloch E, Van Rooij E, Zeiher AM, Kupatt C, et al. Inhibition of microRNA-92a protects against ischemia/reperfusion injury in a large-animal model. *Circulation*. 2013;128(10):1066–75. [PubMed] [CrossRef] [Google Scholar]
68. Fiedler J, Jazbutyte V, Kirchmaier BC, Gupta SK, Lorenzen J, Hartmann D, Galuppo P, Kneitz S, Pena JTG, Sohn-Lee C. MicroRNA-24 regulates vascularity after myocardial infarction. *Circulation*. 2011;124(6):720–30. [PubMed] [CrossRef] [Google Scholar]
69. Meloni M, Marchetti M, Garner K, Littlejohns B, Sala-Newby G, Xenophontos N, Floris I, Suleiman MS, Madeddu P, Caporali A, Emanuelli C. Local inhibition of microRNA-24 improves reparative angiogenesis and left ventricle remodeling and function in mice with myocardial infarction. *Mol Ther*. 2013;21(7):1390–402. [PubMed] [PubMedCentral] [CrossRef] [Google Scholar]
70. Qian L, Van Laake LW, Huang Y, Liu S, Wendland MF, Srivastava D. miR-24 inhibits apoptosis and represses Bim in mouse cardiomyocytes. *J Exp Med*. 2011;208(3):549–60. [PubMed] [PubMedCentral] [CrossRef] [Google Scholar]
71. Wang S, Aurora AB, Johnson BA, Qi X, Mcanally J, Hill JA, Richardson JA, Bassel-duby R, Olson EN, Hill A, et al. The endothelial-specific MicroRNA miR-126 governs vascular integrity and angiogenesis. *Dev Cell*. 2008;15(2):261–71. [PubMed] [PubMedCentral] [CrossRef] [Google Scholar]
72. Icli B, Wara AKM, Moslehi J, Sun X, Plovie E, Cahill M, Marchin JF, Schissler A, Padera RF, Shi J, et al. MicroRNA-26a regulates pathological and physiological angiogenesis by targeting BMP/SMAD1 signaling. *Circ Res*. 2013;113(11):1231–41. [PubMed] [PubMedCentral] [CrossRef] [Google Scholar]
73. Wen Z, Huang W, Feng Y, et al. MicroRNA-377 regulates mesenchymal stem cell-induced angiogenesis in ischemic hearts by targeting VEGF. *PLoS One*. 2014;9(9):e104666. [PubMed] [PubMedCentral] [CrossRef] [Google Scholar]
74. Goyal A, Behring A, Kumar A, Siess W. STK35L1 associates with nuclear actin and regulates cell cycle and migration of endothelial cells. *PLoS One*. 2011;6(1):E16249. [PubMed] [PubMedCentral] [CrossRef] [Google Scholar]
75. Joladarashi D, Garikipati VNS, Thandavarayan RA, et al. Enhanced cardiac regenerative ability of stem cells after ischemia-reperfusion injury: role of human CD34+ cells deficient in microRNA-377. *J Am Coll Cardiol*. 2015;66(20):2214–26. [PubMed] [PubMedCentral] [CrossRef] [Google Scholar]
76. Lei Z, van Mil A, Brandt MM, Grundmann S, Hoefler I, Smits M, El Azzouzi H, Fukao T, Cheng C, Doevendans PA, Sluijter JP. MicroRNA-132/212 family enhances arteriogenesis after hindlimb ischemia through modulation of the Ras-MAPK pathway. *J Cell Mol Med*. 2015;19(8):1994–2005. [PubMed] [PubMedCentral] [CrossRef] [Google Scholar]
77. van Mil A, Grundmann S, Goumans M, Lei Z, Oerlemans M, Jaksani S, Doevendans P, Sluijter J. MicroRNA-214 inhibits angiogenesis by targeting quaking and reducing angiogenic growth factor release. *Cardiovasc Res*. 2012;93(4):655–65. [PubMed] [CrossRef] [Google Scholar]
78. He Q, Li Q, Jin H, Zhi F, Suraj B, Zhu Y, Xia Y, Mao L, Chen X, Hu B. MiR-150 regulates poststroke cerebral angiogenesis via vascular endothelial growth factor in rats. *CNS Neurosci Ther*. 2016;22(6):507–17. [PubMed] [PubMedCentral] [CrossRef] [Google Scholar]
79. Yan B, Yao J, Liu JY. IncRNA-MIAT regulates microvascular dysfunction by functioning as a competing endogenous RNA. *Circ Res*. 2015;116(7):1143–56. [PubMed] [CrossRef] [Google Scholar]
80. Michalik KM, You X, Manavski Y. Long noncoding RNA MALAT1 regulates endothelial cell function and vessel growth. *Circ Res*. 2014;114(9):1389–97. [PubMed] [CrossRef] [Google Scholar]
81. Zhang X, Tang X, Hamblin MH, Yin KJ. Lcong non-coding RNA Malat1 regulates angiogenesis in hindlimb ischemia. *Int J Mol Sci*. 2018;19(6):1723. [PubMedCentral] [CrossRef] [PubMed] [Google Scholar]
82. Leisegang MS, Fork C, Josipovic I, Richter FM, Preussner J, Hu J, Miller MJ, Epah J, Hofmann P, Günther S, Moll F, Valasarajan C, Heidler J, Ponomareva Y, Freiman TM, Maegdefessel L, Plate KH, Mittelbronn M, Uchida S, Künne C, Stellos K, Schermuly RT, Weissmann N, Devraj K, Wittig I, Boon RA, Dimmeler S, Pullamsetti SS, Looso M, Miller FJ, Brandes RP. Long noncoding RNA MANTIS facilitates endothelial angiogenic function. *Circulation*. 2017;136(1):65–79. [PubMed] [PubMedCentral] [CrossRef] [Google Scholar]

83. Trotter KW, Archer TK. The BRG1 transcriptional coregulator. *Nucl Recept Signal*. 2008;6(1):e004. [PubMed] [PubMedCentral] [CrossRef] [Google Scholar]
84. Kurian L, Aguirre A, Sancho-Martinez I, Benner C, Hishida T, Nguyen TB, Reddy P, Nivet E, Krause MN, Nelles DA, Esteban CR, Campistol JM, Yeo GW, Belmonte J. Identification of novel long noncoding RNAs underlying vertebrate cardiovascular development. *Circulation*. 2015;131(14):1278–90. [PubMed] [PubMedCentral] [CrossRef] [Google Scholar]
85. Gomes C, Spencer H, Ford K, Michel L, Baker A, Emanuelli C, Balligand J, Devaux Y. The function and therapeutic potential of long non-coding RNAs in cardiovascular development and disease. *Mol Ther Nucleic Acids*. 2017;8:494–507. [PubMed] [PubMedCentral] [CrossRef] [Google Scholar]
86. Lei Z, Sluijter JP, van Mil A. MicroRNA therapeutics for cardiac regeneration. *Mini Rev Med Chem*. 2015;15(6):441–51. [PubMed] [CrossRef] [Google Scholar]
87. Tibbitt MW, Dahlman JE, Langer R. Emerging frontiers in drug delivery. *J Am Chem Soc*. 2016;138(3):704–17. [PubMed] [CrossRef] [Google Scholar]
88. Van der Ven CFT, Wu PJ, Tibbitt MW, van Mil A, Sluijter JPG, Langer R, Aikawa E. *In vitro* 3D model and miRNA drug delivery to target calcific aortic valve disease. *Clin Sci*. 2017;131(3):181–95. [PubMed] [PubMedCentral] [CrossRef] [Google Scholar]
89. Fenton OS, Olafson KN, Pillai PS, Mitchell MJ, Langer R. Advances in biomaterials for drug delivery. *Adv Mater*. 2018;30 [Google Scholar]
90. Kwekkeboom RF, Lei Z, Bogaards SJ, Aiazian E, Kamp O, Paulus WJ, Sluijter JP, Musters RJ. Ultrasound and microbubble-induced local delivery of MicroRNA-based therapeutics. *Ultrasound Med Biol*. 2015;41(1):163–76. [PubMed] [CrossRef] [Google Scholar]
91. Kwekkeboom RF, Sluijter JP, van Middelaar BJ, Metz CH, Brans MA, Kamp O, Paulus WJ, Musters R. Increased local delivery of antagomir therapeutics to the rodent myocardium using ultrasound and microbubbles. *J Control Release*. 2016;222:18–31. [PubMed] [CrossRef] [Google Scholar]
92. Kwekkeboom RF, Lei Z, Doevendans PA, Musters RJ, Sluijter JP. Targeted delivery of miRNA therapeutics for cardiovascular diseases: opportunities and challenges. *Clin Sci (Lond)*. 2014;127(6):351–65. [CrossRef] [Google Scholar]

Chapter 6

Summarizing discussion and future perspectives

DISCUSSION

This thesis shows that advances in biofabrication, bioengineering and biomaterials can be combined to create more representative *in vitro* models of heart valve disease, and to develop novel drug delivery strategies. Clinically relevant human cardiac disease models are essential to comprehend the complex pathobiology and to identify therapeutic targets, as results obtained in animal models do not directly translate to the clinic. Non-coding RNAs hold great potential for cardiovascular regeneration, but novel drug delivery approaches are required to get these RNA therapeutics to specific organs or tissues and to improve therapeutic efficiency. Therefore, the main objective of this thesis was to develop a 3D human aortic valve disease model, and to engineer an injectable hydrogel to deliver non-coding RNA over several days.

Chapter 1 outlined the clinical relevance of novel treatment strategies for aortic valve disease, described the aortic valve (AV) anatomy, reviewed research on microRNAs involved in valve disease pathobiology and efforts in microRNA delivery, and emphasized requirements for *in vitro* valve disease models. Specifically, for *in vitro* models to be representative for calcific aortic valve disease (CAVD) they need to contain cells of human origin and replicate the native valve tri-layered structure and its biomechanical properties.

Part I focused on the development of the first human 3D heart valve disease model. Nano-indentation was used to measure the biomechanical properties of the individual layers of the native AV, which were replicated in the model by fine-tuning the concentration, ratio, and cross-linking parameters of biopolymers used to mimic the AV extracellular matrix (ECM). Non-diseased aortic valve interstitial cells (VIC) were mixed with these gelatin- and hyaluronic acid-based biopolymers and printed with a bioprinter to create 3D constructs with the same mechanical properties as the native valve. The cells inside the constructs were exposed to osteogenic factors to mimic disease progression.

Furthermore, a first important step towards using the 3D CAVD *in vitro* model in search of novel therapeutics was taken by testing the effect of manipulating microRNA expression on the formation of microcalcifications in CAVD. Specifically, aortic VICs were producing microcalcifications in the 3D constructs as a result of osteogenic stimulation and microRNA-214 expression was either increased or repressed via mimics or anti-miRs, respectively. Overexpressing microRNA-214 resulted in the formation of fewer microcalcifications compared to non-transfected controls. To accurately quantify the number of cells and microcalcification in the 3D constructs, a novel Python script was written using connected component analysis, optimized for extracting information from 3D confocal microscopy images.

Part II is dedicated to the delivery of non-coding RNAs especially for cardiac regeneration. A drug delivery system was engineered to deliver microRNA therapeutics locally to be released over an extended period of time. To that extent, an injectable, self-healing hydrogel was designed to release microRNA therapeutics coupled to gold nanoparticles. The interaction of a polymer chain with a nanoparticle gave this gel shear-thinning and self-assembling properties, making it suitable for injection. The gold nanoparticles were functionalized with a polymer for stability, a peptide to facilitate cellular uptake, and microRNA therapeutics. The gold nanoparticle-coupled microRNAs were released from the hydrogel over the course of several days, maintaining functionality in an *in vitro* assay, and shown to infiltrate the cells in the 3D valve disease model. Furthermore, biodistribution of the gold nanoparticle-coupled microRNA after subcutaneous injection of the loaded hydrogel in mice showed hepatic and renal clearance. This platform is not specific for heart valve disease and can be tailored and used to treat other diseases as well, using other non-coding RNAs, and by injection into different tissues and organs. To that extent, Chapter 5 reviewed the role of non-coding RNAs in cardiac regeneration: the repair of cardiac tissue, which in turn enhances or restores the functional capabilities of the heart. Specifically, it summarized the research in species with native cardiac regenerative capacity to identify the mechanisms of cardiac regeneration, such as cardiomyocyte proliferation and neovascularization, and aimed to select potential useful targets. Understanding the regenerative capacity in lower vertebrates and rodents and their role as scientific models aided in illuminating how non-coding RNAs affect cardiomyocyte proliferation and neovascularization. Prior to using these non-coding RNAs for therapeutic purposes, further research into the pathobiology and disease mechanism is required, and optimal delivery parameters need to be established.

PART I - AORTIC VALVE DISEASE MODEL

The AV is made up of three leaflets that each consist of three layers. These layers have their own unique ECM: the collagen-rich fibrosa layer, the proteoglycan-rich spongiosa, and the elastin-rich ventricularis [1]. During valve disease progression, the VICs undergo myofibrogenic and osteogenic differentiation, making the AV leaflets fibrotic first, and then calcified. This progression is specific to the fibrosa and eventually spreads into the spongiosa. The ventricularis only becomes calcified in later stages of the disease [2,3]. This observation could be explained by VIC sensitivity and reaction to the biomechanics of the ECM. VICs cultured on hydrogel substrates with a stiffness comparable to stenotic tissue readily produced calcifications and aggregates of apoptotic cells were found [4]. Porcine VICs cultured on polyacrylamide (PA) gels with physiological stiffness coated with collagen I differentiated into a myofibroblast-like phenotype only on substrates with stiffness matching the fibrosa, not the ventricularis [5]. Thus, local mechanics in the microenvironment *in vitro* direct pathological differentiation of quiescent VICs to myofibroblasts and osteoblasts [4-6].

Notably, the individual layers of the human AV leaflets have not been separated and subjected to local compressive stiffness tests. Tensile mechanical properties of whole human AV leaflets, and of microdissected fibrosa and ventricularis, have been studied [7-9]. The elastic modulus of strips of human AV leaflet in the circumferential direction was higher than in the radial direction: 15.6 MPa and 2.0 MPa [7]. Micropipette aspiration measured the Young's modulus of normal fibrosa (≈ 3 kPa) and ventricularis (≈ 1 kPa) of porcine valves, [5], and the only data on spongiosa biomechanics stem from atomic force microscopy on porcine valve cryosections [10]. Elastic moduli of the fibrosa, ventricularis, and spongiosa were 13.8 kPa, 12.3 kPa, and 6.1 kPa, respectively. There are notable differences between porcine and humans AVs. For example, human AVs do not have a muscular shelf and have a smaller right coronary leaflet compared to porcine valves [11,12]. These anatomical differences could alter the biomechanical properties. To our knowledge, biomechanical testing of individual leaflet layers of the human aortic valve had not been performed, and existing *in vitro* models thus far cannot account for mechanosensitive cellular responses.

In Chapter 2 we performed systematic microdissection and nanoindentation measurements on excised human AV leaflet tissue to measure the biomechanical properties of the individual layers for the first time. We measured the median Young's moduli of the fibrosa, spongiosa, and ventricularis as 37.1, 15.4, and 26.9 kPa, respectively, and the median Young's modulus of the intact leaflet as 26.7 kPa [13].

Current *in vitro* high-throughput drug discovery platforms do not account for the mechanosensitivity of VICs, an essential and dynamic feature of valve biology. These platforms are based on tissue culture polystyrene (TCPS) that exerts a high, non-physiological stiffness. Similarly, 2D CAVD models based on TCPS do not accurately represent the native VIC microenvironment, resulting in haVIC activation [4,5]. Therefore, these platforms and models do not take into account mechanosensitive cellular responses, limiting the screening and testing capabilities of newly identified therapeutic targets [14]. Thus, a suitably scalable *in vitro* model that replicates layer-specific biomechanical properties is essential to screen and test potential novel therapeutic targets. So far, a range of soft-gel substrates have been used to study VIC phenotype and function. These are predominantly made of poly(ethylene-glycol) (PEG), PEG-dimethacrylate-poly(L-lactide) (PEGdma-PLA), polyacrylamide (PA), or collagen [4,5,10,15]. The PEG hydrogels were between 0.24 kPa and 13 kPa [15], below the values we measured in the native AVs [13]. PEGdma-PLA was used to electrospin AV leaflets with a Young's modulus of 141 MPa compared to 62.4 MPa measured in a porcine AV leaflet [10]. We measured the Young's modulus of an intact human AV leaflet at 26.7 kPa [13]. The PA gels require 10 minutes exposure to UV light (365 nm) [5], making them suitable as a substrate, though not for a 3D model. The extended exposure to UV light would likely harm the haVICs if mixed into the gel

prior to crosslinking. The elastic modulus of stiffer collagen gels was comparable to sclerotic valve tissue, however, the soft collagen gels used were still 2-3 times stiffer than normal AV tissue. Thus, a more accurate representation of the human ECM biomechanical properties in valve disease models could still be designed.

It has been shown that in culture systems, based on hybrid methacrylated gelatin (GelMA) and methacrylated hyaluronic acid (HAMA) hydrogels, VICs can maintain a quiescent VIC phenotype and can support differentiation towards disease phenotypes via pathological cytokines or calcifying stimuli [6,16,17].

Using a 3D bioprinter, we directly replicated the biomechanical properties of human AV layers using GelMA/HAMA hydrogels. We printed a range of hybrid gels of 5-10% GelMA and 1% HAMA, varying crosslinking time from 30-90 s, and identified the formulations matching the native valve Young's moduli for further experiments. Fourteen days in cell culture media did not affect the Young's moduli of these cell-free hydrogels. Human aortic VICs were printed into these GelMA/HAMA constructs. Addition of cells to the hydrogels did not affect the Young's modulus of the fibrosa- and spongiosa-like hydrogels on day 1. After 14 days in culture, the Young's modulus of the spongiosa-like cell-laden hydrogels was unaffected. The Young's modulus of the fibrosa-like cell-laden hydrogels had decreased, indicative of ECM remodeling. This observation was confirmed by increased matrix metalloproteinase 9 (MMP-9) activity and positive staining for newly synthesized collagen. Both fibrosa and spongiosa mechanical properties were mimicked in individual constructs, and printing dual-layered constructs maintained layer-specific biomechanical properties, while the interface remained stable and withstood all processing, handling, and culture without evidence of delamination or degradation. 3D bioprinting provides better cell seeding and attachment over other biofabrication methods, and with lower variability between constructs, as was reviewed in Chapter 1. 3D bioprinting is used for biofabrication and tissue engineering of intricate tissues, including co-culture tumor models, branched vasculature, and cartilage tissues, and is compatible with GelMA hydrogels [18-21]. Specifically, it has been used to produce alginate/gelatin AV conduits, though the application in modeling AV leaflet biomechanical properties is unprecedented [22].

VICs maintained a quiescent phenotype under basal cell culture conditions in our printed constructs. We then stimulated calcification of the constructs using established osteogenic factors, ascorbic acid, dexamethasone, and β -glycerolphosphate [17]. This resulted in formation of microcalcifications and pathological differentiation in non-diseased primary human aortic VICs, which could be observed after 14 days of osteogenic stimulation, specifically in the layer mimicking native fibrosa mechanical properties, similar to disease progression in humans. Furthermore, VICs manipulated and remodeled the ECM in the 3D bioprinted constructs,

indicated by an increase in MMP-9 activity, as is observed in the native valve. Increased MMP-9 activation was also observed in 30 stenotic AVs compared to 6 healthy AVs [23]. Collectively, these findings establish a novel 3D model to study valvular mechanobiology and are an important step towards medium- and high-throughput screening of novel drug targets for valve disease in a biologically highly relevant model.

In Chapter 3 we tested the effect of microRNA-214 manipulation on calcification levels in our *in vitro* model for CAVD. Patients with aortic stenosis displayed higher levels of microRNA-214 in blood samples and in AV tissue samples compared to healthy control patients [24]. In haVICs isolated from non-diseased valves cultured in 2D, overexpression of microRNA-214 *in vitro* resulted in increased production of pro-inflammatory mediators ICAM-1, IL-6, IL-8, and MCP-1, through MyD88/NF- κ B signaling. Additionally, stimulated MyD88/NF- κ B signaling increased known calcification markers Runx2, Msx2, and BMP2 [24]. Furthermore, co-culture of M1 macrophages with VICs resulted in decreased expression levels of TWIST1, a direct target of microRNA-214, resulting in increased calcification [25]. microRNA-214 inhibition reduced calcification, and knockdown of TWIST1 reversed the effect of microRNA-214 inhibition, indicating the mediating role of TWIST1 in macrophage induced calcification in VICs via microRNA-214. Knockdown of microRNA-214 in ApoE^{-/-} mice on a high cholesterol diet reduced AV calcification [25]. Contrastingly, in calcified human AV tissue compared to healthy AV tissue, microRNA-214 was downregulated [26-28]. Thus, the exact role of microRNA-214 in aortic stenosis remains unclear.

For our studies, human aortic VICs from patients undergoing valve replacement surgery, as a result of AV calcification, stenosis, and/or insufficiency, were isolated and cultured in 3D GelMA/HAMA constructs in normal cell culture media or media supplemented with osteogenic factors to stimulate calcification. After 14 days, the number of microcalcifications was significantly higher (5-fold) in the group exposed to osteogenic media, confirming our previous observations that this model is a suitable representation of AV calcification. Additionally, in both normal media and osteogenic media, n =3 constructs were transfected with either microRNA-214 mimic or anti-microRNA-214 to test the effects of increasing or blocking microRNA-214 levels on the formation of microcalcifications. Overexpressing microRNA-214 in the haVICs exposed to OM, resulted in the formation of fewer microcalcifications compared to non-transfected controls exposed to OM. These results tend to support the hypothesis that microRNA-214 can reduce the production of microcalcifications in haVICs. The effects of manipulating microRNA-214 expression on direct targets of microRNA-214 was not measured.

Regardless of the overlap in the methods used in the experiments conducted by Zheng et al. [24] and our experiments described in chapter 3, stimulating miRNA-214 had the opposite effect. The most important difference is that Zheng et al. used haVICs from non-diseased valves in a 2D cell culture setting [24], while we used haVICs from CAVD patients in a 3D *in vitro* model [13]. Thus, conducting these experiments in 3D with non-diseased haVICs would be the most ideal experimental setting to show superiority of a 3D system. In addition, miRNA-214 levels must be quantified in these follow-up experiments to elucidate its role in aortic stenosis.

Furthermore, calcifying capacity can vary between donors ($n = 9$) and between passages [29]. Two kind of calcifying media were tested in 2D culture over 4 passages. haVICs calcified less easily after multiple passages of stimulation with OM (containing organic phosphate) compared to haVICs cultured in pro-calcifying media (normal media supplemented with L-ascorbic acid and inorganic phosphate). We observed fewer microcalcifications in constructs from one of the three donors exposed to OM, yet overall, in these experiments and in previous experiments [13], haVICs produce significantly more microcalcifications after exposure to OM in 3D culture. This requires further investigation, and, to be able to compare different experiments, the field would benefit from a uniform approach in cell culture practice and stimulation of calcification.

Future Directions

This 3D CAVD model provides the foundation for next generation valve disease models. This model can be built upon by inclusion of valve endothelial cells (VEC) to study the interaction between VICs and VECs. This interaction was previously shown to be important in homeostasis, preventing endothelial-to-mesenchymal transformation and osteogenesis of VECs and demands further investigation [30]. Addition of immune cells, such as macrophages and CD8-positive T cells, would make the model a more accurate representation of early valve disease, as in the early pro-inflammatory phases, activated macrophages are thought to promote disease progression through pathological ECM remodeling and osteogenic cytokine release [31], and CD8-positive T cells produce interferon- γ , favoring calcification [32]. Furthermore, native haVICs reside in a dynamic environment. The AV leaflets recoil during systole, and stretch under backpressure during diastole [33]. These dynamic, directional forces could be incorporated in a next generation valve disease model. Dynamic testing has been performed on AV leaflets to investigate the role of cyclic stretch and pressure on VIC phenotype [34]. Specifically, porcine AV leaflets were subjected *ex vivo* in a bioreactor to either normal or pathological stretch (10 and 15%, respectively) and pressure (120/80 and 140/100 mmHg, respectively), resulting in downregulation of α -SMA, Vimentin, and Calponin. This resulted in inhibition of contractile and myofibroblast VIC phenotypes, similar to fibrosa- and spongiosa-layer thickening as observed in aortic valve disease. Therefore, to model the pathobiology

even more accurately, the ideal model includes (1) an anatomically correct valve construct, (2) biomechanical parameters, Young's modulus of 26.7 kPa for non-calcified human AV and the difference in extensibility in the radial and circumferential direction [8,9], (3) both haVICs and haVECs, and possibly immune cells, and (4) a dynamic bioreactor to apply pathological cyclic stretch ($\geq 15\%$) and pressure ($\geq 140/100$ mmHg). It would be possible to study the relation between physical cues, such as pressure and stretch, and biological cues, such as cytokines, growth factors, and non-coding RNA. Figure 1 illustrates a setup for testing shear, stretch, and pressure on a tri-layered co-culture AV construct, and Figure 2 shows an illustrated bioreactor to test an anatomically correct valve construct.

A different avenue for next generation CAVD models is to facilitate a mechanically relevant niche for differentiation of pluripotent stem cells into VICs. Human induced pluripotent stem cell derived mesenchymal stem cells have been differentiated into aortic VICs in poly(ethylene glycol)diacrylate (PEGDA) hydrogels with a Young's modulus between 3 and 15kPa. The cell-laden hydrogels initially had higher moduli around 30kPa, though after 28 days their moduli had dropped to 3.7 kPa [35]. These values are significantly lower than the moduli we measured in excised valve leaflet layers [13]. Combined with the scalability provided by 3D bioprinting, a next generation, (anatomically correct) biomechanically relevant model of an AV with iPSC-derived VICs could provide a solution to some of the main challenges for tissue engineered heart valves; the generation of sufficient numbers of VICs, and rejection of non-autologous cells [36,37].

Broadly, this strategy for matching tissue mechanical properties with scalable 3D-bioprinting of *in vitro* models can be translated to tissues with complex ECM composition and a mechanosensitive resident cell population. This advanced disease modeling approach with human cells, including multiple cell types, is a step towards reducing the number of animals used in pre-clinical research and an advancement in the translation from bench to bedside as animal trials are time consuming and costly.

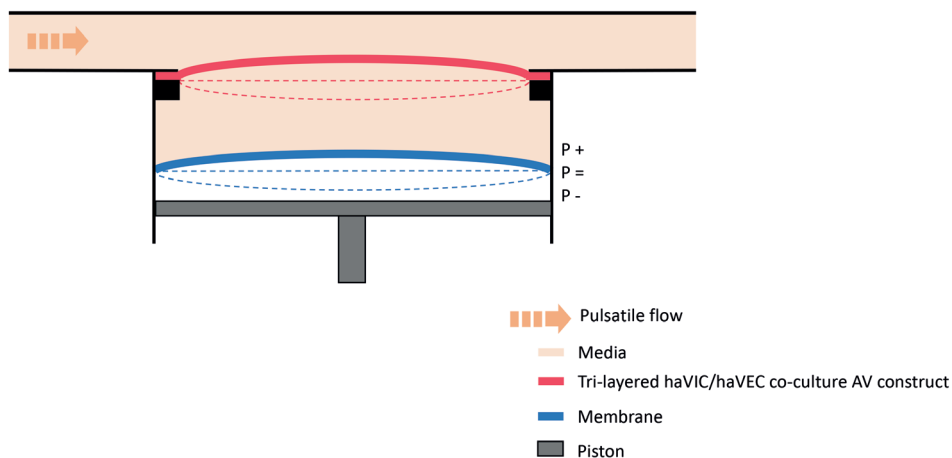


Figure 1 – Illustration of a bioreactor setup that allows for testing the effects of pressure, stretch, and shear stress on (tri-layered) AV constructs that can include both haVICs and haVECs. Moving the piston (grey) increases the pressure on the membrane (blue), causing it to expand and push the construct (red) into the tube, exposing it to (pulsatile) flow. This creates shear stress on the haVECs that line the construct, and the haVICs inside the construct experience stretch on the tube side and compression on the chamber side. Immune cells can be introduced via the media.

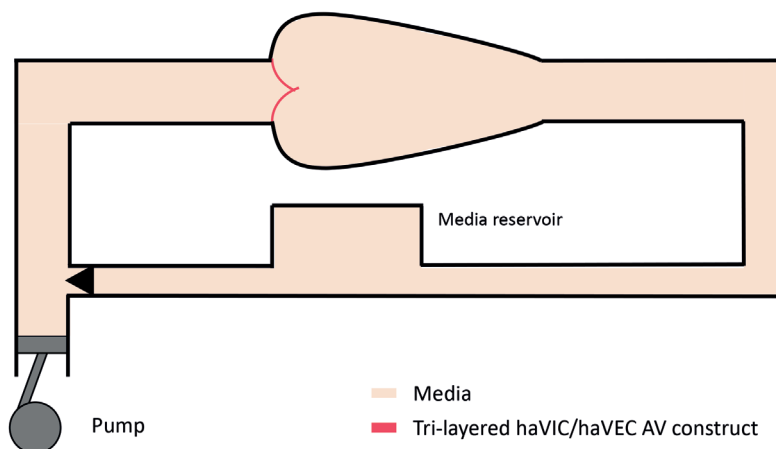


Figure 2 – Illustration of a bioreactor setup that incorporates anatomical geometries for testing anatomically correct AV constructs. The piston pump creates pressure and back pressure across the valve construct, opening and closing the leaflets, inducing radial and circumferential stress on the AV leaflets. The widened section of tubing, representative of the Valsalva sinuses, reduce stress on the leaflets by creating Eddy currents between the leaflet cusps and the sinus wall.

PART II - NON-CODING RNA AND DELIVERY

In Chapter 4 we set out to engineer a drug delivery platform that would be locally injectable and function as a reservoir to ensure microRNA release over an extended period of time. Unmodified, naked oligonucleotides are prone to degradation by serum nucleases, have a low binding affinity for their target microRNAs, demonstrate poor pharmacodynamics/pharmacokinetics (PD/PK), and are incapable of crossing negatively charged cell membranes due to their positive charge [38]. Furthermore, direct, systemic microRNA injection results in high washout and low retention [39]. Therefore, to improve biostability and reduce degradation, we attached microRNA molecules to gold nanospheres (AuNP) that were functionalized with PEG [40,41]. In order to avoid endosomal degradation, we also functionalized the AuNPs with influenza hemagglutinin to stimulate endosomal escape intracellularly.

Slow release carriers are the subject of extensive research to maintain plasma drug levels in the therapeutic range, to reduce undesirable side-effects, to reduce drug degradation, to reduce waste, to eliminate discomfort associated with repeated parenteral administration, to improve patient compliance, and to improve biostability and binding stability [42]. These efforts include non-viral vectors for delivery, such as lipids, microbubbles, polymers, and inorganic materials [40, 43-45]. In general, parenteral administration of therapeutics or drug delivery systems via injection can be achieved easily and in a minimally invasive manner. However, traditional intravenous injections result in relatively short residence time in the body. On the other hand, surgical implantation of a material-based controlled release system provides longer-lasting effects, but is more invasive [42]. Injectable hydrogels with controlled release provide an attractive method to administer drugs locally, in a minimally invasive manner, and with extended biological effect.

Injectable hydrogels based on natural or synthetic polymers have been widely developed, including ECM, collagen, fibrin, alginate, functionalized poly(ethylene glycol) (PEG), or poly(N-isopropylacrylamide) (pNIPAM) [46,47]. Covalent cross-linking methods are commonly used in hydrogels, requiring temperature, light, or pH changes for initiation [48-52]. A pH cross-linkable hydrogel was developed for miRNA delivery based on non-covalent ureido-pyrimidinone (UPy) cross-linking. Near complete release of miRNA molecules from UPy gels was achieved after two days [52]. Despite their relatively facile production, they can provide extra hurdles in biomedical applications, because the reaction is not instantaneous and loaded content can be lost in the process. Some of these hydrogels require external stimuli or instruments, for example a UV light source, for cross-linking.

Contrarily, non-covalent cross-linking yields spontaneous gelation without external stimuli, avoiding the aforementioned challenges. Furthermore, non-covalent gels commonly exhibit shear-thinning and self-healing characteristics, allowing injection and minimally invasive delivery, thereby improving clinical applicability. These kind of hydrogels are based on leucine zipper domains, dock-and-lock proteins, and host-guest interactions [53-55]. For example, Steele et al. [56] demonstrated *in vivo* biocompatibility of a polymer-nanoparticle hydrogel based on PEG-*block*-PLA nanoparticles and hyaluronic acid. Rats were injected with 100 μ l of hydrogel, subcutaneously and intra-muscularly, and after 7 and 14 days the absence of neutrophils, lymphocytes, or other immune cells indicated the lack of an immune response. Furthermore, neither edema, granulation tissue, fibrosis, nor necroptosis was detected. Macrophages were detected on day 3, which, according to the authors, was consistent with a general inflammatory response at the injection site, and it had subsided again by day 7. Subsequently, the hydrogel was injected intramyocardially in rats and no signs of stroke or gross morbidities were observed. After 7 days the animals were sacrificed for full necropsies, and no differences were observed between the test and control group [56]. This indicates that the shear force exerted on the hydrogel within the muscle tissue and myocardium is insufficient to break the non-covalent bonds between the nanoparticles and the polymer.

We therefore used a similar shear-thinning, self-healing hydrogel to deliver the microRNA-functionalized AuNPs. The polymer nanoparticle interactions between a hydroxypropyl-methylcellulose derivative (HPMC-C₁₂) and core-shell nanoparticles [poly(ethylene glycol)-*block*-poly(lactic acid) (PEG-*b*-PLA) nanoparticles] give the hydrogel its advantageous properties. AuNP-miRs were loaded into the PNP gel and sustained linear release under physiological conditions up to 20% over 5 days was observed. The functionality of AuNP-miR-214 was demonstrated *in vitro* using a microRNA reporter assay, achieving approximately 42% knockdown of its target, and in the 3D human CAVD model where it significantly increased the calcification marker alkaline phosphatase. We also assessed biodistribution *in vivo* after subcutaneous injection of PNP-AuNP-miR, showing body clearance after 11 days. This data demonstrates a promising, innovative approach to potentially achieve controlled release of functional microRNA from an injectable, self-healing PNP hydrogel.

This platform can be translated to target other organs or tissues and to treat various diseases that would benefit from local delivery of RNAi therapeutics over a longer period of time. It could also facilitate the delivery of other RNA therapeutics such as small-interfering RNA or long non-coding RNA.

One example would be RNA delivery for stimulating regeneration in the myocardium as highlighted in Chapter 5. Cardiovascular disease is a major cause of death globally, and the number of patients with heart failure is increasing [57]. Currently, heart transplantation is the

only curative option for patients with end-stage heart failure, and the number of donor hearts is dramatically lower than the number of patients on the transplant list. Regardless of the evidence of cardiomyocyte renewal in adults, regeneration of functional myocardium in heart failure is negligible; proliferation of existing cardiomyocytes is insufficient to repopulate damaged myocardium [58]. Recent evidence based on single-cell sequencing and genetic lineage tracing of proliferative cells in mouse hearts did not support meaningful proliferation of cardiomyocytes, nor did it prove the existence of a cardiac stem cell population that replaces lost myocardium [59,60]. Thus, the emphasis is shifting towards employing the limited regenerative capacity of the cardiomyocytes. Reactivation of proliferative capacities of these cells via dedifferentiation, cell cycle re-entry, and cytokinesis, is the focus of research to promote cardiac regeneration [61-66]. Cardiac regeneration is defined as the repair of cardiac tissue, which in turn enhances or restores the functional capabilities of the heart. Cardiac regeneration can be controlled on multiple levels, including cell-cycle manipulation, cellular reprogramming with small molecules, and ECM, protein, and RNA regulation [64,65,67,68]. First, we explored the cardiac regeneration in species with native cardiac regenerative capacity, such as zebrafish, newts and axolotls. Then, we elaborated on the role of microRNAs and long non-coding RNAs in cardiomyocyte proliferation and neovascularization. Other non-coding RNAs, such as circular RNA, PIWI-interacting RNAs, or small inhibitory RNAs were excluded from this chapter, as their role in cardiac regeneration remains to be elucidated. To highlight the role non-coding RNAs can play in cardiac regeneration, research that inhibited or enhanced the expression of specific non-coding RNAs that resulted in significant changes in the regenerative capacity of the myocardium was included.

Future Directions

There are several microRNA therapeutics currently in clinical trials, including miRNA-16 for mesothelioma, miRNA-21 for Alport syndrome, miRNA-29b for fibrosis, miRNA-92 for ischemia, miRNA-103/107 for NASH, miRNA-122 for Hepatitis C virus in 2 trials, miRNA-124 for inflammatory bowel disease, miRNA-155 for lymphoma and leukemia as well as amyotrophic lateral sclerosis (ALS) [69]. Prior to the clinical application of non-coding RNAs, there are multiple hurdles that have to be overcome and requirements that need to be met. The non-coding RNAs need to be stable, specific, and with high binding affinity, and they need to be delivered efficiently to the target tissue. Lipocomplex-based delivery to cardiac tissue has shown issues with blood and serum stability, as well as cytotoxicity, specificity, and low efficiency, and adeno-associated virus vector transfection can lead to prolonged expression beyond the therapeutic window, though it is more specific [70]. Improving biostability, specificity, and uptake were discussed in Chapter 1, as were delivery strategies. Non-coding RNA can be stabilized by chemical modification and delivery strategies include polymer-, lipid-, conjugation-, antibody-, microbubble-, and nanoparticle-

based approaches [40,41,43-45]. Hydrogels have proven to be excellent carriers to overcome mechanical extrusion due to the dynamic environment of the myocardium [56,71].

These strategies need to be tested and validated in models that allow for inclusion of delivery and surgical practices akin to surgery in humans, and that adequately mimic human pathophysiology. Additionally, off-target effects have to be identified and investigated prior to clinical studies.

Moreover, modulation of non-coding RNA expression can have substantial short- and long-term effects. Their targets must be identified and validated in short-term studies. For example, myocardial infarction was induced in pigs and microRNA-199 was delivered to the myocardium using adeno-associated virus vectors. Compared to sham operated animals, treated animals displayed increased contractility, both locally and globally, increased myocardial muscle mass, and reduced scar tissue, correlating to cardiomyocyte proliferation [68]. More importantly, the effect of non-coding RNA modulation must be assessed in long-term *in vivo* studies. Persistent and uncontrolled expression can result in death, as observed in the microRNA-199 study in pigs. Seven weeks after treatment with microRNA-199, persistent and uncontrolled expression resulted in sudden cardiac death due to fatal arrhythmias, demanding more tightly regulated dosing [68]. Another example is the microRNA cluster microRNA-302-376, which is expressed in embryonic cardiac development in mice [72]. It targets the Hippo signal transduction pathway, and expression in post-natal mouse hearts resulted in an increase in the number of cardiomyocytes through cell cycle reactivation. However, persistent re-expression resulted in heart failure due to prolonged immature dedifferentiation states. Transient expression of microRNA-302-367, however, increased murine cardiac regeneration without resulting in heart failure [72]. Therefore, only after performing extensive, rigorous testing, the safety and efficacy of non-coding RNA therapeutics can be assessed in humans [68,73]. Thus, to bring non-coding RNA therapeutics one step closer to clinical applications, research needs to focus on improving delivery, targeting, and dosing, both short- and long-term.

CONCLUSION

This thesis aimed to add a dimension to current models of aortic valve disease and to the delivery of RNA therapeutics. Engineering a 3D bioprinted aortic valve disease model with human valve cells and tailored mechanical properties created the most advanced human CAVD model to date, and laid the groundwork for next generation valve disease models. The work presented in this thesis can be used to map the pathobiology of aortic valve disease and to identify and validate therapeutic targets as is, and it can be the foundation for new models that incorporate multiple cell types and dynamic bioreactor testing. Furthermore, the novel drug delivery platform presented in this thesis can potentially be used to deliver microRNA therapeutics to various organs and tissues, provided that specific functional, immune response, and safety studies are performed, and it can be adapted to deliver other types of RNA therapeutics.

REFERENCES

1. Aikawa, E. Libby, P. A rock and a hard place: Chiseling away at the multiple mechanisms of aortic stenosis. *Circulation* 2017, 135, 1951–1955. [CrossRef] [PubMed]
2. Otto, C.M. Kuusisto, J. Reichenbach, D.D. Gown, A.M. O'Brien, K.D. Characterization of the early lesion of 'degenerative' valvular aortic stenosis. Histological and immunohistochemical studies. *Circulation* 1994, 90, 844–853. [CrossRef] [PubMed]
3. Yabusaki, K. Hutcheson, J.D. Vyas, P. Bertazzo, S. Body, S.C. Aikawa, M. Aikawa, E. Quantification of calcified particles in human valve tissue reveals asymmetry of calcific aortic valve disease development. *Front. Cardiovasc. Med.* 2016, 3, 44. [CrossRef] [PubMed]
4. Yip, C.Y. Chen, J.H. Zhao, R. Simmons, C.A. Calcification by valve interstitial cells is regulated by the stiffness of the extracellular matrix. *Arterioscler. Thromb. Vasc. Biol.* 2009, 29, 936–942. [CrossRef] [PubMed]
5. Chen, J.H. Chen, W.L. Sider, K. Yip, C.Y. Simmons, C.A. Beta-catenin mediates mechanically-regulated, tgfbeta1-induced myfibroblast differentiation of aortic valve interstitial cells. *Arterioscler. Thromb. Vasc. Biol.* 2011, 31, 590–597. [CrossRef] [PubMed]
6. Duan, B. Yin, Z. Hockaday Kang, L. Magin, R.L. Butcher, J.T. Active tissue stiffness modulation controls valve interstitial cell phenotype and osteogenic potential in 3d culture. *Acta Biomater.* 2016, 36, 42–54. [CrossRef] [PubMed]
7. Balguid, A. Rubbens, M.P. Mol, A. Bank, R.A. Bogers, A.J. van Kats, J.P. de Mol, B.A. Baaijens, F.P. Bouten, C.V. The role of collagen cross-links in biomechanical behavior of human aortic heart valve leaflets—relevance for tissue engineering. *Tissue Eng.* 2007, 13, 1501–1511. [CrossRef] [PubMed]
8. Stella, J.A. Sacks, M.S. On the biaxial mechanical properties of the layers of the aortic valve leaflet. *J. Biomech. Eng.* 2007, 129, 757–766. [CrossRef] [PubMed]
9. Vesely, I. Noseworthy, R. Micromechanics of the fibrosa and the ventricularis in aortic valve leaflets. *J. Biomech.* 1992, 25, 101–113. [CrossRef] [PubMed]
10. Hinderer, S. Seifert, J. Votteler, M. Shen, N. Rheinlaender, J. Schaffer, T.E. Schenke-Layland, K. Engineering of a bio-functionalized hybrid off-the-shelf heart valve. *Biomaterials* 2014, 35, 2130–2139. [CrossRef] [PubMed]
11. Mohri, H. Reichenback, D. Merendino, K. 1972, *Biology of Homologous and Heterologous Aortic Valves, Biological Tissue in Heart Valve Replacement*, M. Ionescu, D. Ross, and G. Wooler, Butterworths, London, p. 137.
12. Mohri, H. R. D. and Merendino, K. A. 1972. *Biological tissue in heart valve replacement*. Butterworths, London, pp. 137–194.
13. van der Valk, D.C. van der Ven, C.F.T. Blaser, M.C. Grolman, J.M. Wu, P.J. Fenton, O.S. Lee, L.H. Tibbitt, M.W. Andresen, J.L. Wen, J.R. Ha, A.H. Buffolo, F. van Mil, A. Bouten, C.V.C. Body, S.C. Mooney, D.J. Sluijter, J.P.G. Aikawa, M. Hjortnaes, J. Langer, R. Aikawa, E. Engineering a 3D-Bioprinted Model of Human Heart Valve Disease Using Nanoindentation-Based Biomechanics. *Nanomaterials.* 2018, 8, 296. [CrossRef] [PubMed]
14. Schlotter, F. Halu, A. Goto, S. Blaser, M.C. Body, S.C. Lee, L.H. Higashi, H. DeLaughter, D.M. Hutcheson, J.D. Vyas, P. Pham, T. Rogers, M.A. Sharma, A. Seidman, C.E. Loscalzo, J. Seidman, J.G. Aikawa, M. Singh, S.A. Aikawa, E. Spatiotemporal multi-omics mapping generates a molecular atlas of the aortic valve and reveals networks driving disease. *Circulation* 2018, 137. [CrossRef] [PubMed]
15. Mabry, K.M. Lawrence, R.L. Anseth, K.S. Dynamic stiffening of poly(ethylene glycol)-based hydrogels to direct valvular interstitial cell phenotype in a three-dimensional environment. *Biomaterials* 2015, 49, 47–56. [CrossRef] [PubMed]
16. Hjortnaes, J. Camci-Unal, G. Hutcheson, J.D. Jung, S.M. Schoen, F.J. Kluin, J. Aikawa, E. Khademhosseini, A. Directing valvular interstitial cell myofibroblast-like differentiation in a hybrid hydrogel platform. *Adv. Healthc. Mater.* 2015, 4, 121–130. [CrossRef] [PubMed]
17. Hjortnaes, J. Goettsch, C. Hutcheson, J.D. Camci-Unal, G. Lax, L. Scherer, K. Body, S. Schoen, F.J. Kluin, J. Khademhosseini, A. et al. Simulation of early calcific aortic valve disease in a 3d platform: A role for myofibroblast differentiation. *J. Mol. Cell. Cardiol.* 2016, 94, 13–20. [CrossRef] [PubMed]

18. Xu, F. Celli, J. Rizvi, I. Moon, S. Hasan, T. Demirci, U. A three-dimensional *in vitro* ovarian cancer coculture model using a high-throughput cell patterning platform. *Biotechnol. J.* 2011, 6, 204–212. [CrossRef] [PubMed]
19. Norotte, C. Marga, F.S. Niklason, L.E. Forgacs, G. Scaffold-free vascular tissue engineering using bioprinting. *Biomaterials* 2009, 30, 5910–5917. [CrossRef] [PubMed]
20. Flores, R.L. Liss, H. Raffaelli, S. Humayun, A. Khouri, K.S. Coelho, P.G. Witek, L. The technique for 3d printing patient-specific models for auricular reconstruction. *J. Craniomaxillofac. Surg.* 2017, 45, 937–943. [CrossRef] [PubMed]
21. Bhora, F.Y. Lewis, E.E. Rehmani, S.S. Ayub, A. Raad, W. Al-Ayoubi, A.M. Lebovics, R.S. Circumferential three-dimensional-printed tracheal grafts: Research model feasibility and early results. *Ann. Thorac. Surg.* 2017, 104, 958–963. [CrossRef] [PubMed]
22. Duan, B. Hockaday, L.A. Kang, K.H. Butcher, J.T. 3D bioprinting of heterogeneous aortic valve conduits with alginate/gelatin hydrogels. *J. Biomed. Mater. Res. Part A* 2013, 101, 1255–1264. [CrossRef] [PubMed]
23. Satta, J. Oiva, J. Salo, T. Eriksen, H. Ohtonen, P. Biancari, F. Juvonen, T.S. Soini, Y. Evidence for an altered balance between matrix metalloproteinase-9 and its inhibitors in calcific aortic stenosis. *Ann. Thorac. Surg.* 2003, 76, 681–688. [CrossRef] [PubMed]
24. Zheng, D. Zang, Y. Xu, H. Wang, Y. Cao, X. Wang, T. Pan, M. Shi, J. Li, X. MicroRNA-214 promotes the calcification of human aortic valve interstitial cells through the acceleration of inflammatory reactions with activated MyD88/NF- κ B signaling. *Clin Res Cardiol.* 2018, 108, 691-702. [CrossRef] [PubMed]
25. Li, X.F. Wang, Y. Zheng, D.D. Xu, H.X. Wang, T. Pan, M. Shi, J.H. Zhu, J.H. M1 macrophages promote aortic valve calcification mediated by microRNA-214/TWIST1 pathway in valvular interstitial cells. *Am J Transl Res.* 2016, 8, 5773-5783. [CrossRef] [PubMed]
26. Song, R. Fullerton, D.A. Ao, L. Zhao, K.S. Reece, T.B. Cleveland, J.C. Meng, X. Altered microRNA expression is responsible for the pro-osteogenic phenotype of interstitial cells in calcified human aortic valves. *J. Am. Heart Assoc.* 2017, 6. [CrossRef] [PubMed]
27. Wang, H. Shi, J. Li, B. Zhou, Q. Kong, X. Bei, Y. MicroRNA Expression Signature in Human Calcific Aortic Valve Disease. *Biomed Res Int.* 2017, 4820275. [CrossRef] [PubMed]
28. Coffey, S. Williams, M.J. Phillips, L.V. Galvin, I.F. Bunton, R.W. Jones, G.T. Integrated microRNA and messenger RNA analysis in aortic stenosis. *Sci Rep.* 2016, 6, 36904. [CrossRef] [PubMed]
29. Goto, S. Rogers, M.A. Blaser, M.C. Higashi, H. Lee, L.H. Schlotter, F. Body, S.C. Aikawa, M. Singh, S.A. Aikawa, E. Standardization of Human Calcific Aortic Valve Disease *in vitro* Modeling Reveals Passage-Dependent Calcification. *Front Cardiovasc Med.* 2019, 6, 49. [CrossRef] [PubMed]
30. Hjortnaes J, Shapero K, Goettsch C, Hutcheson JD, Keegan J, Kluin J, Mayer JE, Bischoff J, Aikawa E. Valvular interstitial cells suppress calcification of valvular endothelial cells. *Atherosclerosis.* 2015, 242, 251-260. [CrossRef] [PubMed]
31. Aikawa E, Nahrendorf M, Figueiredo JL, Swirski FK, Shtatland T, Kohler RH, Jaffer FA, Aikawa M, Weissleder R. Osteogenesis associates with inflammation in early-stage atherosclerosis evaluated by molecular imaging *in vivo*. *Circulation.* 2007, 116, 2841–2850. [CrossRef] [PubMed]
32. Nagy, E. Lei, Y. Martínez-Martínez, E. Body, S.C. Schlotter, F. Creager, M. Assmann, A. Khabbaz, K. Libby, P. Hansson, G.K. Aikawa E. Interferon- γ released by activated CD8+ T-lymphocytes impairs the calcium resorption potential of osteoclasts in calcified human aortic valves. *Am J Path.* 2017, 187, 1413-1425. [CrossRef] [PubMed]
33. Sacks, M.S. Smith, D.B. Hiester, E.D. The aortic valve microstructure: effects of transvalvular pressure. *J Biomed Mater Res* 1998, 41, 131. [CrossRef] [PubMed]
34. Thayer P, Balachandran K, Rathan S, Yap CH, Arjunon S, Jo H, Yoganathan AP. The effects of combined cyclic stretch and pressure on the aortic valve interstitial cell phenotype. *Ann Biomed Eng.* 2011, 39, 1654-67. [CrossRef] [PubMed]
35. Nachlas ALY, Li S, Jha R, Singh M, Xu C, Davis ME. Human iPSC-derived mesenchymal stem cells encapsulated in PEGDA hydrogels mature into valve interstitial-like cells. *Acta Biomater.* 2018, 71, 235-246. [CrossRef] [PubMed]

36. Sacks, M.S. Schoen, F.J. Mayer, J.E. Bioengineering Challenges for Heart Valve Tissue Engineering. *Annu Rev Biomed Eng.* 2009, 11, 289-313. [CrossRef] [PubMed]
37. Jana, S. Tranquillo, R.T. Lerman, A. Cells for Tissue Engineering of Cardiac Valves. *J Tissue Eng Regen Med.* 2016, 10, 804-824. [CrossRef] [PubMed]
38. Whitehead, K.A. Langer, R. Anderson, D.G. Knocking down barriers: advances in siRNA delivery. *Nat. Rev. Drug Discov.* 2009, 8, 129-138 [CrossRef] [PubMed]
39. van Mil, A. Doevendans, P.A. Sluijter, J. P. The Potential of Modulating Small RNA Activity in Vivo. *Mini. Rev. Med. Chem* 2009, 9, 235. [CrossRef] [PubMed]
40. Conde, J. Oliva, N. Zhang, Y. Artzi, N. Local Triple-Combination Therapy Results in Tumour Regression and Prevents Recurrence in a Colon Cancer Model. *Nat. Mater* 2016, 15, 1128. [CrossRef] [PubMed]
41. Gilam, A. Conde, J. Weissglas-Volkov, D. Oliva, N. Friedman, E. Artzi, N. Shomron, N. Local microRNA Delivery Targets Palladin and Prevents Metastatic Breast Cancer. *Nat Commun* 2016, 7, 12868. [CrossRef] [PubMed]
42. Langer, R.S. Peppas, N.A. Present and future applications of biomaterials in controlled drug delivery systems. *Biomaterials.* 1981, 2, 201-14. [CrossRef] [PubMed]
43. Fenton, O. S. Kauffman, K. J. Kaczmarek, J. C. McClellan, R. L. Jhunjhunwala, S. Tibbitt, M. W. Zeng, M. D. Appel, E. A. Dorkin, J. R. Mir, F. F. Yang, J. H. Overli, M. A. Heartlein, M. W. DeRosa, F. Langer, R. Anderson, D. G. Synthesis and Biological Evaluation of Ionizable Lipid Materials for the In Vivo Delivery of Messenger RNA to B Lymphocytes. *Adv. Mater* 2017, 29. [CrossRef] [PubMed]
44. Kwekkeboom, R.F. Sluijter, J. P. van Middelaar, B. J. Metz, C. H. Brans, M. A. Kamp, O. Paulus, W. J. Musters, R. J. Increased Local Delivery of Antagomir Therapeutics to the Rodent Myocardium Using Ultrasound and Microbubbles. *J Control Release* 2016, 222,18. [CrossRef] [PubMed]
45. Kargaard, A. Sluijter, J. P. G. Klumperman, B. Polymeric siRNA Gene Delivery - Transfection Efficiency Versus Cytotoxicity. *J Control Release* 2019, 316, 263. [CrossRef] [PubMed]
46. Hernandez, M. J. Gaetani, R. Pieters, V. M. Ng, N. W. Chang, A. E. Martin, T. R. van Ingen, E. Mol, E. A. Sluijter, J. P. G. Christman, K. L. Decellularized Extracellular Matrix Hydrogels as a Delivery Platform for MicroRNA and Extracellular Vesicle Therapeutics. *Adv Ther (Weinh)* 2018, 1. [CrossRef] [PubMed]
47. Bayat, N. Zhang, Y. Falabella, P. Menefee, R. Whalen, J. J. Humayun, M. S. Thompson, M. E. A Reversible Thermoresponsive Sealant for Temporary Closure of Ocular Trauma. *Sci Transl Med* 2017, 9. [CrossRef] [PubMed]
48. Wu, D.Q. Wang, T. Lu, B. Xu, X.D. Cheng, S.X. Jiang, X.J. Zhang, X.Z. Zhuo, R.X. Fabrication of Supramolecular Hydrogels for Drug Delivery and Stem Cell Encapsulation. *Langmuir* 2008, 24, 10306. [CrossRef] [PubMed]
49. Burdick, J.A. Anseth, K.S. Photoencapsulation of Osteoblasts in Injectable RGD-modified PEG Hydrogels for Bone Tissue Engineering. *Biomaterials* 2002, 23, 4315. [CrossRef] [PubMed]
50. Pek, Y.S. Wan, A.C.A. Shekaran, A. Zhou, L. Ying, J.Y.A. A Thixotropic Nanocomposite Gel for Three-Dimensional Cell Culture. *Nat. Nanotechnol* 2008, 3, 671. [CrossRef] [PubMed]
51. Bastings, M.M. Koudstaal, S. KIELTYKA, R.E. Nakano, Y. Pape, A.C. Feyen, D.A. van Slochteren, F.J. Doevendans, P.A. Sluijter, J.P. Meijer, E.W. Chamuleau, S.A. Dankers, P.Y. A Fast pH-switchable and Self-Healing Supramolecular Hydrogel Carrier for Guided, Local Catheter Injection in the Infarcted Myocardium. *Adv Health Mater* 2014, 3, 70. [CrossRef] [PubMed]
52. Bakker, M.H. van Rooij, E. Dankers, P.Y.W. Controlled Release of RNAi Molecules by Tunable Supramolecular Hydrogel Carriers. *Chem. Asian. J* 2018, 13, 3501. [CrossRef] [PubMed]
53. Petka, W.A. Harden, J.L. McGrath, K.P. Wirtz, D. Tirrell, D.A. Reversible Hydrogels From Self-Assembling Artificial Proteins. *Science* 1998, 281, 389. [CrossRef] [PubMed]
54. Lu, H.D. Charati, M.B. Kim, I.L. Burdick, J.A. Injectable Shear-Thinning Hydrogels Engineered With a Self-Assembling Dock-and-Lock Mechanism. *Biomaterials* 2012, 33, 2145. [CrossRef] [PubMed]
55. Rodell, C.B. Kaminski, A. Burdick, J.A. Rational Design of Network Properties in Guest-Host Assembled and Shear-Thinning Hyaluronic Acid Hydrogels. *Biomacromolecules* 2013, 14, 4125. [CrossRef] [PubMed]

56. Steele, A.N. Stapleton, L.M. Farry, J.M. Lucian, H.J. Paulsen, M.J. Eskandari, A. Hironaka, C.E. Thakore, A.D. Wang, H. Yu, A.C. Chan, D. Appel, E.A. Woo, Y.J. *Adv Healthc Mater* 2019, 8, 1801147. [CrossRef] [PubMed]
57. Benjamin, E.J. Muntner, P. Alonso, A. Bittencourt, M.S. Callaway, C.W. Carson, A.P. Chamberlain, A.M. Chang, A.R. Cheng, S. Das, S.R. Delling, F.N. Djousse, L. Elkind, M.S.V. Ferguson, J.F. Fornage, M. Jordan, L.C. Khan, S.S. Kissela, B.M. Knutson, K.L. Kwan, T.W. Lackland, D.T. Lewis, T.T. Lichtman, J.H. Longenecker, C.T. Loop, M.S. Lutsey, P.L. Martin, S.S. Matsushita, K. Moran, A.E. Mussolino, M.E. O’Flaherty, M. Pandey, A. Perak, A.M. Rosamond, W.D. Roth, G.A. Sampson, U.K.A. Satou, G.M. Schroeder, E.B. Shah, S.H. Spartano, N.L. Stokes, A. Tirschwell, D.L. Tsao, C.W. Turakhia, M.P. VanWagner, L.B. Wilkins, J.T. Wong, S.S. Virani, S.S. American Heart Association Council on Epidemiology and Prevention Statistics Committee and Stroke Statistics Subcommittee. *Heart Disease and Stroke Statistics-2019 Update: A Report From the American Heart Association. Circulation.* 2019, 139, e56-e528. [CrossRef] [PubMed]
58. Bergmann, O. Bhardwaj, R.D. Bernard, S. Zdunek, S. Barnabé-Heider, F. Walsh, S. Zupicich, J. Alkass, K. Buchholz, B.A. Druid, H. Jovinge, S. Frisén, J. Evidence for cardiomyocyte renewal in humans. *Science.* 2009, 324, 98-102. [CrossRef] [PubMed]
59. Kretzschmar, K. Post, Y. Bannier-Hélaouët, M. Mattiotti, A. Drost, J. Basak, O. Li, V.S.W. van den Born, M. Gunst, Q.D. Versteeg, D. Kooijman, L. van der Elst, S. van Es, J.H. van Rooij, E. van den Hoff, M.J.B. Clevers, H. Profiling proliferative cells and their progeny in damaged murine hearts. *Proc Natl Acad Sci.* 2018, 115, E12245-54. [CrossRef] [PubMed]
60. Li, Y. He, L. Huang, X. Bhaloo, S.I. Zhao, H. Zhang, S. Pu, W. Tian, X. Li, Y. Liu, Q. Yu, W. Zhang, L. Liu, X. Liu, K. Tang, J. Zhang, H. Cai, D. Ralf, A.H. Xu, Q. Lui, K.O. Zhou, B. Genetic lineage tracing of nonmyocyte population by dual recombinases. *Circulation.* 2018, 1389, 793–805. [CrossRef] [PubMed]
61. Hassink, R.J. Pasumarthi, K.B. Nakajima, H. Rubart, M. Soonpaa, M.H. de la Rivière, A.B. Doevendans, P.A. Field, L.J. Cardiomyocyte cell cycle activation improves cardiac function after myocardial infarction. *Cardiovasc Res.* 2008, 78, 18-25. [CrossRef] [PubMed]
62. Xiao, J. Liang, D. Zhang, H. Liu, Y. Zhang, D. Liu, Y. Pan, L. Chen, X. Doevendans, P.A. Sun, Y. Liang, X. Sluijter, J.P. Chen, Y.H. MicroRNA-204 is required for differentiation of human-derived cardiomyocyte progenitor cells. *J Mol Cell Cardiol.* 2012, 53, 751-9. [CrossRef] [PubMed]
63. Xiao, J. Liu, H. Cretoi, D. Toader, D.O. Suci, N. Shi, J. Shen, S. Bei, Y. Sluijter, J.P. Das, S. Kong, X. Li, X. miR-31a-5p promotes postnatal cardiomyocyte proliferation by targeting RhoBTB1. *Exp Mol Med.* 2017, 49, e386. [CrossRef] [PubMed]
64. D’Uva, G. Aharonov, A. Lauriola, M. Kain, D. Yahalom-Ronen, Y. Carvalho, S. Weisinger, K. Bassat, E. Rajchman, D. Yifa, O. Lysenko, M. Konfino, T. Hegesh, J. Brenner, O. Neeman, M. Yarden, Y. Leor, J. Sarig, R. Harvey, R.P. Tzahor, E. ERBB2 Triggers Mammalian Heart Regeneration by Promoting Cardiomyocyte Redifferentiation and Proliferation. *Nat Cell Biol.* 2015, 17, 627-38. [CrossRef] [PubMed]
65. Senyo, S.E. Steinhauser, M.L. Pizzimenti, C.L. Yang, V.K. Cai, L. Wang, M. Wu, T.D. Guerquin-Kern, J.L. Lechene, C.P. Lee, R.T. Mammalian heart renewal by pre-existing cardiomyocytes. *Nature.* 2013, 493, 433–436. [CrossRef] [PubMed]
66. Xin, M. Kim, Y. Sutherland, L.B. Murakami, M. Qi, X. McAnally, J. Porrello, E.R. Mahmoud, A.I. Tan, W. Shelton, J.M. Richardson, J.A. Sadek, H.A. Bassel-Duby, R. Olson. E.N. Hippo pathway effector Yap promotes cardiac regeneration. *Proc Natl Acad Sci USA.* 2013, 110, 13839–13844. [CrossRef] [PubMed]
67. Aguirre, A. Montserrat, N. Zacchigna, S. Nivet, E. Hishida, T. Krause, M.N. Kurian, L. Ocampo, A. Vazquez-Ferrer, E. Rodriguez-Esteban, C. Kumar, S. Moresco, J.J. Yates, J.R. III. Campistol, J.M. Sancho-Martinez, I. Giacca, M. Izpisua, Belmonte, J.C. In vivo activation of a conserved microRNA program induces mammalian heart regeneration. *Cell Stem Cell.* 2014, 15, 589–604. [CrossRef] [PubMed]
68. Gabisonia, K. Prosdocimo, G. Aquaro, G.D. Carlucci, L. Zentilin, L. Secco, I. Ali, H. Braga, L. Gorgodze, N. Bernini, F. Burchielli, S. Collesi, C. Zandonà, L. Sinagra, G. Piacenti, M. Zacchigna, S. Bussani, R. Recchia, F.A. Giacca, M. MicroRNA therapy stimulates uncontrolled cardiac repair after myocardial infarction in pigs. *Nature.* 2019. [CrossRef] [PubMed]

69. Hanna, J. Hossain, G.S. Kocerha, J. The Potential for microRNA Therapeutics and Clinical Research. *Front Genet.* 2019, 10, 478. [CrossRef] [PubMed]
70. Lesizza, P. Prosdocimo, G. Martinelli, V. Sinagra, G. Zacchigna, S. Giacca, M. Single-Dose Intracardiac Injection of Pro-Regenerative MicroRNAs Improves Cardiac Function after Myocardial Infarction. *Circ. Res.* 2017, 120, 1298-1304. [CrossRef] [PubMed]
71. Koudstaal, S. Bastings, M.M. Feyen, D.A. Waring, C.D. van Slochteren, F.J. Dankers, P.Y. Torella, D. Sluijter, J.P. Nadal-Ginard, B. Doevendans, P.A. Ellison, G.M. Chamuleau, S.A. Sustained delivery of insulin-like growth factor-1/hepatocyte growth factor stimulates endogenous cardiac repair in the chronic infarcted pig heart. *J Cardiovasc Transl Res.* 2014, 7, 232-41. [CrossRef] [PubMed]
72. Tian, Y. Liu, Y. Wang, T. Zhou, N. Kong, J. Chen, L. Snitow, M. Morley, M. Li, D. Petrenko, N. Zhou, S. Lu, M. Gao, E. Koch, W.J. Stewart, K.M. Morrisey, E.E. A microRNA-Hippo pathway that promotes cardiomyocyte proliferation and cardiac regeneration in mice. *Science Translational Medicine.* 2015. 279. 279-289. [CrossRef] [PubMed]
73. Kwekkeboom, R.F. Lei, Z. Doevendans, P.A. Musters, R.J. Sluijter, J.P. Targeted delivery of miRNA therapeutics for cardiovascular diseases: opportunities and challenges. *Clin Sci (Lond).* 2014, 127, 351-65. [CrossRef] [PubMed]

Nederlandse Samenvatting

Nederlandse samenvatting

Dit proefschrift laat zien dat ontwikkelingen in biofabricatie, bio-technologie en biomaterialen kunnen worden gecombineerd om representatieve *in vitro* modellen van hartklepaandoeningen te ontwerpen, waarmee nieuwe strategieën voor medicijnafgifte kunnen worden ontwikkeld. Klinisch relevante modellen van hartklepaandoeningen bij de mens zijn essentieel om de complexe pathobiologie te begrijpen en om therapeutische doelen te identificeren. Niet-coderende RNAs kunnen potentieel een groot effect hebben op cardiovasculaire regeneratie, maar er zijn nieuwe benaderingen voor medicijnafgifte nodig om deze RNA-therapeutica in specifieke organen of weefsels te brengen en om de therapeutische efficiëntie te verhogen. Daarom was het hoofddoel van dit proefschrift om een humaan 3D model van aortaklepverkalking te ontwerpen, een injecteerbare hydrogel om niet-coderend RNA gedurende meerdere dagen af te leveren te ontwikkelen en het effect hiervan te testen in het 3D model.

Hoofdstuk 1 schetst de klinische relevantie van nieuwe behandelstrategieën voor aortaklepaandoeningen en beschrijft de anatomie van de aortaklep (AV). De aortaklep bestaat uit drie interne lagen: aan de aorta zijde de fibrosa, aan de hartkamer zijde de ventricularis, en daar tussen in de spongiosa. De aortaklepcellen (VICs) in deze drie lagen onderhouden de matrix van collageen en elastine die de aortaklep haar stijfheid en elasticiteit geeft. Bij aortaklepverkalking ontstaan microcalcificaties in de fibrosa laag en verspreiden zich uiteindelijk door de klep, wat het functioneren van de aortaklep verhindert. Momenteel is de beste behandeling het chirurgisch vervangen van de aortaklep in het laatste stadium van de ziekte. Er zijn op dit moment geen medicijnen beschikbaar die de verkalking vertragen of stoppen. Daarom evalueert dit hoofdstuk de onderzoeken naar microRNAs die betrokken zijn bij de pathobiologie van klepziektes en naar de toediening van die microRNAs. Om potentiële therapeutica te onderzoeken en te testen is een relevant model van de ziekte essentieel. Op basis hiervan benadrukt dit hoofdstuk de vereisten voor het ontwikkelen van klinisch relevante *in vitro* klepziekte modellen; om representatieve *in vitro* modellen voor aortaklepverkalking te maken, moeten deze cellen van menselijke oorsprong bevatten en de oorspronkelijke drielaagse klep structuur met de biomechanische eigenschappen repliceren.

Deel I richt zich op de ontwikkeling van het eerste menselijke 3D-hartklepziekte model. Nano-indentatie werd gebruikt in Hoofdstuk 2 om de compressieve stijfheid van de individuele lagen van de menselijke aortaklep te meten. Die eigenschappen werden in het model gerepliceerd door de concentratie, verhouding en cross-linking parameters van biopolymeren nauwkeurig op elkaar af te stemmen. Biopolymeren op basis van gelatine en hyaluronzuur werden zo gebruikt om de extracellulaire matrix (ECM) van de aortaklep na te bootsen. Gezonde interstitiële cellen uit de aortaklep (VIC) werden gemengd met deze biopolymeren en geprint

met een bioprinter om 3D-constructen te creëren met dezelfde mechanische eigenschappen als de gezonde klep. De VICs in de constructen werden blootgesteld aan osteogene factoren, die de vorming van microcalcificaties stimuleren, om het ziekteverloop na te bootsen.

Bovendien werd een eerste belangrijke stap gezet in Hoofdstuk 3 in het gebruik van het 3D *in vitro* aortaklep verkalking model bij de zoektocht naar nieuwe therapeutica door het effect van manipulatie van microRNA-expressie op de vorming van microcalcificaties in aortaklep verkalking te testen. Om het aantal cellen en microcalcificaties in de 3D-constructen nauwkeurig te kwantificeren, werd een nieuw Python-script geschreven met behulp van een verbonden componenten analyse, geoptimaliseerd voor het extraheren van informatie uit driedimensionale confocale microscopiebeelden. VICs produceerden microcalcificaties in de 3D-constructen als gevolg van osteogene stimulatie. Daarna werd de expressie van microRNA-214 verhoogd of juist onderdrukt door de toevoeging van RNA “mimics”, die RNA nabootsen, of zogenaamde anti-microRNAs. Het verhogen van microRNA-214 resulteerde in de vorming van minder microcalcificaties in vergelijking met controlegroepen.

Hiermee lieten wij zien dat de 3D representatie van de aortaklep mogelijk is en dat hierin het ziektemodel van aortaklep verkalking nauwkeurig nagebootst kan worden. Ook demonstreerden we dat microRNA-214 een negatief effect kan hebben op aortaklep verkalking, identificeerden we op deze manier microRNA-214 als een potentieel nieuw therapeutisch doel.

Deel II is gewijd aan de toediening van niet-coderende RNAs en aan de potentie van niet-coderende RNAs voor het induceren van hartweefsel regeneratie. Hoofdstuk 4 beschrijft hoe een medicijn-afgiftesysteem werd ontworpen om microRNA-therapeutica lokaal te plaatsen en gedurende een langere periode vrij te geven. In zoverre werd een injecteerbare, zelfherstellende hydrogel ontworpen om microRNA-therapeutica gekoppeld aan gouden nanodeeltjes te laten vrijkomen. De interactie van een polymeerketen met een polymeer nanodeeltje gaf deze gel zijn zelfherstellende eigenschappen, waardoor het geschikt is voor injectie. Onder druk werd de hydrogel vloeibaar, en wanneer de druk wegviel werd de gel viskeus. Aan de gouden nanodeeltjes werd een polymeer voor stabiliteit, een peptide om opname in cellen te vergemakkelijken, en microRNA-therapeuticum gekoppeld. De gouden nanodeeltjes kwamen gedurende enkele dagen vrij uit de hydrogel, waarbij de functionaliteit behouden bleef. Verder werd er aangetoond dat de gouden nanodeeltjes de VICs infiltreren in het 3D-aortaklepziekte model. Bovendien werden de nanodeeltjes met microRNAs na subcutane injectie van de hydrogel in muizen geklaard door de lever en nieren. Dit hydrogel medicijnafgifte platform is niet specifiek voor hartaandoeningen en kan worden aangepast om ook andere ziekten te behandelen, met behulp van andere niet-coderende RNAs. Het afgiftesysteem kan in theorie in verschillende weefsels en organen worden geïnjecteerd.

Hoofdstuk 5 gaat in op de rol van niet-coderende RNAs bij hartregeneratie: het herstel van hartweefsel, wat op zijn beurt het functionele vermogen van het hart verbetert of herstelt. Het vatte het onderzoek samen wat gericht is op diersoorten met een natuurlijke capaciteit voor hartregeneratie. De mechanismen hiervan, zoals proliferatie van cardiomyocyten en neovascularisatie, werden geïdentificeerd, waardoor potentieel therapeutisch bruikbare doelen geselecteerd kunnen worden. Het begrijpen van de regeneratieve capaciteit bij anamnioten, of lagere gewervelde dieren, en knaagdieren, en hun rol als wetenschappelijke modellen helpen bij het verduidelijken hoe niet-coderende RNAs neovascularisatie en de proliferatie van cardiomyocyten beïnvloeden. Voordat deze niet-coderende RNAs voor therapeutische doeleinden kunnen worden gebruikt, is verder onderzoek naar het ziektemechanisme vereist en moeten optimale toedieningsparameters worden vastgesteld, om de effectiviteit te bepalen en ongewenste bijwerkingen te voorkomen. Daarnaast moet de veiligheid, en korte- en langetermijn effecten worden onderzocht.

Dit proefschrift heeft een dimensie toegevoegd aan de huidige modellen van aortaklepverkalking en aan het toedienen van RNA therapeutica. De ontwikkeling van het 3D aortaklepziekte model met humane cellen en op maat gemaakte mechanische eigenschappen heeft geleid tot het meest geavanceerde model op dit moment, en het heeft de basis gelegd voor het ontwikkelen van een volgende generatie ziektemodellen. Het werk uit dit proefschrift kan worden gebruikt om de pathobiologie van aortaklepziekte verder in kaart te brengen en om therapeutische doelen te identificeren. Verder vormt het de basis voor nieuwe modellen waarin meerder celtypes kunnen worden gebruikt en waarop dynamische testen kunnen worden uitgevoerd. Verder kan het medicijnafgiftesysteem mogelijk worden gebruikt om microRNA-therapeutica toe te dienen aan specifieke organen en weefsels, mits immunoreacties en veiligheid worden onderzocht, en kan het worden aangepast om andere soorten RNA toe te dienen.

Curriculum Vitae

Curriculum Vitae

Casper van der Ven was born on February 2nd 1989 in Zutphen, the Netherlands to Theo & Lillian van der Ven. Together with his brother he grew up in Dieren, attending Het Stedelijk Daltoncollege in Zutphen where he graduated in 2007. After studying at MacQuarie University Sydney and travelling around Australia and New Zealand, Casper started University College Utrecht in 2008 where he pursued a Major in Biochemistry and Immunology, with Minors in Economics and in Development Studies. During his Bachelor Studies he spent a semester on exchange at the University of New Hampshire, followed winter courses at Jacobs University Bremen, and chaired multiple committees (Social, Career, Skitrip). Furthermore, he partook in the UCU in Africa development programme in Kenya, interned in Tanzania with EARDP-CI, an NGO focussed on microfinance for local agriculture to analyse implementation of sustainable agricultural practice, and after graduation in 2011 he travelled from Kenya to Cape Town. Upon return to the Netherlands in 2012 he started working with Simavi, a Dutch NGO focussed on sexual and reproductive health and rights, and on sanitation, where he analysed opportunities for private public partnerships.



Later that year he started in the Utrecht University pilot programme “Regenerative Medicine and Technology”, a new collaborative Master’s programme with Technical University Eindhoven, aimed to innovate at the intersection of Medicine, Biomedical Science, and Engineering. Towards the end of the programme in 2014, Casper gratefully accepted a six month internship in the Langer Lab at Massachusetts Institute of Technology (Cambridge, USA) with Dr. Mark Tibbitt, facilitated by Dr. Jesper Hjortnaes and was awarded the Van Wijck-Stam-Caspers beurs, researching drug delivery to heart valves. He then worked an additional six months in the Langer Lab on recycled polymers for cardiac applications with Dr. Lisa Freed. These experiences inspired him to write a PhD research proposal combining the drug delivery expertise at MIT with the cardiovascular and microRNA expertise of Experimental Cardiology at UMC Utrecht.

After Prof. Robert Langer’s and Prof. Pieter Doevendans’ approval, Casper wrote a grant application with Prof. Joost Sluijter to CardioVasculair Onderzoek Nederland (CVON), and was awarded the Young Talent Fellowship in 2015 to pursue this ambitious plan; an unusual, yet exciting start of his doctoral research. A generous invitation of Prof. Elena Aikawa

followed, and the focus on calcific aortic valve disease at Brigham and Women's Hospital and Harvard Medical School (Boston, USA) was incorporated into the thesis. During the two years in Boston, Casper's presentation at the Wyss Institute's "Micro- and Nanotechnologies for Medicine: Emerging Frontiers and Applications" won the "Scientific Excellence" award, he was awarded the Harvard Catalyst Reactor Grant "Big Ideas, Small Features: Utilizing Advanced Microscopic and Nanoscale Technologies to Further Human Healthcare" under Elena Aikawa's supervision, he wrote a grant with Prof. Joost Sluijter to stichting ZABAWAS, and he set up a collaboration between the Langer Lab at MIT and CELLINK AB, a Swedish bioink and biomedicine company, accompanied by an unrestricted personal fellowship. These achievements allowed Casper to pursue the research ideas that are presented in this thesis. The work published in this thesis has been presented at both national and international conferences.

Acknowledgements

Acknowledgements

This thesis is the result of a multidisciplinary collaboration between biologists, chemists, material scientists, engineers, and clinicians, between multiple institutions, who have cooperated to identify and answer the questions posed in this thesis. It is a product of countless hours of labour, love, and frustration, and supported by many people throughout the process whom I would like to thank in this chapter.

The Promotion Committee

Prof. dr. J.P.G. Sluijter - Dear Joost, thank you for giving me the opportunity to pursue and explore my research interests. You have facilitated this graduate research since I approached you with the idea to combine the expertise of two labs, and you took a great leap in starting this endeavour with me, without having the stability and structure a regular PhD position would have. Thank you for creating an environment where I learnt to adapt, to practice patience, to exhibit persistence, and to employ creativity in problem solving. I will remember the pool and bbq parties at your house where the entire group came together and celebrated our achievements.

Prof. dr. P.A.F.M. Doevendans - Dear Pieter, thank you for your supervision, help, and guidance during my PhD project. I appreciate your direct approach and critical questions that cut to the core of the matter. Thank you for opening your home to the entire department for the Christmas celebrations.

Dr. A. van Mil - Dear Alain, over the past five years we have worked together on several projects and you have always been open to my questions. Thank you for being my go-to guy about microRNA and for the feedback on my writings, from abstracts to papers, and ultimately this thesis.

Dr. J. Hjortnaes - Dear Jesper, for almost a decade now you have been a source of inspiration and motivation, and a true mentor. You opened the doors to conduct research in two renowned laboratories in Boston by introducing me to Dr. Mark Tibbitt and to Prof. Elena Aikawa, for which I am grateful beyond words. In addition to aiding me on an academic level and navigating the scientific content, you have cared for me on a personal level beyond our professional relationship, and I aspire to be as good a mentor to someone someday as you have been to me.

The Reading Committee

I would like to thank the members of the independent reading committee, Prof. dr. ir. J. Malda, Prof. dr. M.C. Verhaar, Prof. dr. R. Masereeuw, Prof. dr. ir. T. Vermonden, and Prof. dr. C.V.C. Bouten for reading and reviewing this thesis.

Collaborators & Colleagues

Prof. E.A. Aikawa - Dear Elena, thank you for adding the dimension of Calcific Aortic Valve Disease to my research, and for welcoming me into the family you have created in your labs in Boston. I have developed greatly as a scientist under your mentorship, in mindset, in writing, in public speaking, and in networking. The freedom you gave me and trust you had in me, to handle the Harvard Catalyst project, from grant writing and presentations to leading the follow-up meetings, was empowering and resulted in a valuable experience. I will cherish the memories of the many dinners we had with our lab, and I am eternally grateful for your excellent mentorship and supervision.

Dr. Mark Tibbitt - Dear Mark, it has been exciting to work with you for the past 6 years. What started as a Master's research internship under your supervision culminated in this PhD thesis. Thank you for educating me in the material science required for my projects, for your perspective on my ideas, and for your feedback on my writing. One of the things I admire most is the open and warm atmosphere you created in your group: good science, and good fun! I thoroughly enjoyed the brainstorm sessions and the occasional cheeky pint. Thank you!

Prof. Robert Langer - Dear Bob, thank you for giving me the opportunity to pursue my research dreams in your lab, twice! The unique collaborative, open, and ambitious environment you have created in your group is inspiring and unparalleled. While working there it felt that anything was possible and encouraged to investigate. Thank you for your guidance on which ideas to pursue and for trusting me with the space to initiate a collaboration with an industry partner. I frequently look back on the softball league and the beach parties you have hosted.

Dr. Dewy van der Valk - Lieve Dewy, I cannot thank you enough for your hard work, dedication, and persistence during the time we worked together. During your master internship you exhibited the qualities of and performed at a level of a graduate student. You drove our paper, and ultimately a chapter of this thesis, to completion. More importantly, thank you for your friendship and companionship during this period, in Boston and in Utrecht. Thank you for the dinners, coffees, wines, hiking & camping trips, concerts, and sailing.

Dr. Fenton - Dear Owen, bae, your positive energy in the lab is infectious. Your bench is too, probably. Thank you for simplifying organic, lipid, and protein chemistry for us non-chemists and for your help with my research.

Klaske Siegersma - Klaske, what an unexpected, yet pleasant surprise to work with you towards the very end of my research. Your insights, knowledge, and skills in developing an improved analysis and writing a script have helped me to greatly improve my research. For that I am very grateful. I wish you all the best in the remainder of your PhD research, I am sure you will do very well!

The students I have had the privilege of supervising - Pin-Jou, Dewy, Mayke, Femke, Amber, Raul, and Benjamin. Thank you for letting me be a part of your scientific endeavours, I have learnt from you, and I hope I have been able to teach you something or guide you in your development in return. I am proud of your achievements and accomplishments, and I wish you all the best.

All colleagues in and around the Langer Lab, especially Connie, Tuli, Joe, Sarah, Owen, Jason, Rebecca, Eric, Bennie, Nafiseh, Jimmy, Kevin, Shavani, Robert, Josh, Cody, Karsten, Jamie, Kun, Ritu, Abel, Derfogail, Sunandini, Lina, Katerina, Dahlia & Robbie, Chris, Elena, Yulia, Daniel, Corina, Andrew, Zach, Katie, Andrew, Miralem, Kaitlyn, Adam, Shiran, Ester, Mikhail, Abigail, Asha, Lavanya, Edward, James, Amanda, Collin, Matt, Omar, Lisa, Tom, Katy.

All colleagues in and around the Aikawa-Aikawa Lab and CICS, especially Masanori, Peter, Whitney, Toshiaki, Shunsuke, Jessica, Josh, Ryo, Tan, Florian, Andrew, Maximillian, Marc, Mark, Mark, Mayumi, Jennifer, Mary, Anna, Stefan, Jason.

All colleagues in and around the Experimental Cardiology groep and the UMC Utrecht, specifically Corina, Esther, Iris, Inge, Irene, Joukje, Ineke, Ingrid, Janine, Judith, Lena, Frederieke, Peter-Paul, Sander, Emma, Marjan, Patricia, Marieke, Renee, Elise, Tom, Sandra, Marijn, Nino, Madison, Aoife, Aina, and the students.

All colleagues in and around the Regenerative Medicine Center Utrecht, specifically Joost, Anita, Tineke, Esta, Mattie, Bas, Krista, Dienty, Petra, Petra, Merle, Paul, Chris, Tobias, Elana, and the students.

The Regenerative Medicine PhD - Paul, Koen, and Sarah, thank you for running the show behind the scenes, for organising the courses, for representing us promovendi when necessary, and for all the social activities that you facilitate. And of course the other RM PhD students for creating the warm and welcoming atmosphere in our group, and for your support and help with science.

The people at CELLINK for providing materials, support, funding, and a platform to share my findings, thank you Erik, Héctor, Itedale, Ariel, Tomoko, Elin, Hannah, Jim, Patrick, Maria, Saviz, and Sjoerd.

Friends & Family

Jeff - Mate, thank you for your support and distractions, our shenanigans and adventures, the retreats to your lakehouse, and the trips to Florida, Poland, Morocco, and Austria.

Anneke - Thank you. For the coffees, for the Gumbo, for the support, for the wine, for everything.

Anouk - Life takes you all over the world, regardless, you are there for me when I need you. Thank you.

Iris - Who would have expected that when we met at UCU about a dozen years ago we'd graduate in the same year from the same PhD programme? I know I did not, but I sure am glad we were able to share many valuable experiences in Boston and in Utrecht. I will cherish those memories and I greatly value your friendship.

Ted & Marlien - Somehow we manage to live far apart from each other, yet I have always felt very close to you. Thank you for creating a home away from home, and for welcoming me like family. Together we have shared many memories that I will cherish, and I look forward to creating many more!

Remco & Swenne - Thank you for always taking the time to listen, for always opening the doors to your studio to me, and whoever I happen to bring along that day, for the music that has made the hard days easier, the heavy moods lighter. It has been an honour to be a witness to your creative process, and to perhaps even play a small role in it. Especially the living room concerts I will look back on with fondness. I hope we can continue to organise many more.

Allison & Georgi - Thank you for the many laughs we shared over lunches, coffee, dinner, and wine, for your friendship, and for opening your home to me, whether it was Thanksgiving or any other Tuesday. Boston is a second home to me, and that is because you opened your arms and your hearts, thank you.

Simon & Anna - Simon, what a coincidence, our first encounter: your motorcycle in front of the MIT Sailing Pavilion six years ago. Thank you for your support during this endeavour, for the adventures we shared: motorcycling, camping, sailing, hiking, and surfing. Thank you for the intellectual conversations and shifting my focus from my thesis' specifics to broader perspectives.

Chris - Thank you for the gigs you took me, and the artists you opened my ears to, for the motorcycle trips, for the delicious food and drink at SRV, for inviting me to BEANLOAF, and for the cookouts at your house with your family.

Fedderik & Saskia – Quality over quantity, we do not see each other as often as I would like, but when we do, I fully enjoy the time we spend together. Thank you for the beers, the food, the parties, the Friese nuchterheid in your views, and the adventures.

Patrick & Charley - For a decade we've known each other, and what fun we've had! Hiking, camping, eating, drinking, road trips, cycling, yoga, dog walks, and meaningful conversations. Thank you for your support, especially in the last couple of years. Give Charley a big hug for me, I miss that pup!

Jimbo & the road captains - Thank you for creating a community of gentlefolk around Boston, planning, organising, and running the Distinguished Gentleman's Ride, and mostly for the camaraderie and being a part in something bigger for the benefit of others.

Damian - Thank you for welcoming me into your Boston family, it's been great to learn more about wines with you, to come together for Thanksgiving dinner, and to play advanced tetris when you moved out of the flat in Cambridge. Give Banksy a pet!

Steven - Thank you for all the concerts and gigs, you're a fantastic artist and I lack the words to describe how much your music means to me.

Diemut & Charles - Thank you for bringing art into my science, I thoroughly enjoy thinking out of the box with you and helping with your art projects.

J & the Madhouse Crew - Thank you for always having an open door and a cold beer, for what you do for the motorcycle community in Boston, for taking care of my motorcycle at the time, and for the inspiration for my current build as I finish writing this thesis. J, you are an inspiration as a craftsperson/artist/builder, as a business owner, as a parent, as a friend, as a community member!

Laura & Brian - Thank you for always opening your doors to us, whether in Boston, Berlin, or LA. The coffees, the game nights, the dinners, the hikes, the beach, and the lakes are all happy memories. Laura, thank you for the designing and drawing the illustration on the cover, it is perfect!

Caro - The walks through the woods in Rhijnauwen were a very welcome distraction while finishing this thesis, thank you for creating those peaceful moments.

Irene & John - Thank you.

Mike & Irina - Thank you for opening your home and kitchen for more than a hundred documentary nights! Those evenings loaded with new information and perspectives, combined with good food, good wine, and good people, are very meaningful to me, and I hope we can continue this tradition for many years to come. They have given me a perspective beyond my research focus, and I am very grateful to you for facilitating that.

My flatmates, Edward, Tina, Lucas, Esmee, Sierk, Dewy, Josh, and Ruben, thank you for sharing the best and the worst with me, and mostly, thank you for sharing your home with me.

Boston Billies - Thank you for keeping the connection to our home alive in Boston, and our connection with Boston alive back home. I look forward to our weekends in the woods, the Thanksgiving Dinners, and celebrating our accomplishments. Iris, Margit, Hendrina, Kim, Susanne, Charles, David, Pim, thank you!

Everyone in and around Talud9, the extension of our living room. Here, many articles were read, ideas developed & discussed, and pieces written, accompanied by a proper cup of coffee or an excellent glass of wine. Wouter, Diango, Thom, Freek, Jesse, Elmar, Ruben, Ruben, Dewy, Sterre, Maxime, Max, Jesse, Anneke, Anouk, Rose, Emma, Miriam, Vijay, Marietha, Frédéric, and those I may have missed, thank you.

Theo & Lillian, Mam & Pap - Thank you for being the base for everything, for my development and growth, the home to return to, the family you have built and continue to build for over 30 years now.

Ruben & Noreen - Thank you for your support throughout this endeavour. Your willingness to listen and give advice has meant the world to me. Most importantly, the positive energy you both bring and generate with your attitude and humour to, anything really, is contagious, and I look forward to sharing many more happy moments with you together!

Laura, Liebling, ik houd van je!